DOT/FAA/TC-13/26

Federal Aviation Administration
William J. Hughes Technical Center
Aviation Research Division
Atlantic City International Airport
New Jersey 08405

Durability and Damage Tolerance Testing of a Beechcraft Starship Forward-Wing With Large Damages

April 2017

Final Report

U.S. Department of Transportation
Federal Aviation Administration

NOTICE

Technical Report Documentation Page

1. Report No.	2. Government Accession No.	3. Recipient's Catalog No.
DOT/FAA/TC-13/26		

4. Title and Subtitle	5. Report Date
DURABILITY AND DAMAGE TOLERANCE TESTING OF A BEECHCRAFT STARSHIP FORWARD-WING WITH LARGE DAMAGES	April 2017
	6. Performing Organization Code

7. Author(s)	8. Performing Organization Report No.
John S. Tomblin, Ph.D. and Waruna P. Seneviratne, Ph.D.	

9. Performing Organization Name and Address	10. Work Unit No. (TRAIS)
Department of Aerospace Engineering National Institute for Aviation Research Wichita State University Wichita, KS 67260-0093	11. Contract or Grant No.

12. Sponsoring Agency Name and Address	13. Type of Report and Period Covered
U.S. Department of Transportation Federal Aviation Administration Office of Aviation Research Washington, DC 20591	Final Report
	14. Sponsoring Agency Code AIR-100

15. Supplementary Notes

The Federal Aviation Administration William J. Hughes Technical Center Aviation Research Division Technical Monitors were Curtis Davies, Peter Shyprykevich, and Lynn Pham.

16. Abstract

A methodology synthesizing the life factor, load-enhancement factor (LEF), and damage in composites is proposed to determine the fatigue life of a damage-tolerant composite airframe. This methodology should further extend the current practice during damage tolerance certification to focusing on the most critical damage locations of the structure. In addition, this methodology interprets the structural and load details into the most representative repeated load testing in element level to gain information on the residual strength, fatigue sensitivity, inspection methods, and inspection intervals during full-scale test substantiation. To prevent the unintentional failure of a damaged article during the durability and damage tolerance (DaDT) testing, especially when investigating extremely improbable high-energy impact threats that reduce the residual strength of a composite structure to limit load, rigorous inspection intervals are required. The probability of failure of the damaged structure with the enhanced spectrum loads can be evaluated using the proposed cumulative fatigue reliability (CFR) model, which was validated through a full-scale test demonstration of a damaged article at the critical load path. Information from this model can also be used to allot economical and reliable inspection intervals during service based on target reliability and critical damage threshold. Full-scale DaDT tests conducted with visual impact damage on the aft spar (secondary load path), using the updated LEFs based on the design details of a Starship forward wing structure, demonstrated the repeated life requirements according to the proposed load-life-damage hybrid approach, and the post-DaDT residual strength requirements. The Starship forward-wing DaDT test article with significant damage on the front spar (primary load path) demonstrated the capability of the CFR model to predict the damage growth in terms of reliability and the capability of the model to determine the inspection levels. Although it is not a one-to-one correlation for the damage propagation or its size, the CFR model highlighted load segments that resulted in the gradual progression of local damage, such as possible matrix cracks, and the global impact of high loads that resulted in evident damage growth.

17. Key Words	18. Distribution Statement
Composite, Starship, Damage tolerance, Fatigue, Load-enhancement factor, Life factor, Load-life shift, Cumulative fatigue reliability	This document is available to the U.S. public through the National Technical Information Service (NTIS), Springfield, Virginia 22161. This document is also available from the Federal Aviation Administration William J. Hughes Technical Center at actlibrary.tc.faa.gov.

19. Security Classif. (of this report)	20. Security Classif. (of this page)	21. No. of Pages	22. Price
Unclassified	Unclassified	213	

ACKNOWLEDGEMENTS

The authors would like to acknowledge the technical guidance and support of Mr. Peter Shyprykevich (retired), Mr. Curtis Davies, and Dr. Larry Ilcewicz of the FAA. The support of the Aircraft Structural Testing and Evaluation Center, Composites, and Structures Laboratories of the National Institute for Aviation Research, Wichita State University, Wichita, Kansas, is greatly appreciated. The authors would also like to thank Hawker Beechcraft, Wichita, Kansas, for their support for full-scale structural test planning.

TABLE OF CONTENTS

LIST OF FIGURES

LIST OF TABLES

LIST OF SYMBOLS, ABBREVIATIONS, AND ACRONYMS

α	Weibull shape parameter
α_0	Intermediate shape parameter generated from Sendeckyj analysis
α_R	Static-strength shape parameter (modal value)
α_L	Fatigue-life shape parameter (modal value)
$\hat{\alpha}_{FL}$	Fatigue-life shape parameter for a set of S-N data
$\hat{\alpha}_{IW}$	Fatigue-life shape parameter from Individual Weibull analyses
$\hat{\alpha}_{JW}$	Fatigue-life shape parameter from Joint Weibull analyses
$\hat{\alpha}_{Sendeckyj}$	Fatigue-life shape parameter from Sendeckyj analyses
α_{SLi}	Individual Weibull shape parameter for data in i^{th} stress level
$\hat{\alpha}_{SS}$	Static-strength shape parameter for a set of S-N data
δ	Static-strength reduction factor
σ_a	Maximum/minimum applied cyclic stress
σ_{a_i}	Maximum/minimum applied cyclic stress at i^{th} fatigue cycle
σ_e	Equivalent static strength
σ_r	Residual strength
σ_{r_i}	Residual strength at i^{th} fatigue cycle
$\Gamma()$	Gamma distribution function
γ	Level of confidence
$\chi^2_\gamma(2n)$	Chi-square distribution with $2n$ degrees of freedom at γ–level confidence
$\bar{A}$	Mean value
$\hat{A}$	Characteristic residual strength or fatigue life (or scale/location parameter in a Weibull distribution)
$\check{A}_\gamma$	Lower-bound estimate of $\hat{A}$ with a γ-level of confidence
$\check{A}_R$	Applied/designed stress or fatigue life
C	Sendeckyj fitting parameter
N	Test duration for full-scale test articles in terms of DTL
N_F	Life (scatter) factor
$N_f(\sigma_a)$	Number of cycles to failure for constant-amplitude fatigue loading at σ_a
n	Number of (full-scale) test articles
n_d	Number of data points in the data group
n_f	Number of fatigue cycles
n_{fd}	Number of failures in the data group
P	Load
P_f	Probability of failure
p	Required reliability at γ-level of confidence
R	Desired reliability
S	Sendeckyj fitting parameter
S_F	Reduction to residual strength
TR	Target reliability
X	Scatter factor

$\hat{X}$	Static factor prior to the damage
$\hat{X}_i$	Static factor for the i^{th} fatigue cycle
$\hat{X}_0$	Initial static factor prior to the damage
x	Random variable
4PB	Four-point bend specimen
ADL	Allowable damage limit
BDLL	Beechcraft design limit load
BVID	Barely visible impact damage
CAI	Compression after impact
CAT1	Category 1
CAT2	Category 2
CAT3	Category 3
CDT	Critical damage threshold
CF	Conversion factor
CFR	Cumulative fatigue reliability
DAC	Data acquisition
DaDT	Durability and damage tolerance
DLL	Design limit load
DLT	Design lifetime
DTE	Damage tolerance element
DTH	Digital tap hammer
DUC	Digital universal conditions
DUL	Design ultimate load
FWS	Forward wing station
IR	Infrared
LEF	Load-enhancement factor
LID	Large impact damage
LLD	Load-life-damage
LLRS	Linear loss of residual strength
MIA	Mechanical impedance analysis
MLSP	Modal fatigue-life shape parameter
MSSP	Modal static-strength shape parameter
NDI	Nondestructive inspection
NIAR	National Institute for Aviation Research
NRLL	NIAR research limit load
NRUL	NIAR research ultimate load
POF	Probability of failure
RSRA	Rotor Systems Research Aircraft
RTA	Room temperature ambient
SCF	Stress concentration factor
SLB	Subset of load block
SL1	Stress level 1
SL2	Stress level 2
SMT	Shear-moment-torque (loads)
S-N	Stress vs. number of fatigue cycles survived

TTU	Through-transmission ultrasonic
VID	Visual impact damage

EXECUTIVE SUMMARY

Over the past 25 years, the use of advanced composite materials in aircraft primary structures has increased significantly. In 1994, NASA and the FAA revitalized the use of composites in general and commercial aviation with the Advanced General Aviation Transport Experiments program. Driven by the demand for fuel-efficient, lightweight, and high-stiffness structures that have fatigue durability and corrosion resistance, modern, large commercial aircraft are being designed with more than 50% composite materials. Although there are key differences between metal and composite damage mechanics and durability concerns, the certification philosophy for composites must meet the same structural integrity, safety, and durability requirements as metals. Despite the many advantages, composite structural certification becomes challenging because of the lack of experience with large-scale structures, complex interactive failure mechanisms, sensitivity to temperature and moisture, and scatter in the data, especially in fatigue. The overall objective of this research was to provide guidance into the structural substantiation of composite airframe structures under repeated loads through an efficient approach that weighs both the economic aspects of certification and the time frame required for testing, while also ensuring safety. The research methodology reported here consisted of combining existing certification approaches used by various aircraft manufacturers with protocols for applying these methodologies with a goal to extend them to new material systems and construction techniques.

This methodology synthesizing the life factor, load-enhancement factor (LEF), and damage in composites is proposed to determine the fatigue life of a damage-tolerant composite airframe. It further extends the current practice during damage tolerance certification to focusing on the most critical damage locations of the structure and interpreting the structural and load details into the most representative repeated-load testing in element level to gain information on the residual strength, fatigue sensitivity, inspection methods, and inspection intervals during full-scale test substantiation. Rigorous inspection intervals are required to prevent the unintentional failure of a damaged article during the durability and damage tolerance (DaDT) testing, especially when investigating extremely improbable high-energy impact threats that reduce the residual strength of a composite structure to limit load. The probability of the failure of the damaged structure with the enhanced spectrum loads can be evaluated using the proposed cumulative fatigue reliability (CFR) model, which was validated through a full-scale test demonstration of a damaged article at the critical load path. Information from this model can also be used to allot economical and reliable inspection intervals during service, based on target reliability and critical damage threshold. Full-scale DaDT tests conducted with visual impact damage on the aft spar (secondary load path), using the updated LEFs based on the design details of a Starship forward wing structure, demonstrated the repeated life requirements according to the proposed load-life-damage hybrid approach, and the post-DaDT residual strength requirements. The Starship forward wing DaDT test article with large damage on the front spar (primary load path) demonstrated the capability of the CFR model to predict the damage growth in terms of reliability and the capability of the model to determine the inspection levels. Although it is not a one-to-one correlation for the damage propagation or its size, this CFR model highlighted load segments that resulted in the gradual progression of local damage, such as possible matrix cracks, and the global impact of high loads that resulted in evident damage growth.

1. INTRODUCTION

Damage tolerance methodologies for metallic airframes, both military and commercial, have been implemented for certification in terms of crack growth since the 1970s. Although the fatigue life of composites is generally flat, the impact damage sensitivity, even at static loading, is a major concern. Therefore, the ability of the structure to resist damage (damage resistance) and to perform with the presence of damage (damage tolerance) has been investigated in detail. Several certification approaches have been developed in terms of damage threat or probability of occurrence [1] as an extended methodology to the approach used by Whitehead et al. [2]. To support U.S. Navy certification efforts in predicting the static strength capability of full-scale composite structures, a semi-empirical stiffness reduction model was developed by Horton and Whitehead [3] and assumed that the impact damage acted as a slit after initial failure and arrested at the nearest stiffeners causing a stress (strain) concentration at these stiffeners and adjacent bays. Using this approach, experimental results on several different material systems, impact locations, structural geometries, and energy levels show that the majority of the data points lie within ±10% of the predictive strain. It was recognized that several parameters influence the post-impact structural response. A detailed study conducted by Rapoff et al. [4] on several coupon, element, and full-scale composites with impact damage shows that simple test coupons can accurately represent mid-bay impact damage resistance and damage tolerance of a complex composite structure. This study also shows that the static scatter generally observed in coupon-level composites is greatly reduced in impact-damaged specimens subjected to in-plane loading, while fatigue-life scatter is similar to bolted composites. A fatigue study by Curtis et al. [5] shows that impact damage grows inconsistently under cyclic loading.

Current regulations require airframes to demonstrate adequate static strength, fatigue life, and damage tolerance capability by testing/analysis with a high degree of confidence. These requirements are intended to account for uncertainties in usage and scatter exhibited by materials. The primary means of structural substantiation for most aircraft certification programs is by analysis. It is expected that the analysis will be supported by appropriate test evidence.

To develop a certification methodology for composite structures that has the same level of reliability as observed in metal certification approaches, accounting for the inherent difference between metal and composites, the FAA and U.S. Navy developed a certification approach for bolted composite structures [2 and 6] as part of the McDonnell Douglas F/A-18 certification. Figure 1 shows the material distribution forthe F/A-18 E/F aircraft. This methodology is referred to as the combined load-life approach throughout this report. This approach adopted two key requirements in metallic aircraft certification: (1) the full-scale static test article must demonstrate a strength that is equal to or exceeds 150% of the design limit load (DLL); and (2) the full-scale fatigue test article must demonstrate a life that is equal to or exceeds twice the design service life. This approach analyzes the data scatter in the static strength and fatigue life of composites to establish a certification methodology that has the same level of reliability as that for metal structures. Furthermore, this approach attempts to address the issues related to hybrid (composite and metallic) structures through the combined load-life approach, which will be discussed further in this report. This approach was developed for what, at that time, was current composite usage and did not explicitly account for the damage in composite structures or adhesively bonded structural details. Kan and Whitehead [7] proposed a damage tolerance

certification methodology to determine the reliability of impact damage on a composite structure and to calculate the allowable impact threat at a given applied load and specified reliability. Subsequent application of this methodology for an F/A-18 inner-wing structure demonstrated successful damage tolerance capabilities during certification.

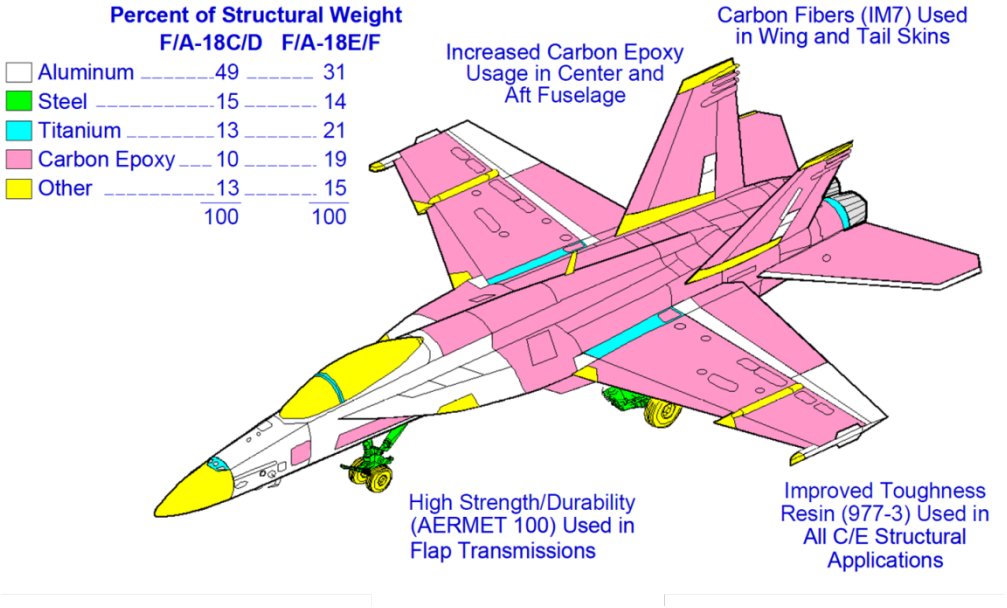

Figure 1. Material distribution for F/A-18 E/F aircraft [8]

The combined load-life methodology was adopted by Shah et al. [9] for the certification of a stiffener runout detail. They found that the strength and life shape parameters were similar to those they developed by Whitehead et al. [2]. This research successfully demonstrated the combined load-life approach for large component tests. Furthermore, the applicability of the combined life-load damage tolerance approach by Kan and Whitehead [7] for the certification of general and commercial aircraft was investigated by Kan and Dyer [10]. This study showed that the combined load-life damage tolerance approach based on military requirements is too severe for the all-composite LearAvia Lear Fan 2100 structure.

Early developments of the Boeing 737 graphite/epoxy horizontal stabilizer [11] and the Airbus A310 [12] and A320 [13] all-composite vertical tail used the combined load-life approach for full-scale demonstrations. A no-growth, damage tolerance design concept was also used in which a composite structure must demonstrate the ability to contain intrinsic manufacturing defects and the maximum allowable service damage in adverse operational conditions and throughout the DLT of the structure. Early composite certification programs recognized the need for damage tolerance structural design concepts and a certification approach for efficient composite structures. A damage-tolerant structure is assumed to have a pre-existing defect or damage that requires a detailed inspection plan under repeated loading. This enables the incorporation of intrinsic/in-service damages into the damage tolerance phase of the analysis and full-scale test substantiation. Damage tolerance methodology should include information pertaining to the critical damage threshold (CDT), and to the allowable damage limit (ADL), to support inspection intervals. Because of the highly heterogeneous nature of composite damage

progression, the analytical predictions are application-specific and require extensive empirical validation. Therefore, probabilistic methods are commonly used for composite structures.

Followed by the early development approach for the NASA/Boeing 737 horizontal stabilizer, the Boeing 777 empennage certification was primarily based on analysis supported by coupon and component test evidence [14]. The certification process includes general requirements for environmental effects in design allowables and impact damage, static strength, and fatigue and damage tolerance with a no-growth approach. By delivering predictions prior to testing, such demonstrations contribute to a solid basis for acceptance of "certification by analysis" by the FAA and the aviation industry. This is consistent with current certification practices that allow the use of analysis for certification when supported by tests.

Several all-composite business aircraft, including the Lear Fan 2100 and Beechcraft 2000 Starship, evolved in the early 1980s and completed FAA damage tolerance certification requirements [15]. The Lear Fan 2100 prototype first flew in January of 1981, but never made it to production. The all-composite Beechcraft Starship was certified in 1989 using the damage tolerance approach, identifying environmental effects and concerns related to bonded joints. To meet FAA damage tolerance requirements, major structural modifications had to be made to the wing. For full-scale durability and damage tolerance (DaDT) tests, a combined load-life approach based on flaw growth threshold stress was employed [16]. The environmental effects were addressed through an analytical approach validated by testing.

Under the Composite Affordability Initiative, Kan and Kane [17] explored the feasibility of extending probabilistic methodology for adhesively bonded composite structures. The level of maturity in three areas was thoroughly reviewed: (1) probability theories and probabilistic methods, (2) probabilistic structural analysis tools, and (3) probabilistic structural criteria and requirements. This program determined that a level of structural reliability with an equivalent level of confidence can be achieved by the probabilistic method as compared to the deterministic method.

1.1 FATIGUE LIFE ASSESSMENT OF FIBROUS COMPOSITE

Sumich and Kedward [18] investigated the use of the wearout model, on the basis of its applicability to matrix-dominant failure modes, to examine the fatigue performance of the Rotor Systems Research Aircraft (RSRA) X-Wing vehicle. Wearout models assume that structural degradation occurs with use and can be monitored by measuring parameters, such as residual strength and stiffness. Halpin et al. [19] discussed this methodology in the early 1970s, and several certification programs, such as the Corsair A-7 outer wing and Fighting Falcon F-16 empennage, have adopted this methodology for composite structures. This method determines fatigue failure when pre-existing damage grows until the specimen can no longer support the applied cyclic load. In addition, the residual runout strength is related to crack length through fracture mechanics. This approach was improved by Sendeckyj [20] using a deterministic equation that converts static, fatigue, and residual strength data into a pool of equivalent static strength data. Sendeckyj's basic model assumes that the failure in a constant-amplitude fatigue test occurs when the residual strength is equal to the maximum cyclic fatigue load. This pooling technique for fatigue data is useful in cases in which there are not enough fatigue data in

individual stress levels for Weibull analysis, which requires a minimum of six specimens in each stress level. This model has been further improved for pooling fatigue tests using multiple stress ratios [21], but has not been validated because it requires a significant amount of test data. Stress ratio or *R* ratio is the ratio of minimum and maximum cyclic stress in a fatigue test.

O'Brien and Reifsnider [22] studied fatigue life analytically using the fatigue modulus concept. This approach assumed that fatigue failure occurs when the fatigue secant modulus (residual stiffness) degrades to the secant modulus at the moment of failure in a static test. In this study, stiffness reductions resulting from fatigue damage were measured for unnotched $[\pm 45]_s$, $[0/90]_s$, and $[0/90/\pm 45]_s$ boron/epoxy laminates. Degradation in the various in-plane stiffness (axial, shear, and bending) was measured using a combination of uniaxial tension, rail shear, and flexure tests. Damage growth and stiffness loss were identified to be load history-dependent. Therefore, the secant modulus criterion was not a valid criterion for general applications. A similar study was conducted on the fatigue behavior of $[0/\pm 45/90]_s$ glass/epoxy laminate by Hahn and Kim [23], in which the secant modulus was used as a measure of damage extent.

Following an extensive review of different damage models, Hwang and Han [24] identified various cumulative damage models using several physical variables, such as fatigue modulus and resultant strain. They introduced a new concept called the "fatigue modulus," which is defined as the slope of applied stress and resultant strain at a specific cycle [25]. Fatigue modulus degradation assumes that the fatigue modulus degradation rate follows a power function of the fatigue cycle. The theoretical equation for predicting fatigue life is formulated using the fatigue modulus and its degradation rate. This relation is simplified by the strain failure criterion for practical applications. Mahfuz et al. [26] analytically studied the fatigue life of an S2-glass/vinyl-ester composite using the fatigue modulus concept. This study revealed that the fatigue modulus is not only a function of loading cycle, but also a function of applied stress level and thickness of the test specimen. This life-prediction methodology requires two parameters that are obtained empirically either at two different stress levels or two different fatigue life times.

Halpin et al. [27] suggested that the fatigue behavior of composites should be based empirically under the design spectra. The main disadvantage of such an approach is that test results are specific to a loading spectrum. Also, a significant amount of test data is required for a complete analysis, like the extensive fatigue sensitivity study conducted by Jeans et al. [28] on bolted and bonded composite joints under various loading spectra. For metals, Miner's rule is often used to study the cumulative damage under a loading spectrum. However, Rosenfeld and Huang [29] conducted a fatigue study with different stress ratios to determine the failure mechanisms under compression of graphite/epoxy laminates and showed that Miner's rule fails to predict composite fatigue under spectrum loading. This was confirmed by several authors in the composite community. A study conducted by Agarwal and James [30] on the effects of stress levels on fatigue of composites confirmed that the stress ratio had a strong influence on the fatigue life of composites. Further, they showed that microscopic matrix cracks are observed prior to the gross failure of composites under both static and cyclic loading.

For practical consideration, Yang and Du [31] investigated the possibility of statistically predicting the fatigue behavior of composites under service-loading spectra, based on some

baseline constant-amplitude fatigue data. Although such a phenomenological statistical model does not account for the intrinsic failure mechanisms that are quite complex in composite materials, it can be very simple for practical applications and requires significantly less empirical effort.

Kassapoglou [32] presented a probabilistic approach for determining fatigue life for composite structures under constant-amplitude loading. This approach assumes that the probability of failure (POF) during any cycle is constant and equal to the POF obtained from static test results and associated statistically quantified scatter. This methodology does not require any fatigue data for calibration or for the expressions of the cycles to failure as a function of stress ratio. The comparison of fatigue life predictions for several stress ratios with a significant amount of experimental data shows good correlation. However, the assumptions used in this model neglect the complex progressive damage mechanism that takes place during repeated loading.

1.2 IMPACT DAMAGE ON COMPOSITE STRUCTURES

A study conducted by Dost et al. [33] on the impact damage resistance of laminated composite transport aircraft fuselage structures empirically determined the relative importance and quantitative measure of the effect of numerous variables, such as material, laminate, boundary condition, impactor type, and their interactions. An extensive study conducted on toughened-epoxy laminates by Dost et al. [34] shows that the damage state and the post-impact compressive strength behavior of composites is a strong function of the laminate stacking sequence. A similar study conducted by Sharma [35] shows that strength degradation due to impact is dependent on the laminate configuration and fiber matrix combination. Also, laminates with more angle plies near the impact surface and unidirectional plies elsewhere showed extensive interply and intraply fiber delaminations at failure relative to laminates with a cross-ply on the impact surface.

Tomblin et al. [36] outlined the philosophy for the damage tolerance certification approach for sandwich structures with several case studies and identified five major tasks for the damage resistance and tolerance characteristics of sandwich structures: (1) damage development due to low-velocity impact, (2) post-impact strength, (3) flaw-growth threshold and damage evolution under cyclic loading, (4) analytical model development, and (5) full-scale/subcomponent testing and verification. These experimental observations should be used for developing and validating a semi-empirical model to predict the damage resistance and tolerance capabilities for a given sandwich panel configuration. Subsequent research by Tomblin et al. [37] investigated the effects of several impact parameters on damage resistance and tolerance, detectability of impact damage using field inspection techniques, and fatigue loading. Further studies by Tomblin et al. [38] on scaling studies of sandwich structures indicate that residual strength is affected by the ratio of specimen size to damage size and is dependent on the number of plies in the facesheets. Furthermore, the studies show that damage development is the dominant energy-dissipation mechanism and depends on the ratio of the impactor mass to the target mass. Based on an investigation conducted on honeycomb and foam-core sandwich panels, Raju [39] showed a strong dependency of the indentation response and the failure mechanism on indenter size and core type. These studies show that information on both dent depth and planar damage size need to be included in certification of the composite structure. It is clear that visual inspection

methods can be misleading and that residual indentation cannot be used as a reliable damage metric for static ultimate-strength and damage tolerance criteria for sandwich structures.

1.3 BACKGROUND FOR CURRENT APPROACH

Based on current safety standards, composite materials are considered insensitive to fatigue failures. Most previous research efforts in damage tolerance have been focused below the CDT using fairly small coupons, and therefore, the results obtained have been more conservative. With the increased use of composite materials in primary structures, there is a growing need to investigate extremely improbable, high-energy impact threats that reduce the residual strength of a composite structure to limit load. Currently, this issue is not explicitly addressed in full-scale substantiation, and no fatigue requirements exist (i.e., only "get home[1]" loads). To verify that the structure has sufficient residual strength to sustain the expected in-service loads, once damages have been introduced, a typical certification program for composite structures is conducted in two phases. The first phase demonstrates the durability of the structure, and the second includes a damage tolerance phase into the durability test. Alternately, the damage tolerance phase can be introduced earlier in the testing with alternative requirements (e.g., rigorous inspection plans or repair after a certain test duration).

Composite structural test loads are enhanced to reduce long test duration requirements, which are a direct result of the data scatter observed in composites relative to metals, using the combined load-life approach proposed for U.S. Navy F/A-18 certification [1], so that the same level of reliability as for metal structures can be achieved. Compared to the metal static and fatigue data, composite materials exhibit high data scatter because of their anisotropic heterogeneous characteristics, such as layup, manufacturing defects and imperfections, test complications, and environment. To interpret that information in a meaningful manner and to incorporate any potential effects into the certification of composite structures, the life factor and the load-enhancement factor (LEF) are two commonly used approaches that require composite scatter analysis. The life factor approach, which has been successful for metallic structures to assure structural durability, accounts for the scatter in life data (e.g., S-N, where S is stress and N is the number of fatigue cycles survived) in terms of the population shape parameter. The life shape parameter that (often referred to as the modal life shape parameter) is obtained by analyzing the distribution of the shape parameters that correspond to S-N curves representing different design details of the structure as described in reference 40. The life factor corresponds to the central tendency (mean) of the population to the extreme statistics (allowable). The underlying objective of the life factor approach is to ensure that the design service goal or life is representative of the weakest member of the population after a specified life in service. Therefore, a successful repeated load test to mean fatigue life would demonstrate the B-basis reliability on the design lifetime. The combined load-life approach showed that the life shape parameters of metal and composites are 4.00 and 1.25, respectively, and they correspond to life factors of 2.093 and 13.558, respectively, for B-basis reliability [1]. Therefore, because of the large scatter in the composite test data, a composite structure is required to test additional fatigue

[1] Loads that the structure has to withstand to safely land the aircraft following a discrete source damage involving extreme cases, such as bird strike, lightning strike, engine fire, and engine rotor burst, which are obvious to the aircraft crew.

life to achieve the desired level of reliability (i.e., test duration of more than 13 DLTs for composite in contrast to 2 DLTs for metal to achieve the B-basis reliability).

An alternative to the life factor approach, which requires an excessive test duration, was to increase the applied loads in the fatigue spectrum so that the same level of reliability can be achieved with a shorter test duration [1]. This alternate approach, known as the LEF approach, was derived from combining the life factor and the static factor (ratio of mean to allowable fatigue strength) at one DLT to form a relationship between the LEF and the test duration. The static factor is defined in terms of a model static-strength shape parameter (MSSP) that is obtained by analyzing the distribution of the shape parameters, which correspond to static strength data sets representing different design details of the structure, as described in reference 40. The formal relationship between the LEF and the test duration provides the flexibility of conducting a durability test of a composite structure with different LEFs and the corresponding test durations to achieve the desired reliability. Although the materials, processes, layup, loading modes, failure modes, etc. are significantly different, most current certification programs use the load-life factors generated for the U.S. Navy F/A-18 certification program. A detailed scatter analysis of several composite databases showed that both load and life factors can be significantly reduced by using strength and life shape parameters generated for materials, processes, loading modes, and failure modes applicable to a specific structure [40]. However, guidance for developing these shape parameters is greatly needed.

Although fatigue life is adversely affected by damage (notch), the scatter in damaged composites, both static and fatigue, tends to decrease due to localized stress concentration. This is favorable for generating static and life factors and results in lower life factors and LEFs. Therefore, scatter analysis of coupons in lower levels of testing building blocks can be used to develop a synergy among the life factor, LEF, and damage in composites. This approach is beneficial for the damage tolerance phase of full-scale substantiation and minimizes the risks associated with the introduction of large damage to durability test articles.

Scatter analysis development, applicable to current composite materials and processes using improved test methodologies, demonstrates lower requirements for the life factor and LEFs. Introducing damage philosophy into the scatter analysis further reduces these factors. The probabilistic approach used in the combined load-life approach shows the potential use of improved shape parameters for estimating the effects of design changes (i.e., gross weight changes) on DLT. This requires a probabilistic approach to redefine basis (A- or B-basis) fatigue life requirements set forth in the combined load-life approach to any deviation from the life (i.e., reduction in life factor due to damage introduction) or load factor (i.e., high spectrum fatigue loads due to gross weight change). For a full-scale test that was conducted using a higher LEF or that completed more than the required test duration, this technique can be used to redefine original design service goals (number of hours equivalent to one life) associated with the fatigue spectrum.

1.4 OBJECTIVES AND OVERVIEW OF RESEARCH

The key objective of this research was to develop a probabilistic approach to synthesizing the life factor, LEF, and damage in composite structures to determine the fatigue life of a

damage-tolerant aircraft. This methodology was extended to the current certification approach to explore extremely improbable high-energy impact threats (i.e., damages that reduce the residual strength of aircraft to limit-load capability and allow incorporating certain design changes into full-scale substantiation without the burden of additional time-consuming and costly tests). Research was conducted in three phases (figure 2):

1. Combined load-life approach
2. Damage tolerance and flaw growth tests
3. Load-life-damage (LLD) hybrid approach

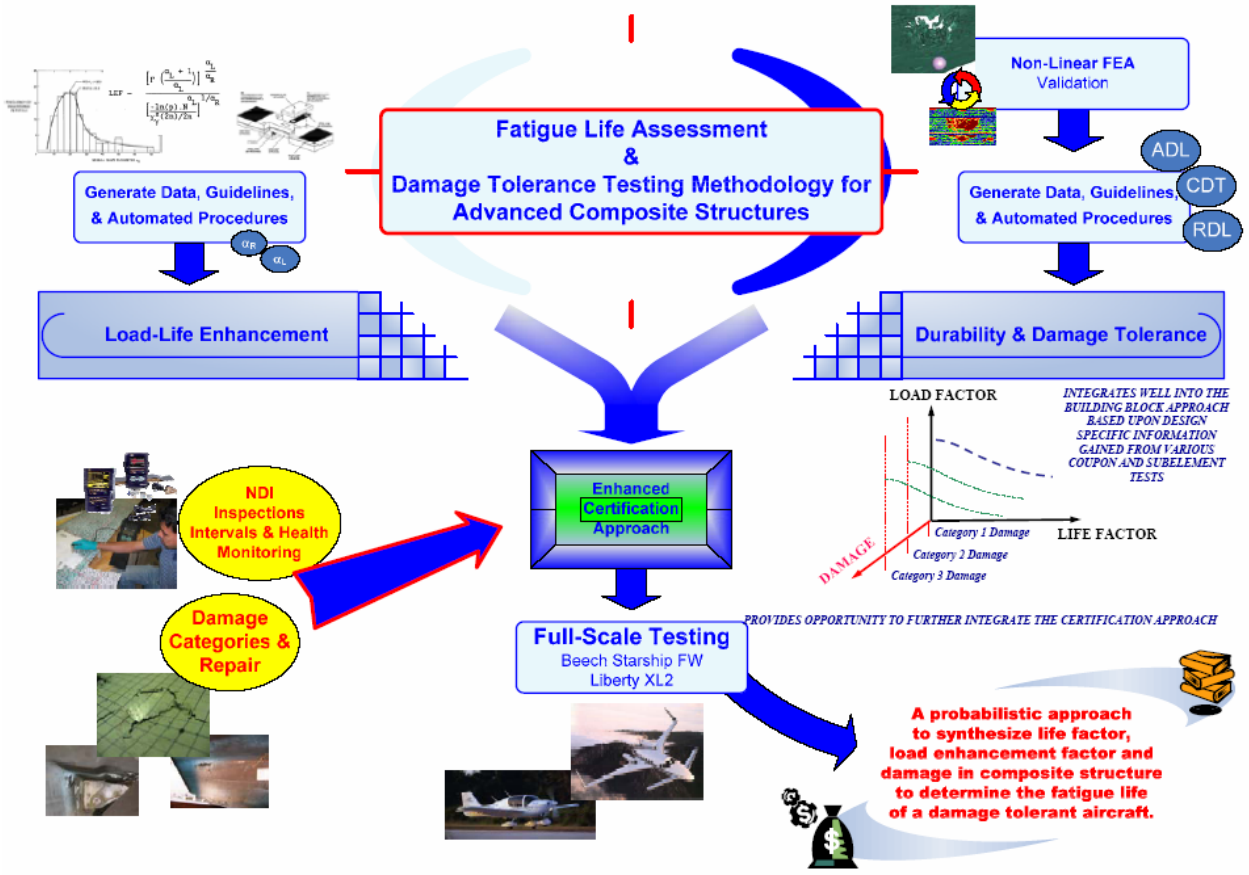

Figure 2. Overview of research

The first task of phase 1 generated a database of fatigue life data for several composite material systems that are commonly used in general aviation. The second task in this phase was to add MSSPs to the database and generate improved LEFs for several example materials. These data were then used to generate necessary load-life combined data (e.g., full-scale demonstrations included in the final stage of the research). The improvements in materials and processes and test methods produced life and load factors lower than the values commonly used in most certification programs based on the combined load-life approach. Data gathered in this phase were used to provide guidance for generating safe and reliable load and life factors pertaining to a specific structure. In addition, a user-friendly computer code that can be used for a scatter

analysis of composites was developed. This code alleviates misinterpretation of any statistical or mathematical processes during the analysis and provides guidance for selecting different techniques appropriate for a particular application. The results of this task are included in reference 40.

Although the composite data scatter for unnotched specimens is considerably high because of the heterogeneous nature of laminated composites and competing failure modes, the notched or damaged composite data show significant reduction in the data scatter because of the localized stress concentration. The primary goal of phase 2 was to capture the effects of damage on the composite data scatter in the element level and interpret this information in a meaningful manner for damage tolerance testing of composite structures. During phase 2, the fatigue characteristics of different categories of damages were studied. These data were combined with data obtained in phase 1 and were used in methodology development and full-scale validation in the final phase. When simulating high-energy damage, especially if it is incorporated in the early phases of testing, care must be taken to control its intensity so as not to exceed the required damage threat level. In addition, a methodology was introduced to investigate the impact of a large defect on the POF of the structure during the DaDT phase. This approach can also be used to allot inspection intervals economically to prevent the unintentional failure of the damaged structure.

The final phase combined data from the first two phases and developed the improved damage tolerance test methodology, a synergy of life factor, LEF, and damage. This methodology highlights the reductions in data scatter due to the improvements in material and process techniques and the test methods of composites, and provides the flexibility of using appropriate life factor and LEF requirements during different phases of the durability and damage tolerance testing of composite structure. This methodology further extends the current practice during damage tolerance certification to focus on the most critical damage locations of the structure and interpret the structural and load details into the most representative repeated load testing in element level. The information gained on the residual strength, fatigue sensitivity, inspection methods, and inspection intervals during element level testing is beneficial to the full-scale test substantiation. A reliability approach to determine the inspection intervals to mitigate risks of unexpected failure during phase 2, especially with large impact damage (LID), was discussed in section 3.4. This methodology was validated with several full-scale test examples of the Beechcraft Starship forward wings with LID on the front and aft spars (figure 3). Full-scale test articles were numbered ST001 through ST006. Following static strength close to ultimate load (no fracture), the aft spar of the ST001 test articles was impacted and tested in phase 2 by renaming it ST001(R). The Beechcraft Starship forward wing was designed to be significantly conservative. Therefore, the Beechcraft design limit load (BDLL) and ultimate loads were adjusted for the purpose of this research following the three static tests, ST001 through ST003, using a conversion factor (CF). The adjusted DLLs and DULs are referred to as National Institute for Aviation Research (NIAR) research limit load (NRLL) and NIAR research ultimate loads (NRUL), respectively.

The front spar of the forward-wing structure is the primary load path and LID that results in a decrease of the residual strength to its limit-load was considered Category 3 (CAT3) damage. The LID that was on the aft spar was considered Category 2 (CAT2) damage and its contribution to the final failure of the structure was secondary. Table 1 in section 3.1.3 describes the

categories of damage. Several element-level tests were conducted to determine the impact parameters for inflicting this damage on full-scale structures. The strategic placement of strain gages around the damage and near-critical areas provided real-time feedback during damage tolerance tests. The strain data provided information similar to a built-in health monitoring system and provided details in real time to assess the state of the damage (i.e., whether there is propagation) and any global effects on the structure due to possible damage growth.

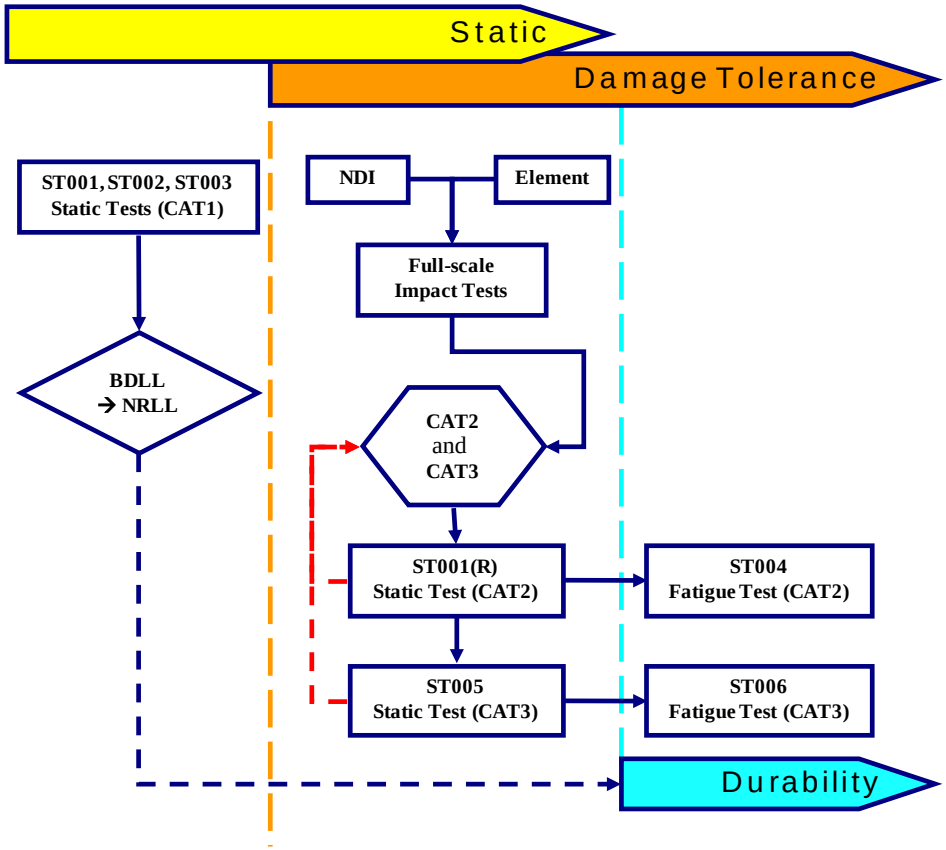

Figure 3. Full-scale testing outline

2. EXPERIMENTAL PROCEDURE

This section contains a brief description of the test articles, instrumentation, nondestructive inspections (NDIs), and procedures for a full-scale test program.

2.1 TEST ARTICLE DESCRIPTION.

The Beechcraft Starship forward wing with a titanium leading edge was selected as the full-scale test article (figure 4). Two left-hand and four right-hand wings were subjected to both static and fatigue testing, while introducing LID that was beyond what is typically induced during full-scale test substantiation. The wing box was of graphite/epoxy construction, and the skin and front spar were constructed of Normex® honeycomb. The aft spar and both root and tip ribs were constructed of solid laminate. The front spar caps were primarily wound graphite roving to match the skin thickness.

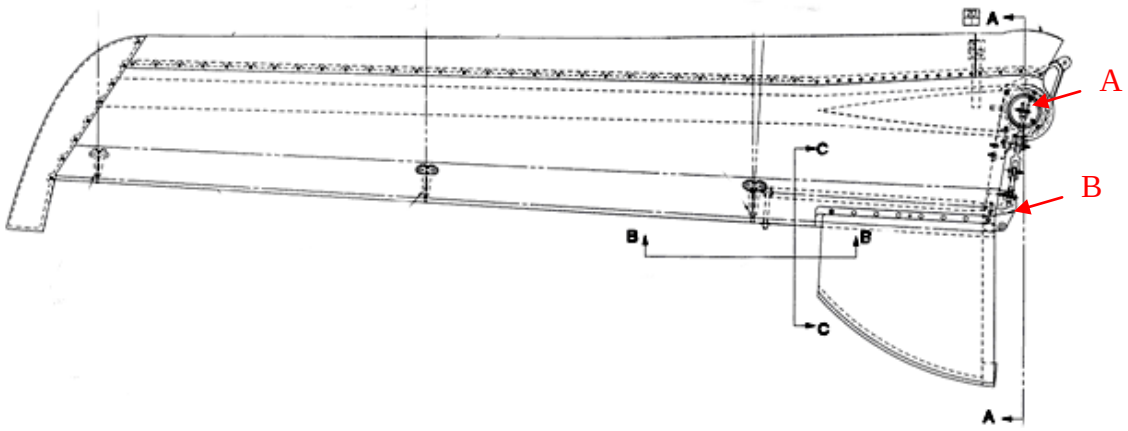

Figure 4. Beechcraft Starship forward wing: (a) constraint point of the front spar and (b) constraint point of the aft spar

2.2 FULL-SCALE TEST SETUP

Static test articles were performed only in cantilever up-bending test configuration. Fatigue tests were performed with a test spectrum that has both up- and down-bending, while maintaining shear-moment-torque (SMT) loads. Test articles were mounted upside down and fixed at the root end to a rigid test fixture. A steel pin that attaches the forward wing to the fuselage was used to constrain translations at the pin cutout lug located at the root end of the front spar caps (point A in figure 4), while restraining the ration of the test article (in the horizontal plane) at the aft spar at the wing root (point B in figure 4).

Load-formers and bonded patches attached to whiffletree assemblies were used to load static (figure 5) and fatigue (figure 6) test articles, respectively. Each actuator was connected to the test rig and to the loading fixture through swivel (universal) joints releasing rotational degrees of freedom to minimize localized bending and unintentional side loads. A static test whiffletree was attached to the actuator through a steel cable-pulley assembly and the control load cell was mounted directly to the whiffletree end through a hinge connector. This arrangement reads the applied load at the whiffletree and eliminates errors induced by the friction of the pulley assembly.

Figure 5. Full-scale static test setup—load formers

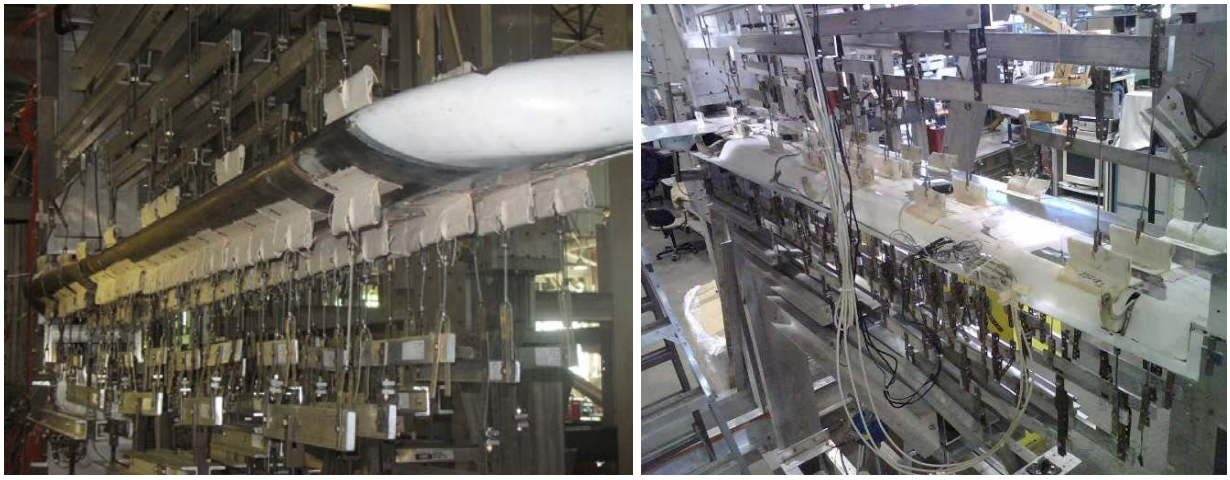

Figure 6. Full-scale fatigue test setup—load patches

2.3 LOAD CONTROL SYSTEM

A closed-loop force feedback MTS® AeroST structural test controller (figure 7) with full-range 493.79 digital universal conditioners (DUC) with MTS AeroPro™ control and data acquisition (DAC) software was used for the full-scale tests. AeroPro software features a powerful arsenal of test accelerating and optimization tools facilitating a streamlined test setup and execution. AeroPro helped speed up pre-test diagnostics and post-test analysis by quickly running targeted queries across large amounts of data to isolate essential information.

Figure 7. AeroST Structural Test Controller

2.4 DATA ACQUISITION SYSTEM

The EX1629, a 48-channel high-performance strain gauge instrument from VXI Technology, Inc., was used to acquire data during full-scale testing. This high-performance DAC system, which is tightly integrated into MTS AeroPro software, is a standalone DAC platform and has a modular 48-channel design (figure 8).

Figure 8. The EX1629 DAC System

2.5 INSTRUMENTATION AND STRAIN SURVEYS

Test articles were strain-gaged with quarter-bridge strain configuration, as shown in figure 9. Because DaDT full-scale tests were conducted overnight, temperature-compensating strain configuration was used to minimize strain anomalies due to ambient laboratory conditions. Because only one leg of the Wheatstone bridge (shown in figure 9) is active and the dummy gage is used only for temperature compensation, this configuration is considered a quarter-bridge rather than a half-bridge, which would contain two completion (external) strain gages.

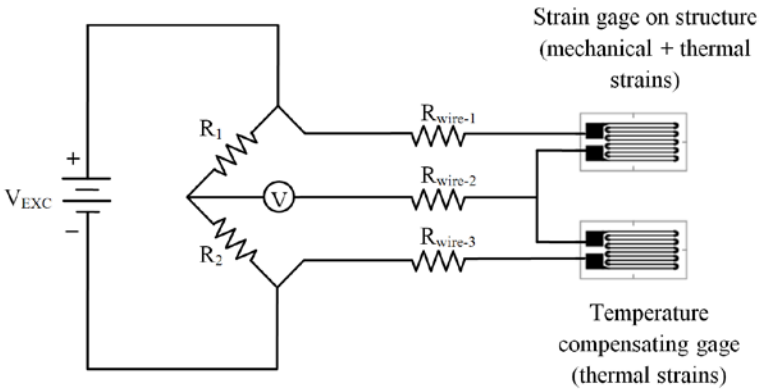

R = resistance
V = excitation voltage

Figure 9. Quarter-bridge configuration with temperature compensator strain gage

When using this configuration, the active strain gage was bonded to the structure and exposed to physical strain, while the dummy (temperature compensation) gage was bonded to a material that has the same temperature characteristics as the strain gage backing material so that it is isolated from physical strains. However, because the dummy gage was placed next to the active gage, they were both exposed to the same ambient conditions. Therefore, the change in resistance due to temperature changes was automatically isolated from the active gage; that is, only change in resistance because of physical strain at the active gage is used to determine the strain value. In addition, the wire lengths were the same for both gages, which canceled the additional resistance added by the wire-connecting strain gages.

2.5.1 Full-Field Strain Evolution

The ARAMIS photogrammetry full-field strain measurement system, as shown in figure 10, was used to measure localized buckling in the region of debonds/defects. The ARAMIS [41] is a noncontact, optical, three-dimensional deformation measuring system. It uses two high-definition cameras to track translation and rotation of the surface details (object characteristics) with subpixel accuracy. Surface details are obtained by applying a stochastic speckle pattern that follows surface displacement during loading (figure 10). The ARAMIS uses this pattern to recognize the surface structure and uses digitized images from both cameras for the triangulation of surface details (micropattern) to determine the precise location of each point. Therefore, this system has the capability of digitizing the precise shape (surface) of the structure during loading. The first set of coordinates for object characteristics is obtained in the undeformed stage. After load application, a new set of coordinates (digital images) is recorded. ARAMIS then compares the digital images and calculates the displacement and deformation of the object characteristics. The ARAMIS photogrammetry system with a typical stochastic speckle pattern is shown in figure 10.

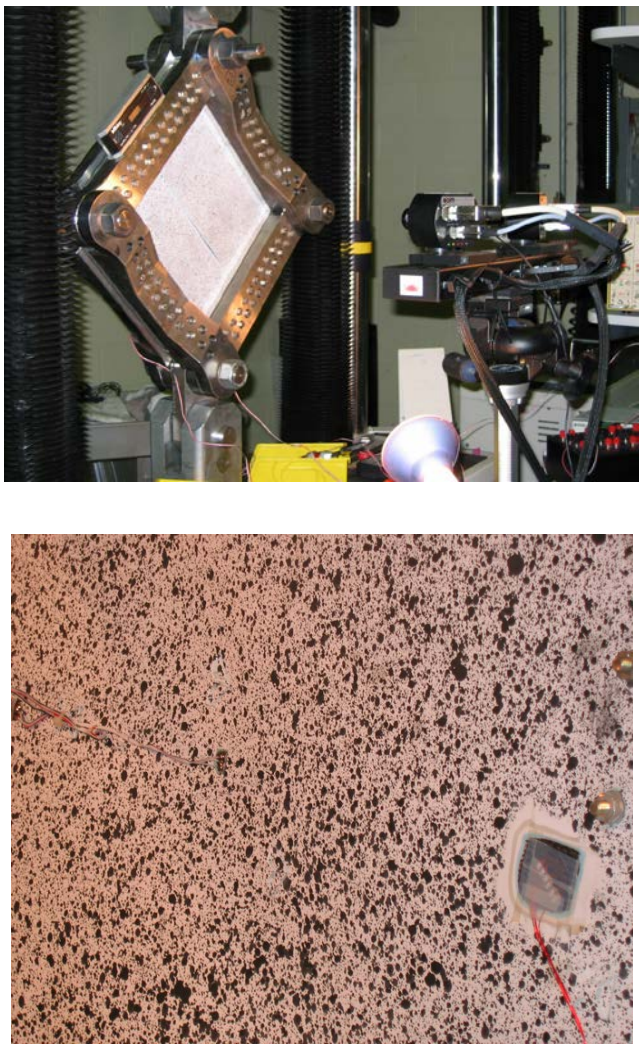

Figure 10. The ARAMIS photogrammetry system and speckle pattern

The ARAMIS is capable of three-dimensional deformation measurements under static and dynamic load conditions to analyze deformations and the strain of real components. In addition, this system is able to eliminate the rigid-body motion component from the displacement results. Therefore, it can be used for specimens that exhibit large displacements. Strain sensitivity of the system is approximately 100-200 microstrains, and the scan area can be as large as 47 by 47 in. Full-field displacement and strain data are then used to examine any propagation of the defects according to the procedures outlined by Tomblin et al. [42], which assess the localized skin buckling (out-of-plane displacement) around the debonded or delaminated region. The full-field strain evaluation of compression after impact (CAI) specimens during static (figure 11) and fatigue loading was measured using the ARAMIS photogrammetry system.

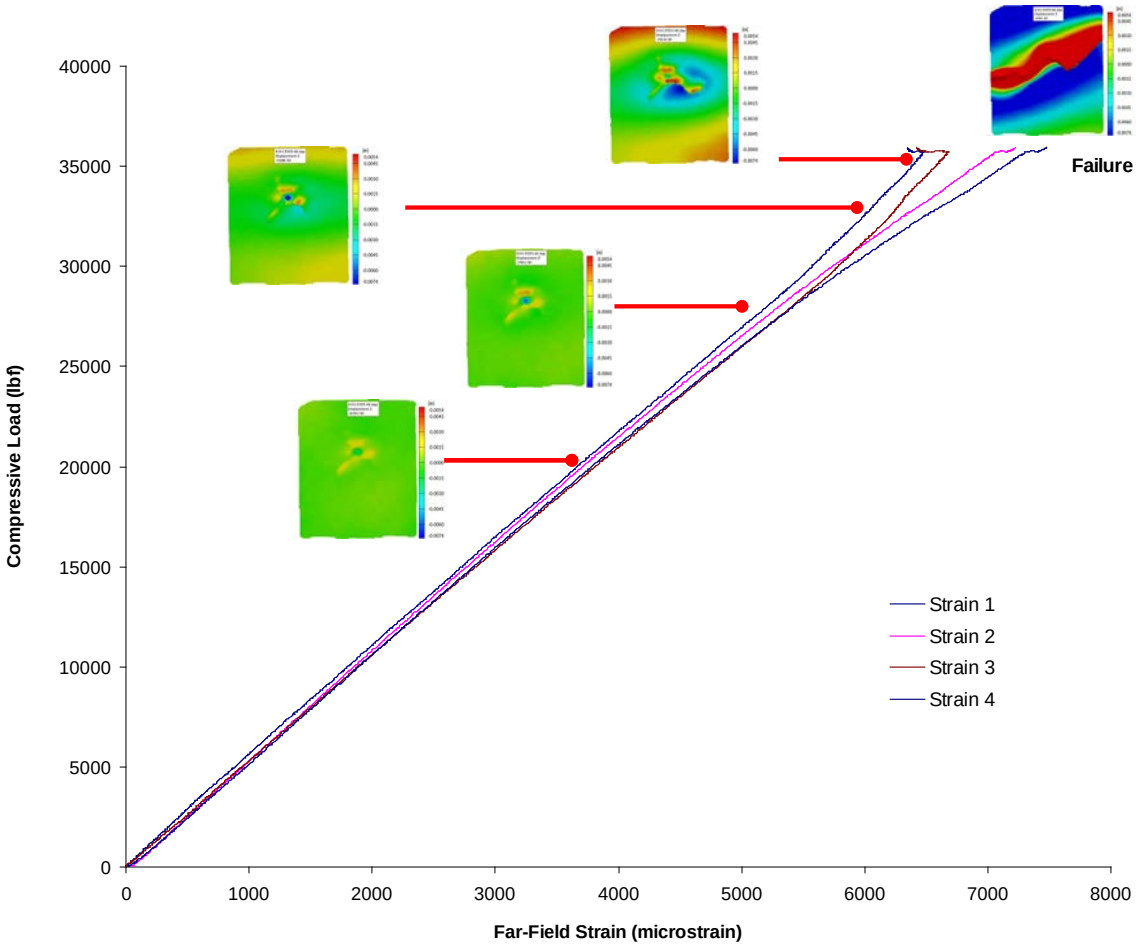

Figure 11. Damage evolution of a CAI specimen under static loading

2.6 NDIs

Unlike with a standard certification program, damages inflicted on damage-tolerant, full-scale articles for this research were more severe (i.e., large CAT2 and 3 damage). Therefore, NDI requirements for damage tolerance testing require detailed NDIs. NDIs on element tests and full-scale articles were performed using several techniques:

- Through-transmission ultrasonic (TTU)
- Ultrasonic flaw detector (pulse-echo)
- Pulsed thermography
- Tap testing

Impacted elements were subjected to TTU NDIs that generated C-scans to quantify the planar-damaged areas using image-analysis software (figure 12). Additional inspection techniques (e.g., microscopy and thermal imaging) were also used for the damage tolerance investigation.

Figure 12. The TTU scanning of a sandwich test specimen

In addition to TTU C-scans, test specimens in the test fixture were inspected with the Sonic® 1200 ultrasonic flaw detector and BondMaster™ 1000 hand-held NDI units. The BondMaster 1000 is capable of resonance, mechanical impedance analysis (MIA), and pitch/catch mode, and the user can select the method best suited for inspecting a particular composite structure. The MIA technique, which was used for inspecting test specimens in this program, measures the stiffness and mass of the material under test and requires no coupling agents. The output was measured in both amplitude and phase. Both handheld units are equipped with color displays and provide real-time data.

Noncontact pulse thermographic inspections were conducted. A brief pulse from a programmable flash lamp that provides a uniform illumination was used to heat the surface of the test area, while an infrared (IR) camera with a frame rate of 60 Hz recorded changes in the surface temperature. As the sample cooled, the surface temperature was affected by internal flaws. Using a thermographic signal reconstruction method, the captured data were converted into full-field NDI images.

Standard tap testing was used to scan the test articles, and detailed inspections were conducted using RD3™ electronic digital tap hammer (DTH). This unit consists of a lightweight hammer containing an accelerometer, which is connected by flexible cable to components and a liquid crystal display. The DTH supplements the subjective tonal discrimination of the operator, which is often the case for the standard coin tap or tap hammer test with a quantitative, objective numeric readout that can be correlated to damage in the structure.

2.7 FULL-SCALE TEST SUBSTANTIATION

The Beechcraft Starship forward wing was designed with a significant amount of conservatism. Therefore, the Beechcraft design limit and ultimate loads were adjusted for the purpose of this research following several static tests using a CF. These redefined limit and ultimate loads are NRLL and NRUL, respectively. Full-scale tests were conducted to address four different aspects of the certification of composite structures (figure 3): static, damage tolerance, durability, and repair.

For durability test articles with impact damage, the original whiffletree locations needed to be modified around areas of damage so that the load was redistributed without significantly influencing the overall SMT loads. Because areas of damage induced on the structure were significantly larger than the ones typically introduced during certification, aggressive NDI and health-monitoring strategies (sections 5.3 and 5.4), in addition to scheduled inspections, were used. Once the LEFs were generated and the CF was determined, the fatigue spectrum loads were generated so that the gross min/max loads preserved the original stress ratios.

2.8 CALCULATION OF LIFE FACTORS AND LEFS

A detailed scatter analysis of the primary composite material used in a Starship forward wing (AS4/E7K8) was carried out by Tomblin and Seneviratne [40], using the approach outlined by Whitehead et al. [1]. The methodologies for obtaining the modal static-strength shape parameter (MSSP), or α_R, and the modal fatigue-life shape parameter (MLSP), or α_L, when determining the life factor and LEFs for a particular structural application, is outlined with examples in reference 40. The procedure for obtaining the factors is shown in appendix A. This appendix also includes tables for A- and B-basis LEFs.

2.8.1 Life Factor Approach

The scatter factor concept, which is the ratio of the lower bound characteristic breaking strength or repeated life to the design breaking strength or repeated life, respectively, shows the penalty paid to gain the required reliability at γ-level of confidence from a finite sample size [43]. In terms of static strength and fatigue life, the scatter factor is the static factor and life factor, respectively. The life factor approach has been used successfully for metal to assure structural durability by testing the structure for additional fatigue life to achieve the desired level of reliability. The underlying objective of the life factor is to ensure that the design life is representative of the condition of the weakest member of the population after a specified life in service.

The ratio of the mean repeated load life to A- or B-basis repeated life is defined as life factor, N_F, and given by equation 1 [1]:

$$N_F = \Gamma\left(\frac{\alpha_L + 1}{\alpha_L}\right) \Bigg/ \left\{\frac{-\ln(p)}{\left[\chi^2_\gamma(2n)/2n\right]}\right\}^{1/\alpha_L} \tag{1}$$

where:

α_L = fatigue-life shape parameter
n = number of articles
p = required reliability at γ-level of confidence (p = 0.99 for A-basis; p = 0.9 for B-basis)
$\chi^2_\gamma(2n)$ = Chi-square distribution with $2n$ degrees of freedom at γ-level confidence

The life factor becomes insensitive to small changes in the life shape parameter beyond a value of 4, which is considered to be the life shape parameter for most metallic structures. The composite MLSP of 1.25 in reference 1 lies within the highly sensitive region of life factor versus shape parameter curve, as shown in figure 13. Therefore, even a small improvement in fatigue data scatter will result in a dramatic reduction of life factor, which reflects the required number of test lives to achieve a certain level of reliability in the DLT [44]. The life shape parameter is obtained from a distribution of shape parameters representing numerous S-N curves of different critical structural details. Therefore, it is common to have a lot of scatter in the S-N data of design details that have competing failure modes and less scatter in notched test data due to stress concentration. Often, the complex state of stress and these competing failure modes, coupled with other variabilities associated with composites, such as batch variability, porosity, and fiber misalignments, tend to cause large scatter in both static strength and fatigue life. Conversely, the stress concentrations in notched composite cause the final failure of the specimen negating or minimizing the collective effects of the above-mentioned secondary variables.

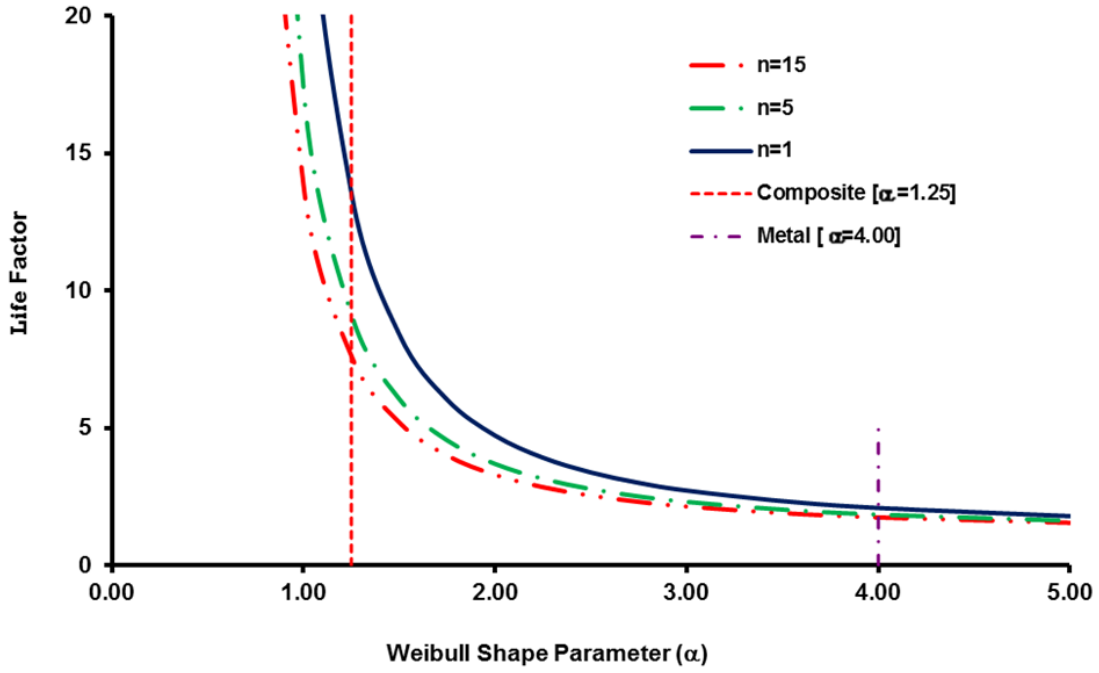

Figure 13. Influence of MLSP on life factor

2.8.2 The LEF Using Scatter Analysis

The objective of the LEF approach is to increase the applied loads in the fatigue tests so that the same level of reliability as life factor can be achieved with a shorter-duration test. Assuming that both the fatigue life and residual strength distributions can be described by two-parameter Weibull distribution, the LEF in terms of test duration, *N*, is calculated using equation 2a, where α_R is the MSSP [1].

$$LEF = \Gamma\left(\frac{\alpha_L + 1}{\alpha_L}\right)^{\frac{\alpha_L}{\alpha_R}} \Bigg/ \left\{\frac{-\ln(p)\cdot N^{\alpha_L}}{\left[\chi^2_\gamma(2n)/2n\right]}\right\}^{1/\alpha_R} \tag{2a}$$

One of the key features that allows the use of the LEF during certification with confidence is the formal relationship between the LEF and life factor, which can be simplified in terms of test duration, *N*, using equations 1 and 2a:

$$LEF = \left(\frac{N_F}{N}\right)^{\frac{\alpha_L}{\alpha_R}} \tag{2b}$$

This approach applies a combined life factor with the load factor to achieve a compromise in the full-scale test requirements as well as the load spectrum. Therefore, this approach is also referred

to as the combined load-life approach. The LEFs are significantly influenced by the MSSPs. Therefore, improvements in these shape parameters for newer forms of materials that exhibit less scatter can significantly reduce the LEF. The influence of the MLSPs on the LEF changes as the test duration increases. For example, as the test duration increases, the influence of the life shape parameter on the LEF increases. This is understandable, as N_F is only influenced by the life shape parameter. Figure 14, which shows the outline of this approach and its application to a full-scale DaDT substantiation of composite structures, is a case where the LEF is applied to the truncated[2] spectrum. This approach results in a single set of spectrum loads regardless of the LEF applied. The loads below the truncation level (prior to applying LEF) do not influence the damage growth. If the spectrum is truncated after applying the LEF, that will result in the inclusion of additional loads that would otherwise have been truncated (eliminated) from the test because they were below the truncation level. When this approach is taken, and if a different LEF is required for the same test, the test spectrum has to be regenerated to ensure that the appropriate loads (above the truncation level) are included during the test.

[2] Truncation level is defined as the high-frequency occurrences with load levels typically below the endurance limit. Fatigue loads below the truncation level are deleted from the fatigue spectrum, assuming that they do not contribute to damage growth, to reduce the test duration.

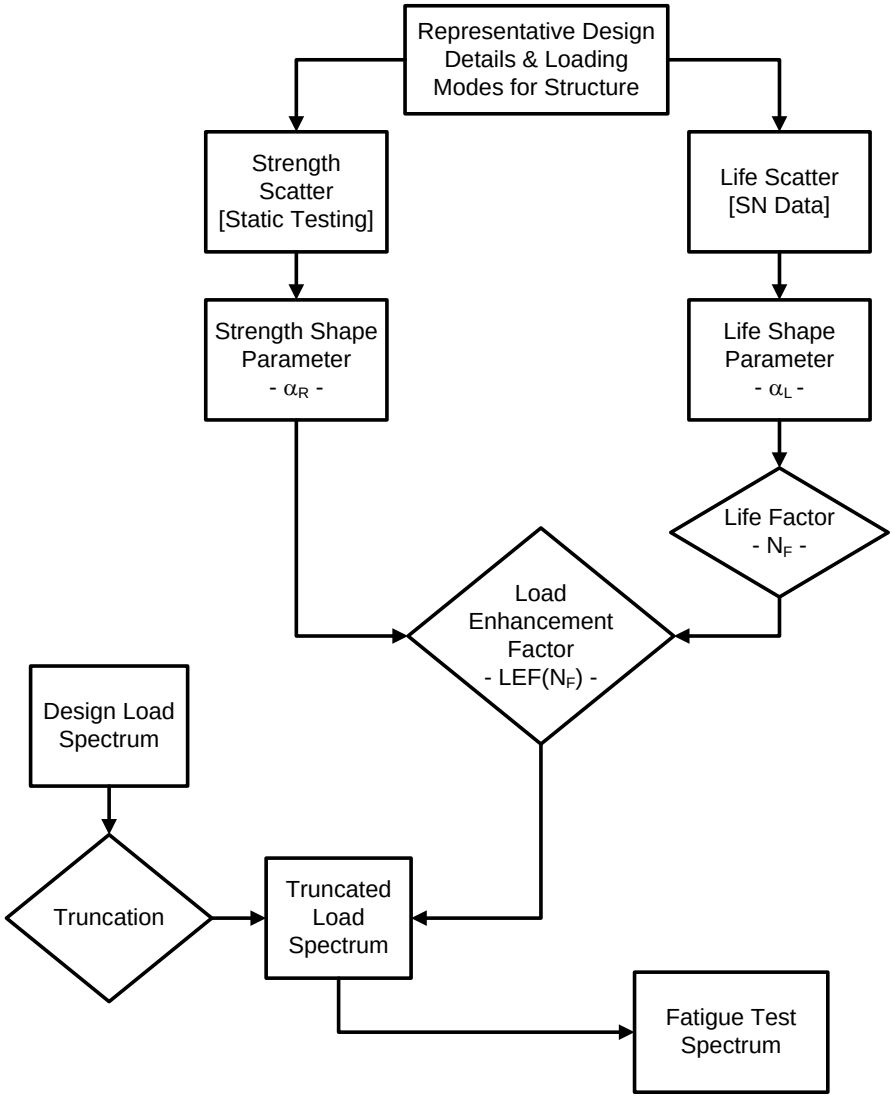

Figure 14. Development of the LEFs for the composite structural test

3. DAMAGE TOLERANCE OF COMPOSITE STRUCTURES

The primary goal in a damage tolerance certification program is to avoid catastrophic failure due to fatigue, corrosion, or accidental damage throughout the operational life of the aircraft. The damage tolerance philosophy is well established for metallic airframes, where proven methods (structural analysis and inspection procedures) and supporting databases exist to detect damage and to predict crack growth and residual strength. However, damage characteristics, inspection procedures, analysis methods, and experimental databases are not well enough understood to apply the damage tolerance philosophy to composite structures, including sandwich construction. The determination of damage-tolerant characteristics of sandwich panels has been limited in previous investigations to relatively few sandwich configurations and damage states [45]. Therefore, there has been a growing interest in damage tolerance methodology in determining the fatigue life of composite structures under repeated loading.

3.1 CERTIFICATION APPROACH

The state of damage within a composite structure is complex and dependent on a number of variables that define the intrinsic properties of the sandwich constructions and the extrinsic damage-causing event. Furthermore, barely visible impact damage (BVID), ADL, and CDT are not clearly defined in terms of a rational damage metric. Traditionally, visual inspection procedures have been used for detecting damage in composite structures (in-service); therefore, BVID became a term that was used. The current definitions of BVID are based on the residual indentation depth, which has been clearly shown to be configuration-dependent and often misleading. An additional issue is the choice of NDI techniques, which dictates the damage metric that defines the BVID criterion.

3.1.1 Damage Tolerance Design Philosophy

The general philosophy applied during damage tolerance certification, shown in figure 15, relates representative damage size to design load requirements. As in the case of metal aircraft, ultimate strength and damage tolerance philosophies are used to maintain a reliable and safe operation of composite structures. As shown in figure 15, this philosophy may typically be described using three distinct regions: (1) BVID, (2) ADL, and (3) CDT.

Nonvisible damage or BVID, or defects that are not detectable during manufacturing inspections and service inspections, must withstand ultimate flight loads in the most adverse temperature and humidity environments and cannot impair the operation of an aircraft throughout its DLT. In the BVID region, it is assumed that the damage may never be discovered during the DLT and must support ultimate design load. Once damage larger than the ADL is observed, it must be repaired when discovered. This damage is visible during service inspections and must withstand a once-per-lifetime load DLL for the specified inspection interval. It is necessary in a damage tolerance design that service damage in this region be found and characterized using practical inspection techniques. The CDT region represents a damage state that should be immediately obvious and found with an extremely high probability using the selected inspection scheme. Usually, this damage occurs in flight and is apparent to the operator. Under this condition, the

CDT is executed, and the aircraft must withstand loads specified under limited maneuvers with and without the pressure necessary for continued safe flight.

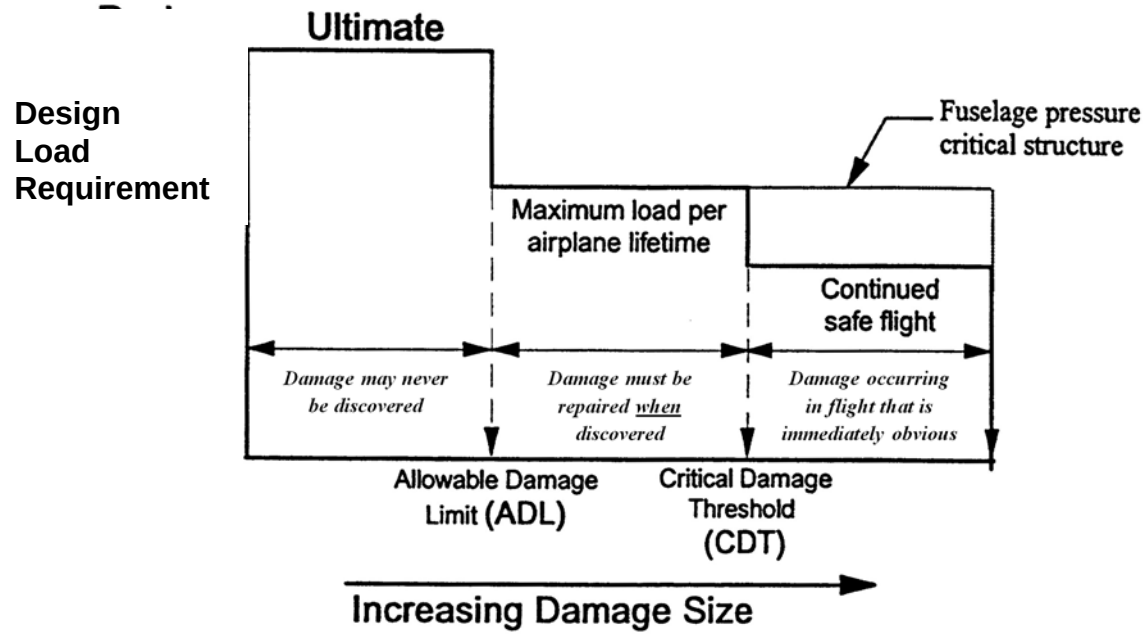

Figure 15. Damage tolerance design philosophy

Figure 16 shows the extent of the impact damage that needs to be considered in the damage tolerance and fatigue evaluation. Both the energy level associated with static-strength demonstration and the maximum energy level associated with the damage tolerance evaluation are dependent on the part of the structure under evaluation and an expected threat assessment. Obvious impact damage is used here to define the threshold from which damage is readily detectable and appropriate actions are taken before the next flight.

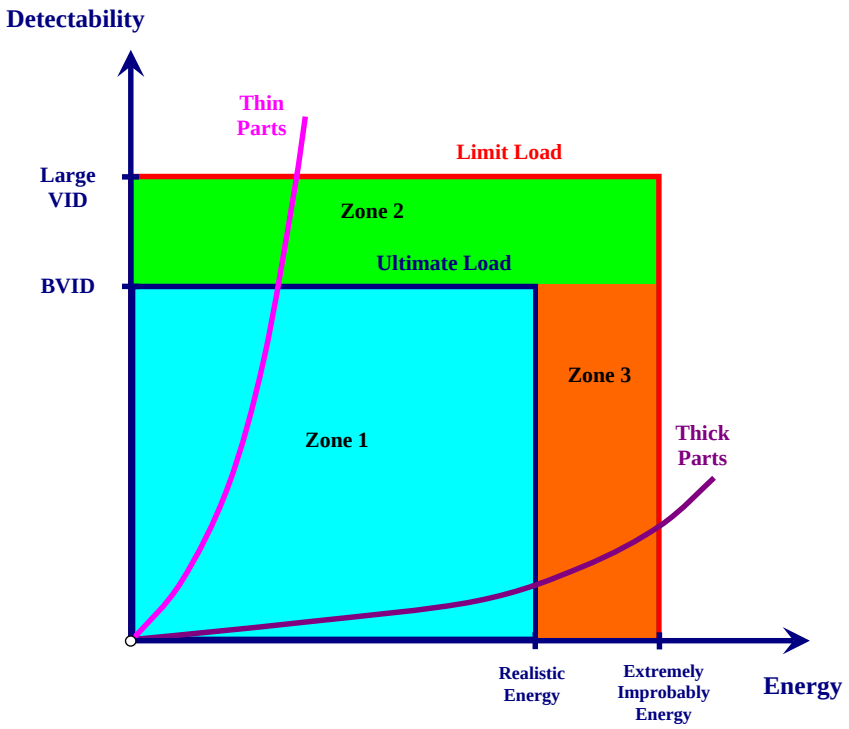

Figure 16. Impact damage characterization

3.1.2 Characterization of Impact Damage

The BVID defines the state of damage at the threshold of detectability for the approved inspection procedure. BVID is the threshold associated with a detailed visual inspection procedure. Detectable damage defines the state of damage that can be reliably detected at scheduled inspection intervals. Visible impact damage (VID) is that state associated with a detailed visual inspection.

Three damage zones are defined in figure 16:

1. Zone 1: Because the damage is not detectable, DUL capability is required.
2. Zone 2: Because the damage can be detected at scheduled inspection, DLL capability is the minimum requirement for this damage.
3. Zone 3: Because the damage is not detectable with the proposed in-service inspection procedures, DUL capability is required, unless an alternate procedure can show an equivalent level of safety. For example, residual strength lower than ultimate may be used in association with improved inspection procedures or with a probabilistic approach showing that the occurrence of energy levels is low enough so that an acceptable level of safety can be achieved.

3.1.3 Damage Categories

Table 1 categorizes damage and defect considerations, with some guidelines for identification and safety considerations pertaining to such defects in primary composite airframe

structures [46]. Most certification approaches consider both Category 1 (CAT1) and CAT2 defects. It is not standard practice to demonstrate CAT3 damage in full-scale test substantiation. Damage tolerance testing in elements, components, and full-scale articles that are included in this program will address the "fail safety" of composite structures for instances of very low probability impact damage that may lower the residual strength of the structure to limit-load capacity.

Table 1. Damage categories and safety considerations for primary composite airframe structures [46]

Category	Examples	Safety Considerations (Substantiation, Management)
1—Damage that may go undetected by field inspection methods (or allowable defects)	BVID, minor environmental degradation, scratches, gouges, allowable manufacturing defects	Demonstrate reliable service life; Retain ultimate load capability; Design-driven safety
2—Damage detected by field inspection methods at specified intervals (repair scenario)	VID (ranging small to large), manufacturing defects/mistakes, major environmental degradation	Demonstrate reliable inspection; Retain limit load capability; Design, maintenance, manufacturing
3—Obvious damage detected within a few flights by operations focal (repair scenario)	Damage obvious to operations in a "walk-around" inspection or due to loss of form/fit/function	Demonstrate quick detection; Retain limit load capability; Design, maintenance, operations
4—Discrete source damage known by pilot to limit flight maneuvers (repair scenario)	Damage in flight from events that are obvious to pilot (rotor burst, bird strike, lightning)	Defined discrete-source events; Retain "get home" capability; Design, operations, maintenance
5—Severe damage created by anomalous ground or flight events	Damage occurring due to rare service events or to an extent beyond that considered in design	Requires new substantiation; Requires operations awareness for safety (immediate reporting)

3.2 THE LLD HYBRID APPROACH

During full-scale fatigue testing, it is common to use a combination of the life factor and LEFs. This research proposes the generation of these factors for a specific certification program using design details, such as materials, layup, and loading conditions, that are related to the composite's structure, rather than using the factors generated for U.S. Navy F/A-18 certification [1]. As shown in references 40 and 44, scatter in the composite data is reduced considerably due to the improvements in materials, process technologies, and composite test methods. Furthermore, it has also been shown that the scatter in composite data tends to be less for notched or damaged specimens [40]. In references 40 and 44, the composite data scatter was evaluated based on the extent of the damage and related to the definitions in section 3.1.3. When

a DaDT article is impacted with a certain kind of damage, such as CAT3, the following assumptions can be made with a high degree of confidence:

- The damaged region becomes the critical location of the structure (i.e., no significant load redistribution that will drive a different failure mode).
- Imminent damage initiation at this location will cause structural collapse or load distribution that can be predicted by analysis for subsequent test validation.

The elements or subcomponents that represent the details of the impacted location can then be tested to obtain a new life shape parameter for that particular structural detail and critical load conditions associated with the failure mode. The first condition is essential, because the MLSP that was obtained using the procedure outlined in reference 1 is replaced by the shape parameter of the fatigue analysis of element or subcomponent tests (i.e., the analysis conducted in section 4.2.3 on impact-damaged elements). The second condition is required, because the failure mode of the structure is assumed to occur as a direct result of the instigation of impact damage. If there is load redistribution instead of complete structural failure, then the use of a newly defined life shape parameter must be superseded by the corresponding life shape parameters of the subsequent damage state of the structure for the remainder of the test (i.e., if CAT2 damage is transferred to CAT3 damage as a result of the damage propagation), then the remainder of the DaDT test requires the use of a CAT3 life shape parameter instead of a CAT2 life shape parameter. DaDT element or subcomponent tests must be designed to address the expected outcome. This approach is shown in figure 17 for a full-scale structural test that was initiated with standard LEFs for the durability phase and then continued using the LLD hybrid approach for the DaDT phase.

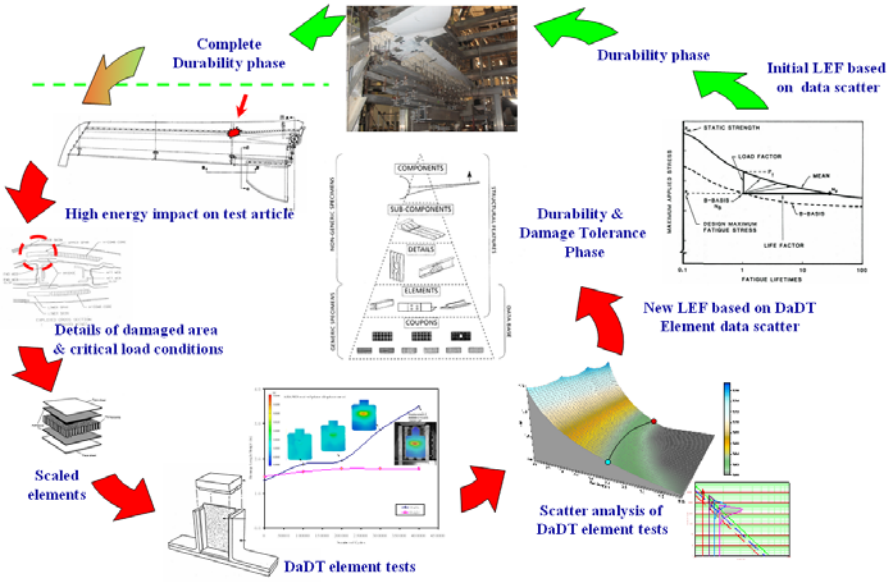

Figure 17. The DaDT test demonstration with LLD hybrid approach

Based on the design analysis and strain surveys, the most critical locations of the structure are selected for damage infliction. The impact parameters are then determined to inflict a certain

kind of damage (i.e., CAT2 or CAT3). This step requires an analysis of the local details, such as materials, laminate stacking sequence, and critical loading modes. For example, a nonlinear finite element analysis of the local details with a continuum damage model (i.e., stiffness degradation due to fiber/matrix cracking and plastic deformation under shear loading, and a contact algorithm to model surface erosion [element removal] on multiple contact bodies during impact [i.e., impactor and the contact surface as well as the interior ply interfaces]) can be used to determine the extent of the damage for a particular impact scenario. Such a detailed model requires significant computing time and is often extremely sensitive to the mesh density, element type, input required for the damage model, etc. Therefore, scaled element tests are recommended where possible, not only to cross-examine the impact parameters prior to impacting the full-scale test article, but also to validate the nonlinear finite element models. The element test can also be used for the scatter analysis of a particular damage scenario. Consequently, the LEFs and life factor corresponding to the selected damage scenario can be calculated for the damage tolerance phase of the full-scale test.

As shown in figure 17, the LLD hybrid approach focuses on the most critical details of the structure and interprets the structural and load details into the most representative element-level, repeated load testing to gain information on residual strength, fatigue sensitivity, inspection methods, and inspection intervals during full-scale test substantiation. Typically, critical damage, such as a CAT3, is readily detectible during a short walk-around inspection. From a safety standpoint, the goal is to focus on the most critical, yet least detectible, damage that may occur during service. This may be CAT2 or CAT3 damage, depending on the detectability and the inspection methods that can be practically applied (i.e., a short walk-around inspection or a scheduled inspection during heavy maintenance).

To demonstrate the application of the LLD hybrid approach, the element test data discussed in section 4.2 were used, which only considered the effects of impact damage on the fatigue life scatter; three sets of LEFs were generated with respect to the extent of the damage and combined with the original AS4-PW LEFs to generate a surface plot of LEFs, as shown in figure 18. First, the LEF corresponding to 3 DLTs using AS4-PW data was selected but the test was only conducted up to 2 DLTs. The structure was then impacted with an LID and the corresponding LEF curve was used to select the LEF for the remainder of the test. The LLD approach introduces the use of multiple LEFs for a particular composite structure, based on the damage category (i.e., the use of different LEF curves representing different damage severities).

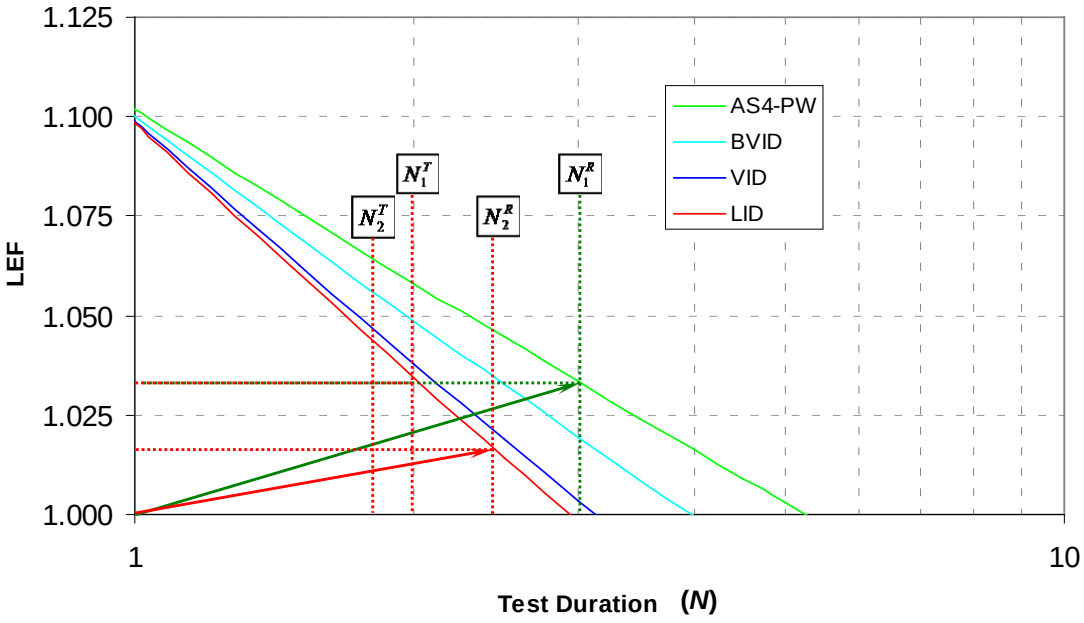

(a)

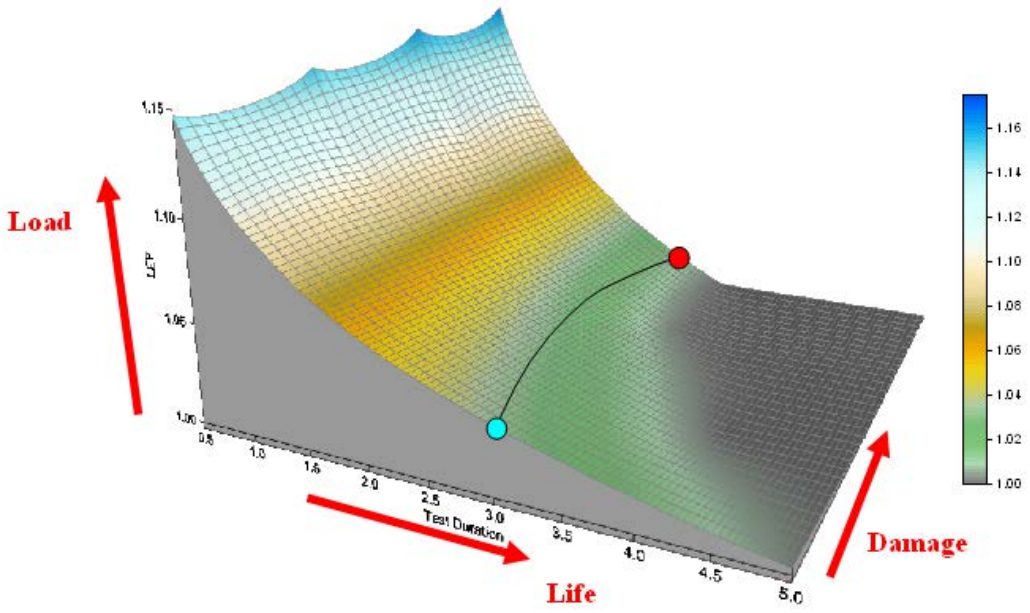

(b)

Figure 18. The LLD hybrid approach: (a) LEF vs. *N* and (b) three-dimensional representation of LEF vs. *N*

3.3 LOAD-LIFE SHIFT CONCEPT

When multiple LEF curves are used for different damage scenarios, a concept called the load-life shift is used to calculate the remaining test duration on the introduction of the new damage to the test article. The load-life shift given in equation 3 calculates the remaining test duration based on the percentage of unsubstantiated design life in the previous test phase:

$$N_2^T = \left(1 - \frac{N_1^T}{N_1^R}\right) \cdot N_2^R \tag{3}$$

In equation 3, subscripts 1 and 2 correspond to the test phase, and superscripts *R* and *T* denote the corresponding repeated life for a particular LEF and the actual test duration, respectively, to demonstrate the reliability of DLT. For example, the test duration of the 3 DLTs (N_1^R) from the AS4-PW curve corresponds to an LEF of 1.033 (figure 18). The test is conducted for 2 DLTs (N_1^T), and the structure is inflicted with the LID. The test duration of 2.5 DLTs (N_2^R) from the LID curve corresponds to an LEF of 1.014 (figure 18). Since two out of the three DLTs required in the first phase of the test have been completed, the remaining test duration (for phase 2) is calculated as 0.83 DLT (N_2^T) using equation 3. Therefore, the total test duration is 2.83 DLTs. The application of the LID coupled with the LLD hybrid approach not only reduces the LEF requirements, but reduces the total test duration. If the impact damage is repaired, the remainder of the test must use the LEFs from the original AS4-PW curve. The load-life shift calculation must now consider the percentage of unsubstantiated DLT prior to the repair to calculate the remainder of the test duration.

The impact of the reduction in the life shape parameter on the life factor is clearly demonstrated in figure 18. Therefore, the test duration/LEF required to demonstrate a certain level of reliability on the DLT or the remaining test life is significantly reduced. However, the risk of structural failure because of LID can be significantly increased with the extent of the damage. This is addressed in section 3.4 in terms of POF and inspection intervals. Once the new LEF that corresponds to the LID is applied, the spectrum loads of the required test duration can be analyzed in terms of the POF to ensure that the structure can tolerate them (i.e., either stable or no damage growth). Inspection intervals can be allotted to monitor the damage state during testing to avoid unintentional failure during the test, because LID has a high probability of growth. In the event that a repair of the impacted damage is deemed necessary to prevent premature failure, then the LEF requirements must be adjusted to reflect the fact that the structure has been restored back to its undamaged state.

One possible application to the LLD hybrid approach is shown in figure 19 [47]. This example requires defining ADL and CDT, as well as the necessary inspection interval for damage-tolerant composite structures. Although current certification requirements do not include the substantiation of LID like CAT3 and beyond, this approach will help determine load-life enhancement factors related to such a test article with LID. The extra information obtained from such an exercise is beneficial for determining the inspection levels to mitigate risks to the structural integrity as a result of a rare damage threat from a high-energy impact. This approach

can also be extended to hybrid structures, because the LEF requirement will be considerably less than the current practice for a composite test article with damage (i.e., an LEF of 1.15 for a test duration of 1.5 DLTs).

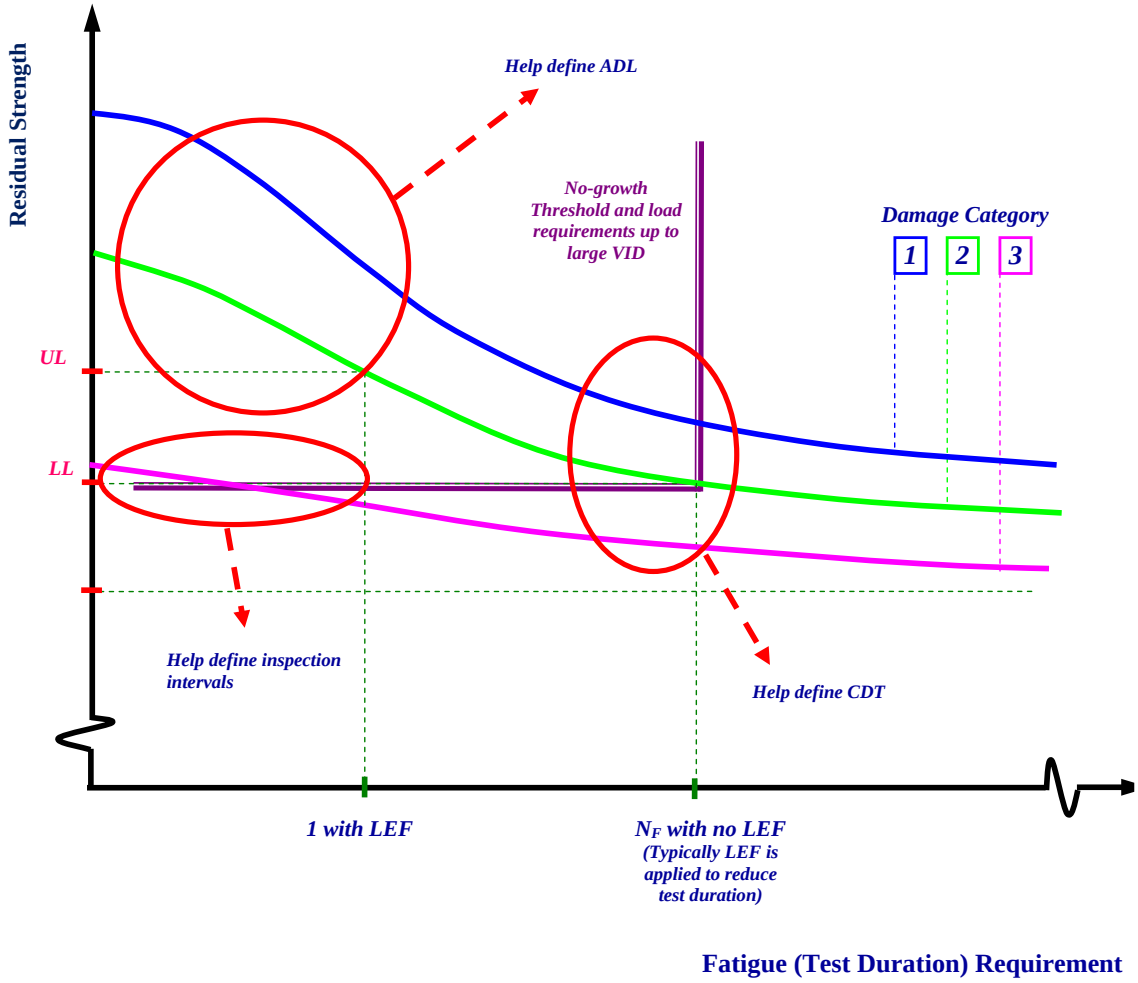

Figure 19. Application of LLD hybrid approach for full-scale demonstration

This concept has also been used to approximate the retirement life of a component based on the data available from service history and MSSPs and MLSPs used during the original certification to generate life factor and LEFs [48]. This approach prevents additional full-scale or large component fatigue tests that are required to determine the remaining life of the fleet.

3.4 DAMAGE THREAT ASSESSMENT BASED ON RELIABILITY

To ensure that unintentional failure of the structure did not occur when using the LLD approach, a reliability-based approach was proposed to evaluate the enhanced spectrum for the remaining test duration after impact resulting in LID. This approach, based on the fundamental reliability concepts used for both the life-factor and LEF approaches, can be used to evaluate the reliability

of damaged test articles and determine the necessary inspection intervals so that the damage is detected before it threatens the structural integrity.

Assuming that the residual strength or fatigue life of a composite structure, denoted by the random variable *x*, follows a two-parameter Weibull distribution, the cumulative distribution function of residual strength or fatigue life can be expressed as:

$$P(x;\alpha,\hat{A}) = 1 - \exp\left[-\left(\frac{x}{\hat{A}}\right)^{\alpha}\right] \tag{4}$$

where $\hat{A}$ is the characteristic residual strength/fatigue life, and α is the shape parameter that determines the scatter of the distribution of random variable *x*. The shape parameter that corresponds to residual strength or fatigue life is calculated, as shown in reference 40. These shape parameters estimate the distribution of strength or life of the full-scale structures. Therefore, the test matrices for determining these parameters must include critical design details and loading parameters that are representative of the full-scale structure. $\hat{A}$, which is also known as the scale parameter or the location parameter, is calculated as:

$$\hat{A} = \left[\frac{1}{n_{fd}} \cdot \sum_{i=1}^{n_d} \left(A_i^{\alpha}\right)\right]^{1/\alpha} \tag{5}$$

where n_d is the number of data points and n_{fd} is the number of failures in the data group. Assuming that the distribution of $\hat{A}$ follows a chi-squared distribution with 2*n* degrees of freedom, and α is known, the lower bound estimate of $\hat{A}$ with a γ-level of confidence [49] is given by:

$$\breve{A}_{\gamma} = \hat{A} \cdot \left[\frac{2 \cdot n}{\chi_{\gamma}^{2}(2 \cdot n)}\right]^{1/\alpha} \tag{6}$$

where the probability of the lower bound estimate is shown as:

$$P(\breve{A}_{\gamma} \le \hat{A}) = \gamma \tag{7}$$

The POF with a γ-level of confidence for an applied stress or fatigue life ($\breve{A}_R$) is shown in equation 8:

$$P(\breve{A}_R) = 1 - \exp\left[-\left(\frac{\breve{A}_R}{\breve{A}_{\gamma}}\right)^{\alpha}\right] \tag{8}$$

Given that $\breve{A}_R$ is the designed stress or fatigue life of a structure, the reliability of the design (= 1-[POF]) with a γ-level of confidence is shown in equation 9:

$$R = \exp\left[-\left(\frac{\breve{A}_R}{\breve{A}_\gamma} \right)^{\alpha} \right] \tag{9}$$

For γ = 0.95, A- and B-basis reliabilities are 0.99 and 0.90, respectively. Substituting equation 6 for the lower bound characteristic value in equation 9 and solving for the designed stress or life or the allowable statistics, $\breve{A}_R$, for the desired reliability, R, can be expressed as:

$$\breve{A}_R = \hat{A} \cdot \left[-\ln(R) \frac{2 \cdot n}{\chi^2_\gamma (2 \cdot n)} \right]^{1/\alpha} \tag{10}$$

For a Weibull distribution with an α-shape parameter, the mean value of the population, $\bar{A}$, is given in equation 11 with respect to the characteristic value:

$$\bar{A} = \hat{A} \cdot \Gamma\left(\frac{\alpha + 1}{\alpha} \right) \tag{11}$$

The scatter factor (x), the ratio of mean-to-design (allowable) value, for desired reliability, R, with γ-level of confidence can be expressed as:

$$X = \frac{\bar{A}}{\breve{A}_R} = \frac{\Gamma\left(\frac{\alpha + 1}{\alpha} \right)}{\left[-\ln(R) \frac{2 \cdot n}{\chi^2_\gamma (2 \cdot n)} \right]^{1/\alpha}} \tag{12}$$

The scatter factor signifies the relation between the central tendency of a data set (mean) and the extreme statistics (allowables) as the life factor given in equation 1. The scatter factor for fatigue life and static strength data are referred to as life factor (N_f) and static factor (S_F), respectively. Solving for reliability, equation 12 yields:

$$R = \exp\left\{ -\frac{\chi^2_\gamma (2 \cdot n)}{2 \cdot n} \cdot \left[\frac{\Gamma\left(\frac{\alpha + 1}{\alpha} \right)}{X} \right]^{\alpha} \right\} \tag{13}$$

and the POF is defined as:

$$P_f = 1 - R \tag{14}$$

Equation 12 shows that the reliability of a particular scatter factor depends on the Weibull shape parameter, α, of the data set and the degrees of freedom, $2n$, where n is the sample size or, in this case, the number of scaled test articles. Figure 20 shows that the B-basis reliability for DLT is achieved with scatter (life) factors of 13.6 and 4.7 for MLSPs of 1.25 and 2.00, respectively. Similarly, the B-basis reliability on DLL is achieved with scatter (static) factors of 1.15 and 1.10 for MSSPs of 20 and 30, respectively, indicating that the typical scatter factor of 1.5 on DUL (1.5◌DLLs) is more than sufficient to demonstrate B-basis reliability for both of these scatter factors. However, equation 13 does not account for the unintentional deviations from service load, service environmental effects, and structural response variability. The effects of these parameters must be evaluated to completely understand the level of safety provided by the static factor of 1.5.

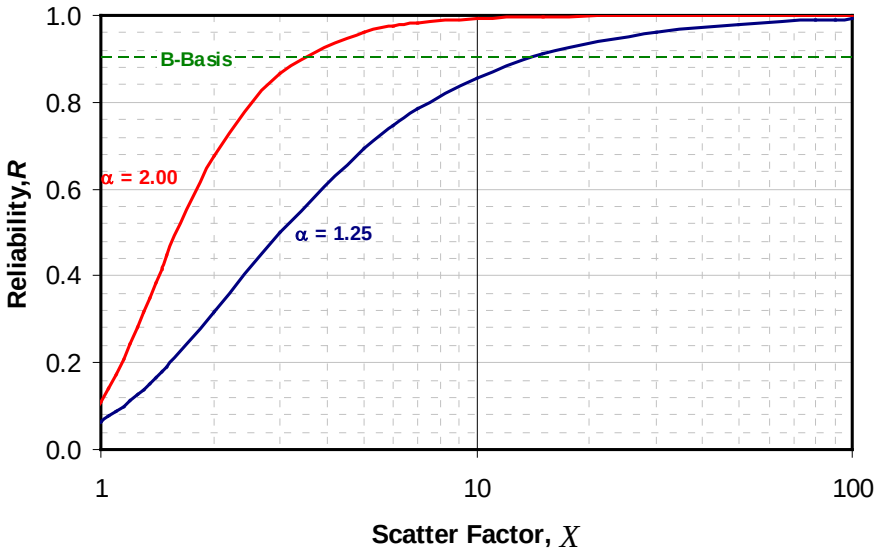

(a) Typical MLSPs

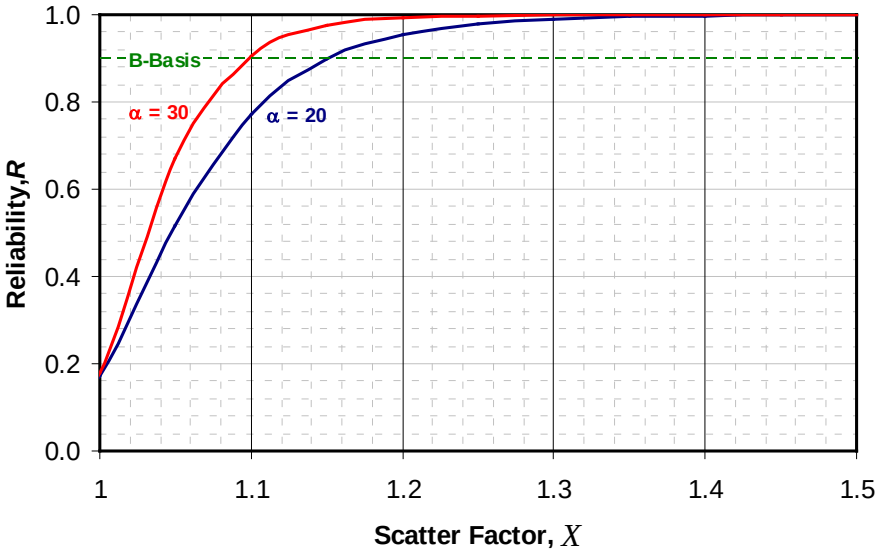

(b) Typical MSSPs

Figure 20. Effects of scatter factor on reliability

3.4.1 Cumulative Fatigue Reliability Model

In the event of impact damage to a structure that is designed with a static factor of 1.5, the residual strength is reduced based on the category of the damage, as defined in table 1.

The reduction to residual strength is denoted by the static-strength reduction factor, δ, and the scatter factor is written as:

$$S_F = \frac{\delta \cdot DUL}{DLL} = \delta \cdot \hat{X} \tag{15}$$

where $\hat{X}$ (=1.5) is the static factor prior to the damage. The POF at a fatigue load segment can be determined by combining equations 13, 14, and 15 as:

$$P_{f_i} = 1 - \exp\left\{ -\frac{\chi_\gamma^2(2 \cdot n)}{2 \cdot n} \cdot \left[\frac{\Gamma\left(\frac{\alpha+1}{\alpha}\right)}{\hat{X}_i} \right]^\alpha \right\} \tag{16}$$

where $\hat{X}_i$ is the static factor for i^{th} segment (i.e., ratio of the residual strength and maximum load at i^{th} segment). Also, the initial static factor for a structure is given in equation 17 with the static-strength reduction factor, δ:

$$\hat{X}_0 = \delta \cdot \hat{X} \tag{17}$$

The POF of the structure during a particular fatigue load segment in the spectrum (load sequence) can now be calculated by summing the POF at each segment up to the current one (n_s), including the current load segment, as shown in equation 18.

$$P_f = \sum_{i=1}^{n_S} P_{f_i} \tag{18}$$

Because reliability is calculated based on the residual strength degradation or wearout, the sequencing effects are reflected in the cumulative fatigue reliability (CFR) model. When the cumulative POF, P_f, reaches unity during a load segment in the fatigue spectrum, it constitutes the structural failure during that load segment as:

$$P_f \geq 1 - TR \rightarrow Failure \tag{19}$$

where *TR* is the target reliability. The CFR model is a measure of the state of a structure with certain damage and a certain number of fatigue cycles, but it is not directly related to the damage propagation. Information pertaining to the damage propagation and the residual strength degradation are incorporated into the model through the coupon and element tests (see section 3.4.3).

3.4.2 Considerations for Application of CFR Model

When applying the CFR model to a structural application, several factors need to be considered to accurately predict safe and economical inspection intervals and fatigue life. Because of its robustness, depending on the criticality (i.e., primary load path or redundant structure) and probability of certain damage threat scenarios related to a structure, the CFR model can be customized to reduce the amount of test data and computations required to achieve a safe, reliable, and economical DaDT test validation program and inspection intervals.

3.4.2.1 The MSSP and static factor

For CAT3 damage, the residual strength of the structure will be reduced to its limit load (see table 1), therefore, $\delta = 2/3$ and $S_F = 1.0$. The reliability of the damaged structure can be determined by substituting a static factor for CAT3 damage in equation 13. Consequently, the POF at DLL is calculated using equation 14 and is shown in figure 21 with respect to MSSPs. As shown in this figure, the POF is significantly increased for MSSPs less than 10. The value of the MSSP obtained using the combined life-load approach was 20 (although it was 32.193 for AS4-PW material based on the scatter analysis in reference 40). These values result in 17.4% and 17.8% reliability or 82.6% and 82.2% POF for DLL, respectively.

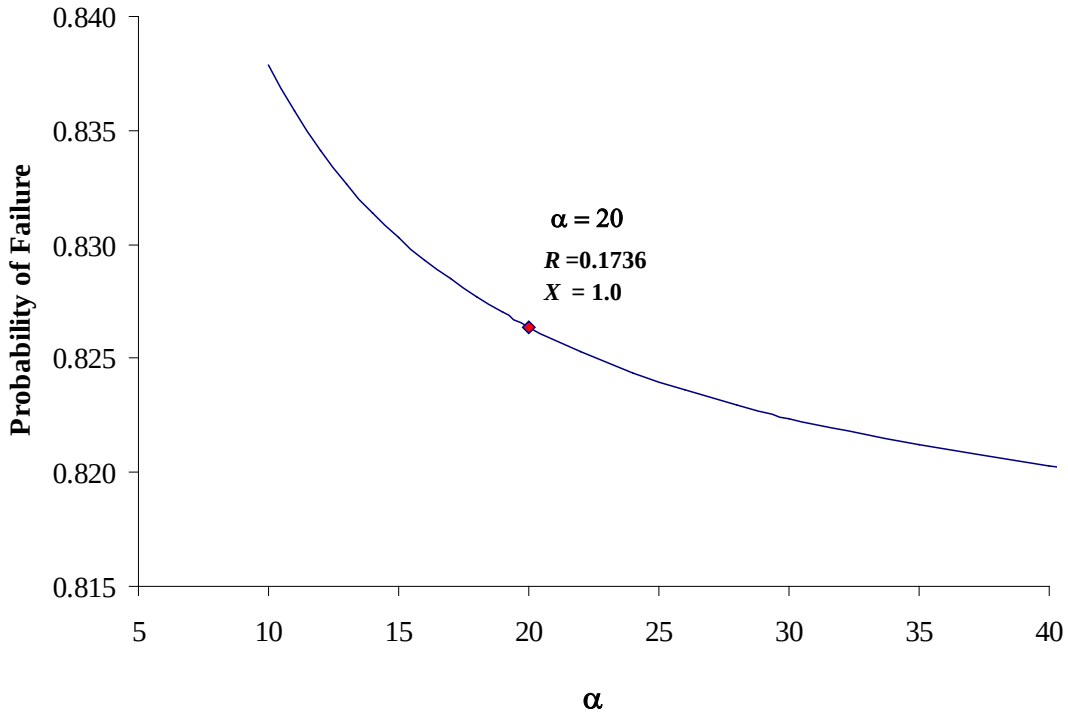

Figure 21. The POF for $S_F = 1.0$

As will be discussed in section 4, the static-strength scatter was reduced significantly for damage tolerance element testing due to stress concentration. Therefore, the reliability of a structure with CAT3 damage, a population representing less scatter (assume $\alpha = 30$), was compared with the traditionally used MSSP (combined life-load approach), $\alpha_R = 20$, and with no impact damage in figure 22. Figure 22 shows that, although the B-basis (90% with 95% confidence) reliability is

diminished at DLL, the post-impact reliability of the structure for some operational loads (simulated by spectrum during the DaDT test) still remains above the B-basis reliability level (i.e., the B-basis reliability of a CAT3-damaged article [based on $\alpha = 30$] is still maintained for operational loads below 91% of DLL, assuming no residual strength degradation).

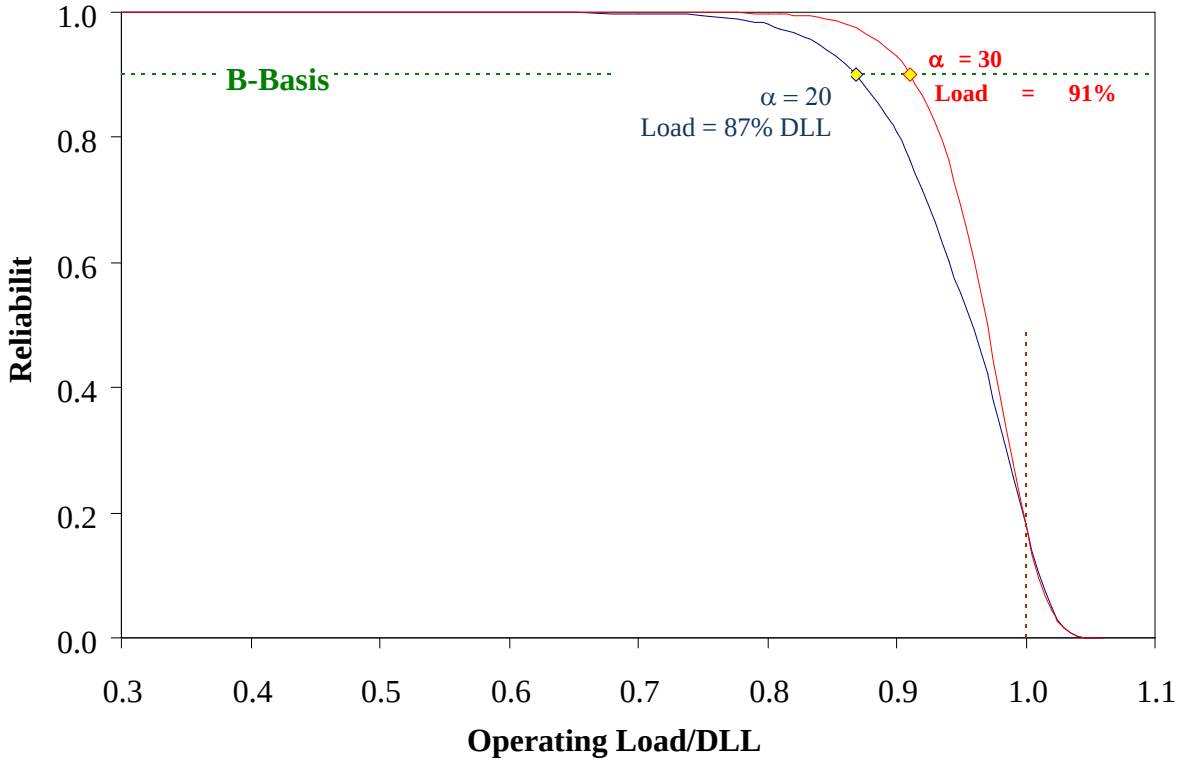

Figure 22. Static-strength reliability at operating loads for a structure with CAT3 damage

Figure 23 compares the post-impact reliability of a CAT3-damaged article from a relatively skewed population ($\alpha = 30$) to the reliability of the undamaged structure from a population with an MSSP of 20 for different operational loads. The B-basis reliability that was maintained for a one-time load application of 130% DLL is reduced to 91% as a result of the CAT3 damage. Because CAT3 damage is expected to be detected within a few flights, it can be repaired and the residual strength of the structure can be restored to DUL.

Note that these reliability calculations do not account for the stiffness degradation or wearout of structural capacity due to repeated loading and do not compare with the one-time application of the operational or applied loads to DLL. It is imperative that residual strength degradation throughout the spectrum is investigated to assess fatigue reliability and, consequently, the POF.

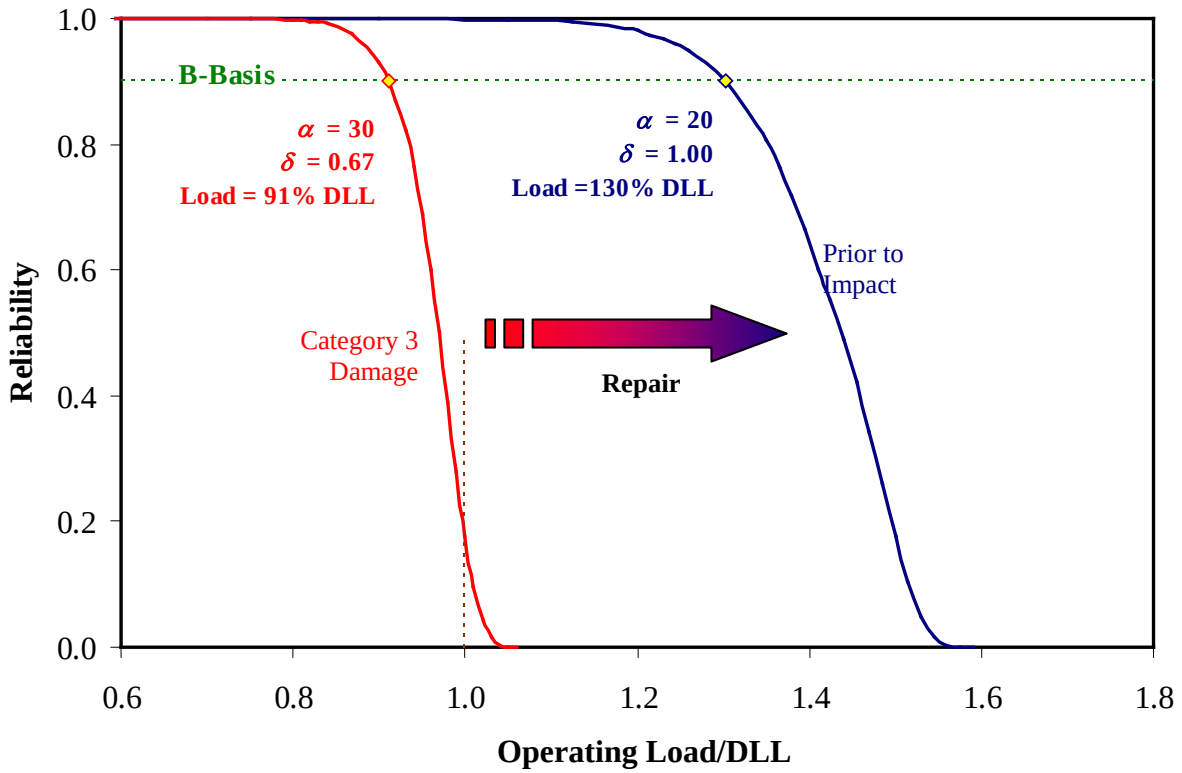

Figure 23. Static-strength reliability comparison before and after impact

3.4.2.2 Residual Strength Degradation–Wearout Models

To obtain the correct reliability, the residual strength of the structure must be re-evaluated after each cycle using a residual strength degradation or wearout technique, and the static factor for the i^{th} segment, $\hat{X}_i$, must be recalculated based on the new residual strength. For a typical aircraft spectrum, this may result in a significant number of calculations, depending on the selection of the wearout model. A closer examination of the reliability results for MSSPs of 20 and 30, shown in figure 22, reveals that, for maximum operational loads below 70% and 80% of limit load, respectively, the POF is negligible.

For load cases that are above the truncation levels, a wearout model is required to evaluate the residual strength of the structure after each fatigue load cycle. Sendeckyj residual strength degradation for constant-amplitude fatigue testing can be expressed as a monotonically decreasing function of the number of fatigue cycles, n_f, as shown in equation 20:

$$\sigma_r = \sigma_a \left[\left(\frac{\sigma_e}{\sigma_a} \right)^{1/S} - C(n_f - 1) \right]^S \tag{20}$$

where σ_e is the equivalent static strength, σ_a is the maximum/minimum applied cyclic stress, σ_r is the residual strength, n_f is the number of fatigue cycles, and S and C are Sendeckyj fitting

parameters. Figure 24 shows a comparison of the residual strength degradation of LID fatigue specimens in section 4.2 (only SL1 and SL3 are shown) based on the Sendeckyj wearout model and linear loss of residual strength (LLRS) for constant-amplitude fatigue, n_f, cycles as

$$\sigma_r = \sigma_e + \left(\frac{\sigma_a - \sigma_e}{N_f(\sigma_a)} \right) \cdot n_f \tag{21}$$

where $N_f(\sigma_a)$ is the number of cycles to failure for constant-amplitude fatigue loading at the maximum applied cyclic stress, σ_a.

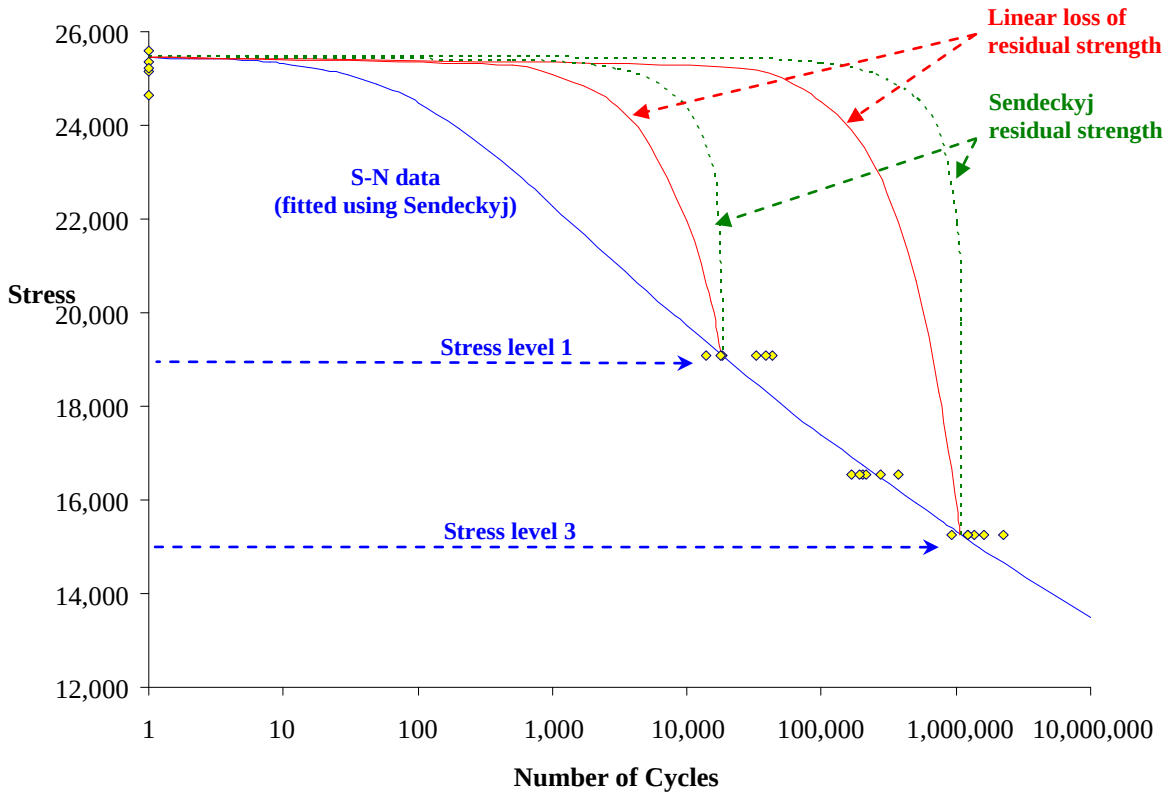

Figure 24. Residual strength degradation for constant-amplitude fatigue loading

When fatigue failure occurs at the n_f^{th} cycle, residual strength is reduced to the maximum applied cyclic stress, and n_f becomes $N_f(\sigma_a)$. Thus, $N_f(\sigma_a)$ can be solved by rearranging the terms in equation 20 as:

$$N_f(\sigma_a) = \frac{1}{C}\left[\left(\frac{\sigma_e}{\sigma_a} \right)^{1/S} + C - 1 \right] \tag{22}$$

As shown in figure 24, when there are no sufficient S-N data to obtain Sendeckyj fitting parameters, the linear loss of residual strength (LLRS) can be used to approximate conservatively the residual strength, and $N_f(\sigma_a)$ can be obtained using a graphical method from the S-N curve. Note that for both wearout equations 20 and 21, fatigue failure occurs when the residual strength reaches the maximum-amplitude fatigue stress level. Further, the CFR model is not restricted to those two wearout models, but includes any appropriate model for calculation of the residual strength after each load cycle. Because these models require a significant number of calculations and most of the loads in a typical fatigue spectrum are below 80 percent of the limit load, a simplified approach is proposed in section 3.4.3. Once the residual strength is determined, the static factor for the i^{th} cycle can be written as:

$$\hat{X} = \sigma_{r_i} \Big/ \sigma_{a_i} \tag{23}$$

For example, by substituting equation 20 or 21, the scatter factor can be determined. It can then be substituted into equation 13 to calculate the reliability. Finally, the POF after the corresponding number of fatigue cycles can be calculated for the applied stress. This exercise was carried out for LID S-N data in section 4.2. The Sendeckyj model was used to fit the S-N data. Residual strength as a function of the number of fatigue cycles was calculated using both the Sendeckyj model and the LLRS. Using the Sendeckyj residual strength, the POF was calculated and is shown in figure 25. Two stress levels were selected for this simulation: 77.5% and 61% of a static failure load, which correspond to 10,000 and 800,000 cycles, respectively. According to the CFR model, the numbers of fatigue cycles corresponding to these two stress levels at 90% reliability or 10% POF were 9,625 and 799,625, respectively.

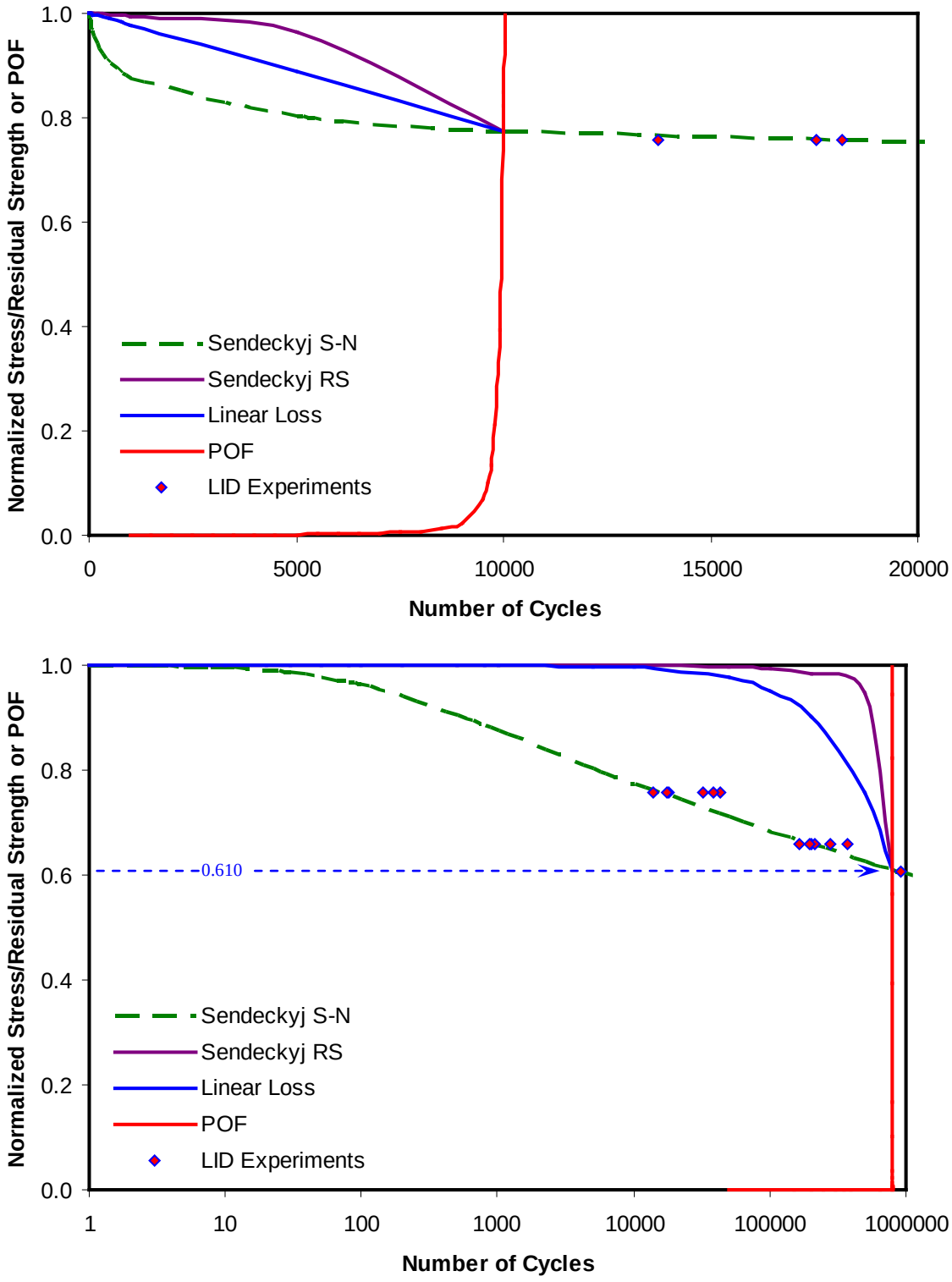

Figure 25. Example of CFR model for constant-amplitude fatigue tests

3.4.3 Benchmark Application of CFR Model

Because of its robustness, the CFR model can be customized to a particular application to obtain reliable inspection intervals and to evaluate the reliability of the structure for operational loads. To demonstrate an application of the CFR model, the Starship forward wing with CAT3 impact damage on its primary load path, forward spar cap was analyzed.

Fatigue test spectrum loads are typically developed using exceedance curves (appendix C) and arranged so that several different blocks representing different flight conditions (i.e., maneuver, gust, etc.) are repeated based on their probabilities of occurrence for a certain mission profile for which the aircraft is designed. Within a block, there are several subsets of load blocks (SLB) that are arranged low to high and high to low as shown in figure 26 (each bar in this figure represents an SLB). These subsets are considered constant-amplitude SLBs that construct the load spectrum. Therefore, CFR calculations can be significantly reduced by considering these SLBs rather than each cycle separately. To be conservative, the residual strength at the last cycle in each SLB is considered as the residual strength throughout that particular SLB.

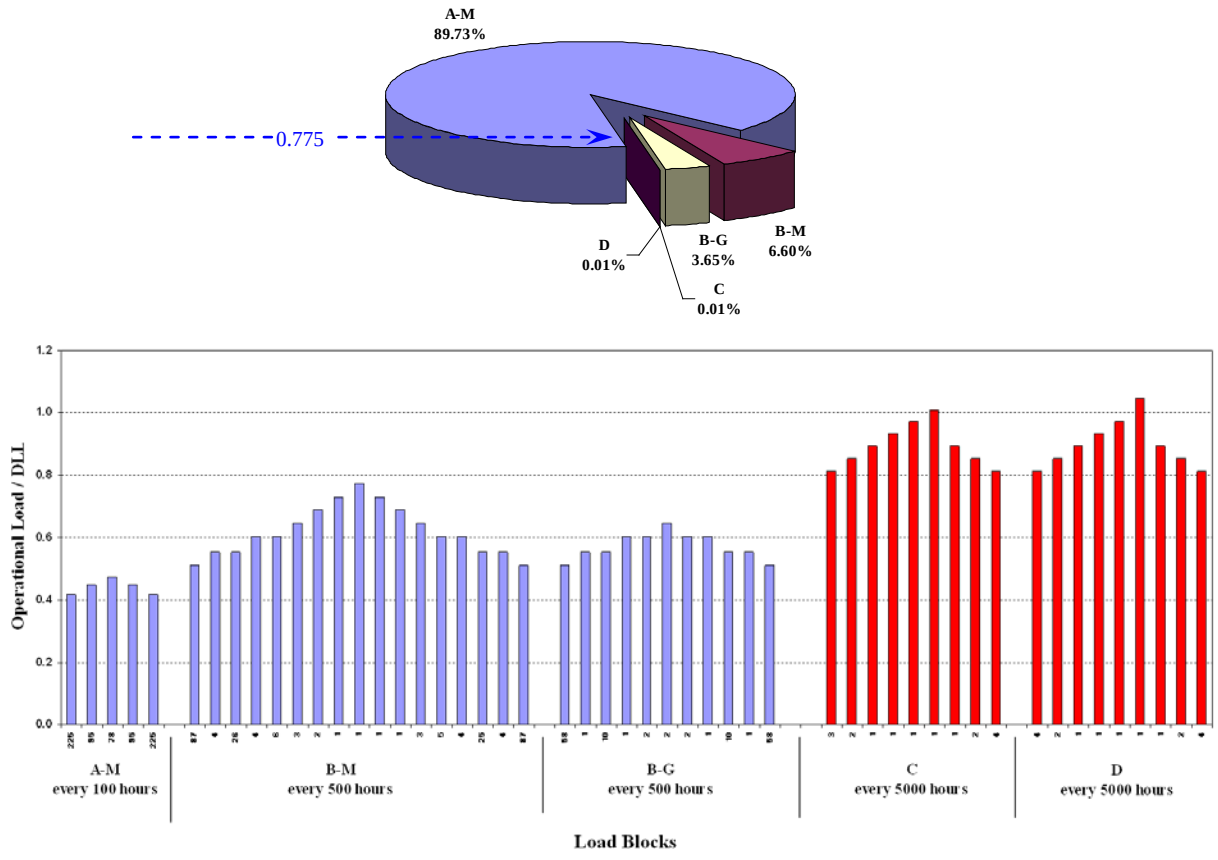

Figure 26. Forward wing cycle count per DLT

The next observation is that, except for blocks C and D, all loads were below 80% of the DLL and represented 99.98% of all cycles within the spectrum. Loads in the block A-M, which constitutes 89.73% of load cycles, were below the truncation load levels. The S-N data in section

4.2 confirm that the stress levels corresponding to these loads are below the endurance limit of LID specimens. Therefore, the residual strength degradation for these loads can be neglected. The majority of loads in blocks B-M and B-G were below 60 percent DLL, whereas the SLBs that were above that load level had only a limited number of occurrences within an SLB. Therefore, the residual strength degradation was extremely small.

The LLRS is an overly conservative wearout model (see figure 24), which only showed 0.3% residual strength loss at one DLT, and approximately 0.03% and 0.04% of that were due to the loads in blocks C and D, respectively. Therefore, for the purposes of establishing inspection intervals and assessing the structural reliability for CAT3 damage, the lower bound estimate of residual strength with γ-level of confidence can be calculated using equation 6 so that this value can be used throughout the spectrum. For one test article and shape parameters of 20 and 32.193, the lower bound estimate indicates a reduction of 5.3% and 3.4%, respectively. This reduction factor results in a residual strength that is considerably less than that using the LLRS and has significantly less impact on the POF than that from varying MSSPs from 20 to 32.193 (figure 27). These two scenarios predict structure failure during 40,007 and 80,025 cycles, respectively.

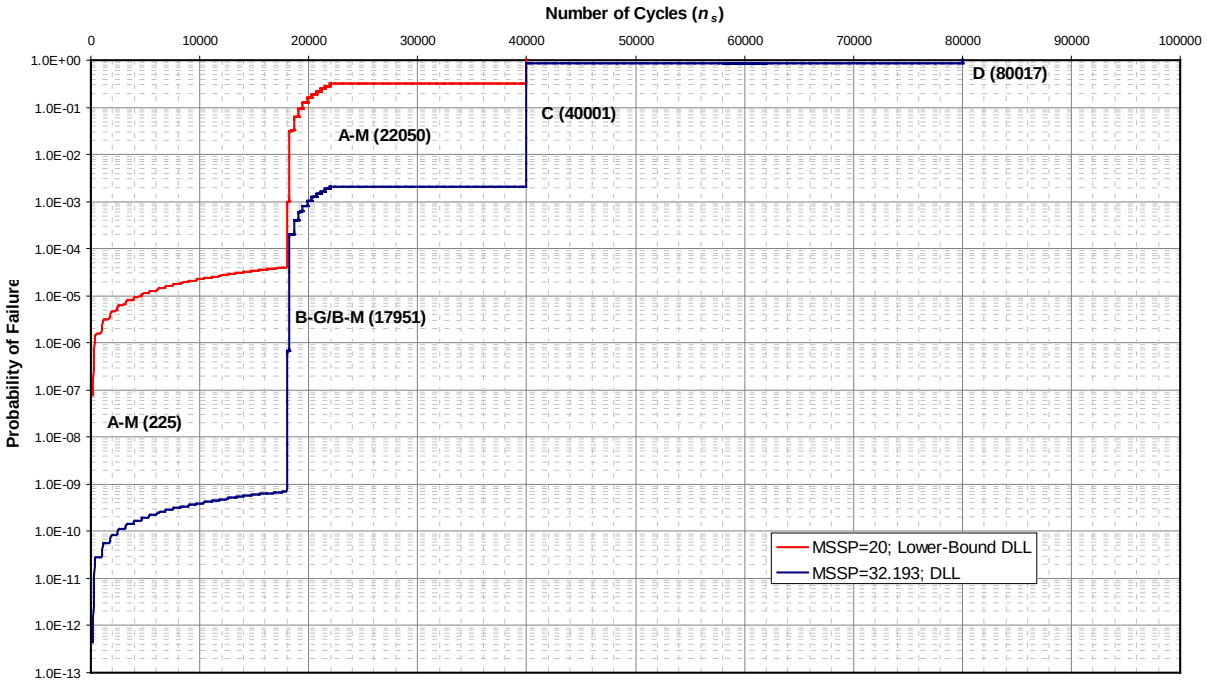

(a) Comparison of MSSPs from 20 and 32.193

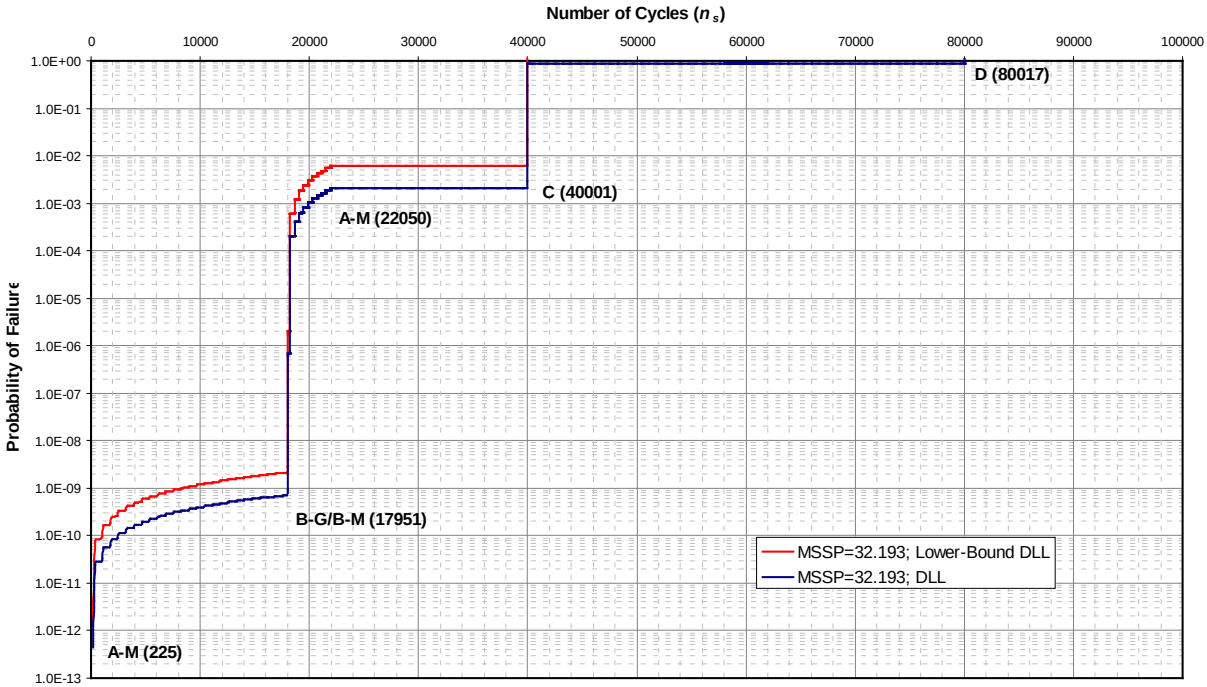

(b) Comparison of assumed residual strength of lower bound DLL and DLL

Figure 27. Cumulative POF for Starship forward wing

3.4.3.1 Determination of Inspection Intervals

The primary objective of establishing inspection intervals is to discover dormant failures as a result of an accident or degradation, which will eventually threaten the structural integrity, to mitigate the risk of structural failure. Regardless of the damage threat level, the approach discussed in the previous benchmark example graphically exemplifies the effects of different load conditions. A sudden increase in the POF (note that the probability in figure 27 is on a logarithmic scale) can be attributed to the likelihood of damage propagation; therefore, inspection levels during testing can be allotted to detect such phenomena. When considering inspection intervals during operations, it is important to consider a target reliability level and a probable damage threat so that the inspection intervals can be allotted to maintain the POF under this threshold. Because the definition of CAT3 damage in table 1 delineates limit-load capability as a requirement, such extremely improbable, yet easily detectable, damage that defines the CDT is practical to establish inspection intervals. It is also expected that this critical damage will not grow before it is detected by scheduled inspection.

Figure 28 shows an example of establishing inspection intervals with a target reliability of 90% using the CFR model for the load spectrum used for the Starship DaDT testing; 11 possible incidents cross the target reliability threshold. During blocks C and D, the POF rapidly increases over 20% and 30%, respectively; therefore, an additional count is added for every 10% increment. Using this graphical method will alleviate any confusion about whether this sudden increase in the POF is caused by one cycle or multiple cycles that are not clearly visible because of thex-scale of the graph. Furthermore, this will reduce the size of the inspection interval for load spectrums that have multiple high-load segments that increase the POF significantly.

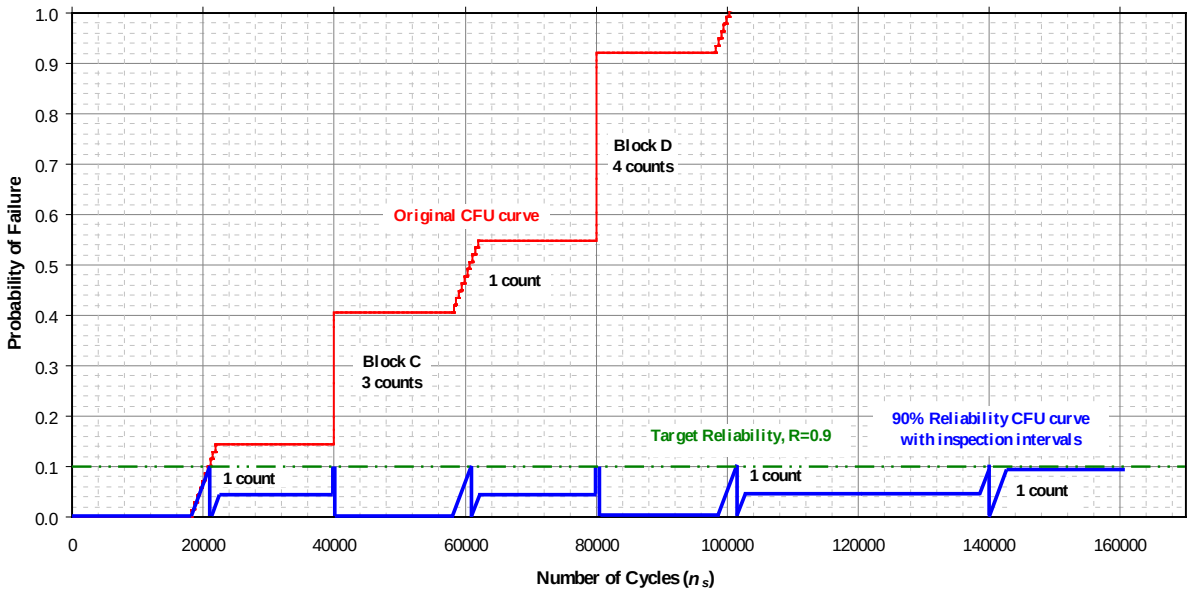

Figure 28. Establishing inspection intervals using CFR curve for target reliability

The inspection intervals in this example (figure 28) are allotted so that the POF does not increase more than 10% (reliability = 1-POF). Also, it is assumed that the damage is detected during

inspections and that the structure is restored to its condition prior to the damage; therefore, the POF is set to zero prior to calculating the remainder using the CFR model. As shown in figure 28, the smallest interval between two points at which the POF reaches the reliability threshold is approximately 19,000 cycles. This value is divided by the life factor (e.g., 9.6) to obtain the inspection interval of 1979 cycles. Conversely, if the total number of cycles in DLT (160,033 cycles) is divided by the number of times that the POF reaches the reliability threshold per DLT (11, for this example), then 1458 cycles result. Because this is smaller than the previously calculated inspection interval of 1979 cycles, the latter should be set as the minimum inspection interval.

If the minimum inspection interval is beyond the cost restrictions or is not practical, the probability of the occurrence of high loads and a more practical damage threat level can be considered to reduce the number of inspections required. Regardless of the scheduled inspection intervals, if an event that is similar to block C or D is experienced or if damage is detected during a walk around, the structure must be immediately inspected and repaired to ensure continued airworthiness. This example also shows that the imminent structural failure due to CAT3 damage, which was approximately 100,000 cycles, was eliminated with scheduled inspections, and the DLT was re-established.

3.4.3.2 Composite Structures Fail-Safe

Of the three zones in figure 16, only zone 3 has a residual strength requirement that varies with alternate procedures/the probability of damage occurrence. In either case, any compromise for residual strength requirements less than the DUL requirement should only be considered when pursuing one of the options under the damage-tolerant, fail-safe means of compliance.

One example of the use of alternate procedures is for the rare damage threat from a high-energy blunt impact (e.g., service vehicle collision). Depending on the selected maintenance inspection scheme, such damage may fall under the category of zone 3. When considering such damage in the composite structure's design, it may be shown to be damage-tolerant and fail-safe, even though the damage is not detectable, based on a very low probability of occurrence. As a result, the design would have sufficiently high residual strength (e.g., below DUL, but well above the DLL to ensure safety without detection for long periods of time). If it is further determined that such impact events usually occur with the knowledge of maintenance or aircraft service personnel, then alternate procedures may be added to the instructions for continued airworthiness. For example, advanced inspection methods, which can detect damage from high-energy blunt impacts, may be used as alternate procedures to minimize the risk of catastrophic failure for such zone 3 damage.

3.5 THE DaDT TESTS

Previous research efforts [45] concentrated on the areas (shown in figure 15) up to the CDT using fairly small coupons; therefore, the results obtained are conservative. This research addressed the damage tolerance design philosophy, within the scope of this program, of investigating larger damages using larger elements and full-scale subcomponents and subcomponents.

To verify that the structure had sufficient residual strength to sustain the expected in-service loads once damages had been introduced, a typical certification program for a composite structure was conducted in two phases. During certification of the Starship forward wing, durability of a minimum quality structure was demonstrated for 1 DLT with an LEF of 1.15, and then damage was included in the durability test and continued for an additional 1 DLT (figure 29). At the end of 2 DLTs, residual strength was demonstrated.

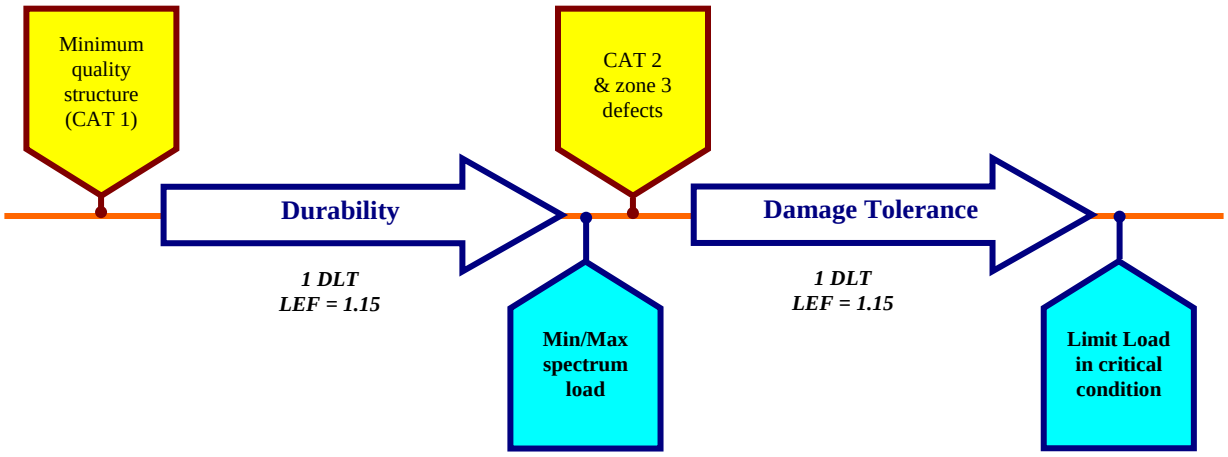

Figure 29. Starship DaDT certification test

To validate the proposed methodology in section 3.4.1, large CAT2 and CAT3 damages were explored through several full-scale tests. Damage tolerance element tests were conducted, as will be discussed in section 4, to investigate the methodology of simulating the damage severities described in table 1 into full-scale test articles. Once LEF results and damage tolerance element tests were completed, the LEF required for the LLD hybrid approach that incorporates scatter in the damage categories into the load-life approach was developed. Full-scale test articles were impacted at the beginning of the test phase, as shown in figure 30. These tests provided information related to establishing inspection intervals and the damage tolerance capability of CAT3 damage.

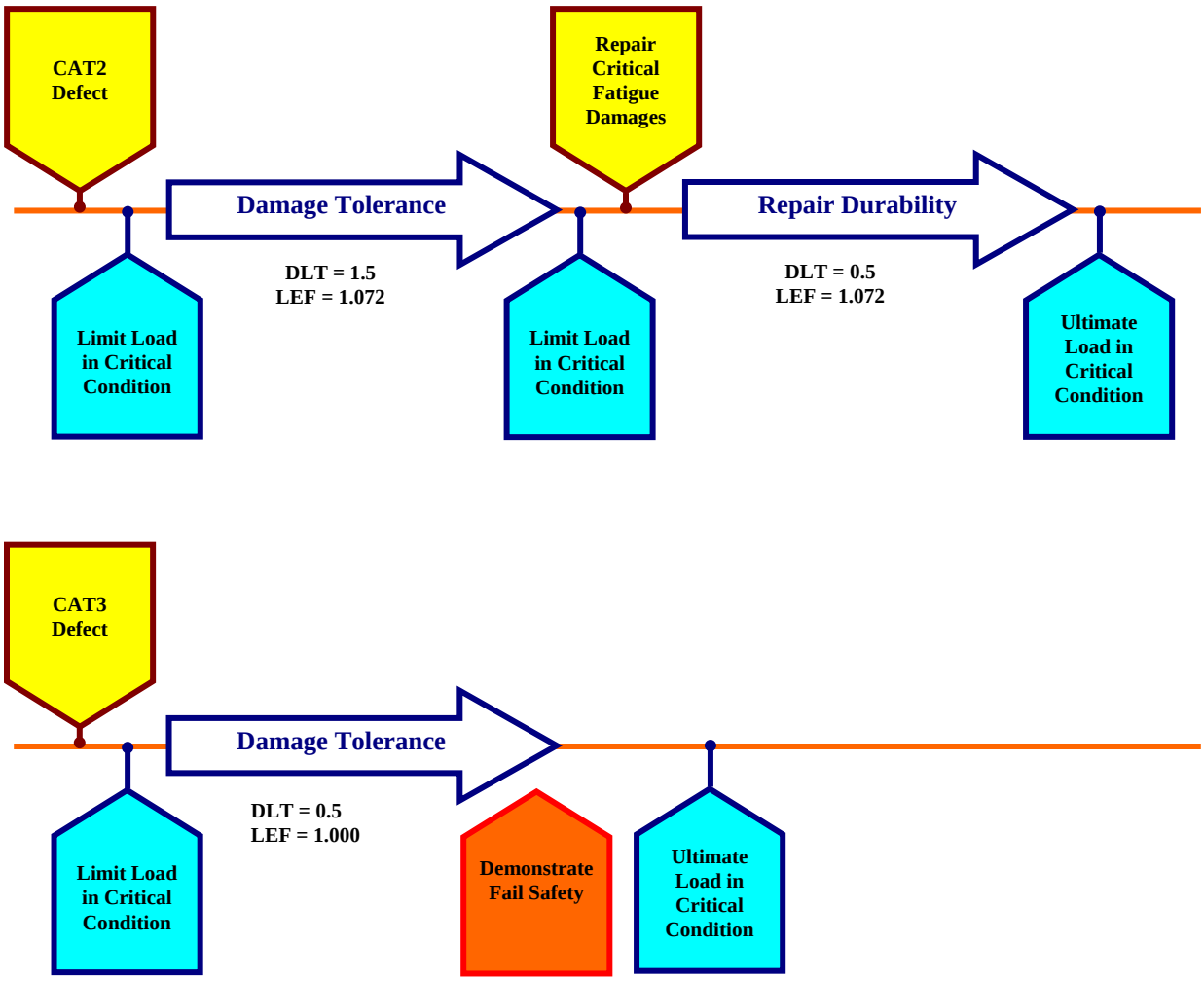

Figure 30. The DaDT testing with CAT2 and CAT3 damages

3.5.1 Damage Infliction

Depending on the certification program, the introduction of defects into the full-scale test article varies either after 1.5 or 2 DLTs, especially in high-threat and low-probability cases. Some damages, such as debonds, delaminations, and the simulation of porous details, may require inclusion during fabrication of the test article.

Several methods are commonly used to produce defects in the full-scale test article. Surface impact produces internal delamination, core crush for sandwich structures, or puncture damage at high energies. Edge impact with a sharp object, such as a chisel, produces edge delamination, which simulates debonds in joints. Cross-head puncture, which produces a cross-shaped defect with severe delaminations, simulates severe impact or lightning strike damages. Use of a welding torch to burn surface plies simulates lightning strikes and engine-burn fire damage. Drilling holes and saw cuts are also commonly used to disrupt the load path in attachment members and joints.

Extreme care must be exercised, especially when inflicting large defects, so that the mechanical means of inflicting damage does not demolish the test article. Procedures must be performed following finite element analysis and careful investigation of strain gage data from the initial fatigue test phase. These data, along with manufacturing experience of typical causes for rejection of parts, help identify the areas where such defects are least desirable and, therefore, threatening the structural integrity. Information related to the scaling effects of damage is crucial to identify the necessary energy levels for impact damages, especially in the simulation of severe damage scenarios, such as CAT3 and above.

For the Starship forward wing, the threshold of detectability (BVID) for impact damage and the limit load envelope were close. The spar cap on the contact side bends and crushes the web, which is of a honeycomb construction, and bounces back, unlike a layered composite, because its construction is similar to a bundle of fibers (see figure 31). Therefore, thick, mostly unitape-wound spar caps required a significant amount of energy and very sharp impactor geometry for perforation, as will be discussed in section 5.2.2.

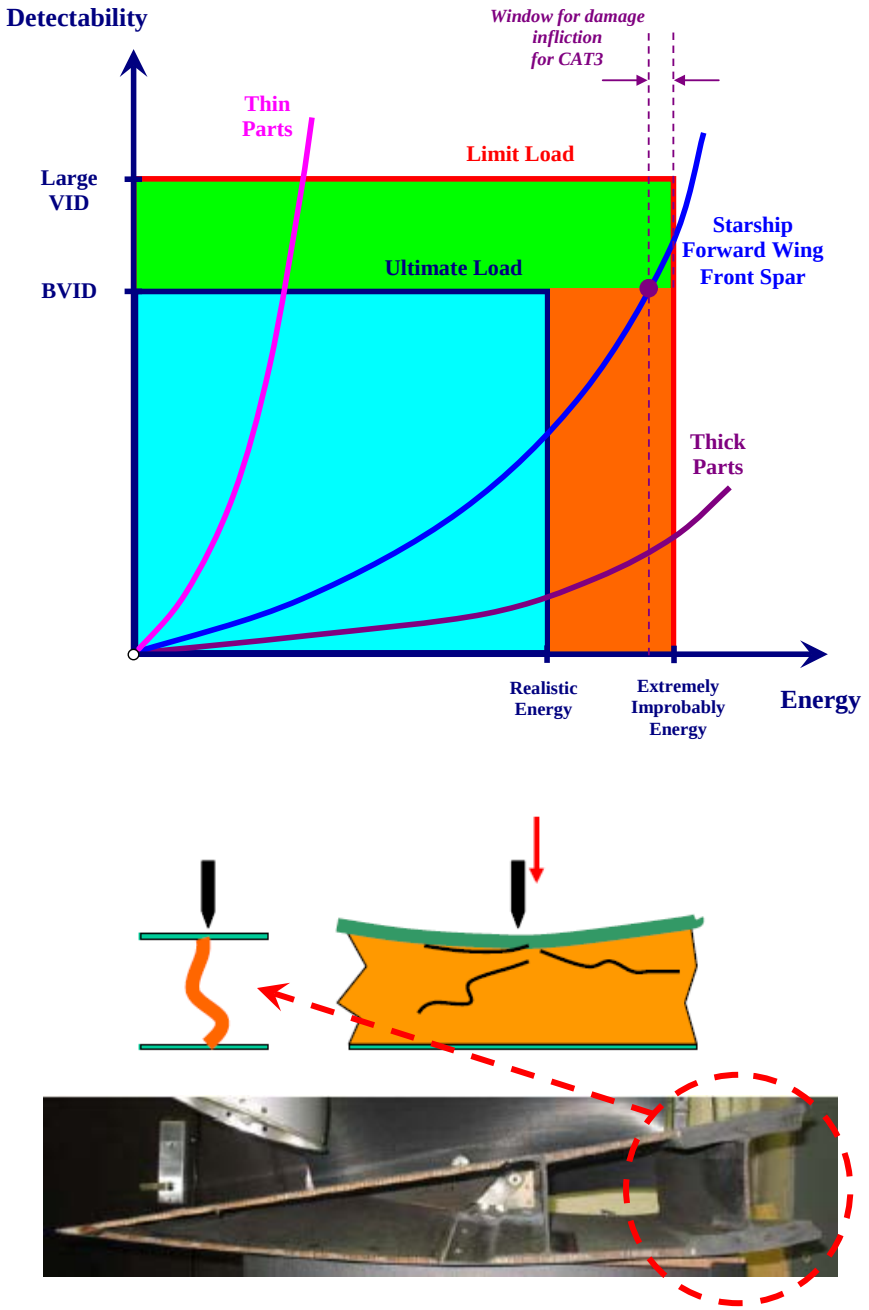

Figure 31. Damage infliction on Starship forward wing

3.5.2 Progressive Damage Growth

Unlike the process for a standard certification program, damages inflicted on a full-scale article are more severe (i.e., large CAT2 and CAT3 damages). Therefore, NDI requirements for damage tolerance testing require detailed NDIs. Signs of internal damage included, but were not limited to, strain and displacement anomalies, fracture or delamination, relative motion of attachment members or joints, audible noises, and localized shift or relaxation in the whiffletree assembly. When these signs were detected, the structure was inspected and observations were documented

in detail with corrective actions, if any. If a localized disassembly was required for an unscheduled detail inspection, care was taken not to damage or alter the structure prior to restarting the test. Standard tap testing was used to inspect the test articles, while detailed inspections were conducted using ultrasound, the BondMaster 1000, thermography, and RD3 electronic DTH. As shown in figure 32, the NDI techniques described in section 2.6 were used for detecting damage onset and growth during fatigue cycling as well as failure analysis after static or residual strength testing.

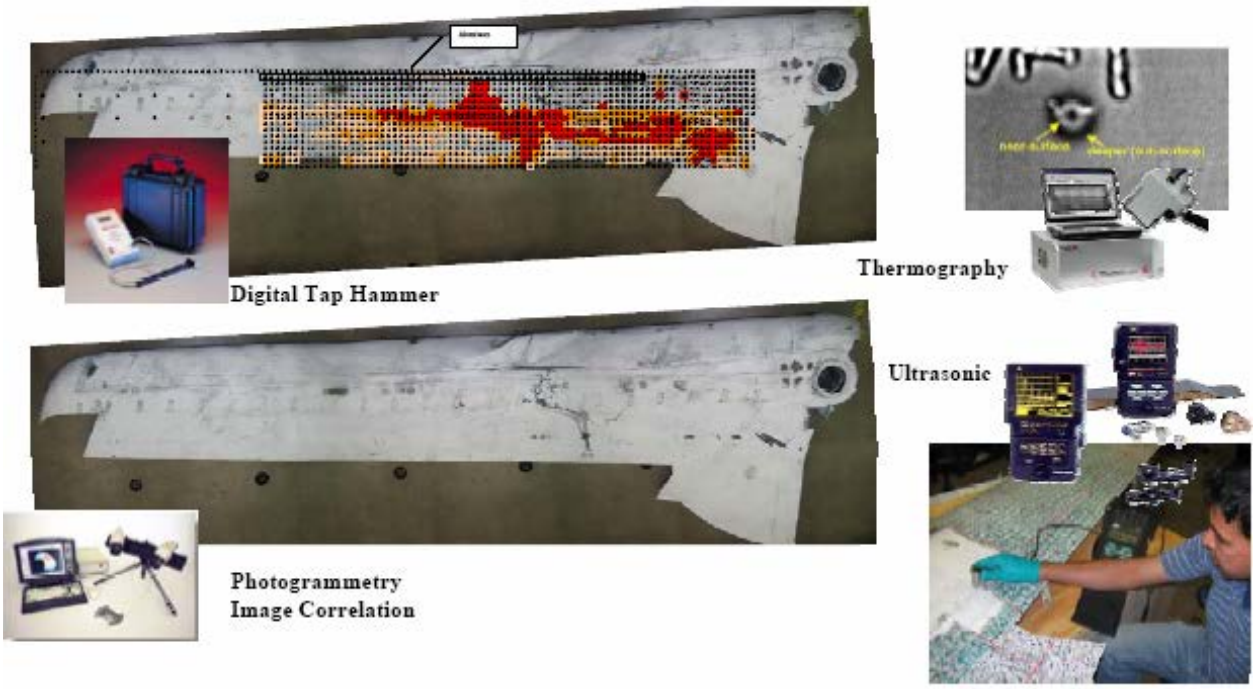

Figure 32. Failure analysis for full-scale testing

4. DAMAGE TOLERANCE ELEMENT TESTS

A detailed damage tolerance element (DTE) study was conducted to determine the flaw growth and data scatter in damaged composite structures. This study focused mainly on impact damages and their effects on the extent of the damaged area, residual strength, fatigue life, flaw growth, and data scatter. The data gathered in this section also provide guidance to scaling of damage extents for full-scale tests.

4.1 EXPERIMENTAL PROCEDURE

In addition to data included for scatter analysis conducted on AS4/E7K8 plain-weave fabric material, a total of 72 CAI specimens and 6 unimpacted (baseline) specimens were tested (table 2). Stress levels were selected to obtain fatigue failures rather than runouts.

Table 2. The DTE test matrix

Category of Damage	Damage Definition	Impact Energy Level (in.-lbf/in.)	Stress Level	Static Strength (%)	Number of Specimens
UI	UI	N/A	Static	100	6
CAT1	BVID	750	Static	100	6
			SL1	80	6
			SL2	75	6
			SL3	70	6
CAT2a	VID	1500	Static	100	6
			SL1	75	6
			SL2	70	6
			SL3	65	6
CAT2b	LID	3000	Static	100	6
			SL1	75	6
			SL2	65	6
			SL3	60	6

UI = Unimpacted; VID = Visible impact damage

The main objective was to evaluate the data scatter with respect to the damage energy level or damage threat. Test panels were fabricated with a 32-ply quasi-isotropic layup (i.e., $[45/0/-45/90]_{4S}$). Test specimens were machined to 6 by 9 in., instead of the ASTM D 7137—the standard test method for compressive residual strength properties of damaged polymer matrix composite plates—recommendation of 4 by 6 in., to minimize the edge effects of LID and to leave sufficient material for damage propagation during cyclic loading. Based on several trial impact and residual strength tests, 750, 1500, and 3000 in.-lbf/in. impact energy levels were selected to represent CAT1, CAT2a, and CAT2b damage, respectively. The damage definitions corresponding to these energy levels were as follows:

- CAT1—Barely visible impact damage (BVID)
- CAT2a—Visible impact damage (VID)
- CAT2b—Large impact damage (LID)

Although these definitions may not have a one-to-one correlation to damages on a full-scale structure, the information pertaining to the scatter analysis is relevant to a damage structure at its critical load path (i.e., minimal global load redistribution due to damage). Following the infliction of the impact damage, residual dent depth and damage extent (using the TTU C-scan) were measured. During fatigue loading, the damage extent was inspected using a BondMaster 1000 hand-held NDI unit using MIA at several predetermined numbers of cycles. The ARAMIS

full-field strain and displacement data were also acquired at the maximum fatigue load at these intervals to delineate the extent of damage. This also allowed for measuring the residual stiffness or the compliance change of these specimens at these fatigue intervals.

All tests were conducted in a room temperature ambient (RTA) environment. Fatigue tests were conducted at a frequency of 5Hz with an R-ratio of 5 using the load control mode. For flaw growth studies, the strain control mode provides more progressive damage data because the maximum and minimum fatigue loads are gradually decreased as the compliance decreases; however, fatigue tests in this study were conducted using the load control mode to simulate fatigue damage on a critical load path that had minimal load redistribution because of loss of stiffness or compliance (i.e., front spar of Starship forward wing). This control mode maintains the initial minimum and maximum fatigue loads by increasing the strain ($+\Delta_\varepsilon$) throughout the fatigue test, in contrast to the strain control mode that reduces the loads ($-\Delta_P$) to maintain the initial strain limits (figure 33). Because of the high sensitivity in strain feedback during fatigue testing, this control may result in frequent test interruptions due to interlocks set to prevent overstraining of the test specimen.

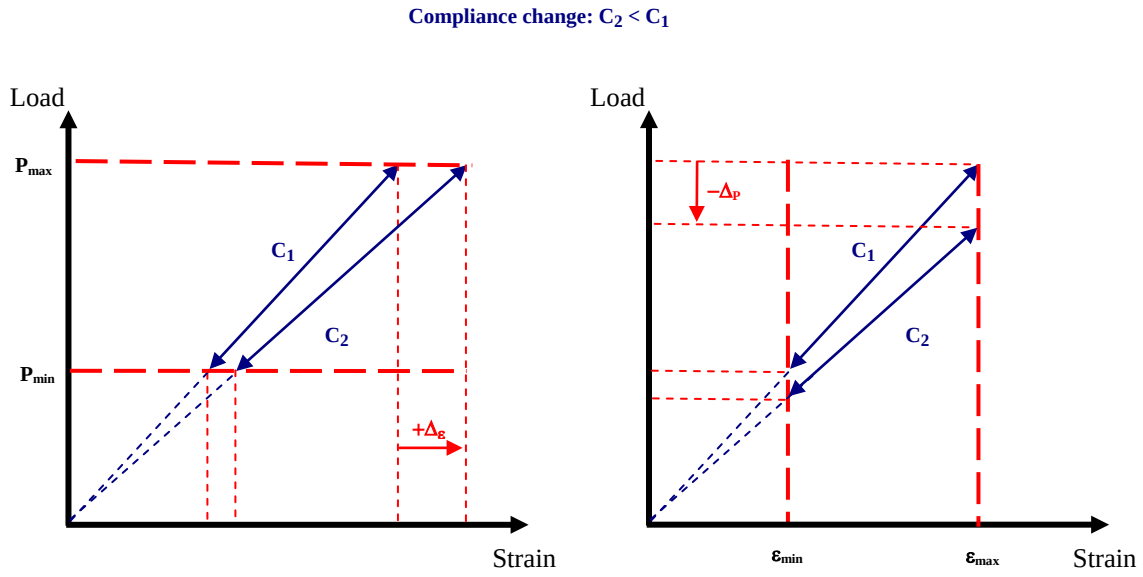

(a) Load control mode (b) Strain control mode

Figure 33. Load strain response for different test control modes

4.2 THE DTE test results

This section contains the NDI, residual strength, and fatigue life of DTE tests. Incipient curves during impact and post-impact inspection results are also included. Further, the scatter analysis of S-N data and flaw growth data are included for these specimens. Figure 34 shows the energy history for different impact energy levels. The plateau regions depict the total energy transferred to the specimen.

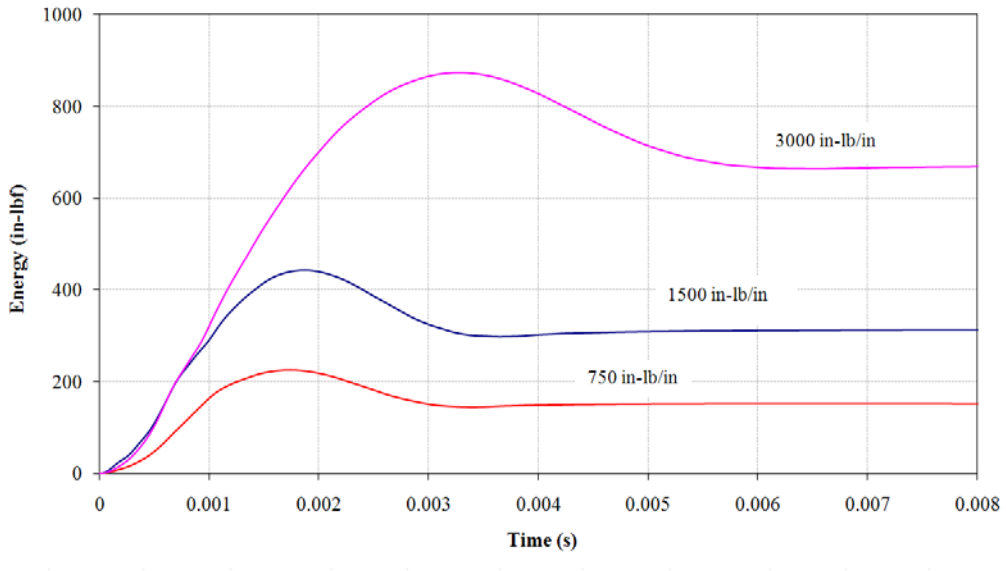

Figure 34. Comparison of energy history for different impact energy levels

4.2.1 Post-Impact Inspections

This section contains the NDI, residual strength, fatigue life, and scatter analysis of damage tolerance element tests. As shown in figure 35, VID was manifested as a large, cross-shaped back-side damage. Although some of the BondMaster 1000 NDI data followed the cross-shaped damage, post-impact TTU C-scans indicated mostly circular damage patterns.

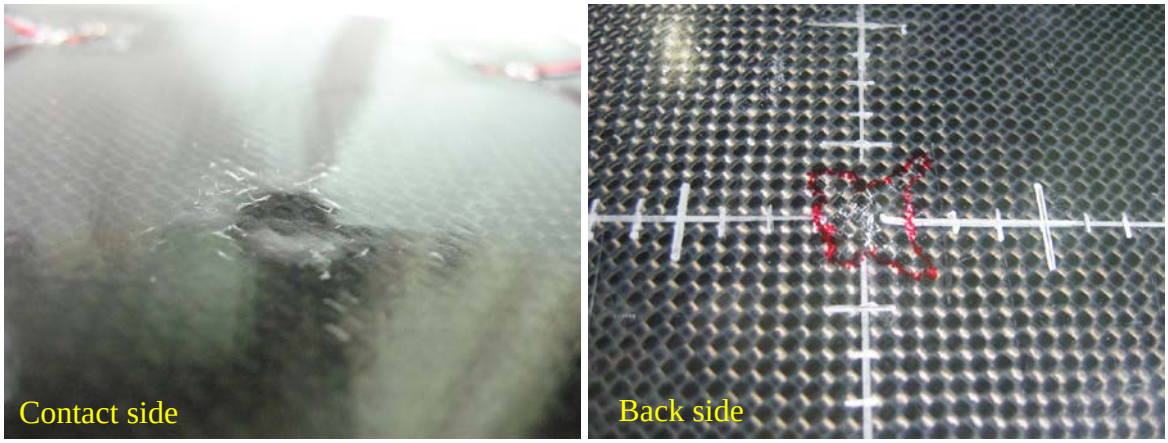

(a) 1500 in.-lbf/in.

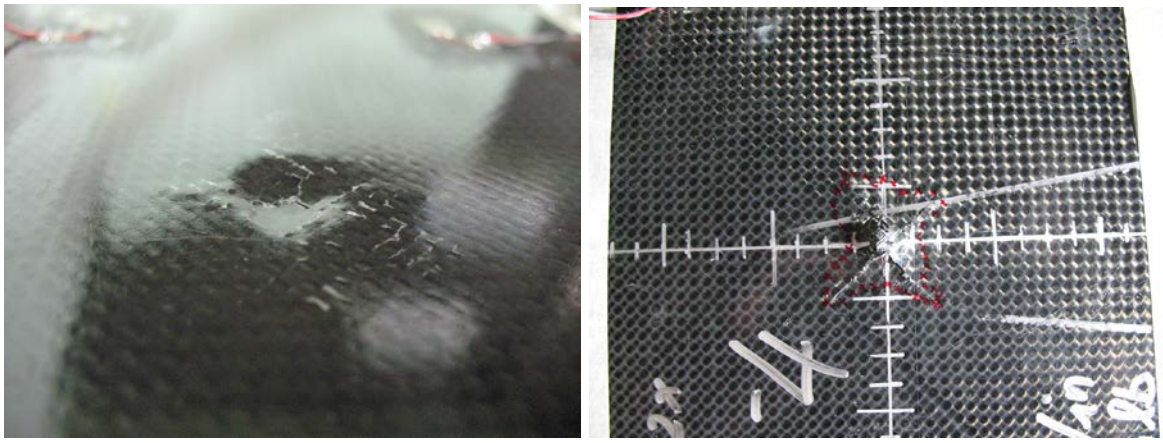

(b) 3000 in.-lbf/in.

Figure 35. Post-impact damage inspection of DTE test specimens

During the impact event, matrix cracks and fiber breakage resulted in a complex damage morphology that was difficult to predict, especially for impacts that did not result in complete penetration. There was significant compressive stress because of contact stress and the resulting bending moment, which was concentrated at the impact location and resulted in fracture along the fiber directions of the composite fabric layers. This was evidenced by the cross-shaped fracture on the back side of the specimens where the outermost fibers were in ±45° orientation (figure 36). The stiffness mismatch in fiber and matrix caused the cracks to form along the fiber directions during deflection.

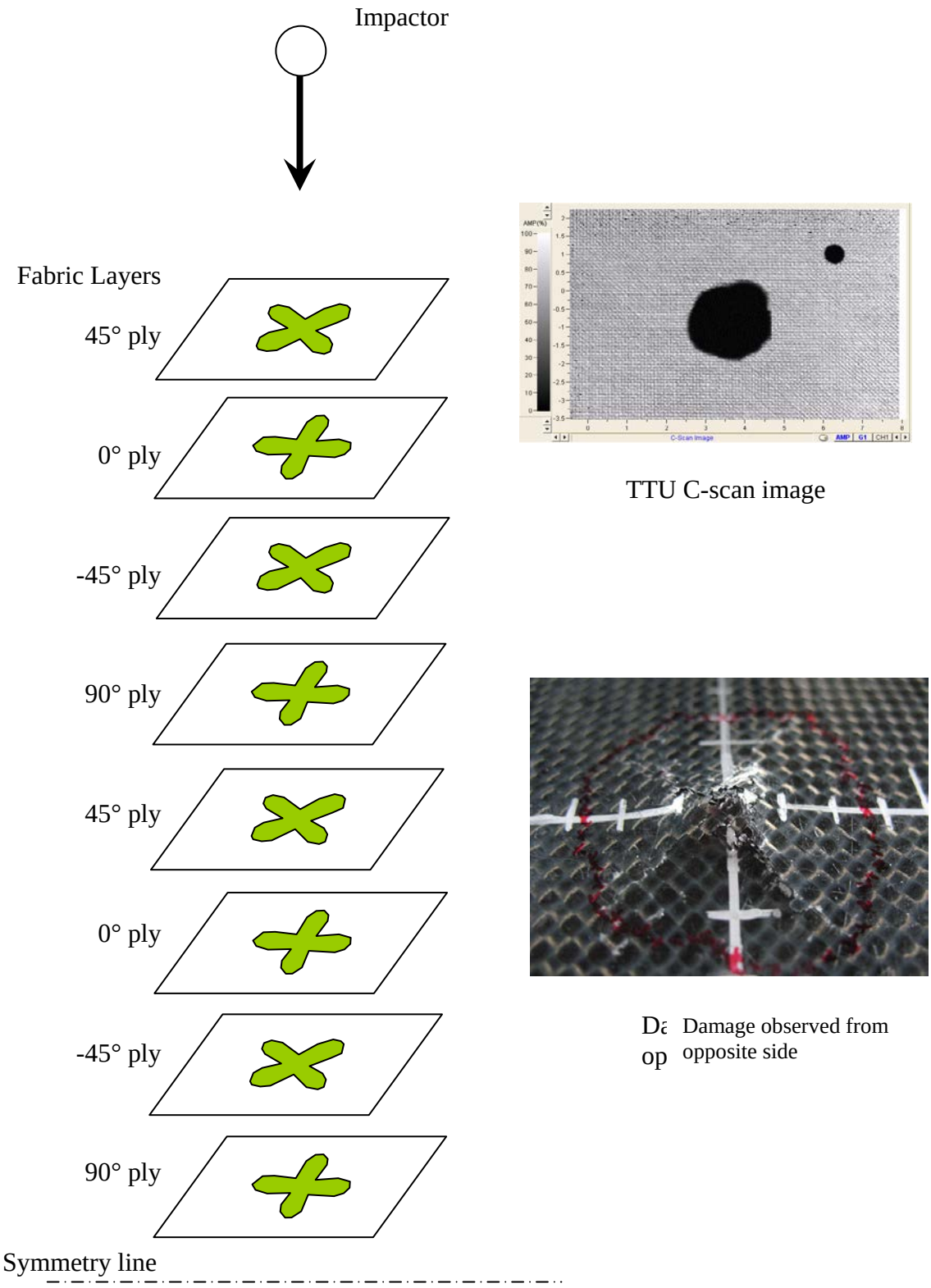

Figure 36. Matrix crack concentration orientation due to impact

For tape laminates, the damage formed an oblong or peanut shape with the major axis oriented in the fiber direction [50]. As shown by Tomblin et al. [51], for low-velocity impact damages on bonded composite joints, because the layup of AS4-PW is quasi-isotropic (i.e., $[45°/0°/-45°/90°]_{2S}$), these cross-shaped damage zones possibly concentrated in a 45° radial spacing, along fiber directions, at each layer through the thickness and smaller cracks in between, resulting in a circular damage shape as observed in TTU C-scans. In addition to cracks, localized contact stress resulted in fiber breaks and transverse cracks on the first few plies that resulted in through-thickness cracks of these plies. At these crack tips, where they meet the lower ply, a high-peel stress was created at the ply interface, which resulted in interfacial cracks or delamination. Because of the intralaminar matrix cracks along the fiber directions, the delamination propagated along the fiber directions of adjacent plies. Because the adjacent fabric plies were oriented 45° apart, the delamination spread in a circular pattern, as is shown in figure 36 (i.e., matrix cracks in adjacent layers coalesce within the small layer of matrix material between plies). Additional microscopic analysis and three-dimensional NDI data are required to verify this conjecture.

As shown in figure 37, the damage area increased as the impact energy increased. For 3000 in.-lbf/in. VID test specimens, a significant amount of energy was translated into large fractures and significantly large deformation (figure 38); therefore, the rate of increase in the damage area was reduced. As shown in figure 39, the contact force reached a maximum of 4000 lbf as the energy level increased, which resulted in a significant perforation, thereafter reducing the delaminated area in the planer direction.

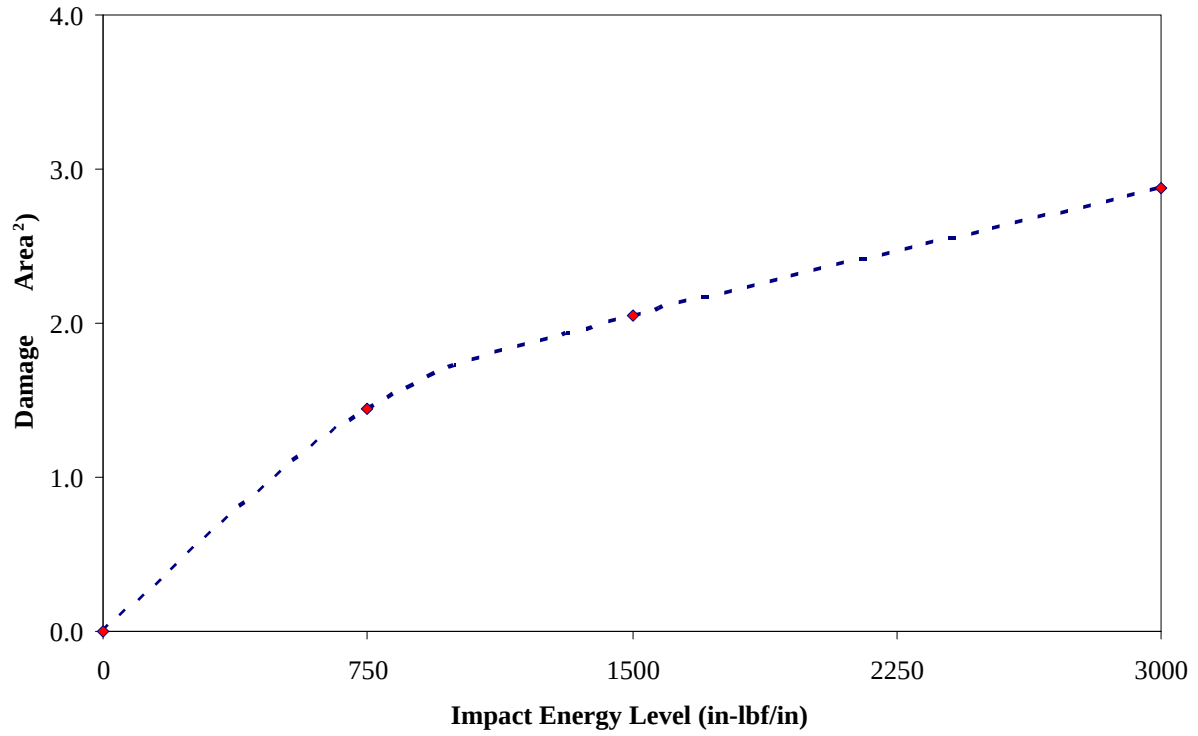

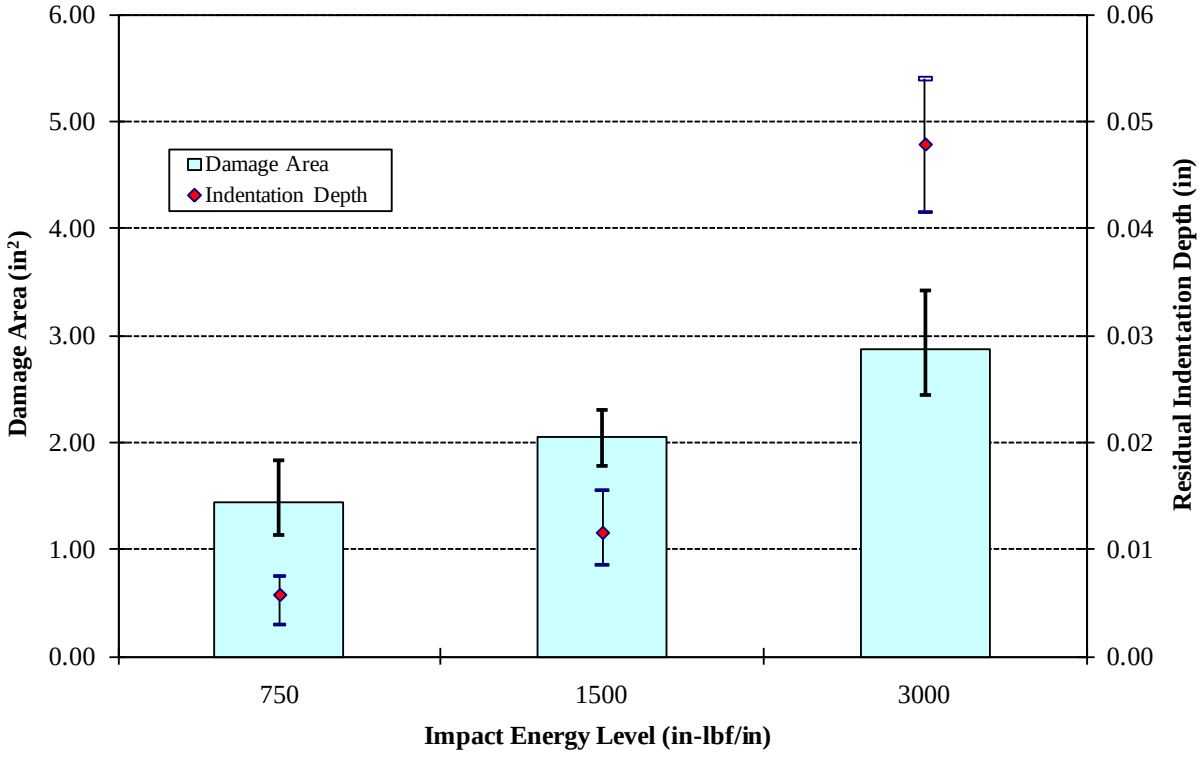

Figure 37. Post-impact inspection results for DTE tests

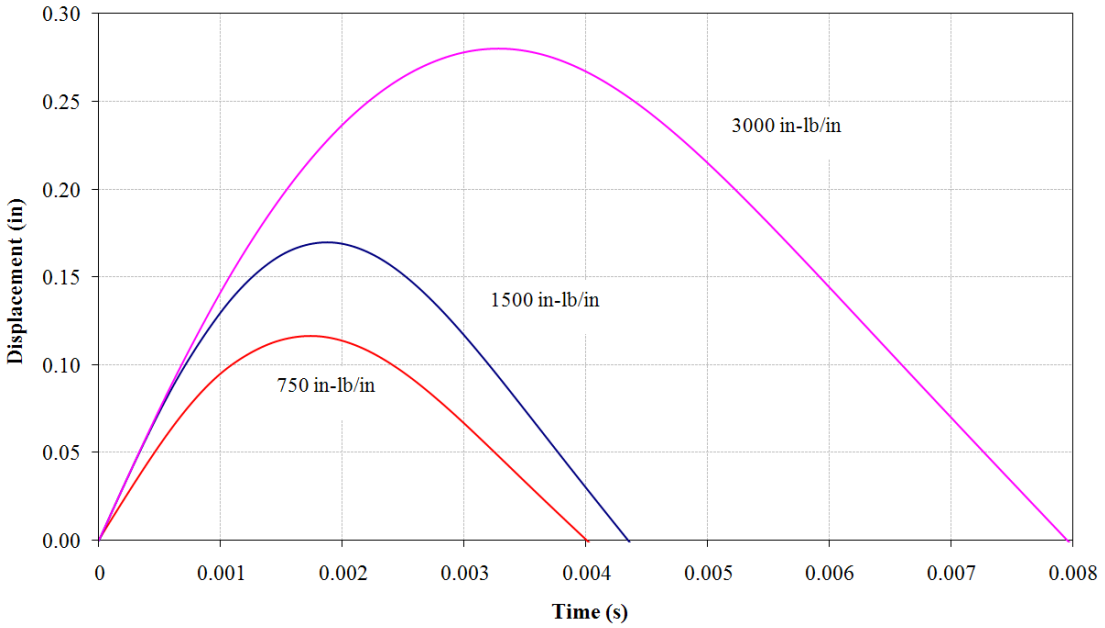

Figure 38. Comparison of displacement history for different energy levels

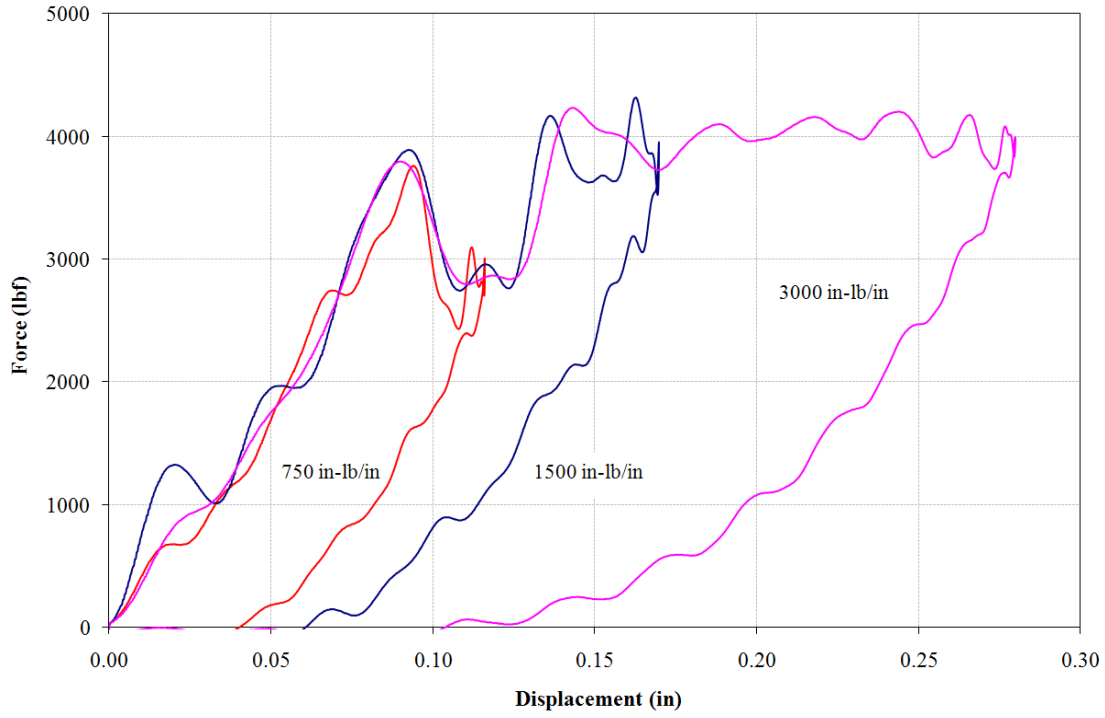

Figure 39. Comparison of force displacement for different energy levels

Figure 40 shows that, compared to BVID, VID showed a reduction of approximately 17% in residual strength, whereas LID showed a reduction of approximately 29%. The stress concentration factor (SCF), the stress amplifications in the vicinity of the defect (geometric

discontinuity), were calculated as 1.55, 1.87, and 2.19, for BVID, VID, and LID, respectively. These SCFs correspond to a damaged structure, assuming that the post-impact load path has not significantly changed. The loss of residual strength and post-impact damage inspections showed that LID specimens were sufficient to mimic CAT2b damage at the element level. Therefore, the scatter in the CAT2b damage structure was assumed to be represented by the scatter analysis of the LID specimen, as shown in section 4.2.3.

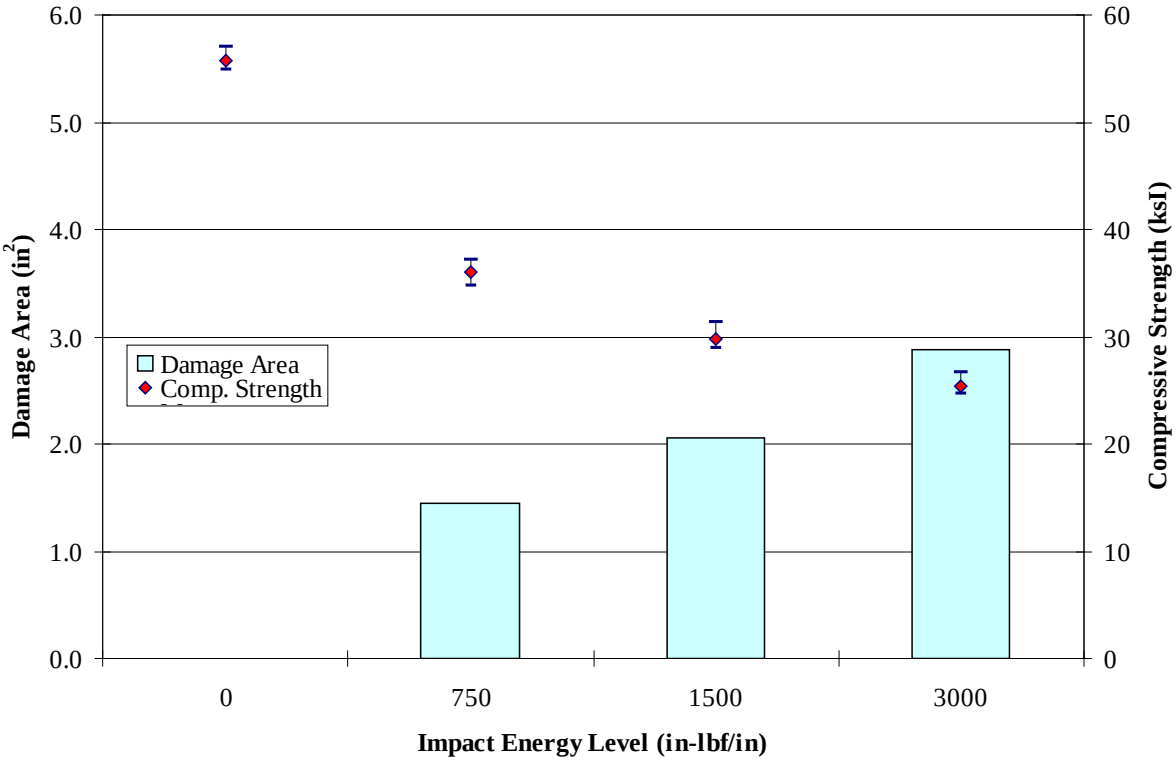

Figure 40. Damage area and residual strength results comparison for DTE tests

Figure 41 shows a summary of DTE test data for all three damage categories. The S-N data were also compared with the Sendeckyj wearout model data. For LID specimens that had larger perforations than either BVID or VID, the initial stiffness degradation was not as prominent because the majority of the damage had already propagated through-thickness (initial plateau region in figure 41). Note that the residual strength and the fatigue life of CAI specimens tested in this section were likely affected by the finite specimen width, especially for LID.

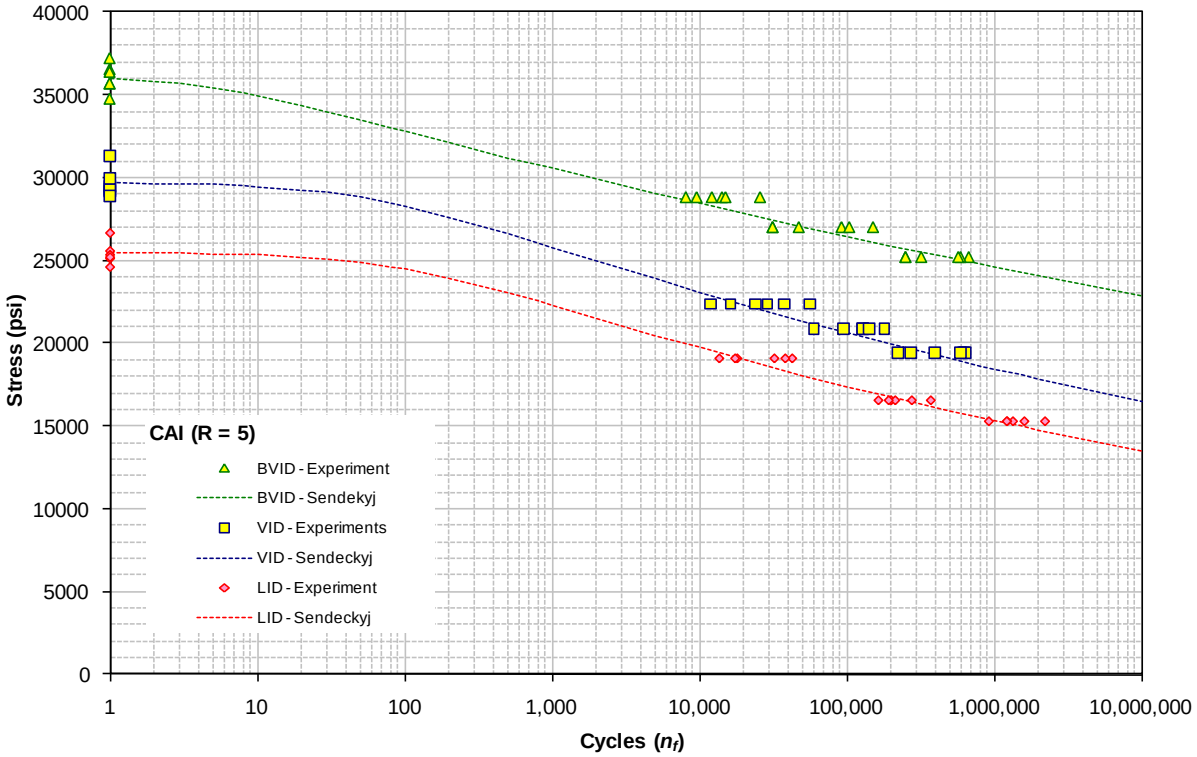

Figure 41. The S-N curves for DTE test specimens

4.2.2 Flaw Growth and Compliance Change

Typically during fatigue loading, specimen compliance gradually decreases, as discussed in reference 40, primarily because of stiffness degradation in the matrix material caused by microcracking when a sudden drop in load-carrying capabilities is observed (i.e., when the fiber failure occurs, the specimen fails). In the case of DTE specimens, the impact damage for the LID fatigue specimen at SL2 (65%) propagated as shown in figure 42. As figure 42 shows, the initial cross-shaped damage area, which was delineated by the BondMaster 1000, rapidly grew into a circular shape. As shown in figure 36, this is due to the coalition of small cracks that were present (C-scan images), but not detectible to the BondMaster 1000 prior to fatiguing. Although the damage stopped growing in the load direction (length) after approximately 75,000 cycles, it grew continuously in the direction perpendicular to the load until final failure (260,091 cycles).

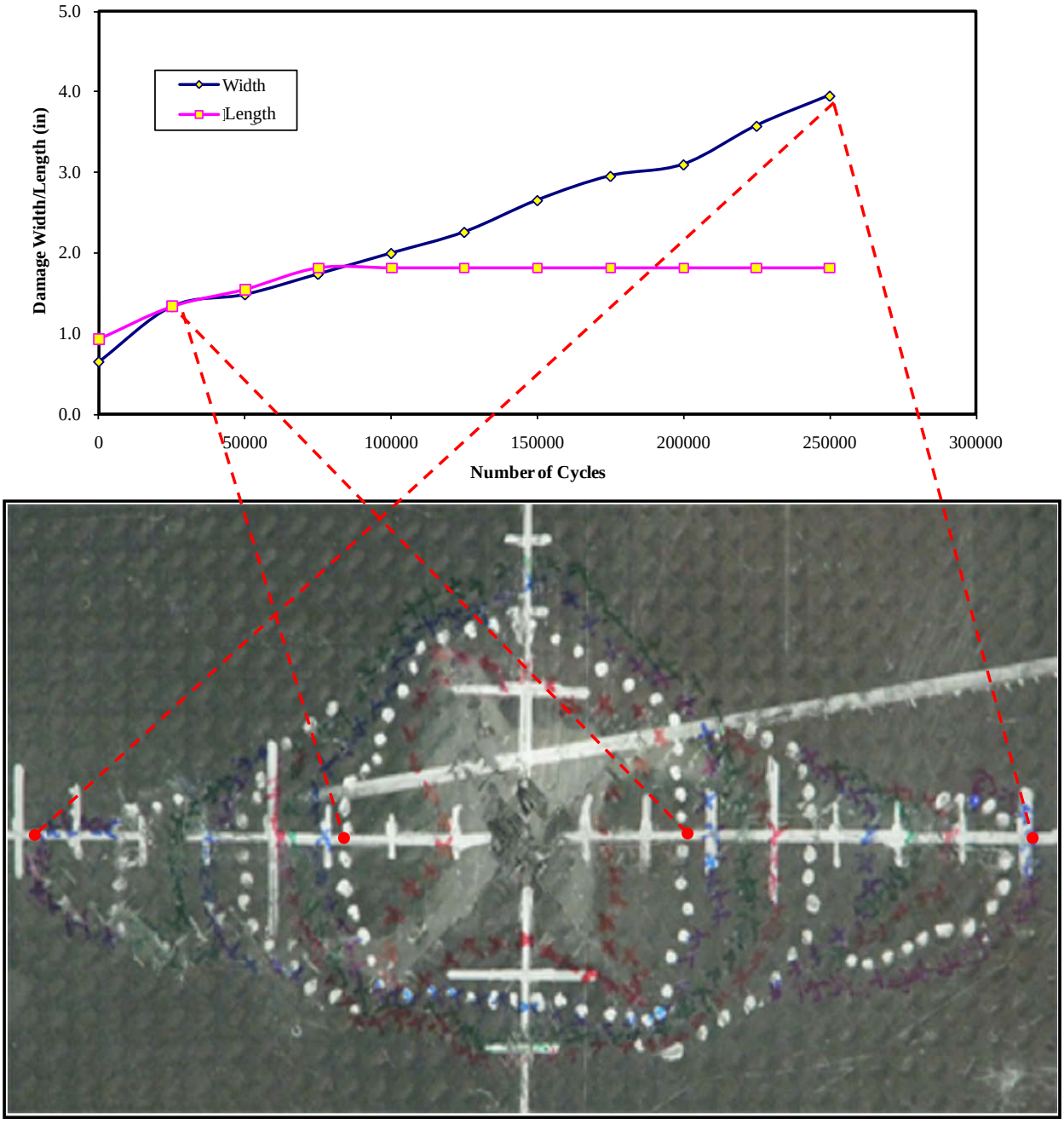

Figure 42. Progressive damage propagation for SL2 of LID

As shown in figure 43 for SL3 (60%) of LID, the length of the damage remained constant throughout the test. However, the width of the damage remained contained up to 200,000 cycles and then increased steadily until final failure at 492,163 cycles. ARAMIS full-field displacement measurements also confirmed the increase in damage width and significant out-of-plane displacement after 200,000 cycles. Therefore, the flaw growth threshold for this damage scenario and stress level was 200,000 cycles. Additional ARAMIS data are included in appendix B.

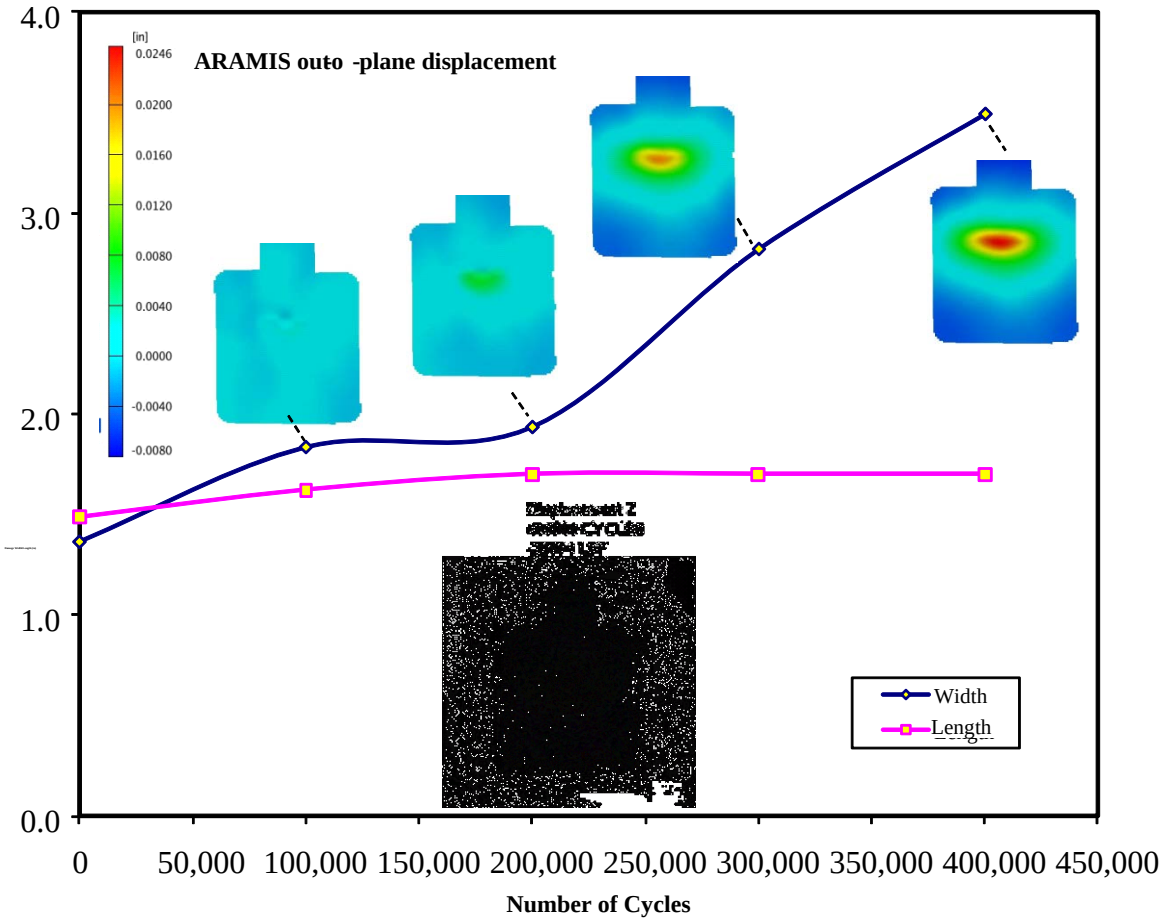

Figure 43. Progressive damage propagation and out-of-plane displacement for SL3 of LID

Typically, the NDI or full-field displacement/strain measurements are not acquired during a fatigue test, because they are time-consuming and expensive. However, specimen compliance can be calculated by simply outputting data during fatigue testing, without interrupting the fatigue test, and calculating the slope of the load-displacement curve. As shown in figure 44, the compliance of the SL3 specimen dropped dramatically after 200,000 cycles, confirming the NDI observations. The SL2 specimen compliance gradually decreased after 50,000 cycles. Therefore, it was recommended that specimen compliance, especially for notched specimens, be monitored throughout the fatigue test to better understand the failure mechanism and the damage propagation.

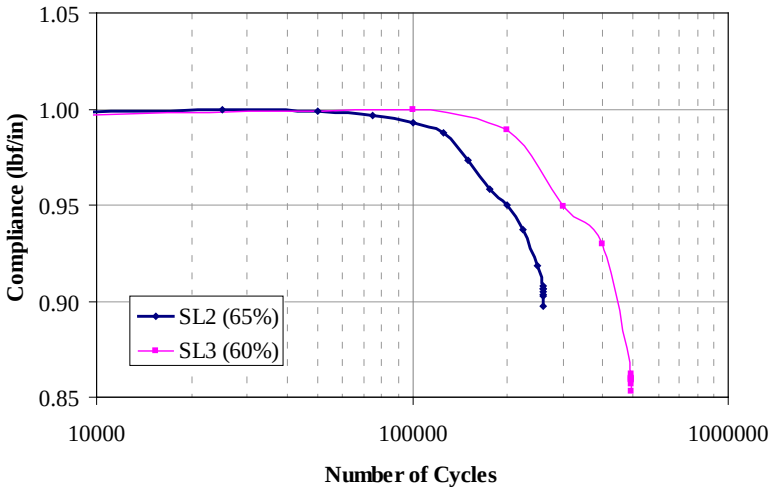

Figure 44. Compliance change (normalized by initial compliance) in LID fatigue specimens

4.2.3 Scatter Analysis of DTE Test Data

The scatter analysis of S-N data shown in table 3 was conducted using individual Weibull, joint Weibull, and Sendeckyj analyses (figure 45). The latter two are pooled analytical techniques for calculating the shape parameter of fatigue life distribution.

Table 3. Scatter analysis results of DTE tests

Damage Category	Static Strength		DaDT			
	Weibull Analysis		Sendeckyj Analysis (α_L)		Weibull Analysis (α_L)	
	α_R	β (psi)	With Static	Without Static	Individual	Joint
BVID	45.771	36413	1.774	2.234	2.446	2.355
VID	32.222	30103	2.182	2.658	2.991	2.779
LID	36.676	25776	2.466	2.799	3.272	3.250

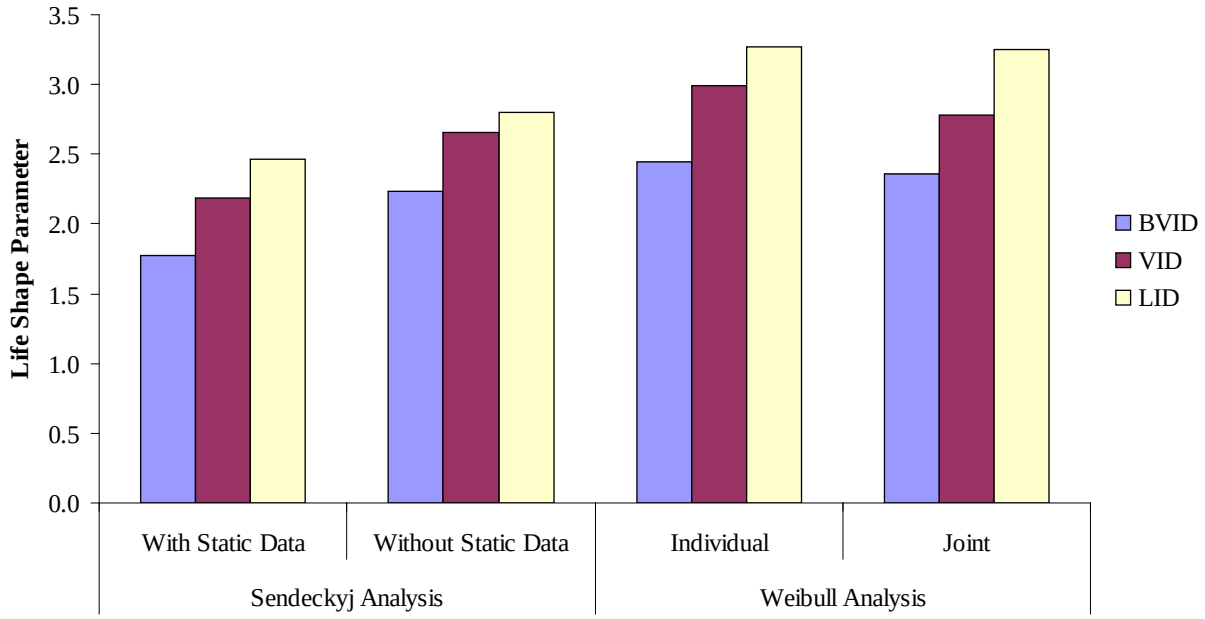

Figure 45. Comparison of DTE life shape parameters

Sendeckyj analysis was conducted with and without static data. For the LEF data shown in reference 40, life scatter increased when the static data points were included in the analysis. All four analysis methodologies showed that scatter in fatigue data was reduced as the damage threat level increased. This was mainly due to the stress concentration caused by the increased severity of impact damage. The post-impact visual inspections revealed that the probability of detection of damage increases proportionally with the increased energy level or severity. In a service environment, these inspections will mitigate the risk of severe damage, such as CAT2b, being left undetected, and the damage will be found within a few flights. The reduction in scatter, however, supports the analysis of static strength or fatigue life of a damaged structure using scatter-based methods and results in fewer repeated load tests to achieve a certain level of reliability. These items will be further discussed in section 3.4.3, in terms of application to a full-scale DaDT test article.

5. FULL-SCALE VALIDATION

Figure 3 showed an overview of the full-scale test plan. Initially, several static test articles were used to determine the ultimate loads and the corresponding limit load for the DaDT tests outlined in this section. The appropriate CF, along with the LEFs developed in reference 40 for the Beechcraft Starship material, and design details were used to generate the load spectrum. Unlike the FAA certification program of Starship forward wing, the defects were introduced to the structure at the beginning of fatigue tests. The damages introduced to the structure also represents considerably larger and higher impact damages than those used for the original certification program. The durability test articles were inspected periodically using conventional and detailed inspection procedures in addition to monitoring strain anomalies for possible damage progression.

5.1 FULL-SCALE TEST PROGRAM

As shown in figure 3, the results from five static and two fatigue tests of the Starship forward wings were included in this program. These wings were used to demonstrate various means of compliance, validate the approach for full-scale demonstration based on LEF and N_F as outlined in reference 40, and validate the methodology discussed in section 3.4.1. Full-scale tests were planned to address static, damage tolerance, and durability. To reduce the number of tests required, these tests were planned with some overlap of the above-mentioned three core categories outlined in figure 3. The outlined test plans for these tests consisted of two stages: (1) the static with strain survey and damage tolerance phases, and (2) the durability with damage tolerance and repair phases. Stage 1 included three forward wing static tests to generate static-strength data for baseline comparison and to accomplish strain surveys of these articles. These surveys were used to establish the spectrum-loading magnitudes relative to durability tests. Then, two static articles were tested with CAT2 and CAT3 damage to ensure residual-strength requirements for damage-tolerant fatigue test articles.

In stage 2, two fatigue articles were tested under spectrum loading with CAT2 and CAT3 damage that was similar to that in the damage tolerance phase of stage 1. CAT2 damage in the first fatigue article was intended to investigate damage behavior at the ADL and the residual strength of the structure to sustain expected in-service loads. Such information is crucial for determining inspection intervals. Test duration was selected based on the calculated LEF and N_F related to design details of the Starship forward wing. This was done to verify the methodology presented in reference 40. Further, the construction of this test article demonstrated that the global failure mechanism is insensitive to damages inflicted on the secondary load path. The second fatigue test article with CAT3 damage was intended to obtain information pertaining to the onset of damage growth in a primary load path. This damage was selected as it would provide vital data for the definition of the CDT and help define the inspection intervals. The post-impact residual strength of the CAT3 article was close to limit-load capabilities. Therefore, no LEF was applied to the fatigue spectrum for this article. It was understood that damage would grow in this article and, therefore, the damage growth was closely monitored.

Real-time data monitoring was crucial to identify damage propagation during the full-scale DaDT test, especially because large areas of damage were expected to grow. The monitoring provided instant feedback of the structural response for applied loads and mitigated risks of unexpected test failures or anomalies that would have been otherwise left undetected. The strategic allocation of and placement of strain gages for these articles was crucial to achieve this goal. The strain data provided information similar to a built-in health monitoring system and provided details in real time to assess the state of the damage (i.e., whether there has been propagation, and any global effects on the structure due to possible damage growth).

5.1.1 Forward Wing Stations

The Starship forward wing station (FWS) references the center of the attach pin as FWS 19.76. For data in this report, the FWS is measured along the front spar.

5.1.2 The NDIs

Strain gages were mounted at critical locations and around damages to detect possible flaw growth and were periodically monitored throughout the test. The test articles were inspected in detail (either by removing the whiffletree or by removing the specimen completely from the test setup) prior to and after each 1/4 DLT of cyclic loading using ultrasound, in addition to periodic inspections based on strain anomalies around the defect. For initial static testing, full-field strain measurements were used to monitor the damage containment and propagation.

5.1.3 Conversion of Beechcraft Design Loads to NIAR Loads

Initially, four full-scale static tests were conducted in an up-bending configuration to evaluate the load-carrying capability of forward wings beyond the Beechcraft-designed ultimate load so that the baseline loads for fatigue tests could be established. Therefore, for this research, the NRLL and the NRUL were redefined based on the preliminary static full-scale test data. The ST001, ST002, and ST003 test articles were tested as is, assuming CAT1 damages (figure 3). The ST001 was loaded up to 200% of the BDLL and unloaded. Because the strain/displacement responses were linear, this article was later inflicted with CAT2 damage on the aft spar-top skin at FWS 45, renamed as ST001(R), and static tested to evaluate structural strength. Initial static test results, along with strain measurements, are provided in appendix D, and a summary of load data is shown in table 4. For the first three tests, the first sign of fracture that affected the global strain responses of the test article was noted based on axial gage A4, which was located on the upper skin at FWS 34.0 on the aft spar (figure 46). Strain gage diagrams were different based on the areas of interest in each test article. Details of strain and displacement gage locations are provided in appendix D.

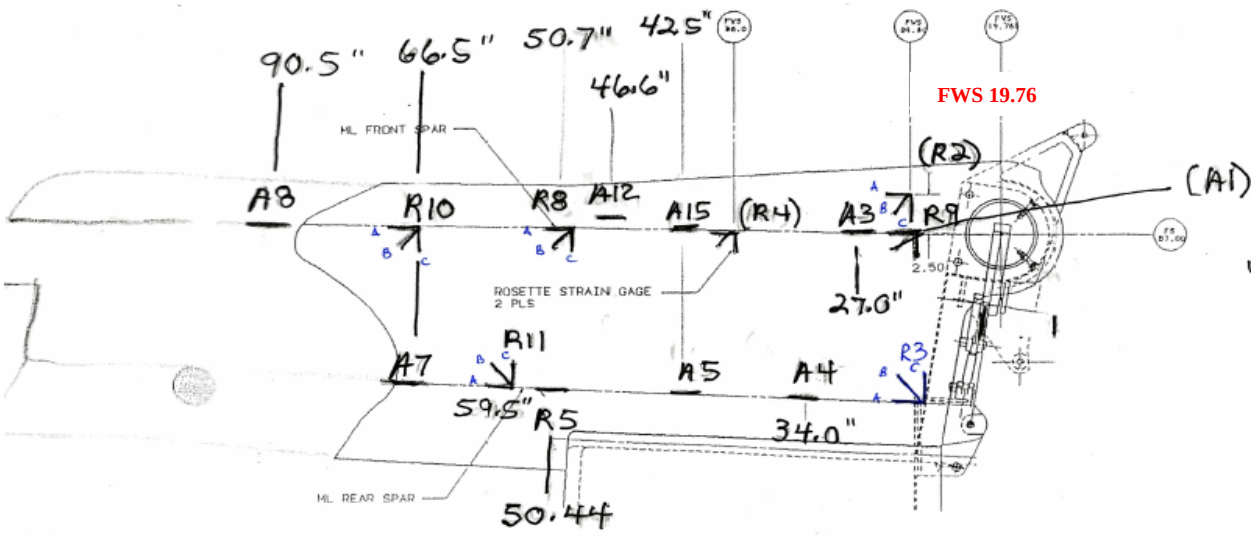

Note: Parentheses indicate gages on lower surface.

Figure 46. Strain gage locations for ST003

Strain data and post-test failure analysis indicated an initial bondline fracture between the aft spar and top skin toward the root rib, which resulted in skin buckling around this area. For ST001(R), the axial gage A1, located on the lower skin FWS 24.8 on the front spar, indicated the first sign of global fracture. Prior to that, strain gages around the impact damage indicated the onset of local damage propagation around 9150 lbf. Although data points were not sufficient to generate a reliable basis value, Weibull analysis was conducted using rank regression in fracture loads for fracture data in table 4 (see figure 47), with the understanding that the data were insufficient to generate reliable basis values. Shape and scale parameters for the Weibull distribution of fracture loads were 20.977 and 15,472, respectively. Then, the B-basis of fracture load was calculated using equation 10. The B-basis fracture load is approximately 87% of the average fracture load for an up-bending load configuration and is presumed to be conservative. This load is considered the ultimate load for tests conducted in this research (NRUL). Consequently, the NRLL was calculated as two-thirds of the NRUL, which resulted in a CF of 1.4 to convert BDLL to NRLL (table 5).

Table 4. Load summary for full-scale static strength tests

Test Article	Wing	Damage Category	Load (lbf)		
			Onset of Damage Propagation—Local	First Sign of Fracture—Global	Fracture
ST001	Right	CAT1	-	11,091.56	unloaded
ST002	Left	CAT1	-	11,304.44	14,640.43
ST003	Right	CAT1	-	10,231.09	16,123.50
ST001(R)	Right	CAT2	9,149.90	11,627.80	14,694.60

Table 5. The NIAR limit-load summary

	Positive Limit	Negative Limit
Moment (in.-lb)	511,168	-124,431
Shear (lb)	8,533	-2,212
Torque (in.-lb)	-27,090	6,962

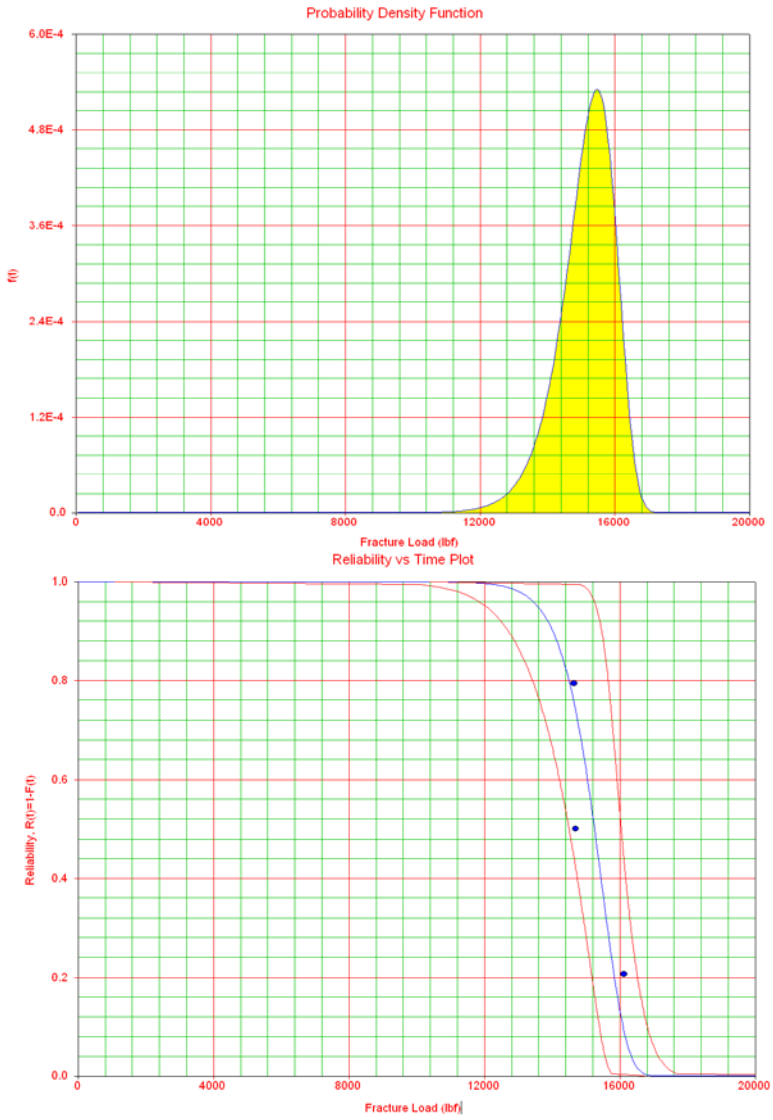

Figure 47. Probability density function and reliability plot for fracture loads

5.1.4 The LEFs for Starship Forward Wing Tests

Table 6 shows a comparison of LEFs calculated for AS4/E7K8 PW Starship material and NAVY data [1]. The LEF for AS4/E7K8 plain-weave fabric material was first calculated using the individual Weibull method, which was used for the NAVY's combined load-life analysis. Next, pooled S-N data were analyzed using the Sendeckyj wearout model to generate the second set of LEFs.

Table 6. Comparison of LEFs for AS4/E7K8 and NAVY

Number of Test Lives (N)	NAVY	Individual (AS4/E7K8)	Sendeckyj (AS4/E7K8)	Sendeckyj (AS4/E7K8) +Individual (Adhesive)
1.00	1.177	1.096	1.099	1.102
1.25	1.161	1.066	1.081	1.088
1.50	1.148	1.041	1.066	1.076
2.00	1.127	1.004	1.042	1.058
2.50	1.111	–	1.025	1.044
3.00	1.099	–	1.010	1.033
4.00	1.079	–	–	1.016
5.00	1.064	–	–	1.003
6.00	1.052	–	–	–
9.00	1.026	–	–	–
14.00	0.998	–	–	–
MSSP	20.000	32.193	32.193	32.193
MLSP	1.250	4.056	2.475	1.880
N_F	13.558	2.070	3.431	5.267

Individual Weibull analysis revealed the LEFs and N_F to be unconservative (i.e., the same as traditional metal life factors, because both fatigue data included in the analysis had significantly less scatter). However, fatigue specimens were obtained from the same batch of materials, and only six specimens per stress level were tested. Such data may not be sufficient for individual Weibull analysis. In contrast, Sendeckyj analysis pooled the test data from all stress levels, including residual strength data, and created a large sample size. Because forward wing construction of the Starship included several adhesive joints, both adhesive strength and life shape parameters (obtained using individual Weibull because of large scatter observed in adhesive data) were pooled with composite analysis data to generate LEFs and are included in table 6. For full-scale DaDT testing in this research, the LEFs were used, although the adhesive data included in the analysis were for a different adhesive than what was used in the structure.

The ST004 DaDT article was tested for 2 DLTs (N = 2), therefore an LEF of 1.058 was required. However, the test article was run with an LEF of 1.072, which was calculated based on the data available at the time the ST004 DaDT test was executed. Based on the FAA-LEF data, except for the DTE test data, the LEF of 1.072 corresponds to a test duration of 1.6 DLTs. This, along with a CF of 1.4, resulted in a cumulative factor of 1.5 for the fatigue loads.

5.1.5 Application of LEFs

The LEFs can be applied to the fatigue spectrum in several ways: (1) to 1-g mean fatigue load, (2) to amplitude (Δg), and (3) to minimum and maximum load. In addition to the LEF, the CF is an additional factor that was applicable to this research, and these factors were combined to obtain the cumulative LEF (equations 24–26) in several ways.

$$P_{1-g} = \left[\left(Load_{1-g} \right) \cdot CF \cdot LEF + \left(\frac{\Delta Load}{\Delta g} \right) \cdot \Delta g \right] \tag{24}$$

$$P_{\Delta g} = \left[\left(Load_{1-g} \right) \cdot CF + \left(\frac{\Delta Load}{\Delta g} \right) \cdot \Delta g \cdot LEF \right] \tag{25}$$

$$P_{Moment} = \left[\left(Load_{1-g} \right) \cdot CF + \left(\frac{\Delta Load}{\Delta g} \right) \cdot \Delta g \right] \cdot LEF \tag{26}$$

$$P_{Cumulative} = \left[\left(Load_{1-g} \right) + \left(\frac{\Delta Load}{\Delta g} \right) \cdot \Delta g \right] \cdot CF \cdot LEF \tag{27}$$

When applying the LEFs to mean fatigue loads, as shown in equations 24–26, the mean load is offset in either the positive (for positive mean loads) or negative (for negative mean loads) direction. For cycles with load reversal (stress ratio, R <0), this causes a reduction in load magnitudes in the opposite loading direction (i.e., shifts the mean load), as shown in figure 48. Consequently, this alters the damage growth caused by reversible loads to the composite structure. Furthermore, for higher LEF values, this may convert a tension-compression cycle to a tension-tension cycle or a compression-compression cycle for positive- and negative-enhanced mean loads, respectively. Specimen-level data for composite materials show that reversible load cases (R <0) are critical and have a significantly lower fatigue life than that of tension-tension or compression-compression (R >0) cases in reference 40. Therefore, to avoid changes to stress ratios and an unintentional reduction in fatigue damages to the test article, equations 24–26 are not recommended for applying the LEF to a spectrum loading with negative stress ratios (tension-compression loading).

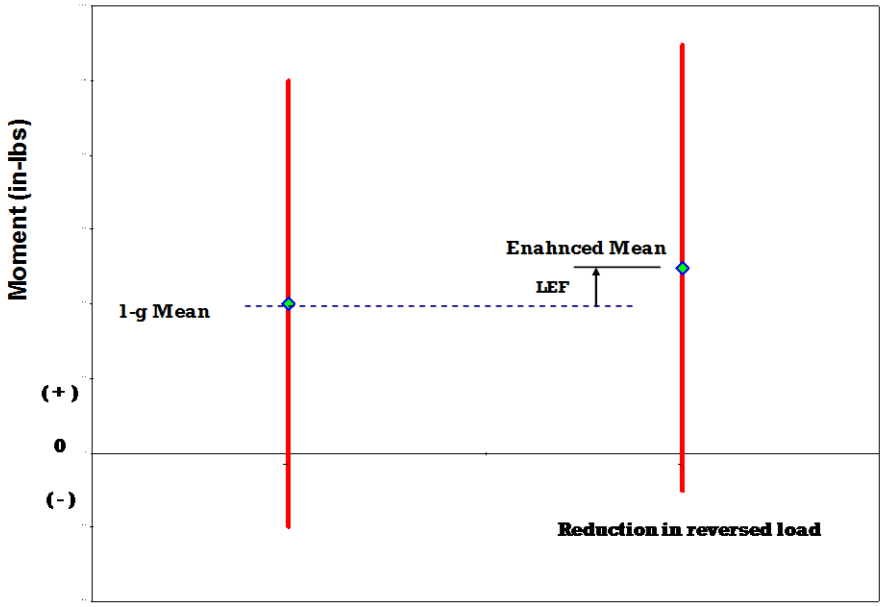

Figure 48. Application of LEF only to mean load

The application of the CF and LEF to both 1-g mean and amplitude, as in equation 37, results in considerably high loads, but maintains the same stress ratios throughout the spectrum. Therefore, full-scale fatigue test spectrum loads are generated by applying the CF and LEF (a cumulative LEF) to the minimum and maximum SMT loads. By doing this, the reversible loads are enhanced rather than shifted, depending on the sign of the maximum or minimum SMT load, and the stress ratio is maintained after load enhancement. A comparison of these four methods of applying the CF (= 1.4) and LEF (= 1.072) to SLBs in the Starship forward wing spectrum is shown in figure 49 for each load block. During a typical full-scale substantiation program where the CF = 1.0, equations 26 and 27 become identical and apply the LEF to the minimum or maximum SMT load. As shown in figure 49, except for the cumulative method in equation 27, most of the reversible loads were converted into positive shear loads.

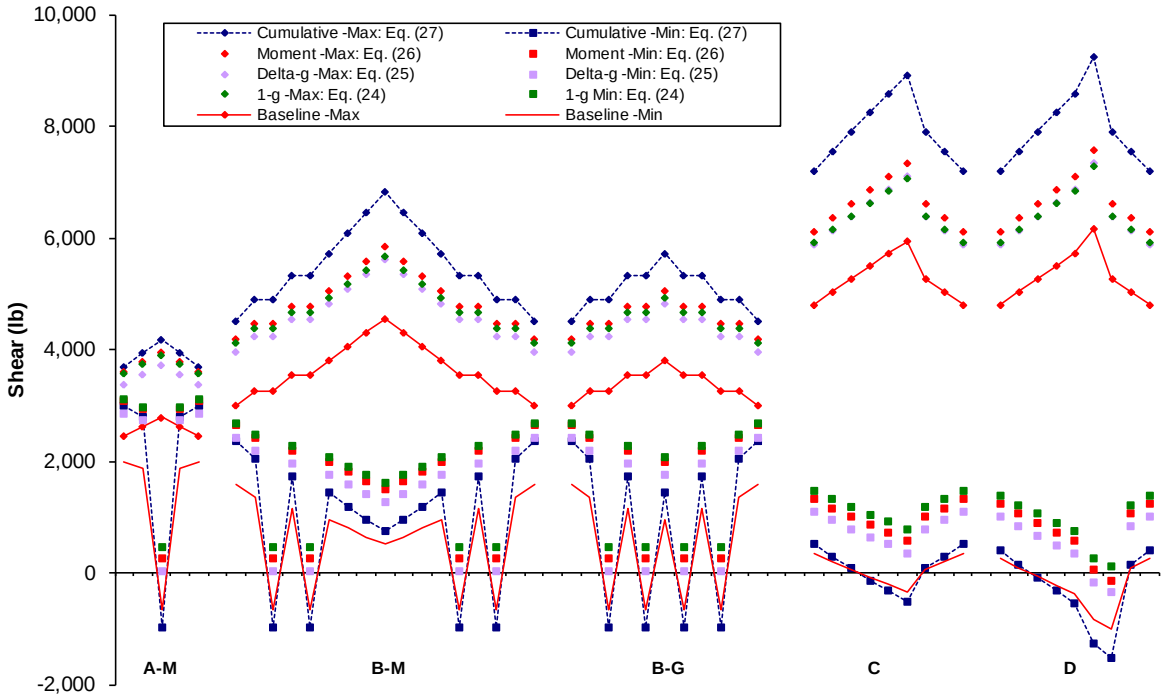

Figure 49. Comparison of methods for applying LEF to a load spectrum

5.1.6 Fatigue Spectrum Generation

One Beechcraft DLT of the test article is equivalent to 20,000 flight hours (figure 50) and corresponds to a spectrum of 160,034 full cycles, which includes 1-g and 3-g maneuvers as well as positive and negative gust conditions. Load-block sequencing in the fatigue spectrum is shown in table 7 for 1 DLT. To adopt the nomenclature of the LEF according to the combined life-load approach [1], a fatigue spectrum that is equivalent to 1 DLT of the test article was considered as one test duration (N = 1). Prior to fatigue loading, the test articles were used to demonstrate both positive and negative limit loads. At predetermined intervals, durability test articles were loaded to static positive and negative limit loads to compare possible compliance changes (i.e., due to stiffness loss or damage propagation).

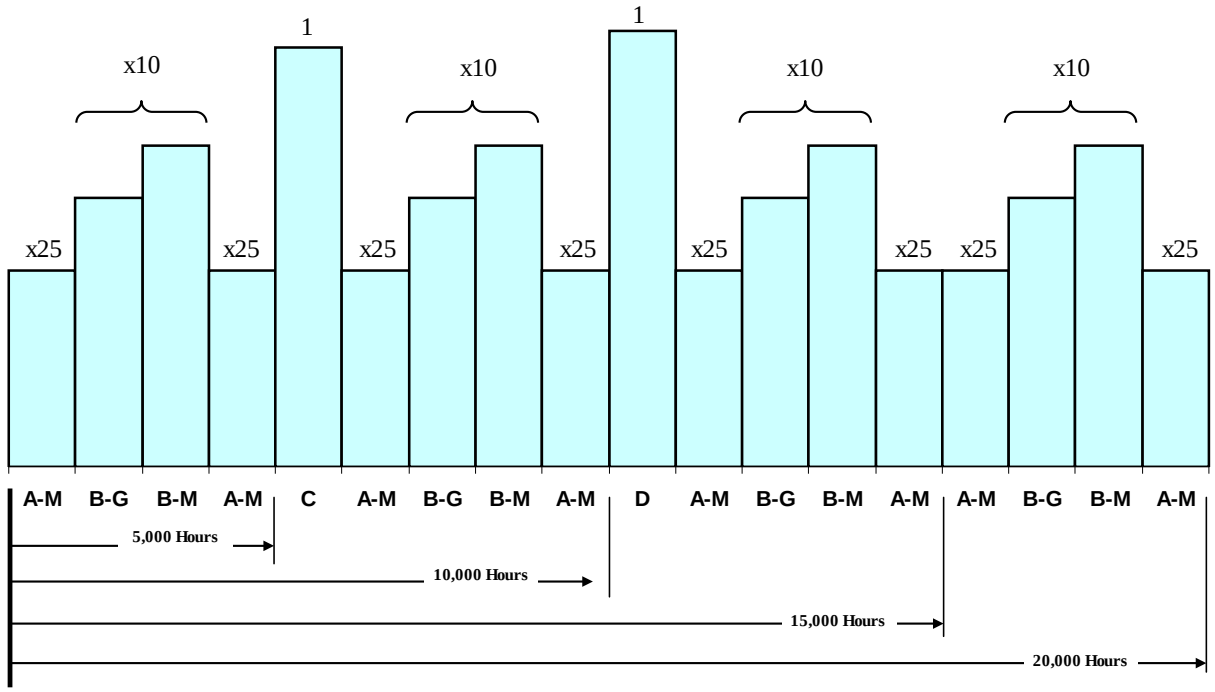

Figure 50. Loading sequence (spectrum) for 1 DLT

Table 7. Load sequence for 1-DLT test

Sequence	Loading Block	Repetitions	*n* per Block	Σ*n*	Cumulative Flight Hours	Lifetimes
a	Start	–	–	–	–	0
b	Ramp to: NRLL+	1	–	–	–	–
c	Ramp to: Zero	1	–	–	–	–
d	Ramp to: NRLL-	1	–	–	–	–
e	Ramp to: Zero	1	–	–	–	–
f	Ramp for fatigue	1	–	–	–	–
1	Block A-M	25	718	–	–	–
2	Block B-G	1	146	–	–	–
3	Block B-M	1	264	–	–	–
4	Repeat 2 and 3	9	410	–	–	–
5	Block A-M	25	718	40,000	4,999	0.250

Table 7. Load sequence for 1-DLT test (continued)

Sequence	Loading Block	Repetitions	*n* per Block	Σ*n*	Cumulative Flight Hours	Lifetimes
6	Ramp to: Zero	1	–	–	–	–
7	Repeat a - f	1	–	–	–	–
8	Block C	1	16	–	–	–
9	Block A-M	25	718	–	–	–
10	Repeat 2 and 3	10	410	–	–	–
11	Block A-M	25	718	80,016	10,000	0.500
12	Ramp to: Zero	1	–	–	–	–
13	Repeat a - f	1	–	–	–	–
14	Block D	1	17	–	–	–
15	Block A-M	25	718	–	–	–
16	Repeat 2 and 3	10	410	–	–	–
17	Block A-M	25	718	120,033	15,001	0.750
18	Ramp to: Zero	1	–	–	–	–
19	Repeat a - f	1	–	–	–	–
20	Block A-M	25	718	–	–	–
21	Repeat 2 and 3	10	410	–	–	–
22	Block A-M	25	718	160,033	20,000	1.000
23	Ramp to: Zero	1	–	–	–	–

n = Cycle; Σ*n* = Total Number of Cycles

The Starship forward wing original certification test spectrum [52] was modified for the current research. This modification included converting maneuver and gust SMT loads at 1-g by the CF to define new limit and ultimate conditions as discussed in section 5.1.3, and application of the LEF to the spectrum as discussed in section 5.1.5. The spectrum contained gust and maneuver load blocks that were repeated several times as recommended [53], with shear-load sequences arranged from low to high and high to low within each block (figure 51). Blocks A-M and B-M represent maneuver conditions, and blocks B-G represent gust conditions. Blocks C and D are torque conditions, where positive and negative Δ*g* loads were calculated based on maneuver and gust torque conditions, respectively.

Appendix C includes the SMT loads used for the spectrum, with and without LEF = 1.072, after applying the CF = 1.4. The resultant bending moments and torque for the applied shear loads in figure 51 are shown in figures 52 and 53, respectively.

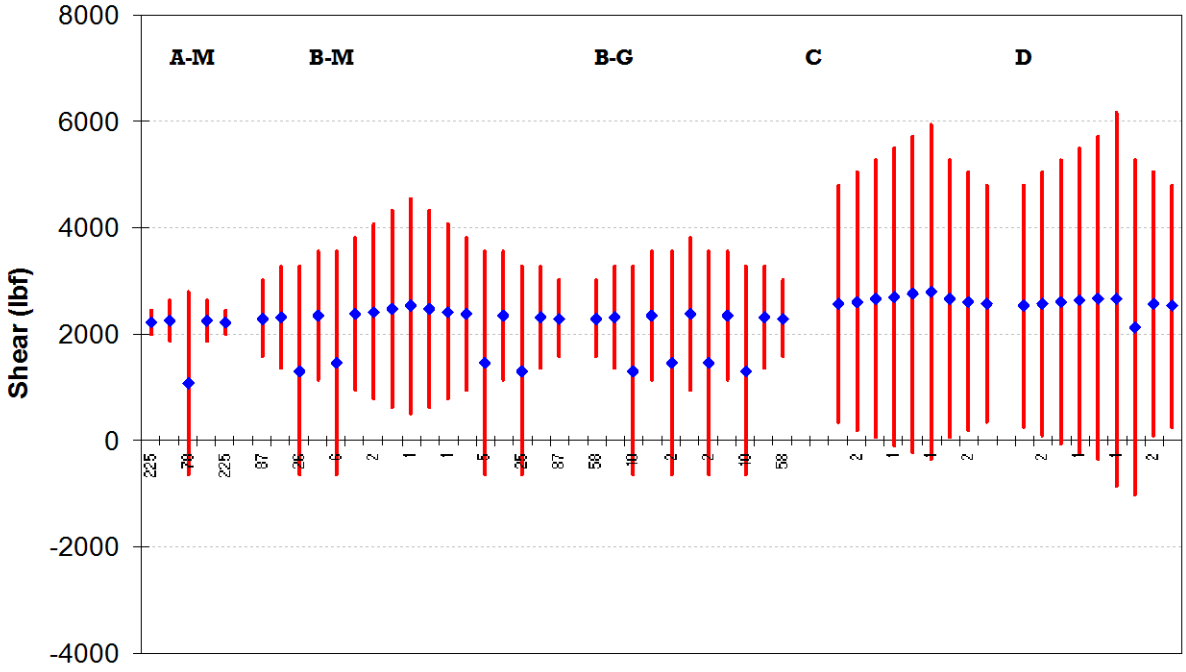

Figure 51. Maneuver and gust shear-load spectrums, CF = 1.0 and LEF = 1.0

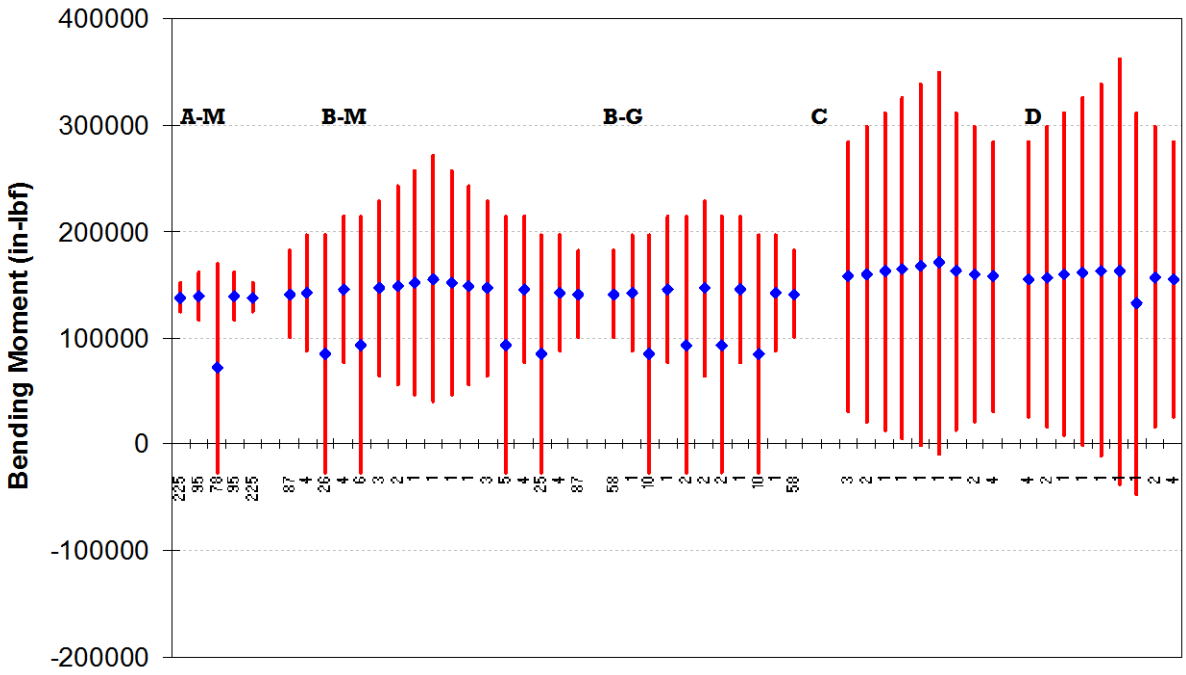

Figure 52. Maneuver and gust bending moments, CF = 1.0 and LEF = 1.0

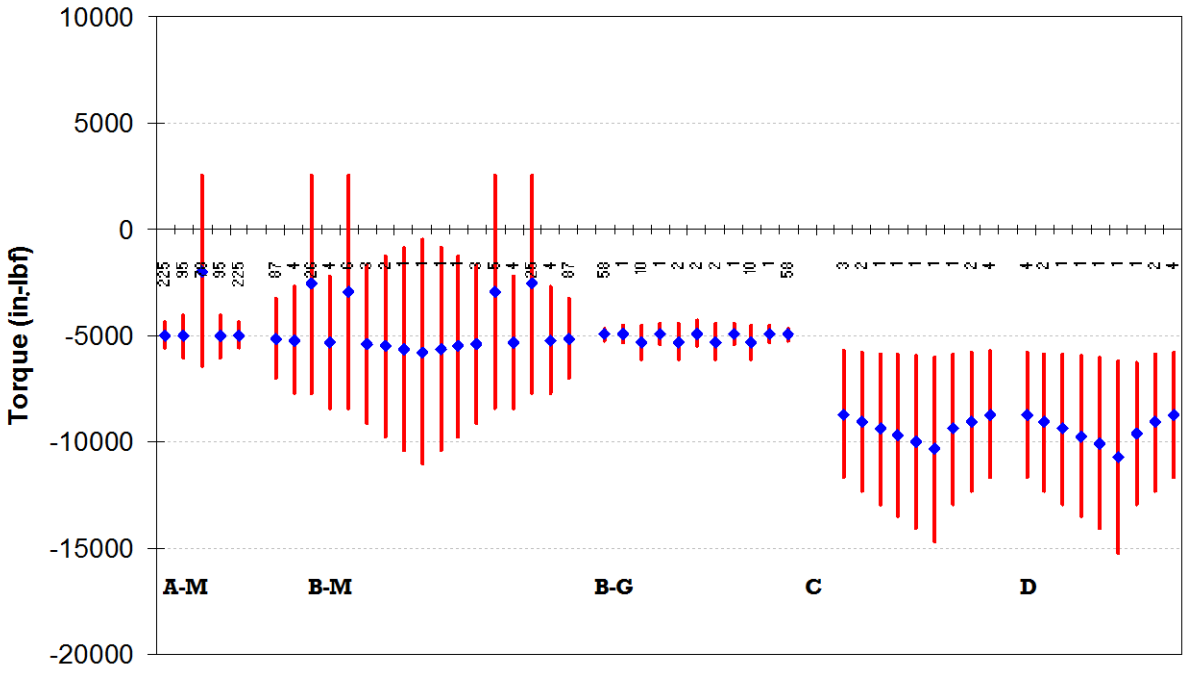

Figure 53. Maneuver and gust torque, CF = 1.0 and LEF = 1.0

5.1.7 Modified Load Patches

The application of significantly large damages (i.e., CAT2 and CAT3), which are beyond original certification requirements, resulted in the removal of several load patches around the ST004 and ST006 DaDT test article damages to accommodate damage growth, make room for strain gage installation, and minimize localized out-of-plane loads. Such modifications were performed with caution so that SMT loads would not be severely altered, especially around the damage area, as shown in figure 54.

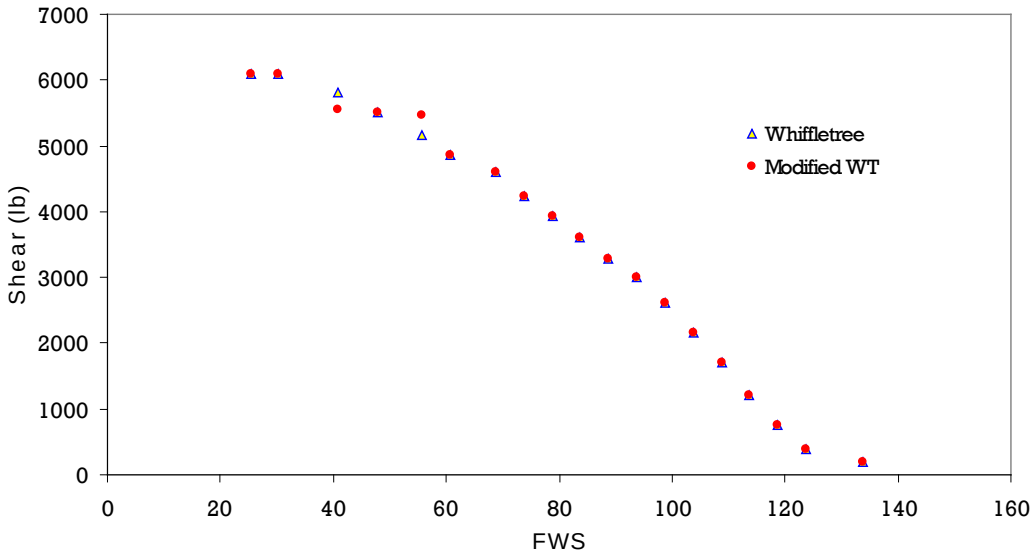

(a)

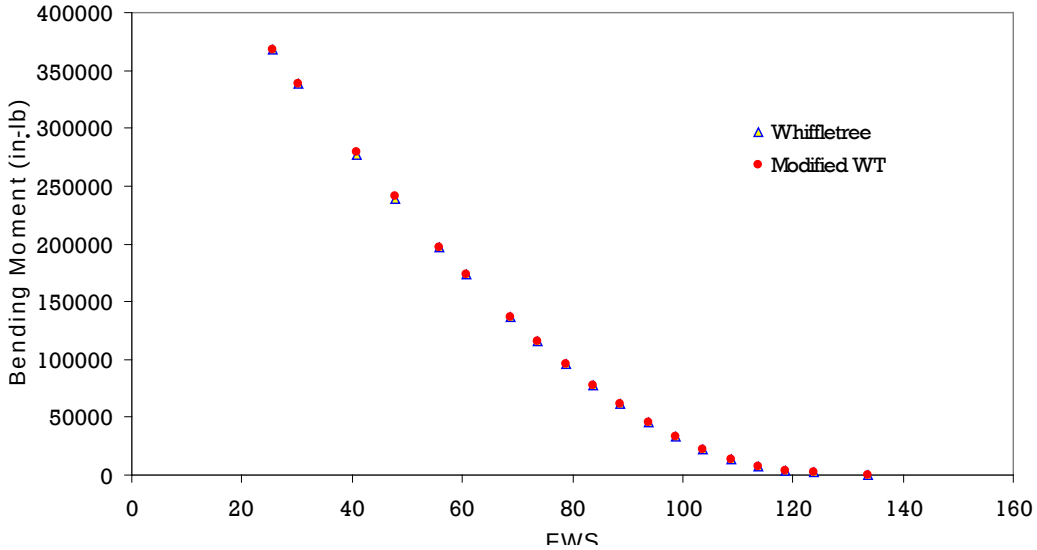

(b)

Figure 54. Effects of modified patch locations of ST004 on (a) shear and (b) moment

5.1.8 The DaDT Test Results

Both ST001(R) and ST004 test articles were impacted with 225-g-ft-lb energy impact with a 3-inch-diameter metal sphere to obtain CAT2 damage at FWS 45 on the top skin of the rear spar. ST001(R) was static-tested to evaluate the structural strength, whereas the ST004 test article was fatigue-tested with an LEF for 2 DLTs. Following 2 DLTs, ST004 was tested to evaluate residual strength in the up-bending loading configuration. The ST005 article was impacted with 1000-g-ft-lb energy using a sharp wedge impactor at FWS 65 at the front spar (top skin) and static-tested in the up-bending configuration to evaluate structural strength. This energy level was selected to represent CAT3 damage to the structure, and the location was selected to investigate the effects of such a defect on the primary load path of the structure. Similar damage was inflicted on the ST006 fatigue test article. Following impacting, test articles were subjected to NDI to quantify the damage using ultrasonic and DTH inspection techniques.

5.2 DAMAGE INFLICTION

To obtain CAT2 and CAT3 damages that satisfied the load and visibility requirements shown in table 1, several trial impact tests were conducted using static-tested forward wings. Because of the design details shown in figure 31 and the failure mechanism during impact, damaging the forward wing to satisfy these requirements was challenging. Energy level requirements for both impact categories were significantly higher than what is typically used during certification programs. These energy levels were selected after numerous trial tests to satisfy both load and visibility requirements for each damage category. Even with extremely high energy levels, a sharp impactor (wedge) was used to penetrate the front spar cap and satisfy visibility requirements for CAT3 damage.

5.2.1 CAT2 Damage on ST001(R) and ST004

Table 8 summarizes the impact trials conducted to determine CAT2 impact parameters. Based on the information gathered from these impact trials, damage was inflicted on the aft spar of ST001(R) with an energy level of 225-g-ft-lb using a 3-inch steel sphere at FWS 45 (figure 55). For comparison, the durability article ST004 was impacted with a similar energy level at the same location.

Table 8. Summary of impact trials to determine CAT2 impact parameters

Spar	Location (FWS)	Mass (lb)	Impactor	Support Span (in.)	Height (in.)	Energy Level		Notes
						in.-lb	ft-lb	
Front	126.0	14.5	Bowling Ball	12	40	580	48	No visible damage on the surface or on the web
Front	126.0	14.5	Bowling Ball	Steel base	80	1160	97	No visible damage on the surface; some fracture along web-flange intersection
Front	126.0	14.5	Bowling Ball	Steel base	110	1595	133	No visible damage on the surface; some fracture along web-flange intersection
Front	112.0	31	3-inch Sphere	16	36	1116	93	No visible damage on the surface; some fracture along web-flange intersection
Front	106.0	31	3-inch Sphere	16	80	2480	207	No visible damage on the surface; some fracture along web-flange intersection
Front	51.0	31	3-inch Sphere	16	110	3410	284	No visible damage on the surface; some fracture along web-flange intersection
Aft	78.7	31	3-inch Sphere	16	72	2232	186	Skin fracture + indent (web is not visible)
Aft	54.7	31	3-inch Sphere	16	72	2232	186	Skin fracture + indent; no damage to web (close to control surface mount)
Aft	124.5	14.5	Bowling Ball	16	72	1044	87	Indent + possible 2.75" fracture in the aft web
Aft	114.5	20.5	Bowling Ball	16	110	2255	188	Indent + possible 5.5" fracture in the aft web
Aft	102.5	45.5	Bowling Ball	16	72	3276	273	Indent + possible 8" fracture in the aft web
Aft	89.5	37.5	3-inch Sphere	16	72	2700	225	Skin fracture + indent (web is not visible)
Front	89.5	37.5	3-inch Sphere	16	72	2700	225	No visible damage on the surface; web fracture
Aft	45.0	37.5	3-inch Sphere	16	72	2700	225	Visible damage on surface + fracture in the web away from the control surface mount

Note: Events are listed in chronological order.

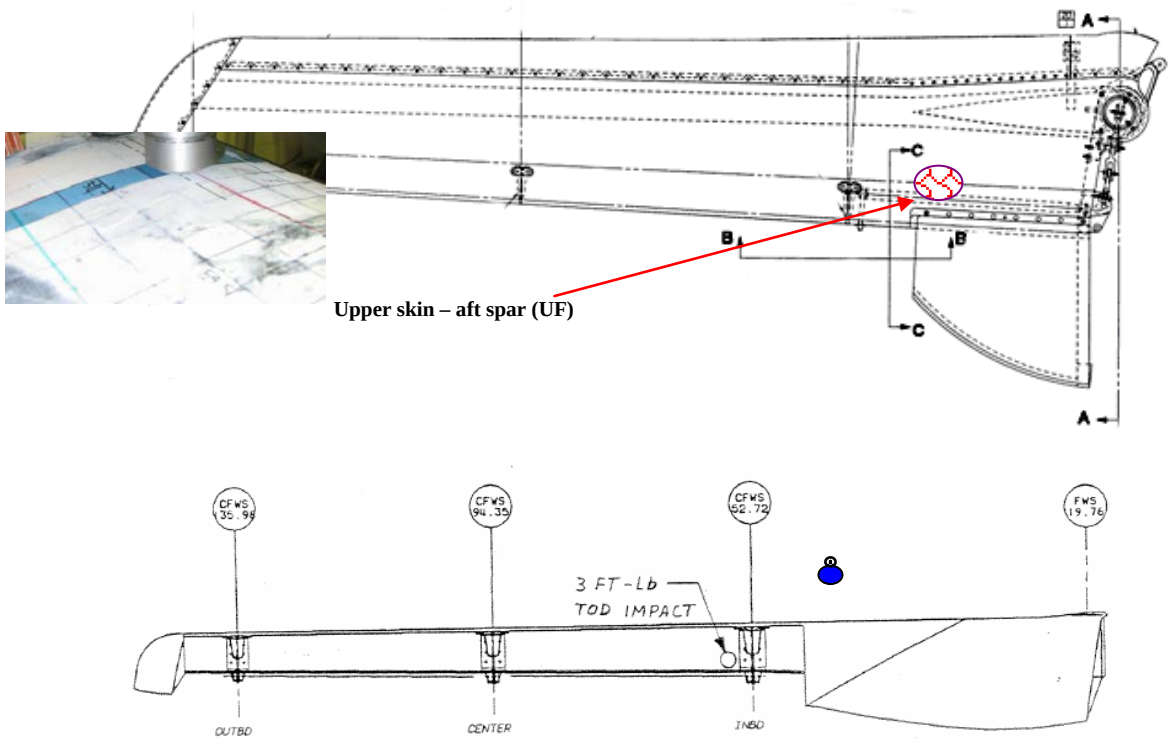

Figure 55. Damage location on ST001(R) and ST004

Figure 56 shows the visual inspections following CAT2 impact on the ST004 test article. Damage to the top skin at the contact location and to the aft web was clearly visible. Detailed post-impact NDI results are included in section 5.3.

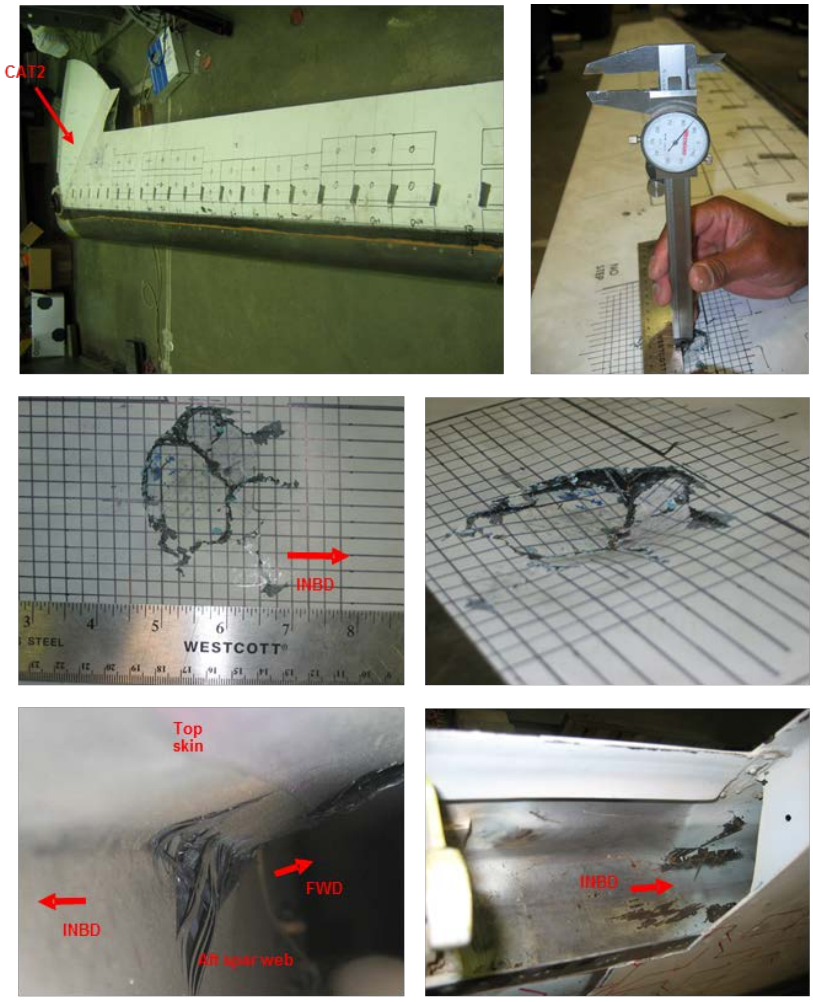

Figure 56. Visual inspections of CAT2 damage on ST004

5.2.2 CAT3 Damage on ST005 and ST006

ST005 was inflicted with CAT3 impact damage and static-tested for residual strength. The required energy level and impact geometry were selected based on several impact trials, as listed in table 9. Previously tested static-test articles ST001 and ST002 were used for the impact trials. For these trials, 1- and 3-inch-wide wedges (figure 57) were selected as impactors. Even with the maximum energy level of 997-g-ft-lb, damage to the spar cap was limited to localized surface damage at the contact line, as shown in figure 58(a), and did not satisfy the visibility requirements of CAT3 damage. However, there was a substantial amount of fracture and delamination to the front web, which was not visible until the leading edge was removed (figure 58(b)). In addition to full-scale impact trials, several 24-inch-long specimens were extracted from the top and bottom spar caps of full-scale static article ST003. These specimens were damaged either by drilling a hole in the center or by impacting. They were then tested in four-point bend configuration to evaluate the residual strength compared to the undamaged case. Details of this test are provided in appendix E.

Table 9. Summary of impact trials to determine CAT3 impact parameters

Test Article	FWS (Front Spar)	Wedge	Mass (lb)	Height (ft)	Energy Level (ft-lb)
ST002	120.5	1-inch	15	6	90
		1-inch	15	10	150
		1-inch	50.5	10	505
	108.5	3-inch	50.5	15	758
		3-inch	50.5	10	505
ST001	66.5	3-inch	73.3	13.6	997

(a) 1-inch wedge (b) 3-inch wedge

Figure 57. Gravity-assisted drop tower setup for CAT3 impact trial tests

To increase the contact force and drive penetration, the top front spar cap of the ST005 static article was impacted with a 1000-g-ft-lb energy level using a machined 1-inch sharp wedge impactor at FWS 65. This FWS was selected because of the aluminum secondary web that is located forward of the front spar to stabilize the thick front spar caps from rotating on the thin web. This secondary web runs from FWS 26.76 to FWS 64.5 and is mechanically attached to the top and bottom skin overhang (flange) forward of the front spar and leading-edge closeout rib.

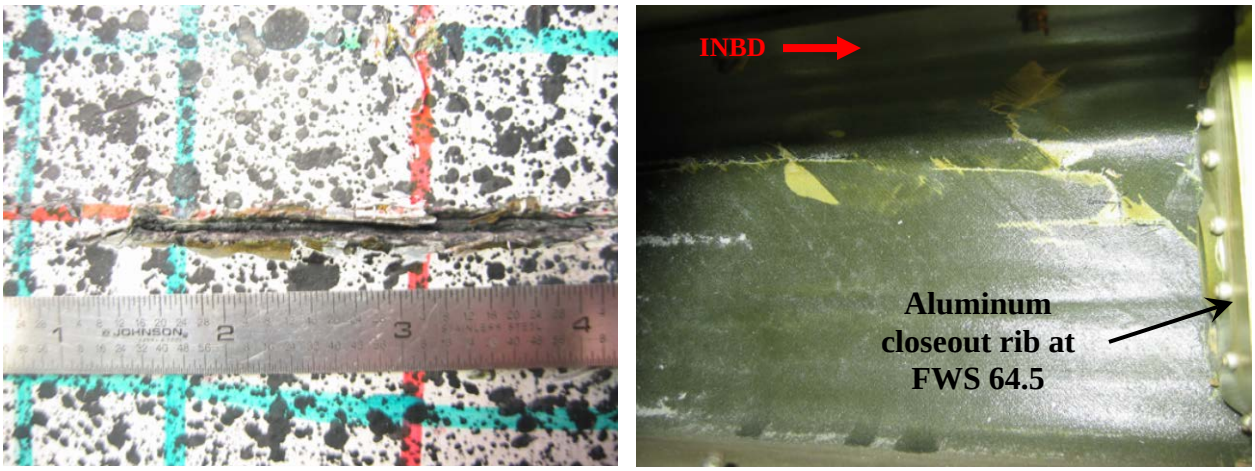

(a) Front Spar (Top Skin) Impact Location (b) Damage to Web Below Impact Location

Figure 58. CAT3 damage results for impact trial tests

An aluminum closeout rib at FWS 64.5 was mechanically fastened to the secondary web, and bonded to the upper and lower spar caps and front spar web (figure 59). This provided additional strength in the direction of impact at the contact location (FWS 65), thereby minimizing front spar web crush, as shown in figure 31. This resulted in penetration rather than springback of the spar caps (and web crush) that was observed in trial tests conducted on ST002 (table 9).

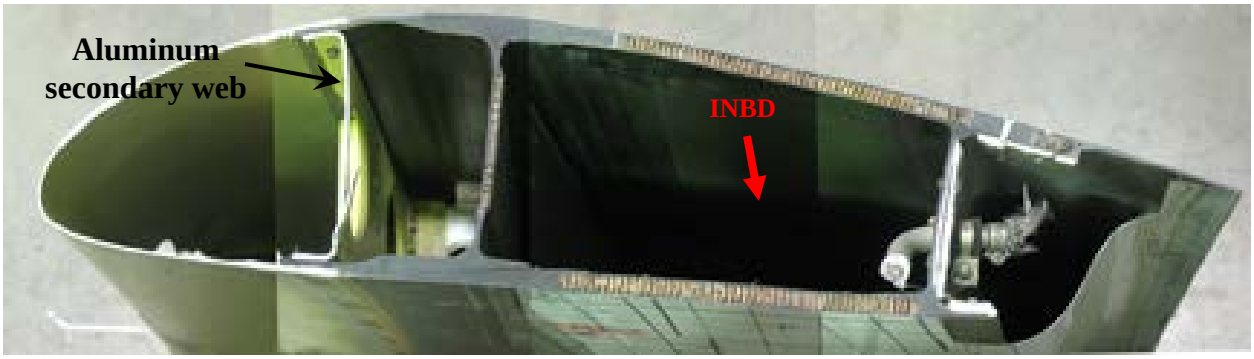

Figure 59. Cross-sectional view near FWS 65

A cradle fixture was built with a matching wing profile at supports (figure 60) to rigidly hold the test article during impact. Unlike the case of trial impacts, this fixture arrangement resulted in complete penetration, which was clearly visible during a walk-around inspection. A 1.75-inch hole was drilled on the leading edge using a hole saw to inspect the damage to the front side of the front-spar web. Based on the law of conservation of energy (and assuming no frictional effects on the drop-weight guide), the velocity of the impactor assembly was calculated as approximately 30 ft/sec prior to contact. Figure 61 shows the 1-inch-circular damage on the top front spar cap of ST005, which was later tested to determine the residual strength under up-bending load configuration. As shown in this figure, significant delamination and fracture were observed on the web, especially closer to the upper spar cap. Ultrasonic NDI inspections as well as DTH tests were performed to delineate the damage extent, and results are included in section 5.3.

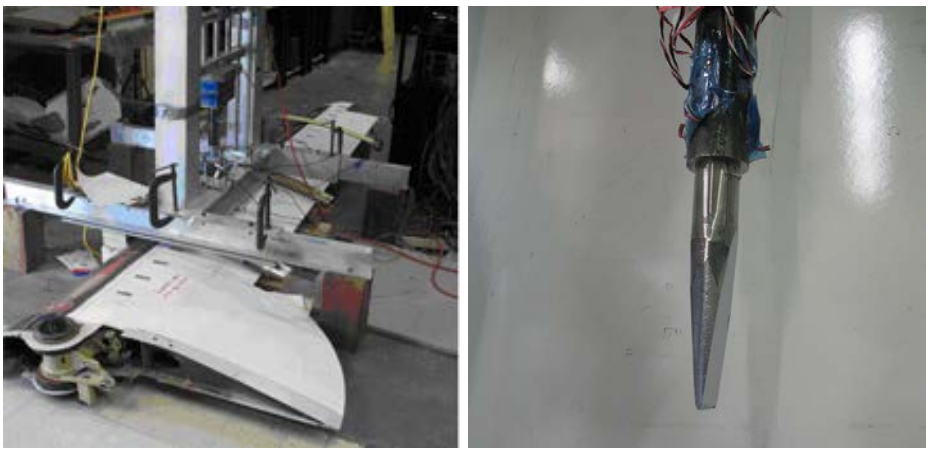

(a) Gravity-Assisted Drop Tower (b) Sharp Wedge Impactor

Figure 60. CAT3 impact test setup for ST005 and ST006

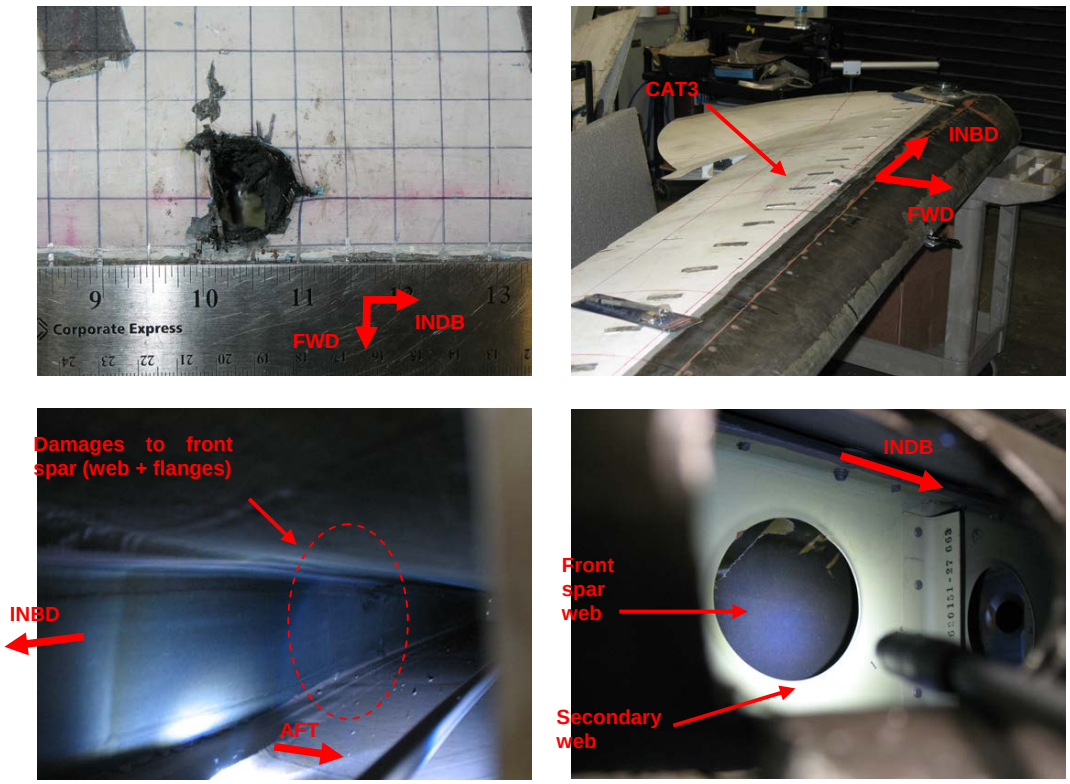

Figure 61. CAT3 impact damage on ST005 at FWS 65

The DaDT test article ST006 was impacted with the same energy level using the same impactor at the same location (i.e., the front spar top skin at FWS 65) for comparison purposes. Figure 62 shows the 1.25-in. circular damage on the top front spar cap of ST006, which was tested for DaDT. As observed on ST005, this impact damage was clearly visible during a walk-around inspection, and there were significant delamination and fractures observed on the web. Furthermore, post-impact visual inspection revealed that the lower bottom aft flange of the front

spar was disbonded, and the bottom skin (opposite the contact location) was delaminated, as shown in figure 62. Ultrasonic NDIs and DTH tests were performed to determine the extent of damage and those results are included in section 5.3.

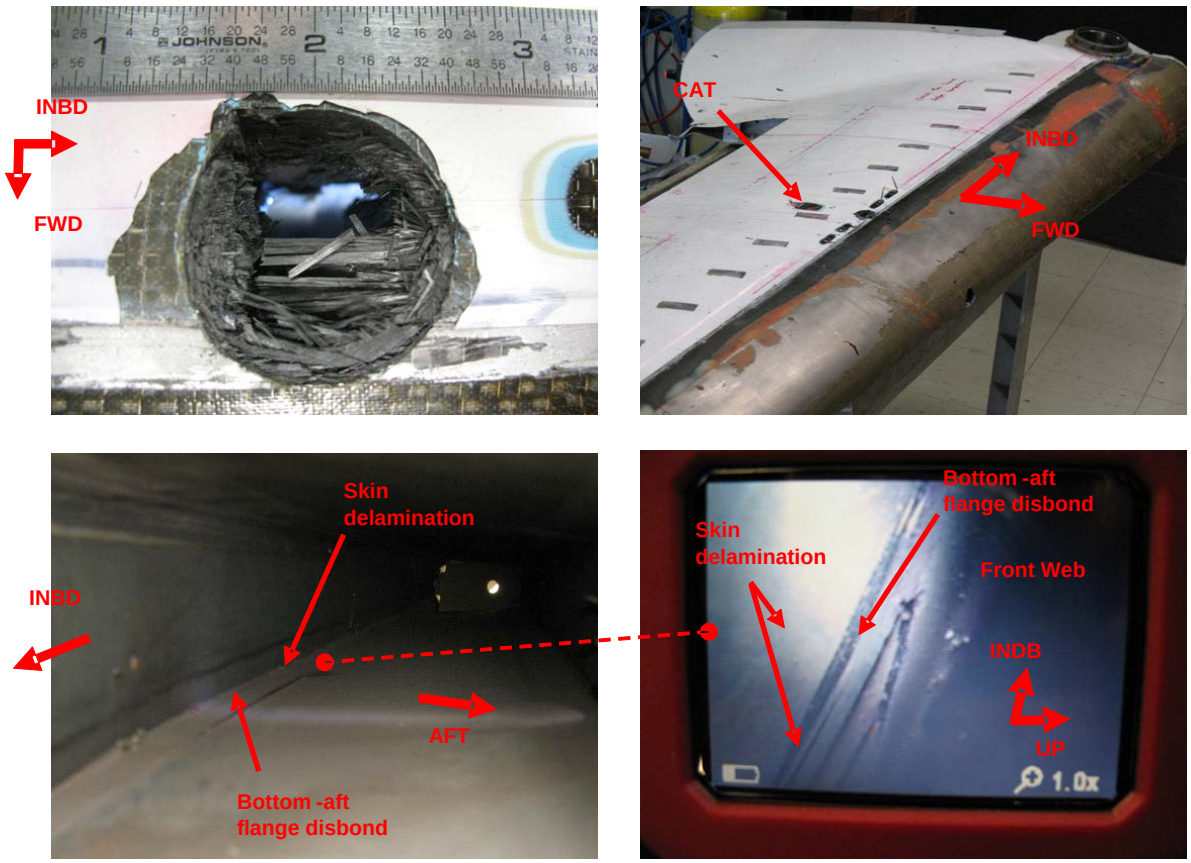

Figure 62. CAT3 impact damage on ST006 at FWS 65

5.3 THE NDI RESULTS

Several NDI techniques were used to inspect the test articles following damage infliction to delineate the extent of damage to the structures. Figure 63 shows the NDI results of CAT2 damage inflicted on ST004 prior to cyclic loading. This unit consists of a lightweight hammer containing an accelerometer, which is connected by a flexible cable to components and a liquid crystal display. It supplements the subjective tonal discrimination of the operator with a quantitative, objective numeric readout that can be correlated to fractures, delaminations, or debonds in the structure. Baseline data were recorded prior to impact using a grid, as shown in figure 63(b). Because the thickness of the structure changes significantly around the inspection area, these baseline data were essential for subsequent NDIs (i.e., post-impact and during fatigue testing) so that the localized relative stiffness change could be measured by isolating the inherent tonal variations due to thickness or stiffness changes. Initial DTH readings confirmed ultrasonic A-scan (pulse-echo) inspections. In addition, a Thermoscope II, a handheld, high-speed IR camera, was used to track changes in the surface temperature following a brief pulse of a xenon

flash lamp. As the local structure cooled, the surface temperature was affected by internal flaws, such as debonds, voids, or inclusions, which obstruct the flow of heat into the structure. Because of the system's lack of availability this unit was used only on ST004.

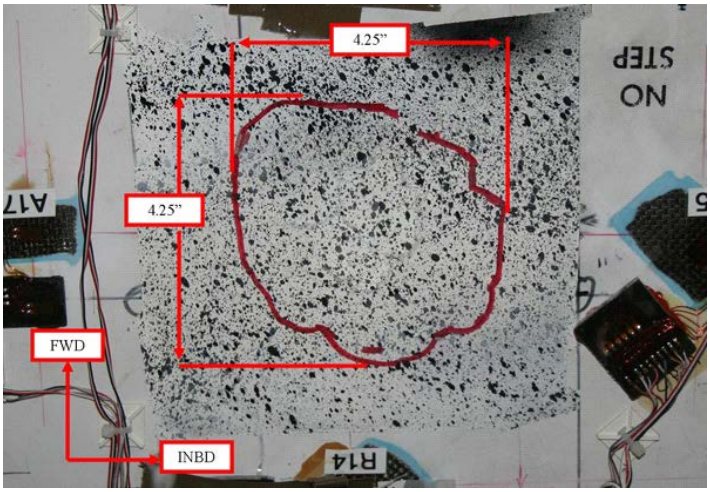

(a Ultrasonic (pulse-echo))

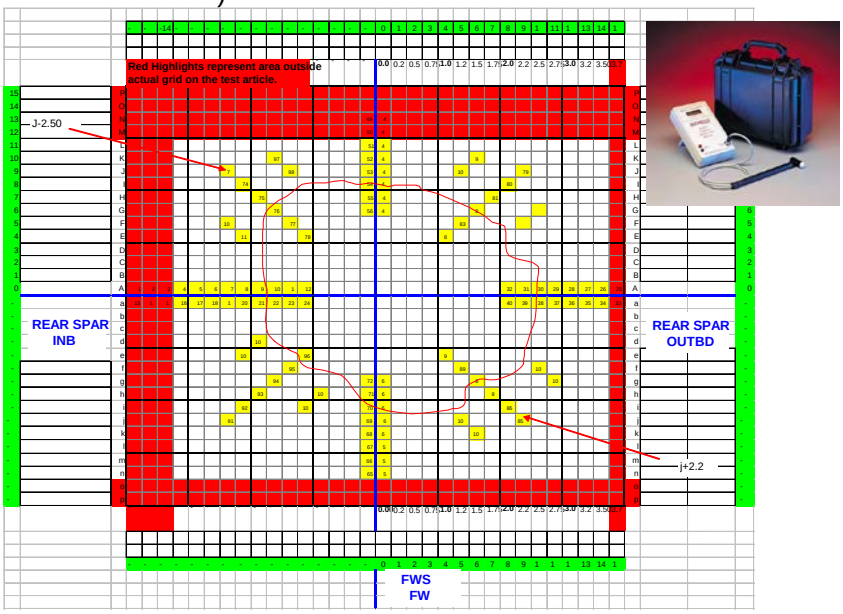

(b) DTH

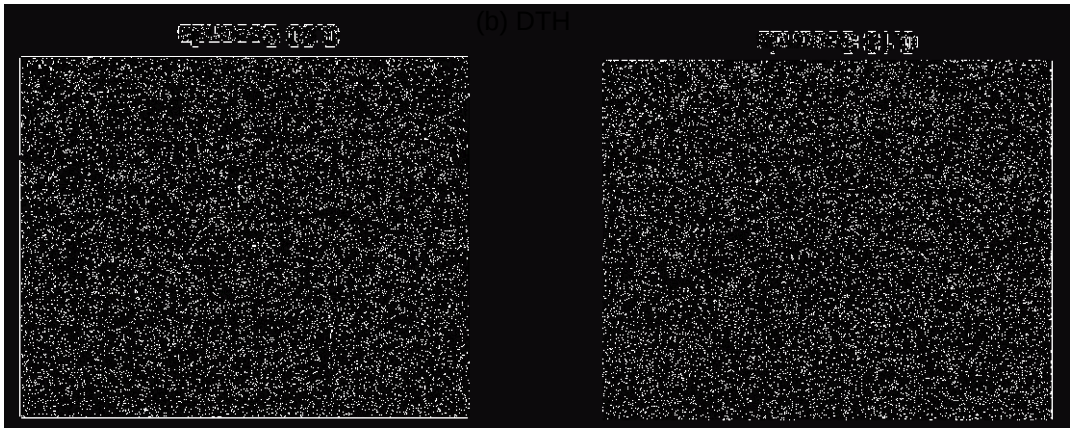

(c) Pulsed thermography

Figure 63. The NDI results of CAT2 damage on ST004 prior to cyclic load

Figure 64 shows the NDI results obtained from the Sonic 1200 ultrasonic, the BondMaster 1000, and the DTH following the CAT3 impact damage on ST005 test article. The first two methods show the localized damaged region, while the latter delineated an approximately 5.5-inch-long (along the spar cap) and 3.75-inch-wide damaged area. The ultrasonic reading in this area was weak, but confirmed DTH findings. Conversely, NDI results obtained from these techniques on ST006 correlated well, defining a 6.5-inch-long and 3-inch-wide damaged area (figure 65).

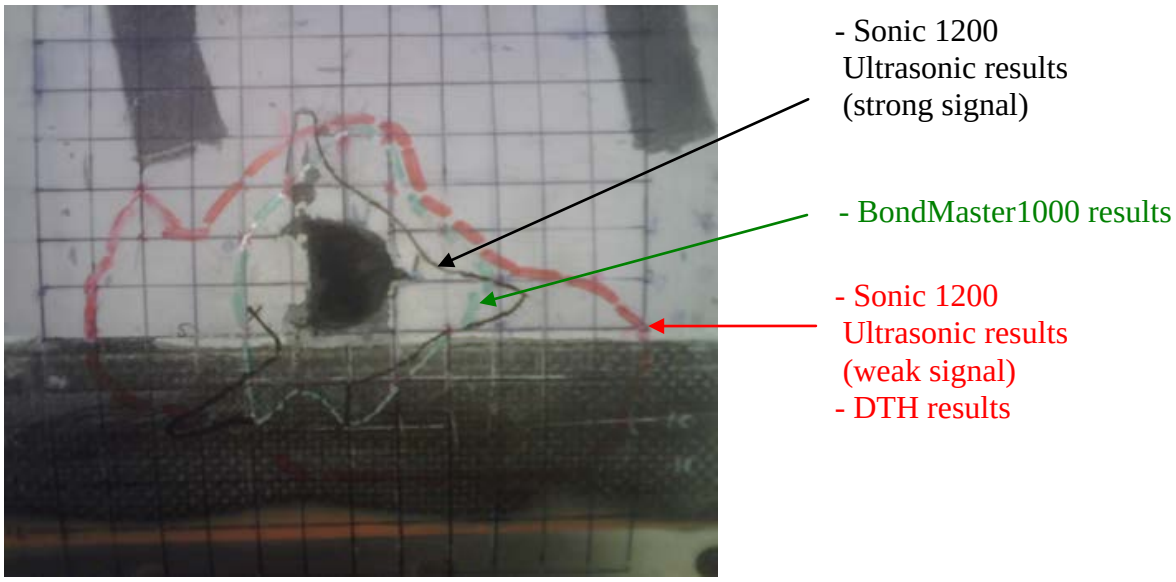

Figure 64. The NDI results for CAT3 damage on ST005

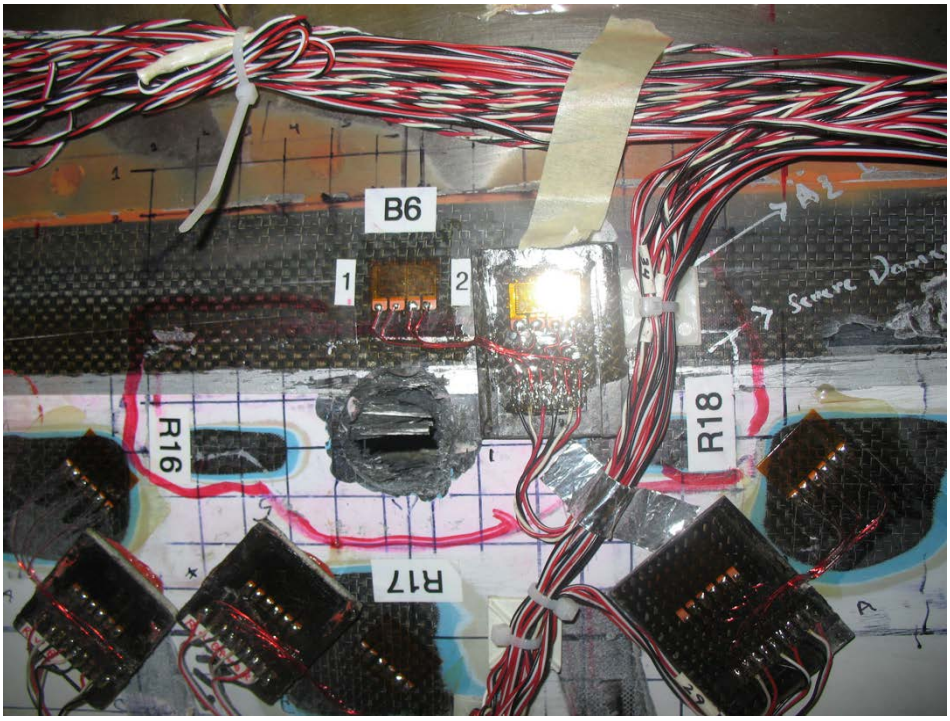

Figure 65. The NDI results for CAT3 damage on ST006

Although ST005 and ST006 were impacted with the same impact parameters (i.e., energy and setup), NDI results showed that the resulting damage to the structure was somewhat different. The visual inspections of the damage on ST005 indicated several large fractures on outer plies in addition to penetration, while it was primarily penetration in the case of ST006. Although the amount of energy used to impact these two test articles and the type of impactor used were the same, such minor variations as frictional energy loss and impact location can influence the resulting damage and, therefore, the residual strength could be significantly different.

5.4 DAMAGE CONTAINMENT AND PROPAGATION

5.4.1 Quasi-Static Loading

This section contains the static test results for ST001(R) and ST005 articles with CAT2 and CAT3 damages, respectively. Additional strain and displacement data for both test articles are provided in appendix D.

5.4.1.1 The ST001(R)—CAT2 damage on aft spar

The strain gage diagram for ST001(R) is shown in figure 66. Several additional gages were mounted closer to the damage to monitor damage propagation during quasi-static loading. According to the damage definition, a structure must withstand the limit load with CAT2 damage. As shown in figure 67, CAT2 damage propagation was initiated at approximately 107% of the NRLL. As shown in figure 68, the strain data adjacent to the impact damage indicate that the damage propagation was initiated at approximately the NRLL. This strain gage was located 1 in. inboard of the damage boundary and was extremely sensitive to any anomalies around the damage. These strain data indicate that ST001(R) was able to contain the CAT2 defect up to the NRLL. The final failure occurred at 172% of the NRLL. Note that the ultimate fracture load for this article was significantly higher than the NRLL.

Figure 69 shows that, prior to failure, axial strains along both the top and bottom skins of the front spar were not affected by CAT2 damage on the aft spar of ST001(R). This comparison was based on strain values observed during the ST002 test article (with CAT1 damage) at the same load level. Axial strain along both front and aft spars indicated that the anomalies in figure 67 were localized and did not affect the final fracture. This was largely due to the fact that for the up-bending loading configuration, the front spar, which is significantly stiffer than the aft spar, was the primary load path. Therefore, for the CAT3 damage configuration, the front spar was selected.

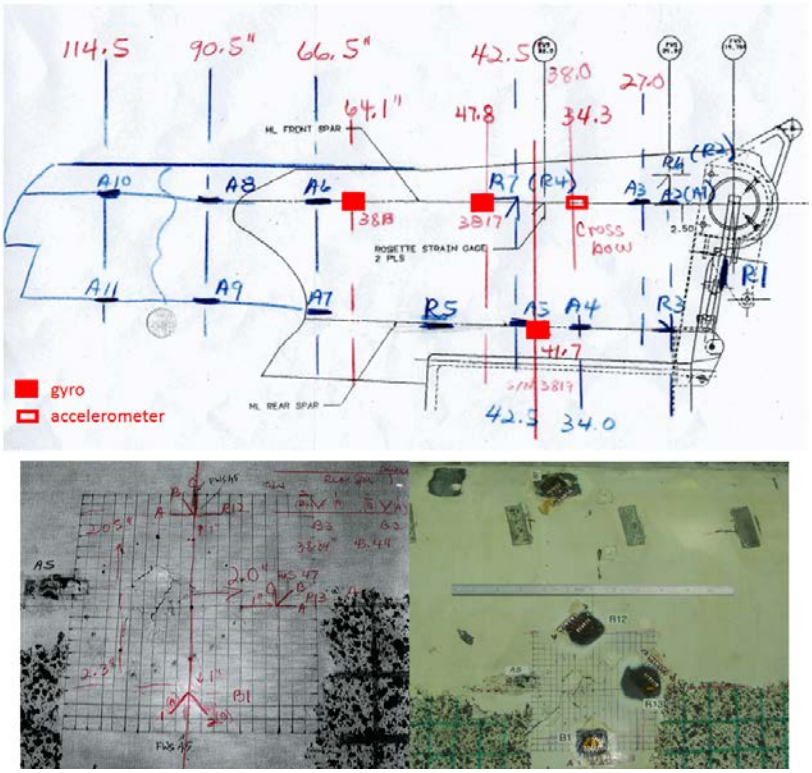

Figure 66. Strain gage location for ST001(R) static test article

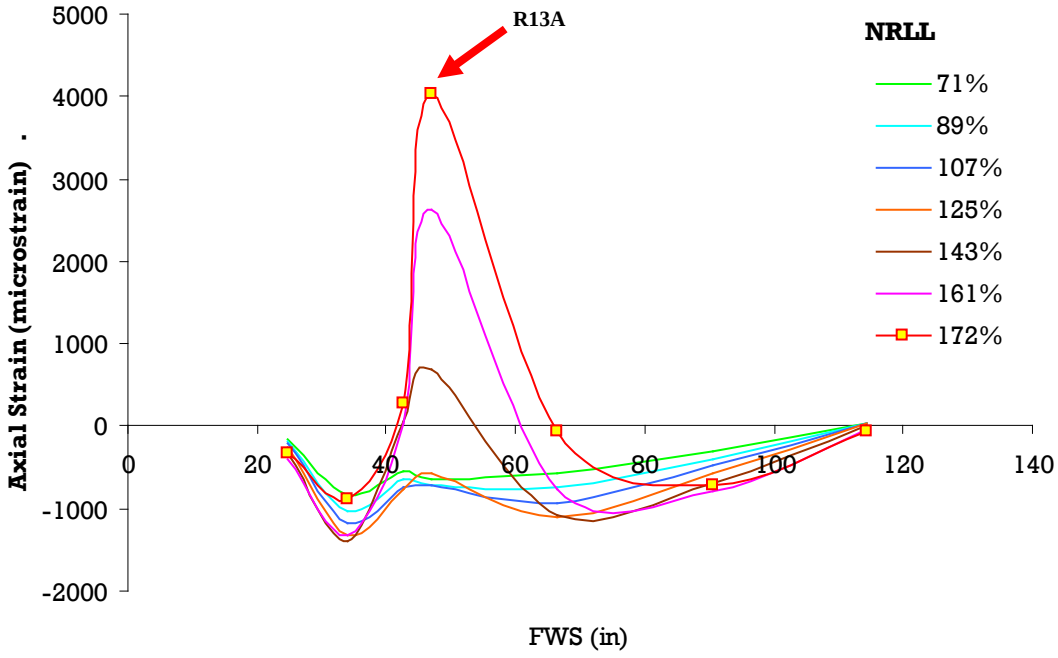

Figure 67. Strain evolution on upper skin of aft spar of ST001(R)

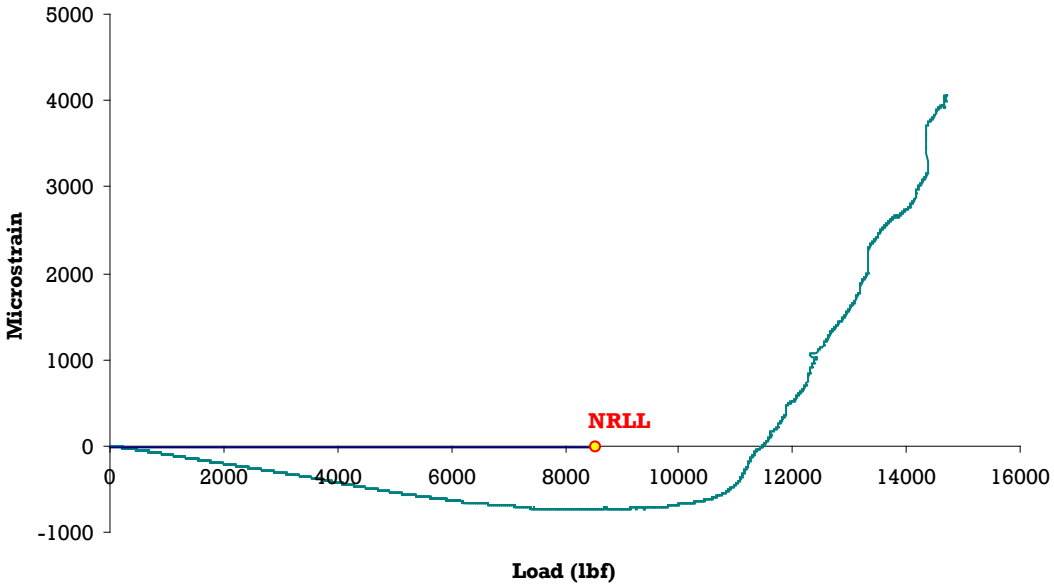

Figure 68. Strain evolution of R13A of ST001(R)

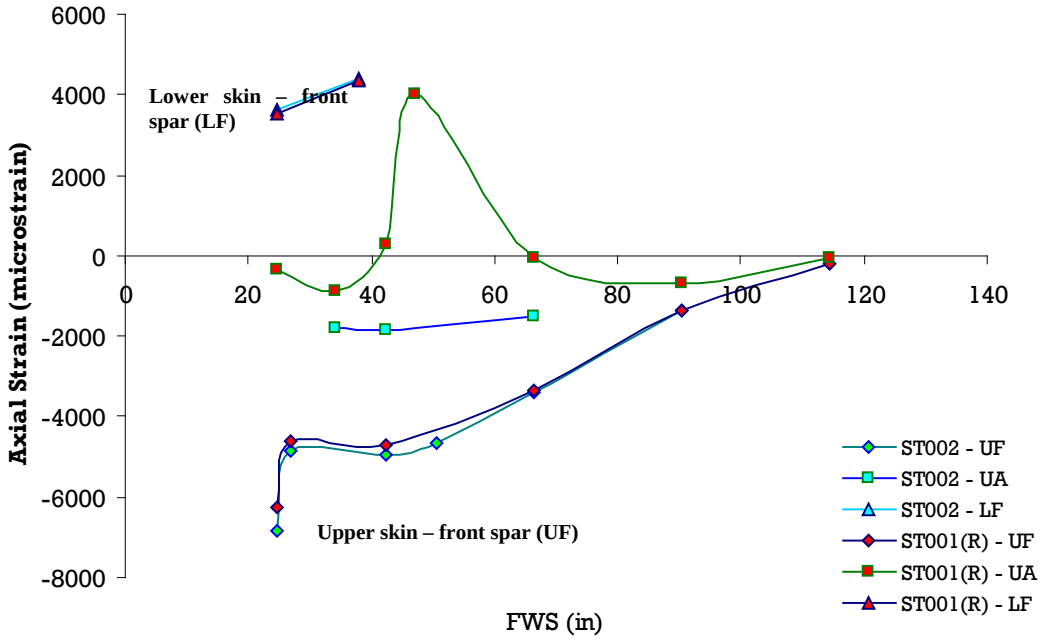

Figure 69. Axial strain comparison of ST001(R) and ST002 (172% of the NRLL)

5.4.1.2 The ST005—CAT3 Damage on Front Spar

Figure 70 shows the locations of strain gages for the ST005 static test article. Several additional gages were mounted adjacent to the damage to monitor damage propagation during quasi-static loading. As shown in figure 71, during loading of the ST005 test article, strains in the aft spar increased gradually. Figure 71 also shows that, inboard of FWS 40, the strain along the aft spar

was reduced significantly, indicating that the loads were diverted to the steel lug at the end of front spar. At approximately 60% of the NRLL, there was a gradual strain drop at FWS 66.5 on the rear spar, which is directly aft of the CAT3 damage, and then an increase in strain toward the failure. This was primarily due to skin buckling at this location, which may have later resulted in skin debond. The rest of the rear spar indicated a linear response until failure.

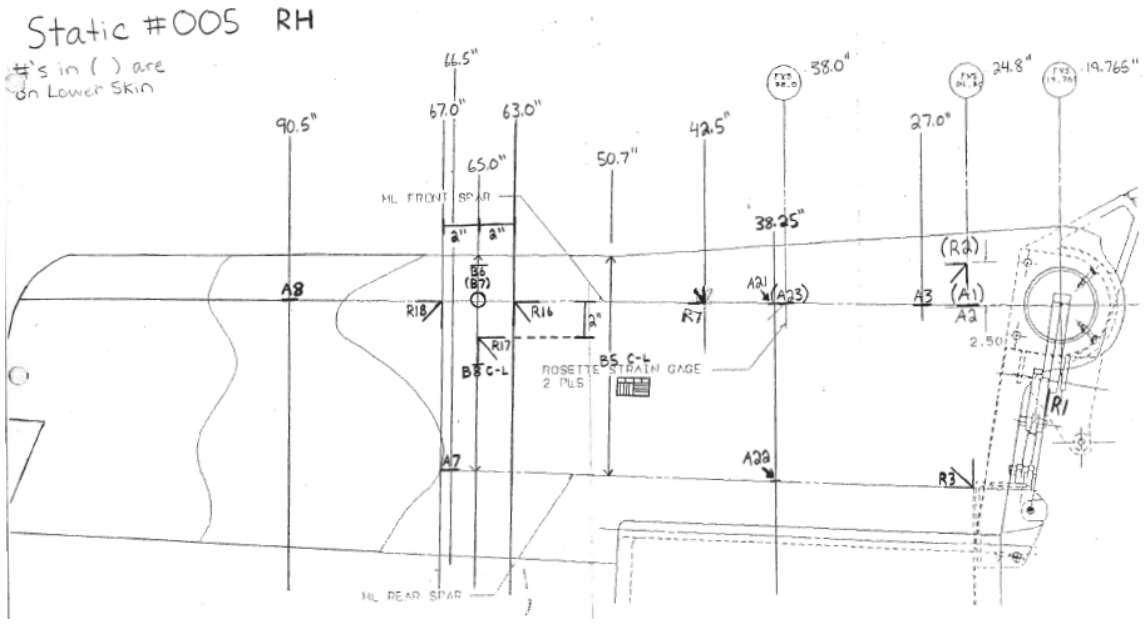

Note: Numbers in parentheses on lower skin

Figure 70. Strain gage locations for ST005 right wing static test article

As expected, damage propagation was noted adjacent to CAT3 damage on the front spar just prior to failure, following a series of audible cracking noises (figure 72). Unlike the case of ST001(R), this directly resulted in catastrophic structure failure. The rosette, which was located 2 in. aft of the damage, indicated significant nonlinear strain anomalies after 60% of the NRLL, causing skin buckling (as noted on the aft spar) and a possible load redistribution due to damage growth. A similar anomaly was noted from a gage located forward of the damage, but at approximately 65% of the NRLL, indicating possible damage growth, because this area is relatively thick; therefore, buckling was not the case. Both gages were located on an axis perpendicular to the direction of the compressive stress on the upper spar cap caused by the bending moment. The damage growth occurred in the direction that was expected. All the strain anomalies on the front spar were limited to the vicinity of the impact damage, because the remaining gages had a linear response until failure.

Unlike the case of CAT2 damage on the rear spar, CAT3 damage on the front spar had a significant impact on limit-load carrying capability and failure mode. Failure load (5768 lbf) corresponded to 68% of the NRLL, which was 94% of the BDLL.

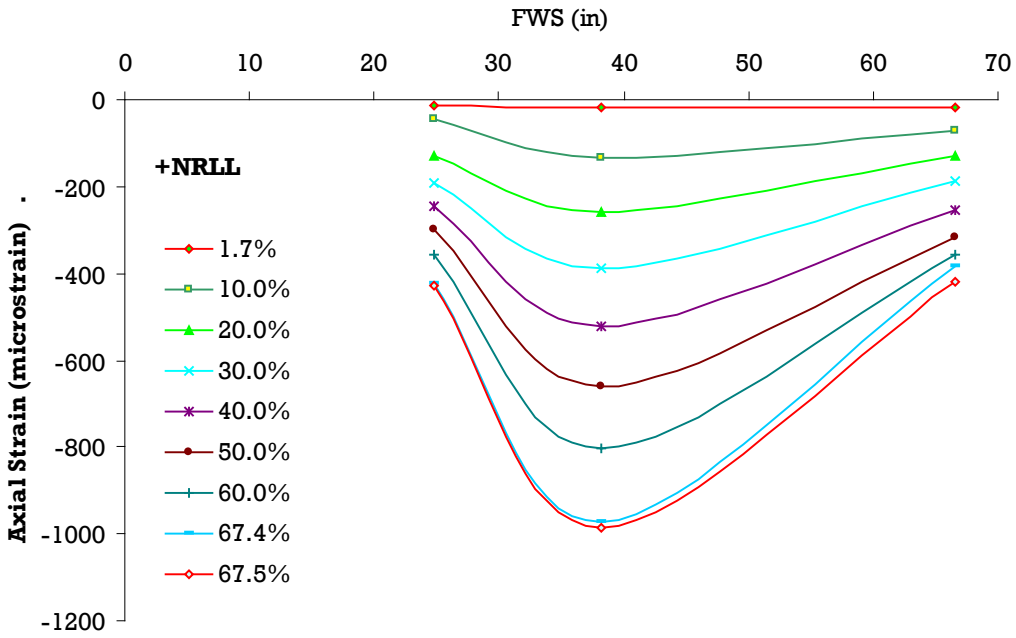

Figure 71. Strain evolution on upper skin of aft spar of ST005

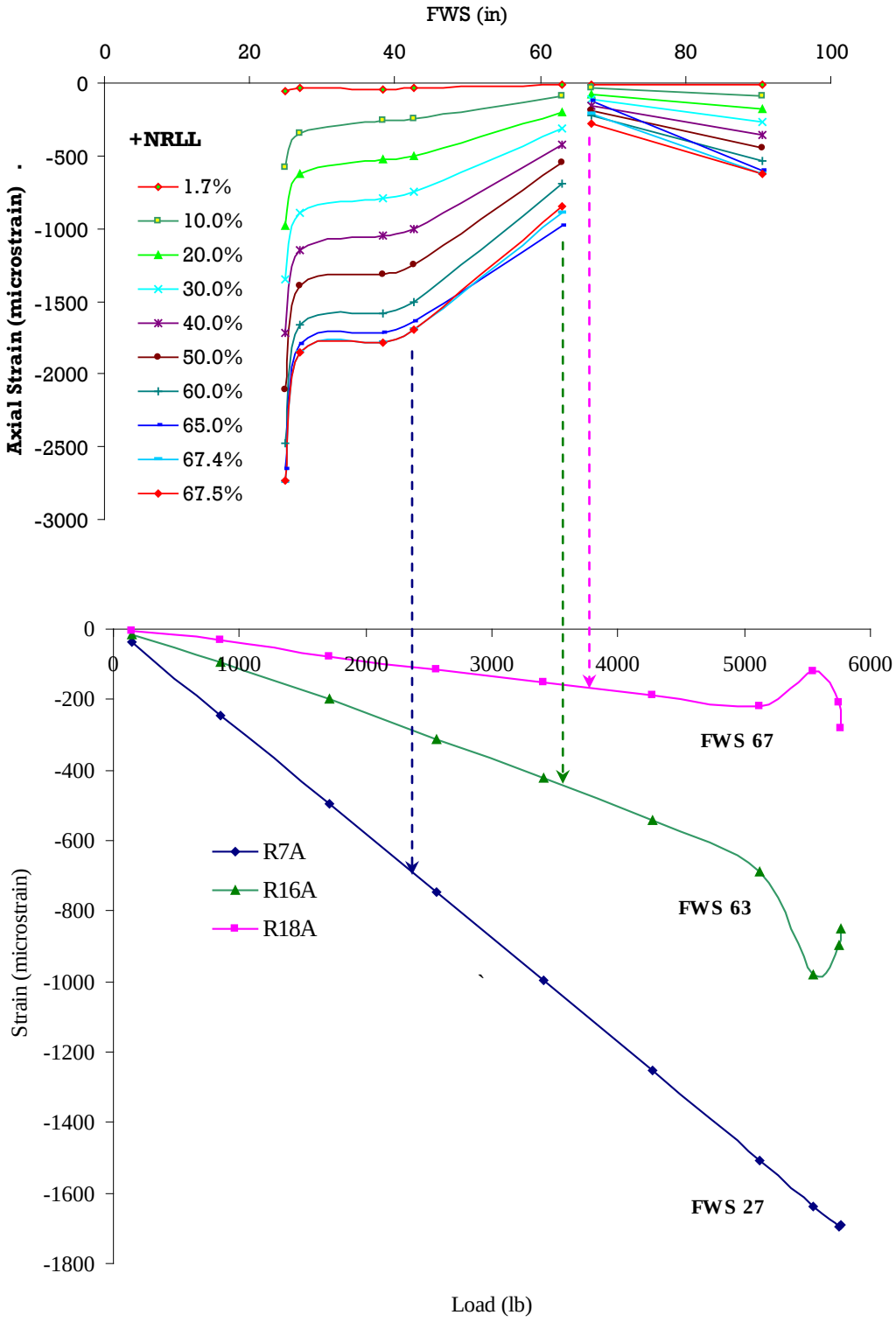

Figure 72. Axial strain along front spar top skin of ST005

5.4.2 Spectrum Fatigue Loading

This section contains the DaDT test results for ST004 and ST006 articles with CAT2 and CAT3 damages, respectively. Additional strain and displacement data for both test articles are provided in appendix D. In addition to the NDI techniques outlined in section 5.3, strain gage data, especially around the damage, were used as a health monitoring device for the test article during cyclic loading. Strain data were accumulated from all channels at the middle SLBs of A-M, B-M, and B-G. Because blocks C and D had the highest loads and only a limited number of cycles, strain data were acquired during each of their load cycles. Strain data were able to detect the onset of damage propagation as well as the load redistribution, thereby indicating that they were more efficient and capable than ultrasonic NDIs in providing information in real time with minimal interruptions to the test progress. To isolate possible environmental effects, temperature-compensation gages were mounted on the durability test articles.

5.4.2.1 The ST004—CAT2 Damage on Aft Spar

Prior to cyclic testing, the ST004 DaDT test article was loaded to positive and negative limit loads, as shown in table 7. Figure 73 shows the locations of the main strain gages for that test article. Axial strains from ST001(R) static and ST004 DaDT test articles along the top and bottom front spar caps as well as the upper skin along the aft spar are compared in figure 74. Strain data on ST004 were somewhat higher than that of ST001(R). This can partially be attributed to the fact that ST001(R) is a right wing and ST004 is a left wing, and therefore required minor changes to the fixture assembly. Furthermore, load-former and load-patch whiffletree loading assemblies in static and durability testing, respectively, may have caused some of these discrepancies (see figure 75).

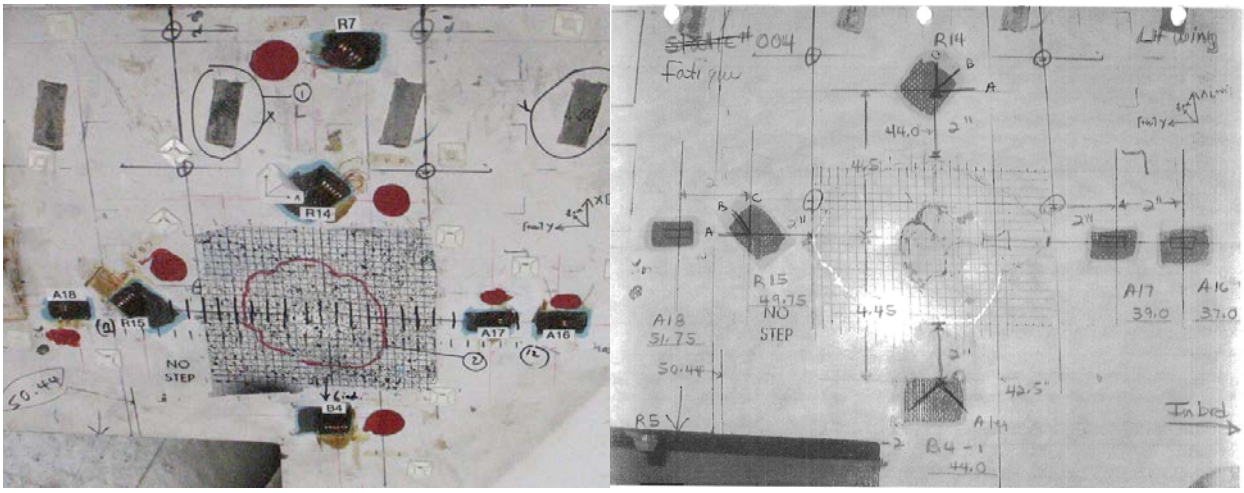

Figure 73. Strain gage locations for ST004 DaDT test article

The ST004 fatigue test article was periodically monitored throughout the fatigue tests. It was inspected in detail prior to cyclic loading and after each 1/4 DLT of cyclic loading. Periodic inspections and strain anomalies around the defect were monitored to investigate damage containment and propagation. As shown in Figure 76, at the beginning of cyclic loading, there

was a strain drop inboard of impact damage, possibly due to the settling of the structure around the impact damage during initial cyclic loading. This also resulted in an increase in strain at FWS 24.8, possibly due to load redistribution. Furthermore, impact damage propagated outboard between 1.5 and 2 DLTs (figure 76) and then arrested, as shown in figure 77.

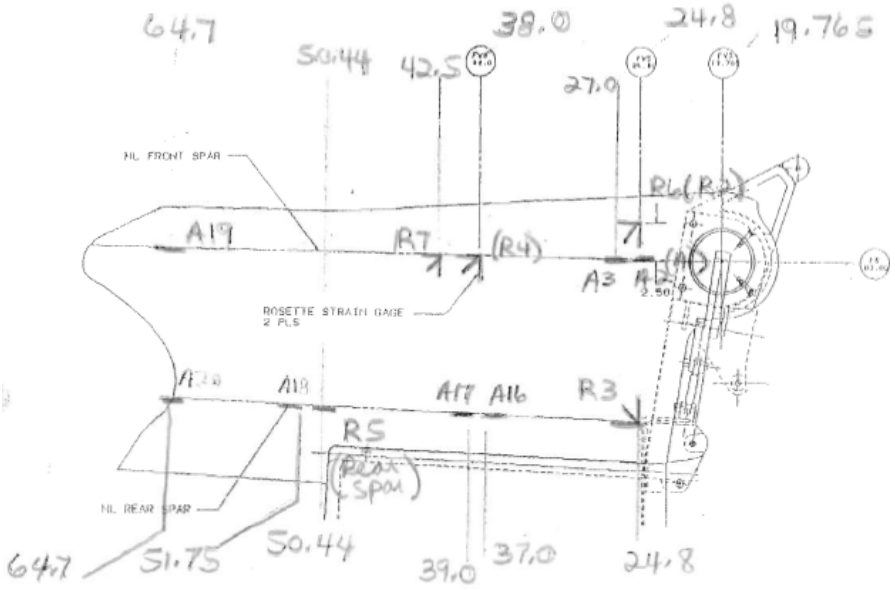

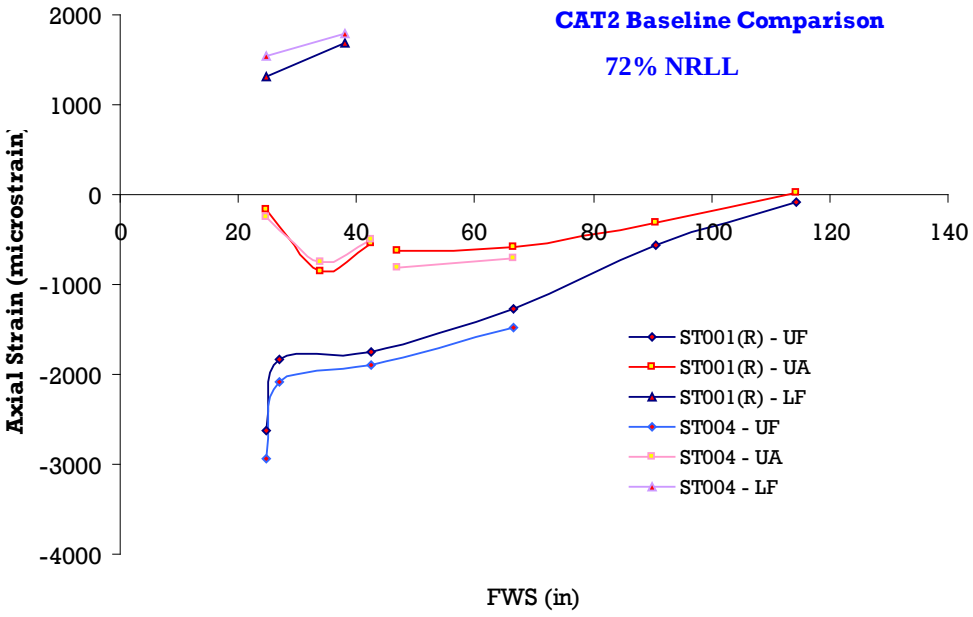

Figure 74. Axial strain comparison of ST001(R) and ST004 prior to cyclic loading

(a) Load formers—static (b) Load patches—fatigue

Figure 75. Full-scale test setup for quasi-static and fatigue loading

During the residual strength test of ST004 after 2 DLTs, a loud, cracking noise was heard at approximately 155% of the NRLL, and strain anomalies around the damage were noted. Figure 77 shows that the impact damage rapidly propagated outboard along the aft spar between 155% and 165% of the NRLL and gradually propagated thereafter. Far-field strain gages along the aft spar did not increase beyond 160% of the NRLL, indicating that the load did not

redistribute around the damaged area. Therefore, the aft spar reached its maximum structural capacity. All strain and global displacement data showed several spikes and significant strain anomalies after 155% of the NRLL, indicating structural failure. Review of video after the test also confirmed the damage growth revealed by the strain anomalies.

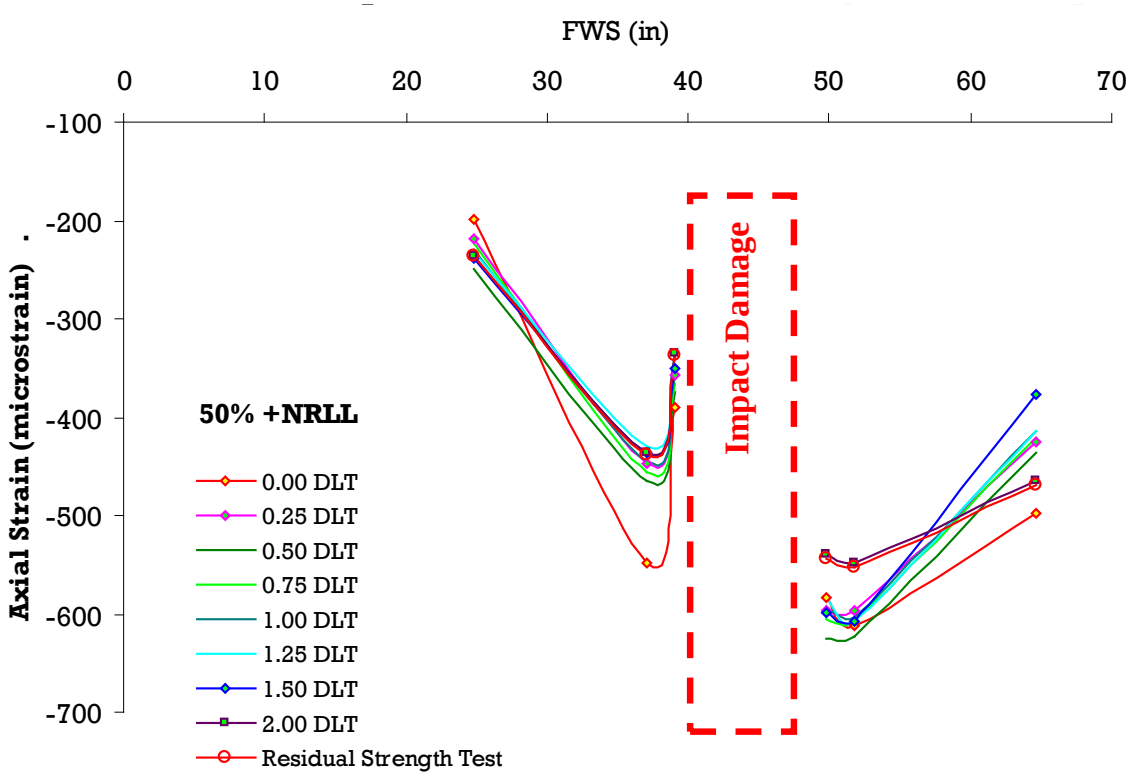

Figure 76. Damage progression along aft spar top skin of ST004 during DaDT test

Strain data during the residual strength test of ST004 after 2 DLTs are compared with ST001(R) static test data at 50%, 100%, and 150% of the NRLL in figure 78. Data show that the structural stiffness of ST004 decayed after 50% of the NRLL, as compared to the data obtained from the ST001(R) test (i.e., strain data on ST004 were lower than those of ST001(R) after 50% of the NRLL). This was confirmed by the strain and global displacement data that indicated a nonlinear response at approximately 50% of the NRLL. Moreover, an audible noise (i.e., a loud pop) was noted at around 40% of the NRLL, and that may have caused an internal failure, which resulted in a nonlinear strain/displacement response.

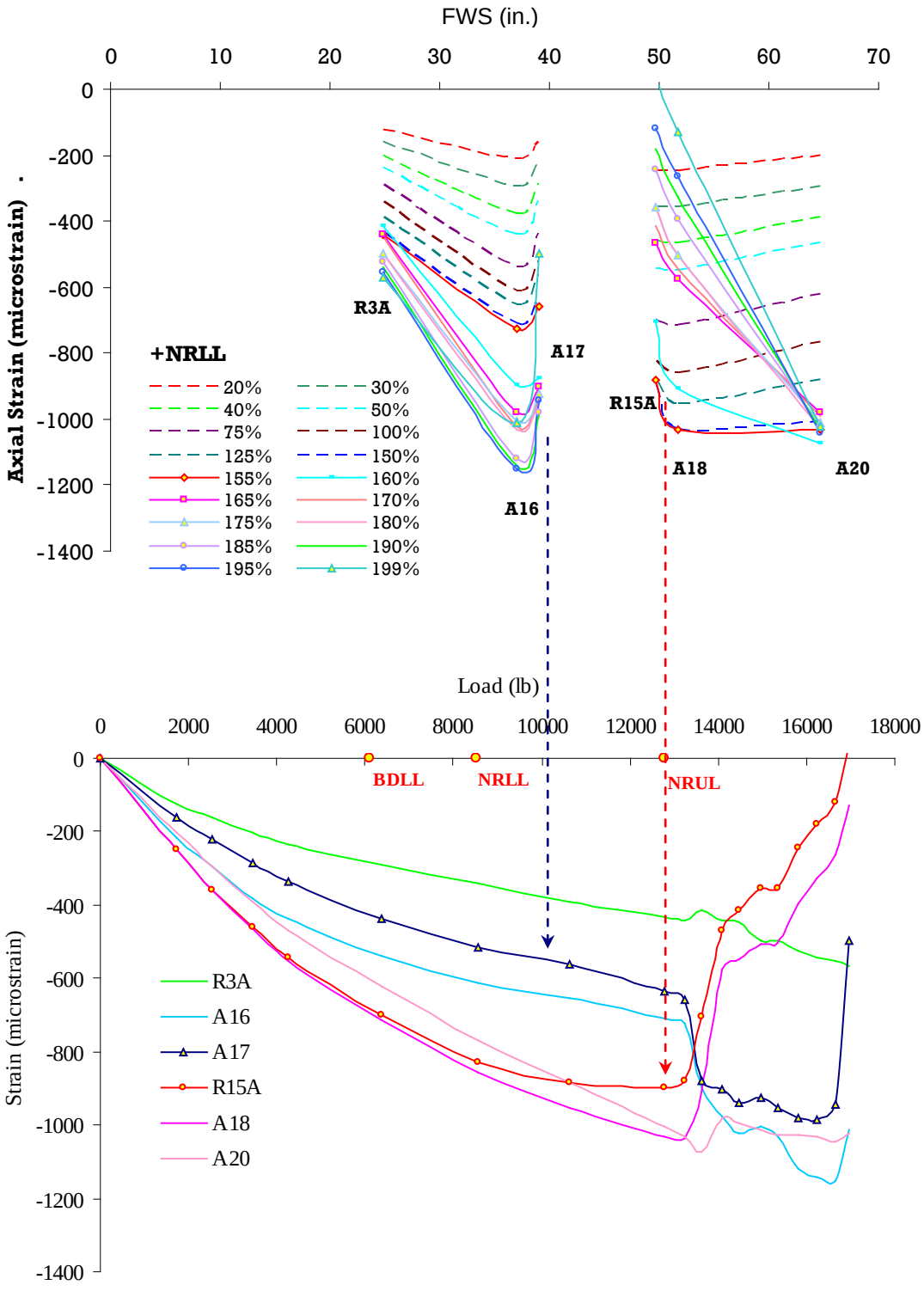

Figure 77. Damage progression along aft spar (top skin) of ST004 during residual strength test after 2-DLT cyclic test

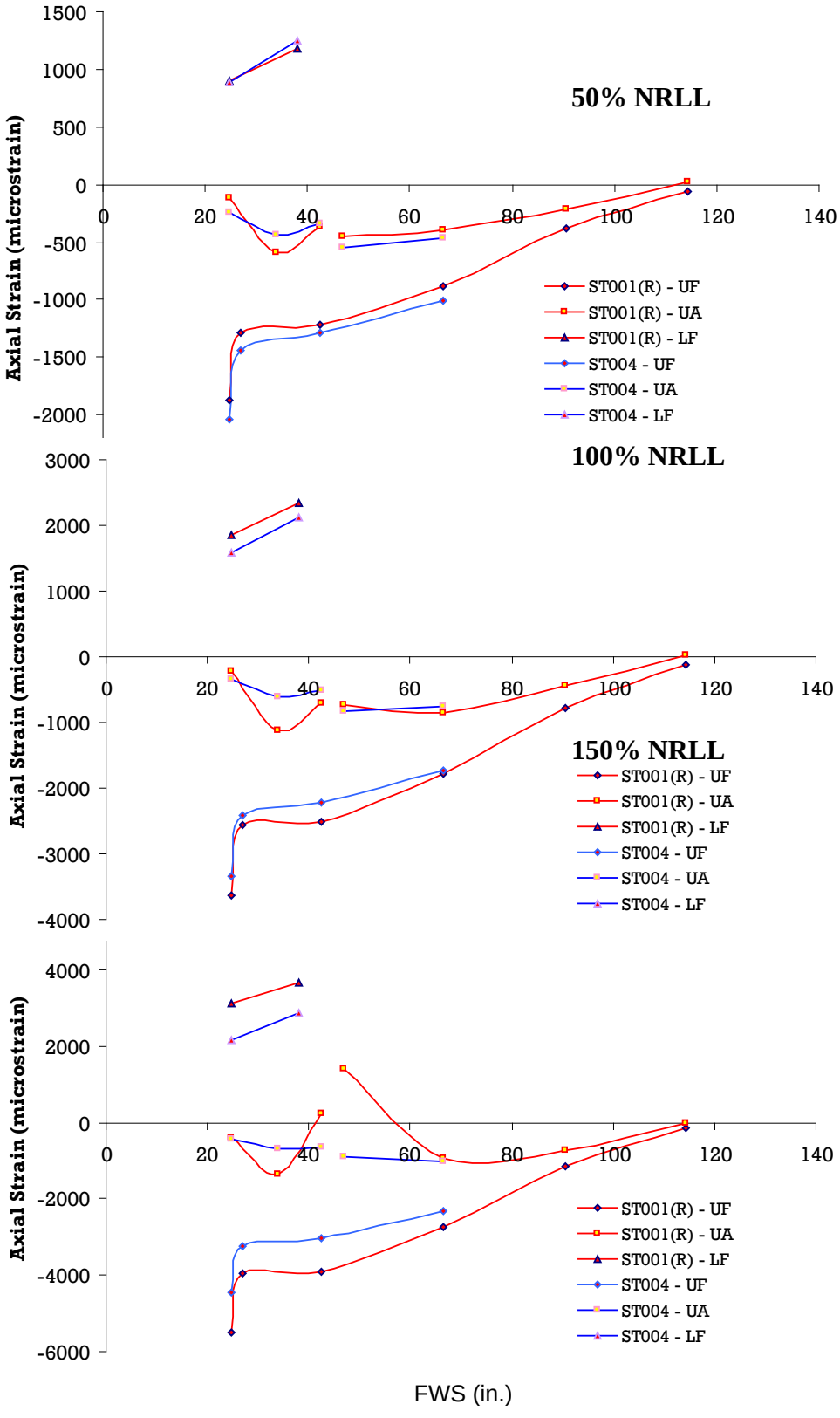

Figure 78. Comparison of axial strain evolution along forward and aft spar of ST001(R) and ST004 during residual strength test after 2-DLT cyclic test

5.4.2.2 The ST006—CAT3 Damage on Front Spar

For ST006 fatigue testing, a CF of 1.4 would result in some spectrum loads that were higher than the load corresponding to the static residual strength of the NRLL (5768 lbf) with a similar damage, especially in blocks C and D. Blocks C and D were inserted in the spectrum after 0.25 and 0.50 DLT, respectively. Because the first inspection was scheduled prior to 0.25 DLT, the damage would be located and repaired in-service, assuming that the structure survived. The majority of loads, except three center load segments (figure 26) in blocks B-M were below 5768 lbf. All spectrum loads in blocks A-M and B-G were below 68% of the NRLL. To ensure that the fatigue loads were below the static failure load of ST005, neither the CF nor the LEF was applied to the load spectrum. This simulated a composite primary structure that had a CAT3 damage in the primary load path undergoing typical service loads. The load sequence was the same as shown in table 7, except the periodic limit load checks were limited to 50% BDLL, and the residual strength test was conducted after block D, just after half of DLT. The inspection intervals were allotted as shown in table 10 to closely monitor any damage propagation and to validate the benchmark predictions in section 3.4.3.

Table 10. Load sequence for ST006 DaDT test and inspection intervals

Sequence	Loading Block	Repetitions	*n*-Block	Σ*n*	Flight Hours	Lifetimes	Scheduled Inspections
a	Start	–	–	–	–	–	X
b	Ramp to	1	–	–	–	–	–
c	Ramp to: Zero	1	–	–	–	–	–
d	Ramp to:	1	–	–	–	–	–
e	Ramp to: Zero	1	–	–	–	–	–
f	Ramp for	1	–	–	–	–	–
1	Block A-M	10	718	7,180	–	–	X
2	Block A-M	15	718	17,950	–	–	X
3	Block B-G	1	146	18,096	–	–	–
4	Block B-M	1	264	18,360	–	–	–
5	Repeat 3 and	4	410	20,000	–	–	X
6	Repeat 3 and	5	410	22,050	–	–	X
7	Block A-M	10	718	29,230	–	–	X
8	Block A-M	15	718	40,000	4,999	0.250	X
9	Ramp to: Zero	1	–	–	–	–	–
10	Repeat a - f	1	–	–	–	–	–
11	Block C	1	16	40,016	–	–	X

Table 10. Load sequence for ST006 DaDT test and inspection intervals (continued)

Sequence	Loading Block	Repetitions	*n*-Block	Σ*n*	Flight Hours	Lifetimes	Scheduled
12	Block A-M	10	718	47,196	–	–	X
13	Block A-M	15	718	57,966	–	–	X
14	Repeat 2 and 3	5	410	60,016	–	–	X
15	Repeat 3 and 4	5	410	62,066	–	–	X
16	Block A-M	10	718	69,246	–	–	–
17	Block A-M	15	718	80,016	10,000	0.500	X
18	Ramp to: Zero	1	–	–	–	–	–
19	Repeat a - f	1	–	–	–	–	–
20	Block D	1	17	80,033	10,002	0.500	X
21	Ramp to: Zero	1	–	–	–	–	–
22	Residual	1	–	–	–	–	–

Figure 79 shows the strain gage location for the ST006 DaDT test article. Periodic health monitoring results using strain gages on the front spar are shown in figure 80. For clarity, this figure only shows data from the main inspection intervals excluding the data acquired periodically during fatigue loading. During the first set of B-G/B-M blocks, the axial gage immediately outboard of the damage decreased, whereas the rest of the strains in the front spar increased. This indicated that there was a damage propagation outboard of the defects with a global influence (unlike in the case of CAT2 damage on the aft spar) because the front spar is the primary load path.

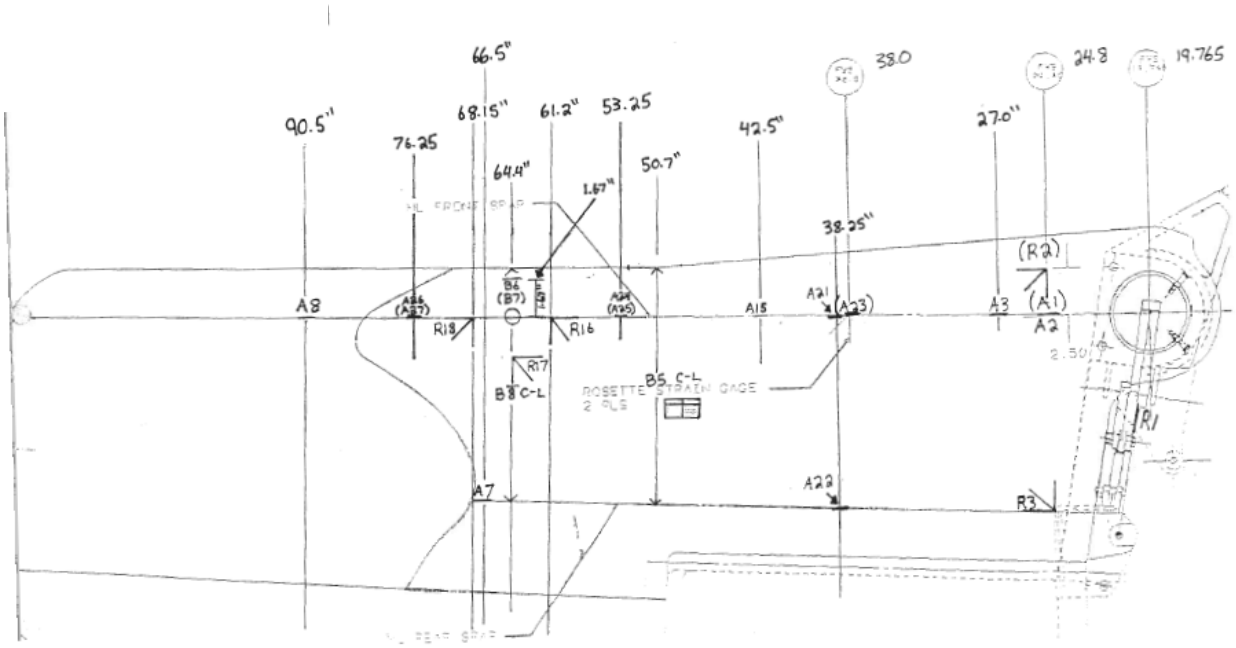

Note: Numbers in parentheses are located on lower skin

Figure 79. Strain gage locations for ST006 right wing DaDT test article

In addition to the gages on the front spar, both gages that were front and aft of the damage, B6-1 and R17A, respectively, indicated that the stress field around the damage increased during the first set of B-G/B-M blocks, possibly due to minor damage propagation. This set of load blocks was not as severe as the ones in blocks C and D, but it had significantly higher repetitions (4100 cycles) than the latter load blocks. Therefore, the damage progressed gradually (as shown in figure 80) during the first and second set of B-G/B-M blocks, resulting in a minor matrix fracture that consequently caused localized material degradation (compliance change), but was not severe enough to be detected by ultrasonic inspection equipment. Blocks C and D had only 16 and 17 cycles, respectively, but significantly higher loads than was the case for B-G/B-M loads, which caused approximately the same amount of strain increment. Furthermore, ultrasonic equipment was able to detect damage growth, and visual inspections confirmed damage to other parts of the structure as well (section 5.5.2).

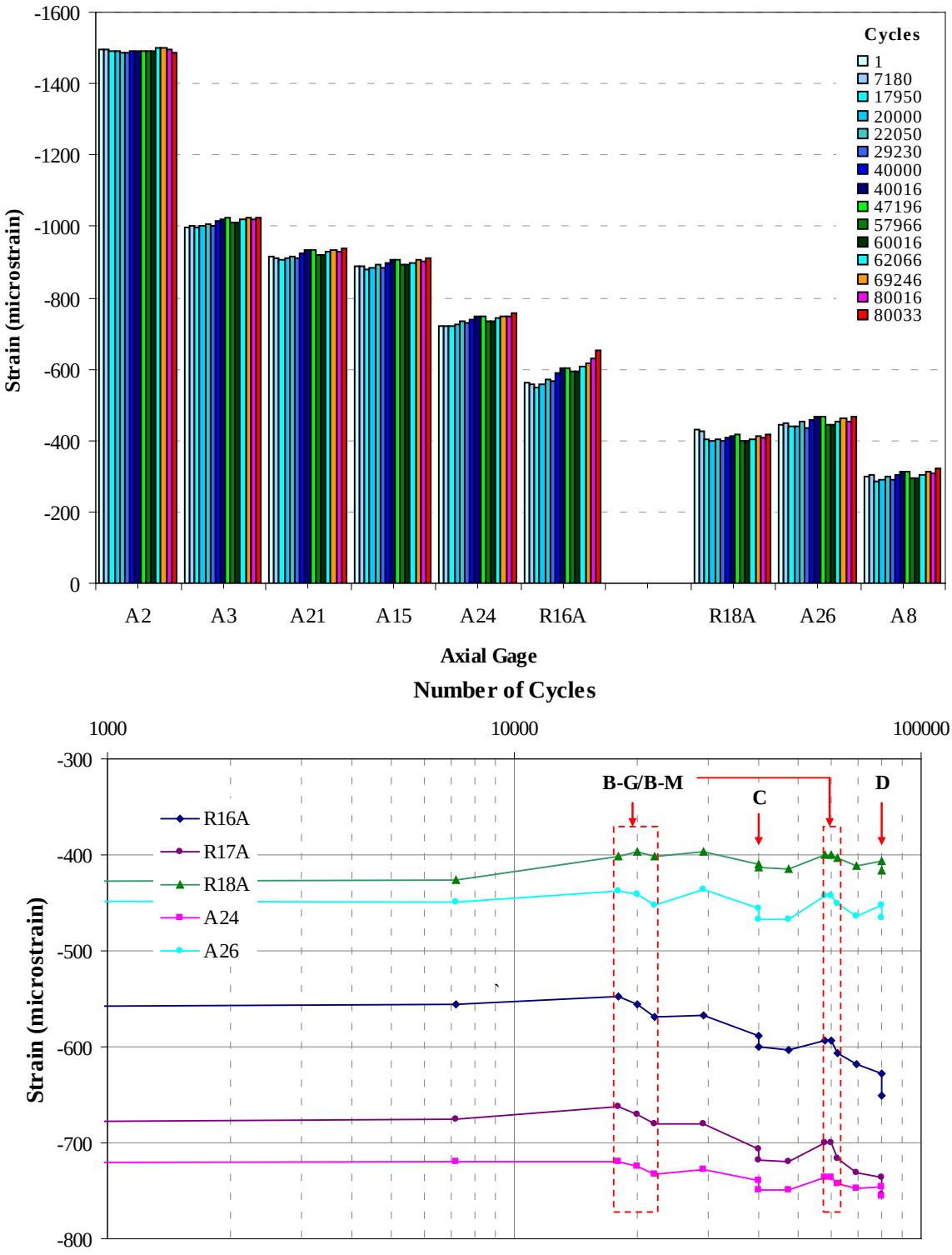

Figure 80. Strain evolution on front spar of ST006 DaDT test article

Damage growth during B-G/B-M, C, and D was depicted in terms of probability of structural failure due to the damage progression shown in figure 27. Although this is not a one-to-one

correlation for the damage propagation or its size, the CFR model shows the gradual progression of local damage in a linear scale (figure 81), (such as possible matrix cracks observed during B-G/B-M blocks of fatigue testing of ST006, as well as the global impact of high loads, such as blocks C and D) on the structure.

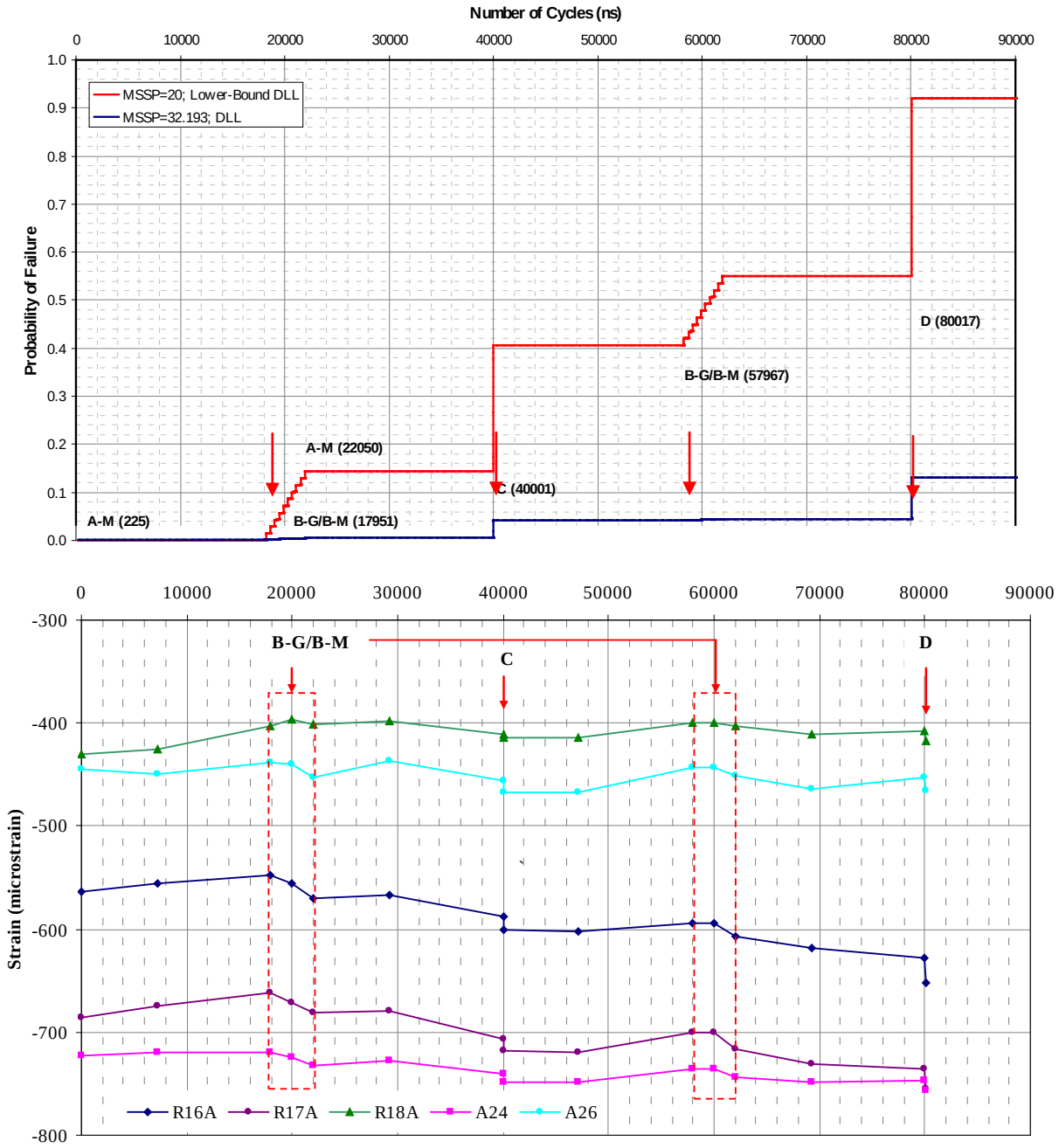

Figure 81. Cumulative POF for Starship forward wing and strain data for ST006 DaDT test article

After cycling through block D, ST006 was tested quasi-statically to evaluate the residual strength. Figure 82 shows a comparison of axial strain along front and aft spars of ST005 and

ST006 (before and after fatigue loading). Except for the strain adjacent to the damage, the front spar indicated a similar strain distribution for all three cases, whereas ST005 static test strains on the aft spar were somewhat higher than with ST006. The discrepancy of strain data around the damage can largely be attributed to the difficulties associated with achieving CAT3 damage on a thick part (such as the spar cap), as shown in figure 31, and minor changes to damage parameters can significantly change the state of damage in such an article. The residual strength test failed at 95.5% of the NRLL, soon after a fracture propagated through the CAT3 damage, as was observed during static testing of the ST005 article. Examination of strain evolution on the front and aft spars (figure 83) shows that the CAT3 damage further propagated outboard, between 80% and 85% of the NRLL, which was significant enough to affect the aft spar at the same FWS. Strain gage A7, which was located on aft spar at FWS 66.5, indicated a sudden drop at 7039 lbf, and a loud, cracking noise was heard from the back side, closer to this gage, possibly due to the top skin disbonding from the aft spar or skin delamination. At this point, several gages around the CAT3 damage also indicated sudden changes, possibly due to stress relief and damage propagation. Although strains inboard of CAT3 damage did not indicate sudden changes, the R16 gage indicated possible local skin buckling in a 45° direction with respect to the front spar.

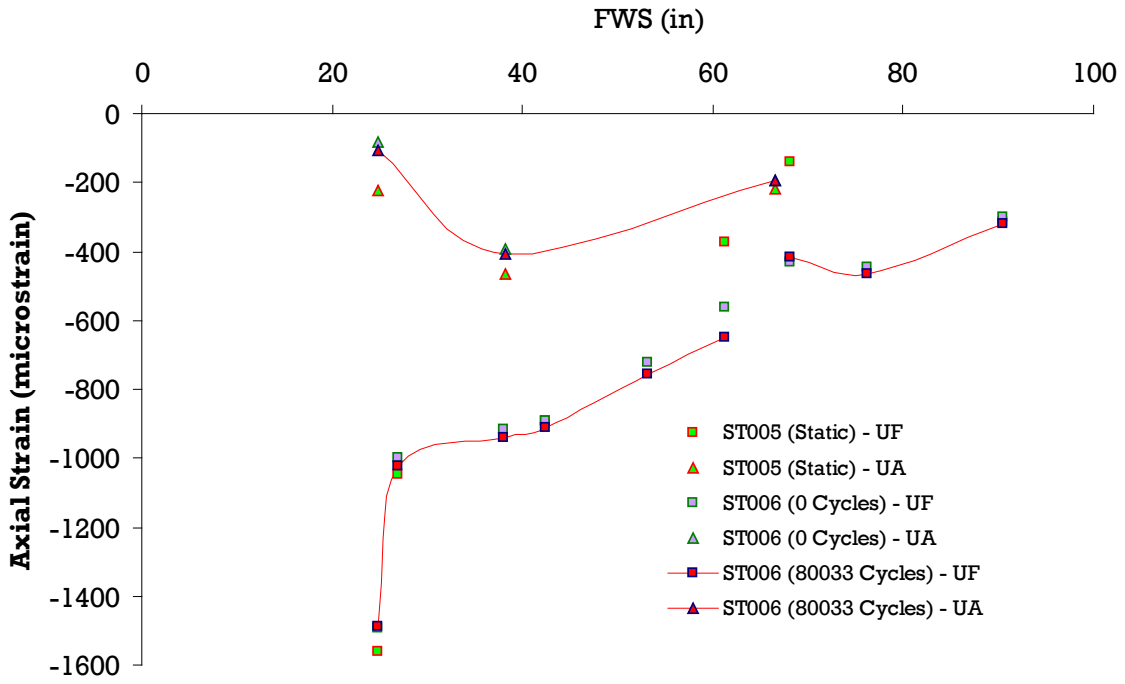

Figure 82. Comparison of axial strains along front and aft spars (36% of the NRLL)

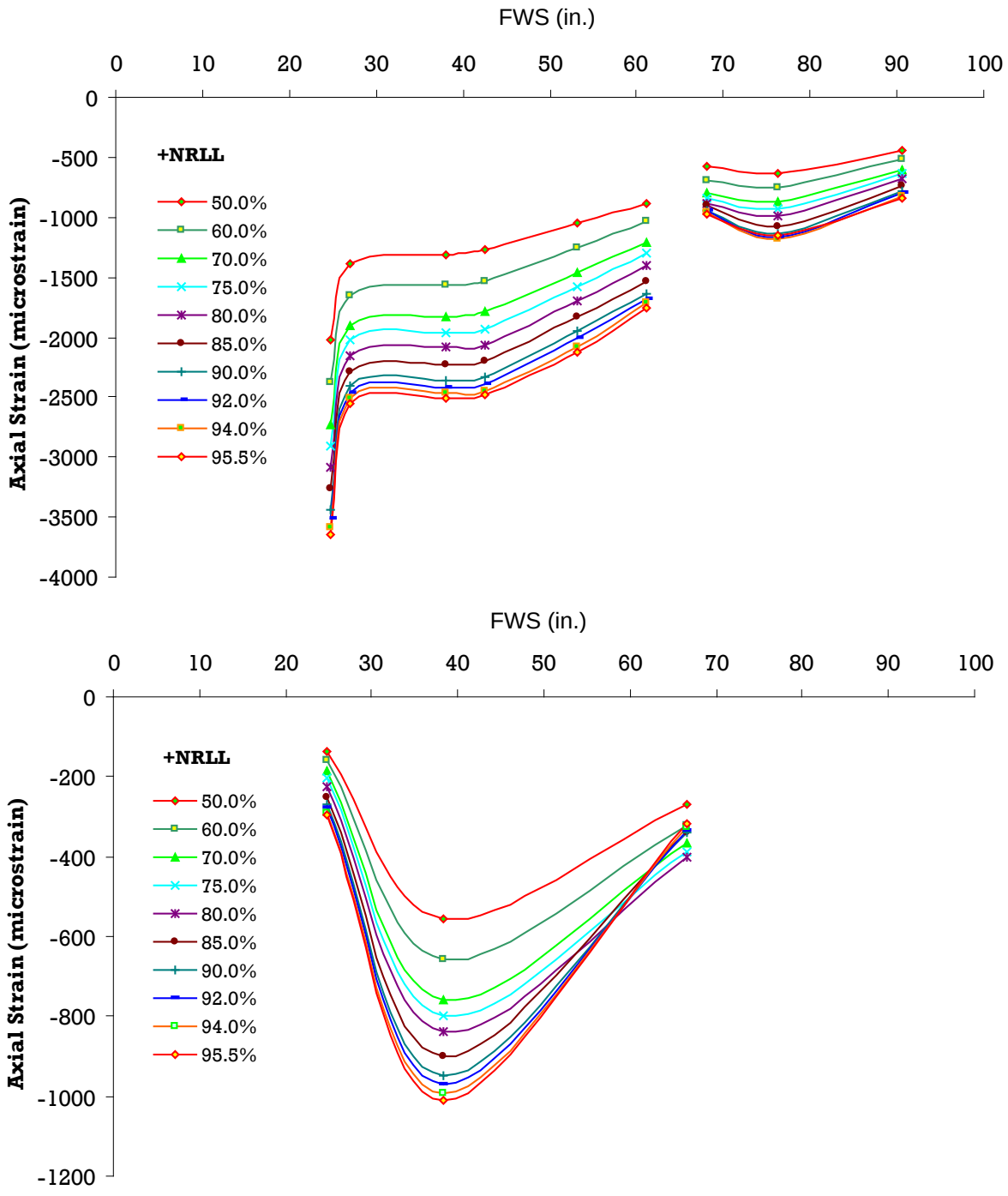

Figure 83. Strain evolution on front and aft spars during residual strength test after 80,033 cycles

Once the residual strength test was completed, the CFR model was re-analyzed by modifying the post-impact residual strength (prior to fatigue cycling), so that the LLRS at the end of fatigue was equal to the failure load (post-DaDT residual strength). Assuming that the residual strength was reduced to lower-bound limit load, the POF during post-DaDT quasi-static loading for

different load levels is shown in figure 84. As shown in this figure, when the POF was between 80% and 85% of the NRLL, the load level in which the loud, cracking noise and strain anomalies were observed during the ST006 post-DaDT residual strength test increased dramatically. Based on an MSSP of 20 and a post-impact residual strength equal to the lower-bound limit load, the POF at 82.5% of the NRLL (corresponding to 7039 lbf) was approximately 24%. It decreased to 4.2% for an MSSP of 32.193 as a direct result of there being less scatter in the data pooled when calculating MSSP.

Although use of the lower bound limit load for residual strength of a CAT3-damaged article resulted in an overly conservative fatigue life, it accentuated the loads that can cause damage when small matrix cracks coalesce to form larger cracks or trigger the onset of propagation of an existing damage. Therefore, this criterion can be used to determine the inspection intervals necessary to detect damage prior to imminent failure. This approach can be used as a starting point and then, based on the probability of occurrence of such a high-energy impact scenario and the probability of detectability following such an impact scenario, it can be tailored to a particular structure to address economic concerns.

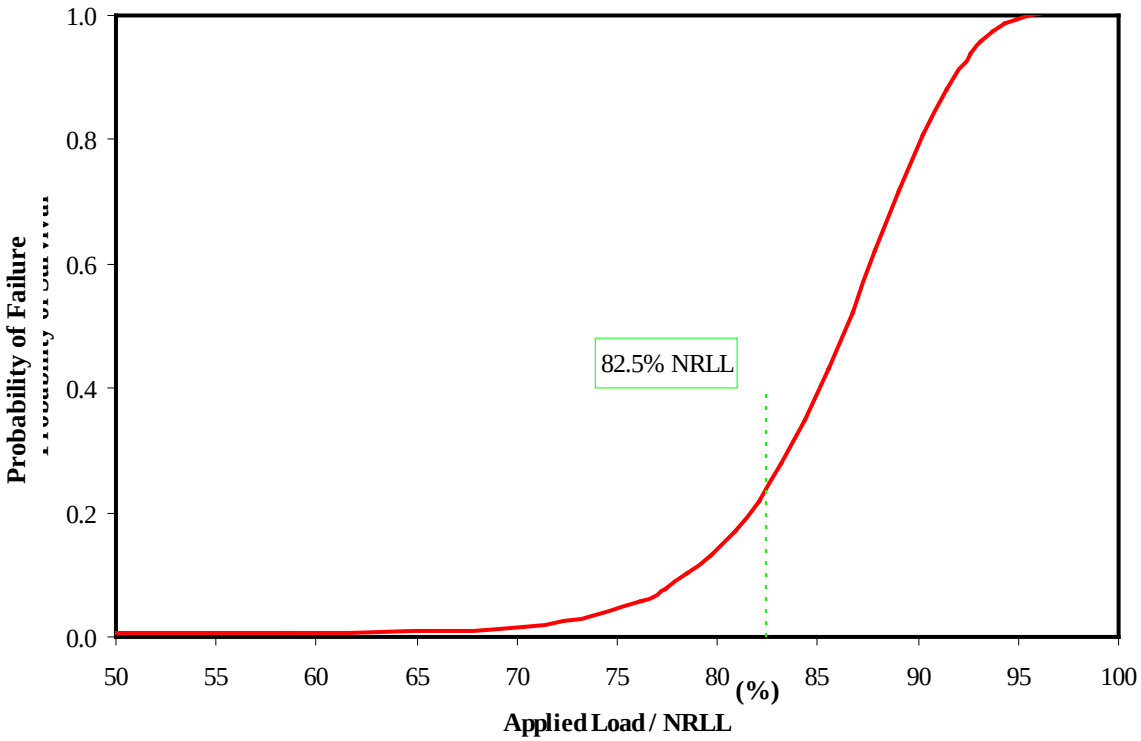

Figure 84. The POF for corrected residual strength after block D (80,033 cycles)

5.5 SCHEDULED INSPECTIONS OF DaDT TEST ARTICLES

In addition to the strain surveys discussed in section 5.4.2, periodic NDIs and visual inspections were carried out for DaDT test articles. In addition to the damage surroundings, visual inspections on critical areas and heavily loaded areas, such as root lug, test fixture attachments, and some of the leading edge load patches, were periodically carried out so that the unexpected

failure of these test articles could be prevented and corrective action, if necessary, could be taken immediately.

5.5.1 The ST004—CAT2 Damage

At approximately 0.5 DLT, a fastener at FWS 43 that attaches the leading edge to the top spar cap (flange) indicated pull-through failure and resulted in local skin buckling, as shown in figure 85(a). Because the focus of this test was on the composite structure, the test was resumed. By 1.5 DLTs, this fastener had completely failed through the leading edge. Shortly after completing 1.5 DLTs, fatigue testing of article ST004 was halted and was removed from the test fixture to investigate significant displacements observed around the fixed end of the test article. Although there was no significant propagation of the impact damage inflicted on the aft spar at FWS 45, several fasteners along the leading edge indicated pull-through failure (figure 85). Initially, this was observed only around FWS 43 during up-bending, but several fasteners outboard and inboard of FWS 43 later indicated fastener pull-through failures and severe leading-edge buckling around these locations.

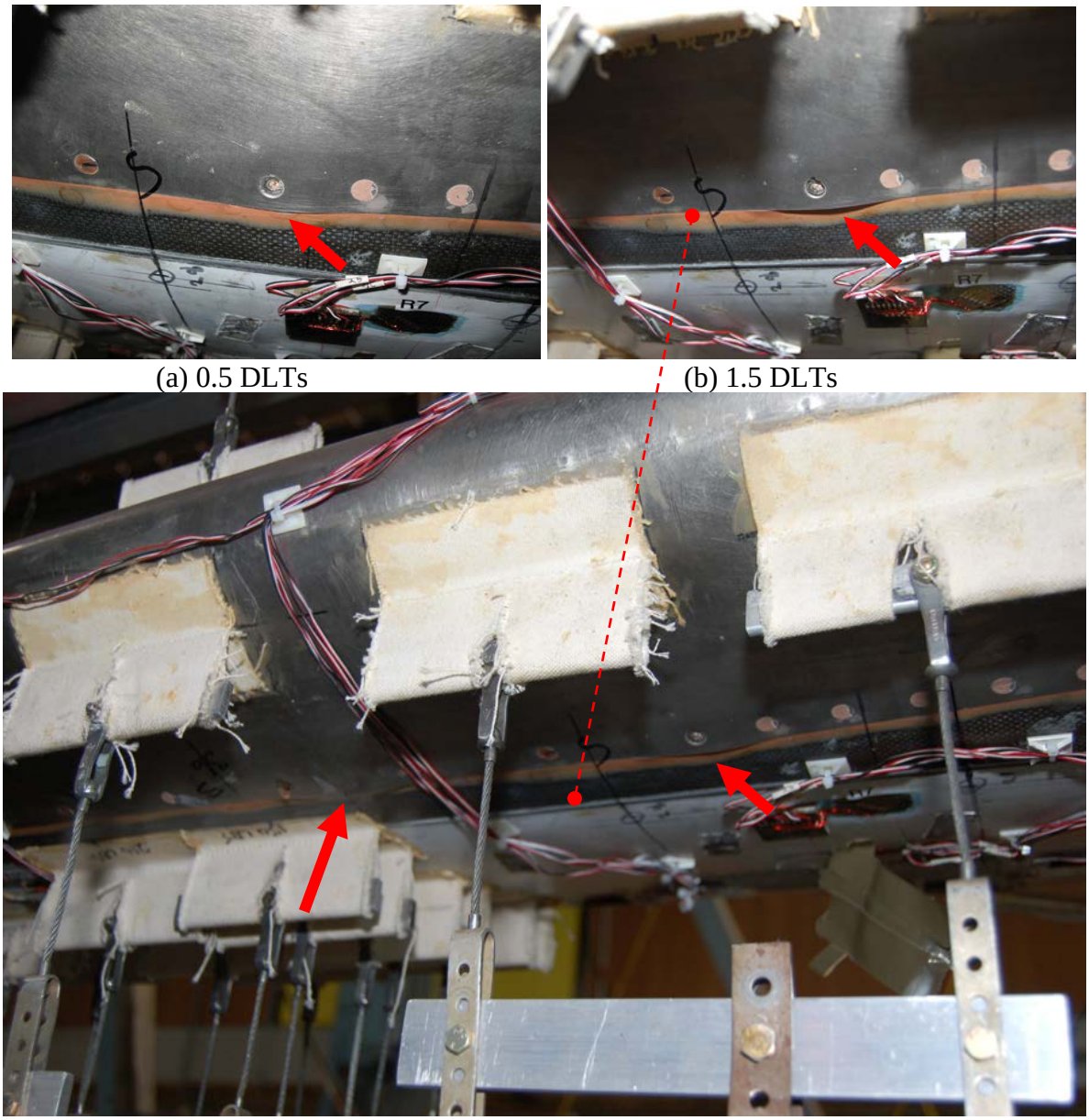

(a) 0.5 DLTs (b) 1.5 DLTs

(c) 1.5 DLTs

Figure 85. Leading-edge fastener-pullout failure (top surface) test article: (a) close-up at .05 DLTs, (b) close-up at 1.5 DLTs, and (c) overview at 1.5 DLTs

In addition to leading-edge fastener failures, a fracture was observed on the bottom skin overhang adjacent to the sleeve of the steel lug at the fixed-end (figure 86). Significant relative (rotational) displacements between the composite structure and the steel lug were observed during fatigue loading, thereby indicating internal damage to the structure. The test article was removed from the fixture and inspected for possible fracture on the steel tube or on the composite structure. Once the lug was removed from the ST004 fatigue article, several fractures and hole damages were noted, as shown in figure 86. Top and bottom flanges of the root rib were disbonded from the skin closer to the lug area. Further inspection revealed that the backside of the root rib was still attached to the skin and, therefore, no repairs were performed. Moreover,

the fastener holes located at the web to attach the main lug, skin, and surface fractures were noted, but they were not repaired. Furthermore, the leading-edge fastener-pullout failed sections were left unrepaired. A fastener hole adjacent to the sleeve was damaged during lug removal and repaired using Hysol® EA 9394™ paste adhesive and chopped fibers (figure 87).

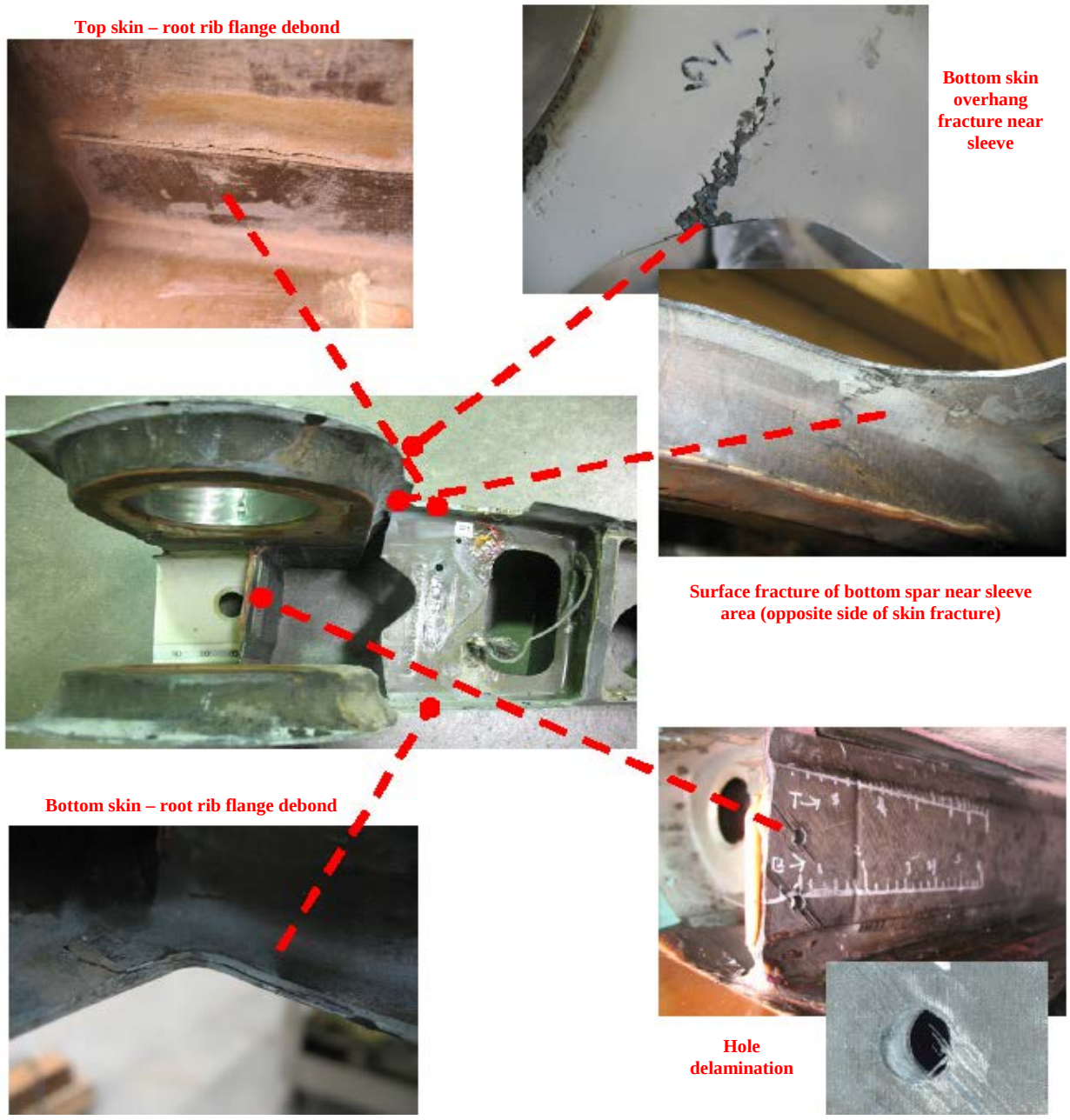

Figure 86. Damages noted on ST004 fatigue article after 1.5 DLTs

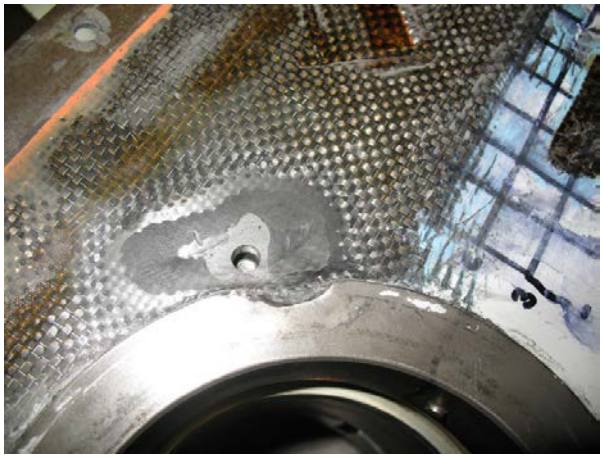

Figure 87. Hole repair after 1.5-DLT inspections

The lug area and the web closer to the lug were further inspected using ultrasound and a DTH, which found no evidence of failure or delaminations other than the damages shown in figure 86. Therefore, the test article was mounted back in the test fixture, and cyclic loading was continued until 2 DLTs. Positive and negative limit-load tests revealed no evidence of compliance change or significant strain anomalies.

An inspection of ST004 following 2 DLTs of cyclic loading noted a leading-edge fastener-pullout failure on the bottom skin that spread from FWS 64 to FWS 85 (figure 88). In this area, no damage to the composite structure was found. Furthermore, the bottom skin fracture near the sleeve grew approximately 5 more inches between 1.5 and 2 DLTs of cyclic loading.

To minimize the risk of damaging strain gages around the damage, DTH readings were taken only on the colored areas in figure 89. DTH inspections revealed that the initial damage grew along the red areas. Blue sections indicate minor stiffness degradation, possibly due to fracture or microcracks. Green sections indicate no growth. Figure 89 also indicates that the damage area continued to grow until 2 DLTs. Neither standard tap test nor ultrasonic inspections were able to detect these anomalies.

Figure 88. Leading-edge fastener-pullout failure (bottom surface) after 2 DLTs

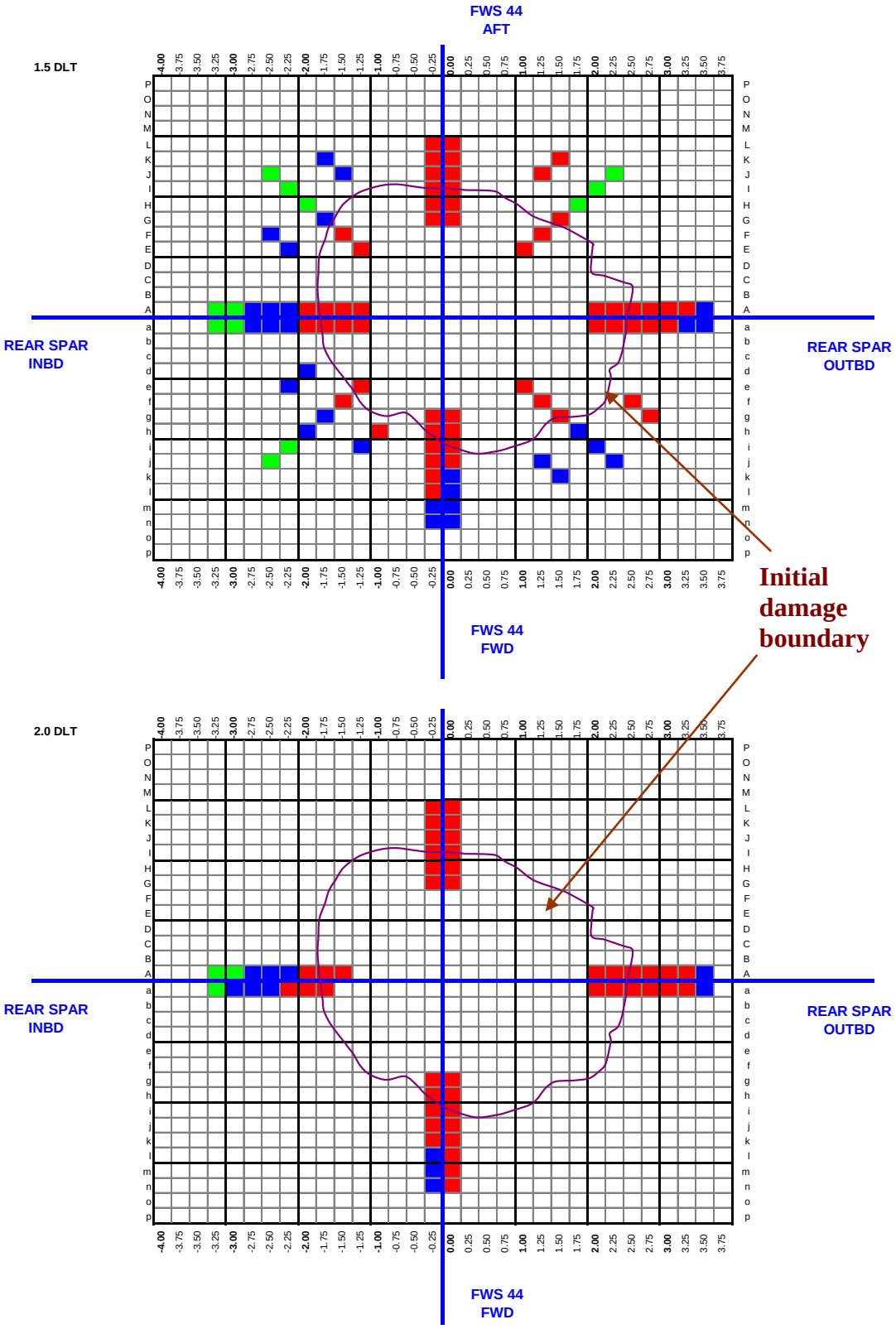

Figure 89. Damage propagation of ST004 DaDT article—DTH

5.5.2 The ST006—CAT3 Damage

Because the CAT3 damage on the primary load path of ST006 was expected to grow before reading 0.25 DLT (as shown in figure 27) and the fatigue loads were closer to the failure load of ST005 that was impacted with a similar damage, the inspection intervals were shortened and fatigue testing was conducted by closely monitoring the strain gages and conducting frequent NDIs and visual inspections. Although the strain anomalies were detected during B-G/B-M load blocks (see section 5.4.2.2) and creaking/popping sounds increased, neither visual nor ultrasonic inspections detected any changes to the damage boundary delineated prior to the test.

Inspections following block C indicated that the leading edge at the root separated from the bottom skin (figure 90). In addition, the squeezed-out adhesive at the attachment doubler located at the root end of the aft spar disbonded from the close-out rib. Strain anomalies around this region (gage R3) also confirmed a sudden strain drop after block C, thereby confirming a local failure/load redistribution. Furthermore, ultrasonic NDI results indicated possible damage progression along the FWS across the CAT3 damage (figure 91). Red and black markings indicate the damage boundary prior to fatiguing and after load block C, respectively. This confirms the explanation given in section 5.4.2.2 for strain anomalies around CAT3 damage.

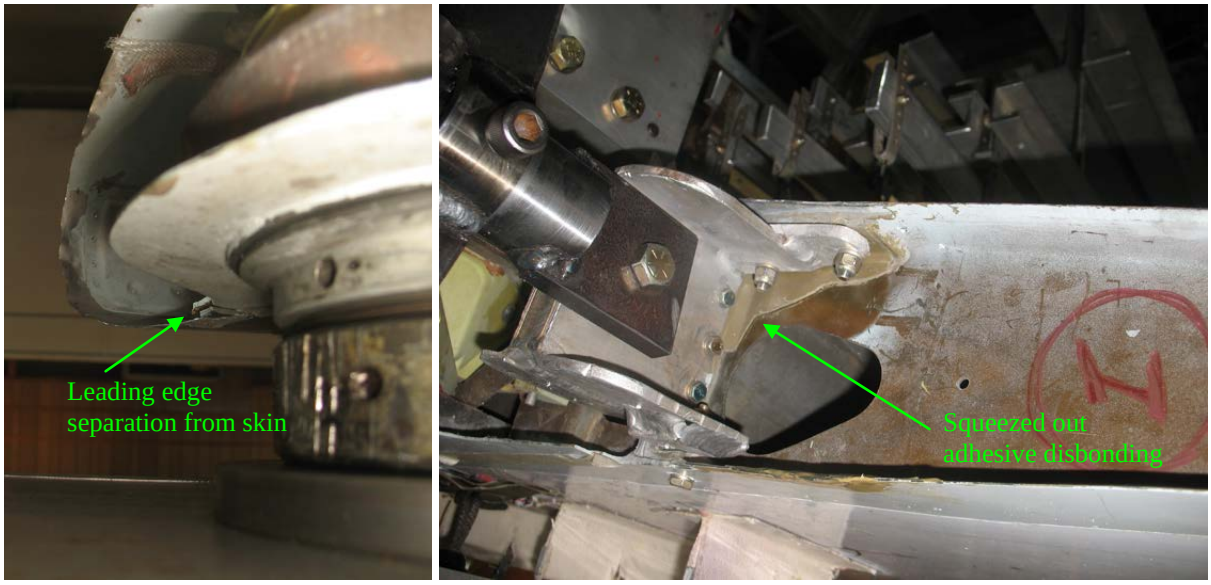

Figure 90. Visual inspection findings after load block C (40,016 cycles)

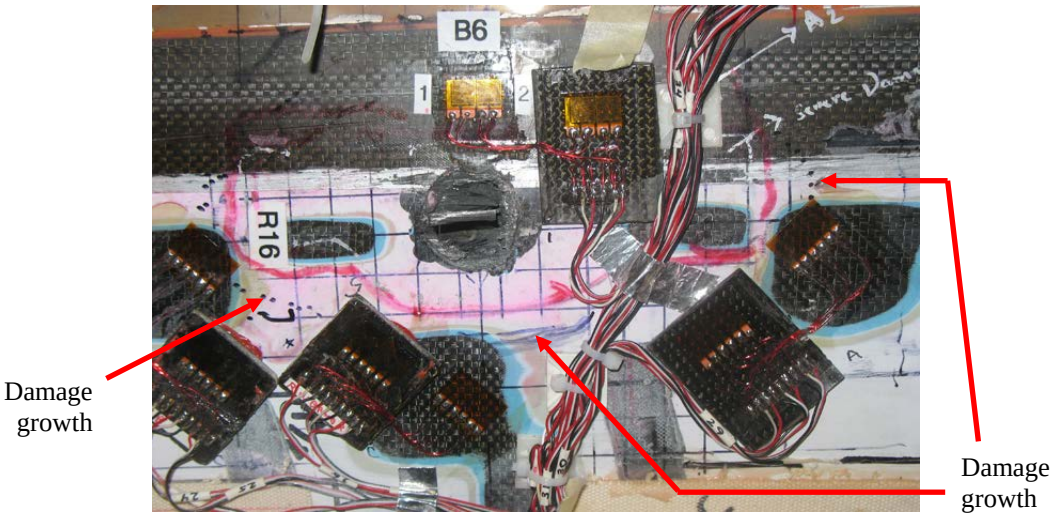

Figure 91. Ultrasonic NDI results after load block C (40,016 cycles)

No significant damage was detected until after load block D when the damage noted in figure 90 increased (as shown in figure 92). Furthermore, the leading edge indicated that local buckling between rivets on both the top and bottom sides ruptured the filler material that was applied closer to the root end between the periphery of the leading edge and skin.

Figure 92. Visual inspection findings after load block D (80,033 cycles)

5.6 POST-TEST FAILURE ANALYSIS

Once the static and residual strength tests were completed, detailed post-test inspections, along with video and strain gage data, were used to evaluate the failure mechanism of each Starship forward wing. In addition, a DTH was used to determine the fractured areas with respect to the untested forward wing.

5.6.1 Static Test Articles

Both static test articles, ST002 and ST003, indicated similar failure mechanisms and fracture surfaces (figure 93). Visual inspections and tap tests showed the following:

- Widespread upper-skin fracture, leading-edge permanent buckling (yielding), and skin debond/delaminations between FWS 51 and FWS 76
- Upper skin debond around rear spar toward root end

- Lower skin fracture along aft spar
- Multiple skin delaminations and fractures toward root end

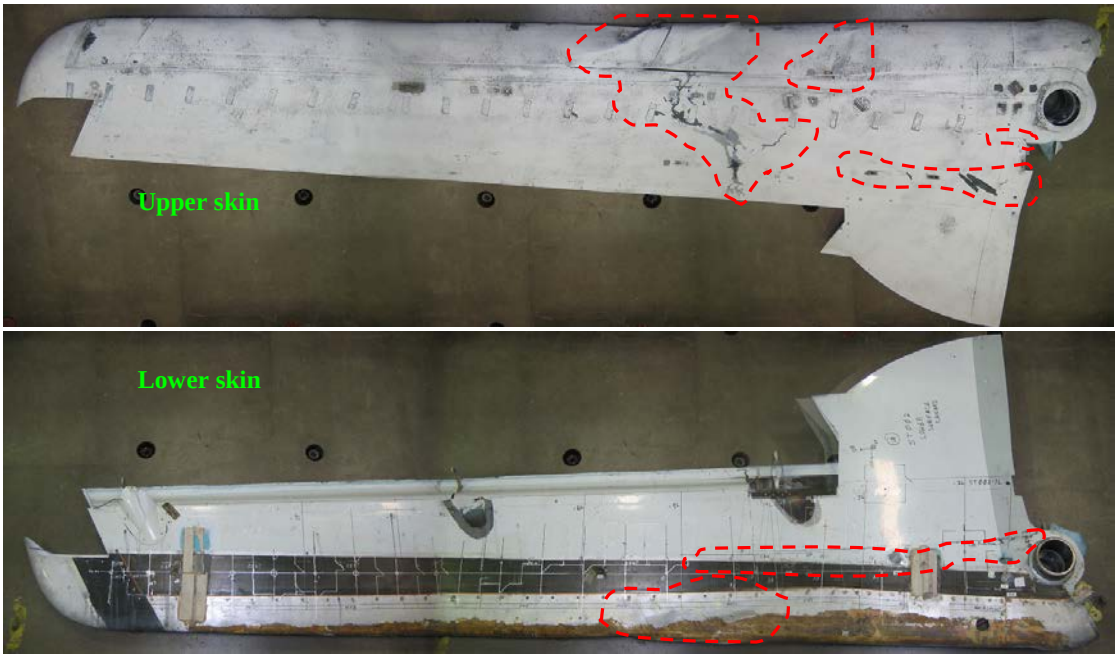

(a) The ST002

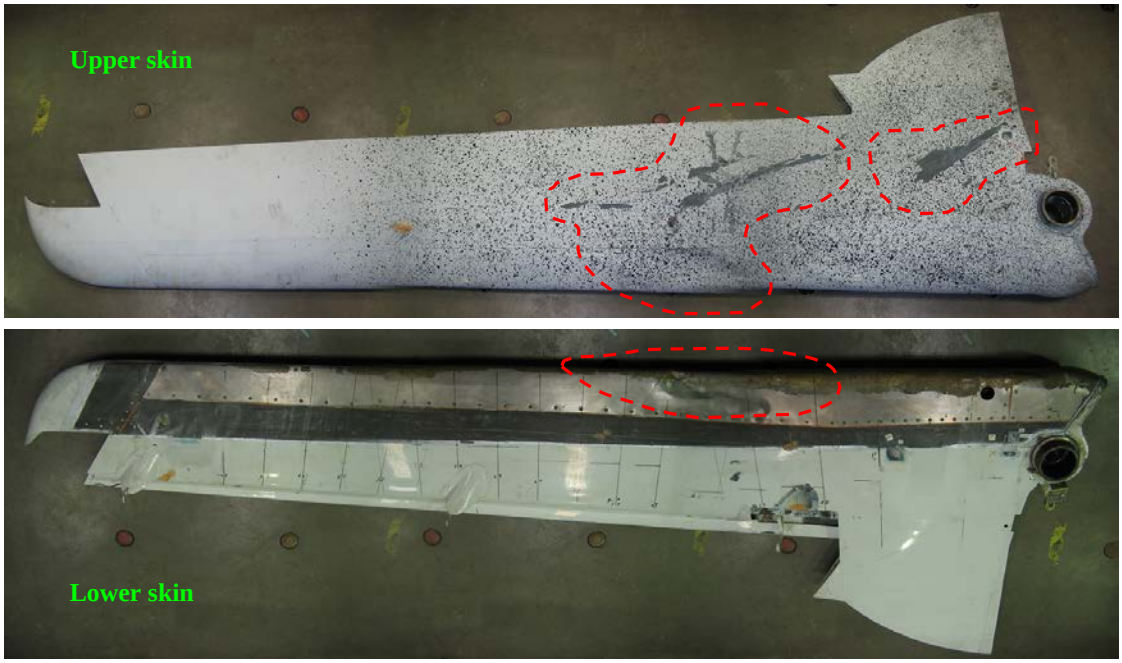

(b) The ST003

Figure 93. Post-test visual inspections

Once the leading edge was removed, severe damages to the web and front-spar flanges were noted, especially around the outboard closeout rib of the aluminum secondary spar (figure 94). This close-out rib and aluminum spar were also severely deformed because of high brazier loads due to wing-box bending [54]. Flexural stress on the front web because of bending resulted in 45° fractures (see figure 94). After sectioning the test article around these stations, it was determined that the top and bottom spar caps were intact with no fractures.

Figure 94. Post-test inspections of ST003 on removal of leading edge

Figure 95 shows primary damage locations delineated by DTH inspections of ST002 and ST003. A major fracture on the top skin indicated that the skin fracture initiated because of shear buckling (45° alignment). Results also indicated that top-skin delamination of the aft spar toward the root end may have been due to mode I or pullout loading that resulted from torsional buckling of the top skin. Based on DTH data, damage to the bottom skin was limited to the area directly under the major fracture on the top skin and closer to the root end of the aft spar.

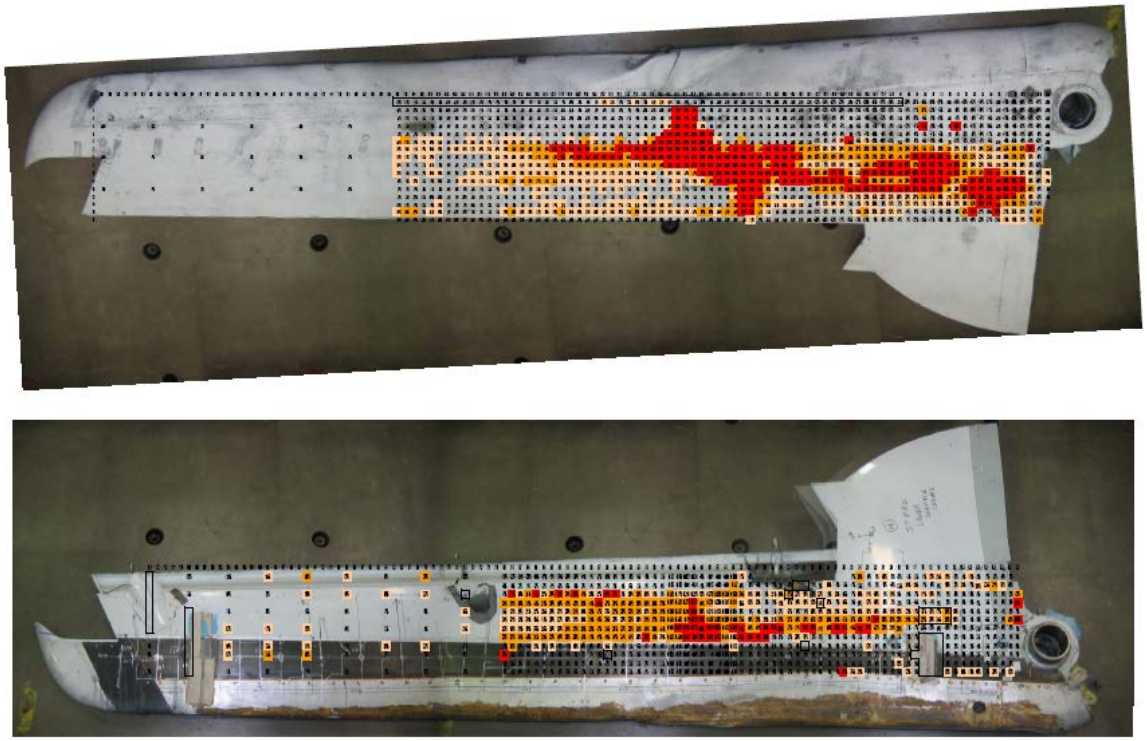

(a) The ST002

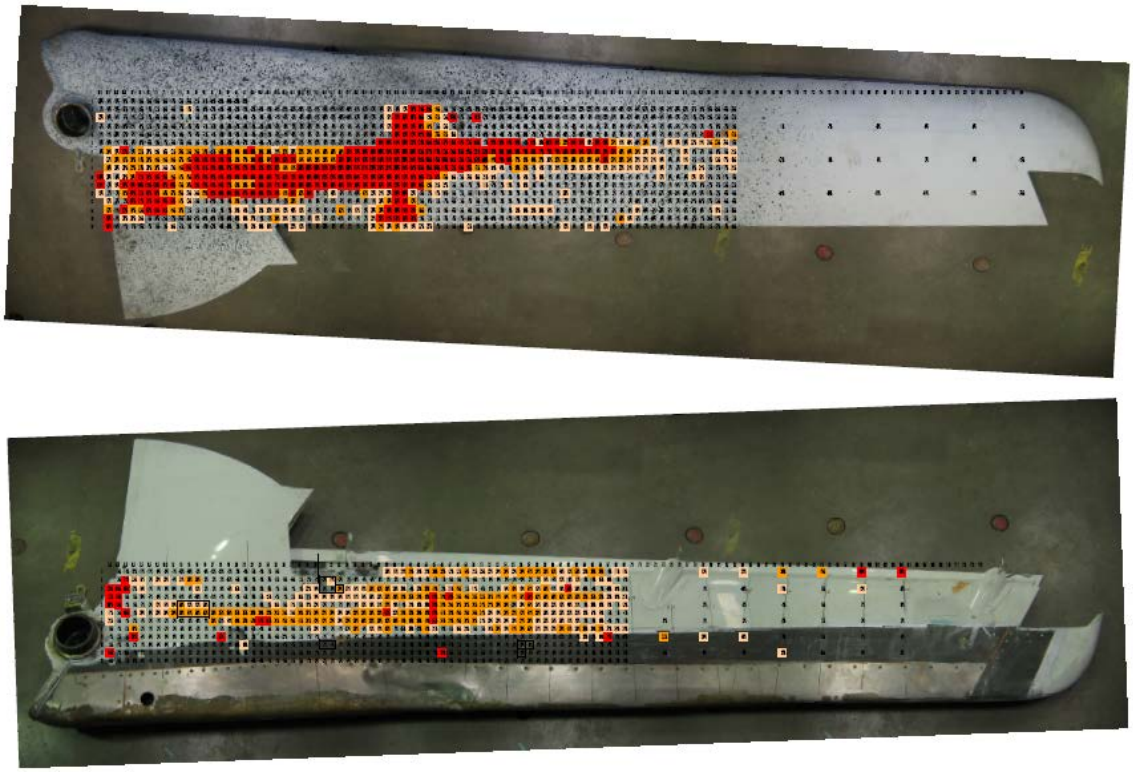

(b) The ST003

Figure 95. Post-test DTH results overlay

Strain gages of ST002 on the rear spar toward the root end (A4) indicated a sudden decrease in strain followed by an audible noise, indicating initial disbond/delamination at approximately 11,275 lbf (see figure 96). A video captured during testing also indicated significant skin buckling and twisting of the structure at approximately 14,000 lbf and notable aft skin disbonding at approximately 14,600 lbf. The strain anomalies indicated that the disbond started from the root and propagated outboard toward the failure. The first major failure, which was not related to the skin delamination, occurred just outside the elevator attachment hinge bracket at FWS 52.7 because of compressive loads on the top flange of the aft spar. Following that, the aft web continued to be crushed as the load increased. Consequently, the article started twisting as the aft lost its load-carrying capability. Immediately following this, the major fracture occurred as the load redistribution caused the front web to fail under increased brazier and torsional loads.

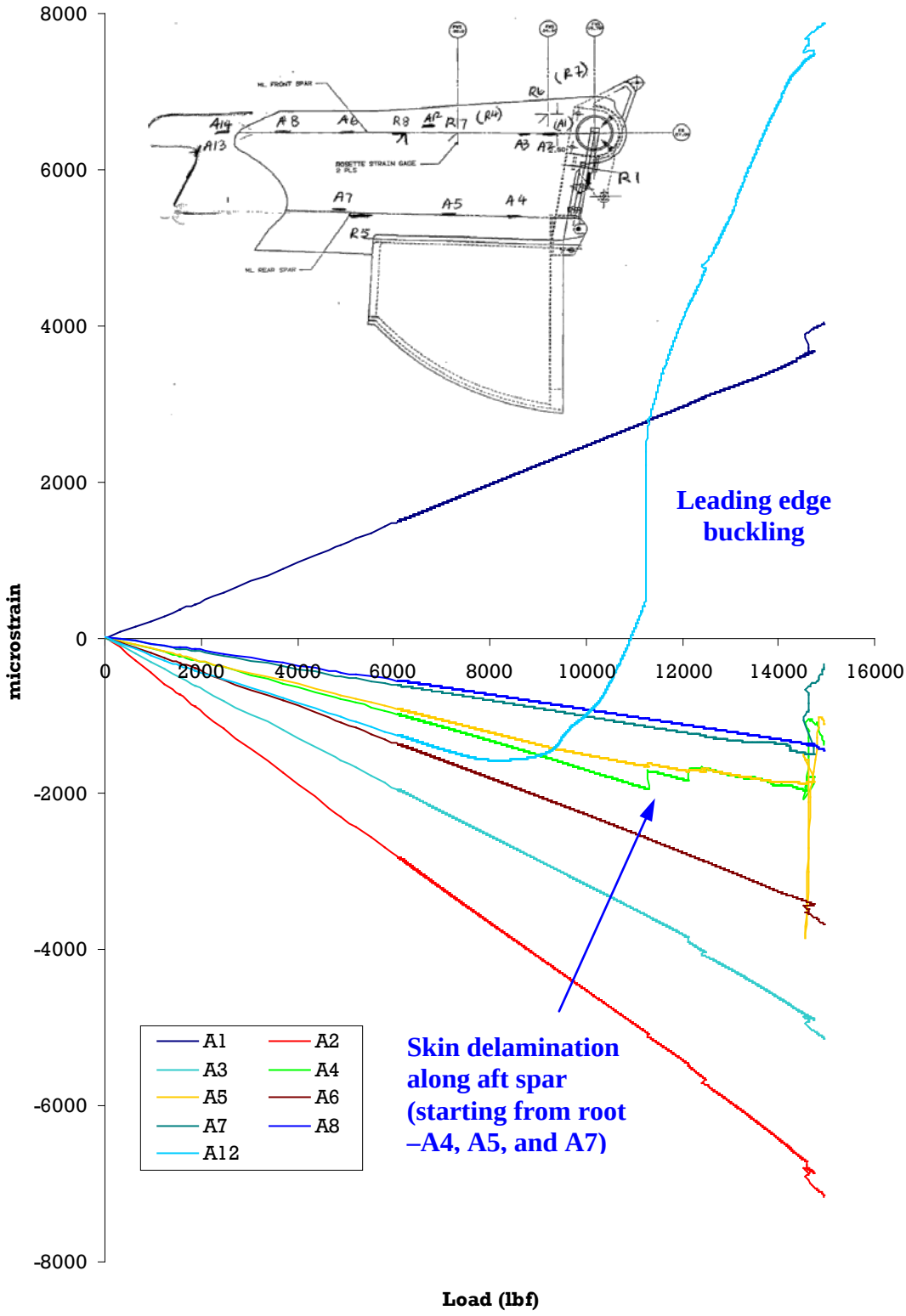

Figure 96. Failure mechanism determination using strain anomalies—ST002

5.6.2 The CAT2 Damage on Aft Spar—ST001(R) and ST004

The primary failure mode of ST001(R) and ST004 was the same as for ST002 and ST003 (i.e., aft web crush due to brazier loads causing rotation, which resulted in higher brazier loads and torsional loads on the front web followed by shear buckling). However, there were no major fractures that propagated across front and aft spars in either ST002 and ST003. Instead, a large diagonal delamination propagated instantaneously across CAT2 damage following a loud, cracking noise (figure 97). Based on the videos and strain data around the damage, this occurred at 13,330 lbf (167% of the NRLL) for ST001(R), and at 13,370 lbf (157% of the NRLL) for ST004 during residual strength after 2 DLTs.

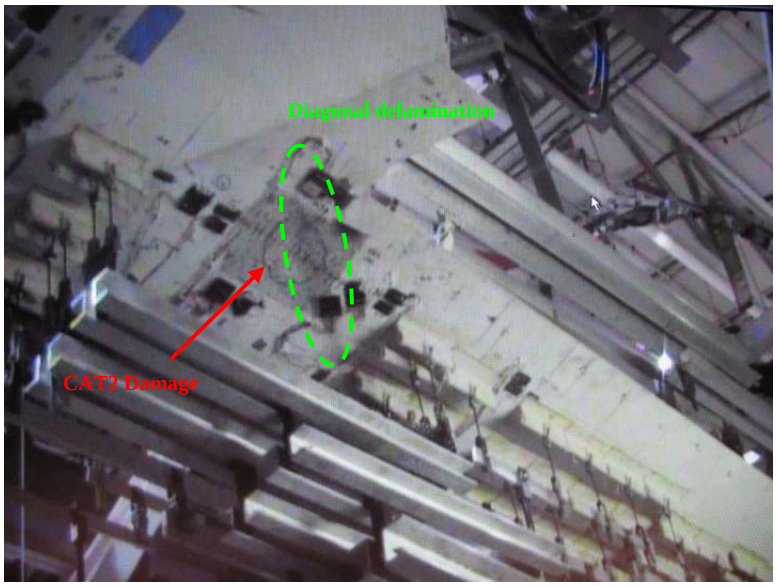

Figure 97. Diagonal delamination across CAT2 damage on aft spar after 160% of the NRLL

Visual inspections after residual strength tests revealed no indication of apparent fractures in addition to post-impact and post-DaDT damages for ST001(R) and ST004, respectively.

5.6.3 CAT3 Damage on Front Spar—ST005 and ST006

Both ST005 and ST006 test articles with CAT3 damages on the front spar failed (figures 98 and 99, respectively), which followed skin delamination at the trailing edge just outboard of the elevator attachment hinge. The video showed that, prior to failure, the skin underwent compression buckling rather than shear buckling mode, which had been observed during previous tests (sections 5.6.1 and 5.6.2). It also indicated that the primary failure was initiated at CAT3 damage. This was expected, because the CAT3 damage creates a significant stress concentration around the damage. Furthermore, damage to the front web below the CAT3 damage resulted in a significant reduction in flexural strength of the front spar. Once the top spar cap fractured across the damage instantaneously, the aft spar failed and a major crack formed across FWS 66.5. As shown in figure 98, damage was primarily across the region delineated by ultrasonic inspections, trailing-edge delamination, and leading-edge buckling around FWS 66.5.

Also, both front and aft webs and top flanges across this region indicated severe fracture and delamination due to compressive loads.

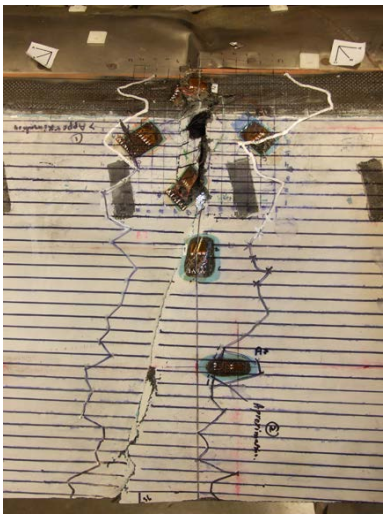

(a) Ultrasonic results

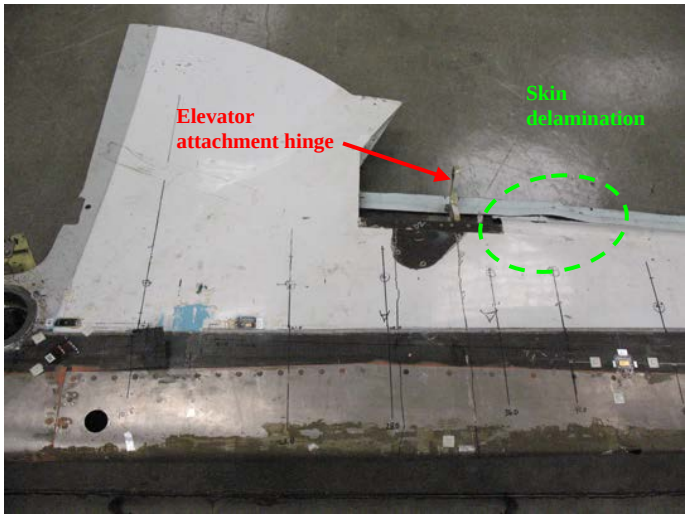

(b) Trailing edge skin delamination

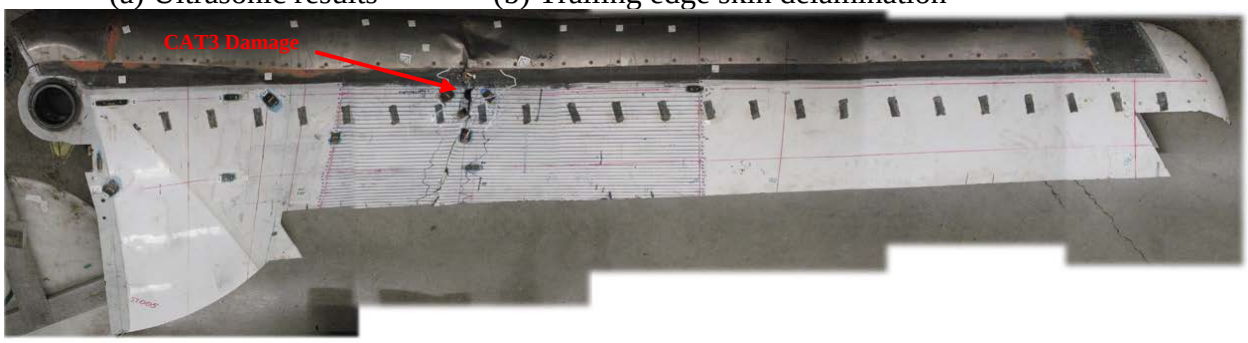

(c) Top view

(d) Bottom view

Figure 98. Ultrasonic and visual post-test inspections of ST005

Figure 99. Post-test visual inspections of ST006 DaDT test article after residual strength test

5.7 SUMMARY OF FULL-SCALE TEST VALIDATION

Table 11 includes a summary of shear loads for full-scale static and residual strength tests of Starship forward wings. Based on initial full-scale static testing, a CF of 1.4 was established to convert Beechcraft design loads to the NIAR research loads. The ST001(R) static test article with CAT2 damage on the top skin of the aft spar at FWS 45 indicated no growth until the NRLL. Detailed investigation of strain data, videos, and post-test inspections revealed that the compressive loads were responsible for the failure of the aft web, which was damaged during impact testing. Following the impact tests, and after NRUL, a long delamination formed diagonally across the CAT2 damage because of shear buckling and increased mode I stress. Subsequently, the rotation of the article increased the torsional loads, and redistributed loads increased the brazier loads on the front web, just outboard of the secondary aluminum spar (in front of front spar), causing that to fail as well.

Table 11. Summary of shear loads for full-scale tests

Damage Category	Test Article	Test Configuration	Final Fracture		Significant Damage Growth		Onset of Strain Anomalies	
			Static Strength (lbf)	Residual Strength (lbf)	Static Strength (lbf)	Residual Strength (lbf)	Static Strength (lbf)	Residual Strength (lbf)
CAT1	ST001	Static	–	–	–	–	11,092	–
	ST002		14,960	–	14,640	–	11,304	–
	ST003		16,123	–	–	–	10,231	–
CAT2	ST001(R)	Static	14,695	–	–	–	11,628	–
	ST004	Fatigue	–	16,982	–	14,631	–	13,230
CAT3	ST005	Static	5,768	–	–	–	5,121	–
	ST006	Fatigue	–	8,145	–	–	–	6,825

Cyclic testing of the DaDT test article with CAT2 damage for 2 DLTs with LEF = 1.072 indicated no significant damages to the composite structure, although there were several fastener pull-through failures in the leading edge. The LEF was based on the materials used for the construction of the forward wing and was considerably lower than that based on the combined life-load approach. Furthermore, in addition to the LEF, spectrum loads were multiplied by CF = 1.4, resulting in a cumulative LEF of 1.5. Standard tap testing revealed no growth, but DTH data and strain anomalies indicated minor damage growth after 1 DLT. The post-DaDT residual strength test of this article indicated nonlinear strain/displacement anomalies and an audible cracking noise at approximately 40% of the NRLL and final failure at approximately 157% of the NRLL. Therefore, the ST004 DaDT test article demonstrated ultimate load capability after a required test duration with an LEF based on the approach outline in section 5.1.4. Based on the scatter analysis of the VID element test results and the LLD hybrid approach (figure 18), it was found that the required test duration for an LEF of 1.072 corresponds to 1.35 DLTs.

To disrupt the primary load path by creating CAT3 damage, the front spar of ST005 was impacted. Catastrophic failure was observed at 68% of the NRLL (just above 95% BDLL), indicating that this damage was more severe than typical CAT3 damage. For comparison purposes, the ST006 DaDT test article was impacted with similar impact parameters at the same location and was cyclic-tested. Based on the residual strength after impact, the CF = 1.4 resulted in spectrum loads that would be higher than the residual strength of this article. Although the scheduled inspections would occur prior to these high loads, for the fatigue spectrum of the ST006 DaDT article, the CF was not applied to ensure that the maximum fatigue load was below the post-impact residual strength. The inspection intervals were designed with a target (minimum) reliability of 90% (i.e., the inspection intervals were allotted prior to the POF of a structure with CAT3 damage reaching 10%). Strain anomalies and periodic inspections confirmed the CFR predictions for damage growth, in terms of the POF. Quasi-static testing conducted after 0.5 DLT of ST006 indicated that the post-DaDT residual strength of the article

was approximately 95.5% of the NRLL. This was more than 40% higher failure load than that for the ST005 static test article with CAT3 damage. This was probably due to the sensitivity of the impact response to a minor variation to the impact parameters and impact location. As shown in the detectability versus the impact energy chart in figure 31, a small increase in the impact energy level can significantly affect the limit load capability of the structure. Furthermore, a minor variation to the impact location can significantly alter the structural response due to changes in stiffness characteristics and boundary conditions. This shows the difficulties and risks associated with the infliction of CAT3 damage on test articles and illustrates the need for detailed analysis prior to damage introduction.

6. CONCLUSION AND RECOMMENDATIONS

The primary objective of this research was to develop an approach to synthesizing the life factor, LEF, and damage in composite structures to determine the fatigue life of a damage-tolerant aircraft. The methodology proposed in this research extends the current damage tolerance test approach and provides information necessary for defining inspection intervals for composite structures by studying the effects of extremely improbable, high-energy impact damage.

The research was completed in three major phases. First, the effects of generating LEFs based on the most critical design details of a composite structure in coupon level was interrogated. The approach for obtaining the MSSP and the MLSP to calculate the LEFs for different test durations was investigated in detail using static and fatigue test data, respectively, for several different composite material systems. Second, the process of scaling different impact threats in a full-scale structure down to a representative element level was discussed. It was shown that the scatter in notched (damaged) composite test data was significantly lower than that of unnotched composite. Such improvements in fatigue life-shape parameter can significantly reduce the life factor. However, the life factor becomes insensitive to small changes in the life-shape parameter beyond a value of 4, which is considered to be the life-shape parameter for metal. The composite modal life-shape parameter of 1.25, which was used for the combined load-life approach, lies within the highly sensitive region of life factor versus shape parameter curve; therefore, even a small improvement resulted in a dramatic reduction of life factor, which reflects the required number of test durations to achieve a certain level of reliability in the design life. The main goal in the first phase was to perform the scatter analysis to support the durability testing of a damage-tolerant, full-scale test article with large damages. The analysis in this step forms the supporting data for the load-life-damage (LLD) hybrid approach that can be applied to a full-scale durability test article during the damage tolerance phase. Finally, several full-scale tests were conducted by combining the LEFs developed in the first phase and the scatter analysis conducted on damage tolerance element tests in the second phase to validate the LLD hybrid approach for determining the fatigue life.

6.1 THE LLD HYBRID APPROACH FOR FULL-SCALE SUBSTANTIATION

Typically, the load spectrum of a full-scale test article is truncated by eliminating the segments with stress levels below the endurance limit. To further reduce the required test duration to achieve the desired level of reliability on the design lifetime, life factor and LEFs are combined and applied to the truncated load spectrum. In addition, for the RTA test, environmental factors

should be applied to the truncated spectrum to account for the environmental effects on composite materials. When applying these factors, the stress ratio of the original spectrum and the expected failure mode must be preserved, and the final loads must be below the static strength to avoid unintentional failures. When damage is introduced to the structure, care must be taken to prevent unintentional failures. If the damage region becomes the critical location of the structure (i.e., without significant load redistribution that will drive a different failure mode), and imminent damage instigation at this location results in the structural catastrophic failure or a load redistribution that can be predicted by analysis, the scatter analysis can be conducted on elements that represent the critical location with an equivalent damage (e.g., LLD) approach. Specimen design and the loading mode for such an exercise has a direct impact on the fatigue test results and the data scatter; and rigorous NDI techniques may be required to monitor flaw growth (i.e., finite-width CAI specimens that are fatigue-tested in load control test mode will represent damage on a critical load path with no load redistribution due to damage growth). The new life shape parameter can be used to calculate the life factor corresponding to the structure, given that the above-mentioned conditions are met. Because of the notch sensitivity of composites, their life scatter is reduced as the impact energy level is increased. Therefore, the LLD approach, in most cases, will result in a lower life factor and LEF requirements compared to the values obtained from the original MSSP and MLSP of the structure. In the event that a repair of the impacted damage is deemed necessary to prevent premature failure or that damage propagation resulted in a load redistribution predicted by analysis, the LEF requirements must be adjusted to reflect the fact that the structure has been restored to its undamaged state.

6.1.1 Load-Life Shift

The LLD approach introduces the use of multiple LEFs for a particular composite structure, based on the damage category (i.e., the use of different LEF curves representing damage severity). The load-life shift calculates the remaining percentage of the DLT to be substantiated after completing a certain number of repeated lives with respect to the required repeated lives for the corresponding LEF. Once the test article is inflicted with damage, the remaining test duration is calculated by multiplying the required repeated lives that correspond to the new LEF and the above-mentioned percentage of design life. The example discussed in this paper showed that this approach not only reduced the LEF requirements for a test article with a large area of damage, but also reduced the remaining test duration as a result of the reduction in the data scatter of notched (damaged) composite element test data.

6.1.2 Determination of Inspection Intervals Using the CFR Model

To prevent the unintentional failure of a damaged article during DaDT testing, especially when investigating extremely improbable high-energy impact threats that reduce the residual strength of a composite structure to its limit load, rigorous inspection intervals are required. The POF of the damaged structure for the enhanced spectrum loads can be evaluated using the CFR model proposed in this research. The information obtained from this model can also be used to allot economical and reliable inspection intervals to detect the extent of damage prior to imminent failure or unstable propagation that threaten the structural integrity. This approach can also be extended to determine the inspection interval during service based on target reliability and CDT.

6.2 FULL-SCALE TEST SUBSTANTIATION

The first three full-scale static tests were conducted to determine the ultimate strength of the Beechcraft Starship forward wing structure. It was determined to be 1.4 times the DUL; therefore, the load spectrum of the ST004 durability tests was multiplied by a factor of 1.4 prior to applying the LEF. The static residual strength test of the test article, ST001(R), with CAT2 damage on the aft spar, indicated that the damage grew just after the newly defined ultimate load. There was significant whiffletree shifting, and the test was aborted.

6.2.1 Validation of LLD Hybrid Approach

The LEFs developed based on the critical design details of a Starship forward wing were significantly lower than the LEFs developed for F/A-18 certification (NAVY approach). The scatter analysis of damage tolerance element tests showed that the initial LEF requirements can be further reduced by introducing LID to the test articles. Full-scale test validation of the LLD approach that was carried out using the Starship forward wing DaDT test article, with CAT2 damage on the aft spar, demonstrated no significant fatigue damage to the composite structure or no significant damage propagation that could be detected by standard NDI techniques. The strain anomalies indicated minor damage propagation, which was later arrested, between 1.5 and 2 DLTs. Based on the scatter analysis of visual impact damage element test results and the LLD hybrid approach, it was found that the applied LEF of 1.072 corresponds to a required test duration of 1.35 DLTs. However, the DaDT test was conducted for 2 DLTs, and then the post-DaDT residual strength was evaluated. The test article demonstrated ultimate strength capacity during a post-DaDT residual strength test. These data showed that the damage growth occurred after satisfying the repeated load requirements according to the LLD hybrid approach, and the minor damage growth on the secondary load path (aft spar) did not alter the residual strength capacity of the structure. In addition, the failure mode of the post-DaDT test was similar to the post-impact static residual strength test; therefore, the minor damage growth observed through strain anomalies did not alter the overall failure mechanism.

6.2.2 Validation of CFR Model

The forward wing DaDT test article with CAT3 damage on the front spar, which is the primary load path, demonstrated the capability of the CFR model to predict the damage growth in terms of reliability and the capability of the model to determine the inspection levels. Although it is not a one-to-one correlation for the damage propagation or its size, the CFR model highlighted load segments that resulted in the gradual progression of local damage, such as possible matrix cracks, and the global impact of high loads that resulted in evident damage growth. Although the standard NDI techniques were unable to detect the minor damage growth during certain spectrum loads, the CFR model highlighted the probability of damage growth for those loads and the strain gage data confirmed the growth.

Real-time data monitoring is crucial to identifying damage propagation during the full-scale DaDT test, especially because the number of LID scenarios is expected to increase. The monitoring provided instant feedback of the structural response for applied loads and mitigated the risk of unexpected test failures or anomalies that would have otherwise gone undetected. The

strategic allocation and placement of strain gages for these articles is crucial to achieving this goal. The strain data provide information similar to a built-in health monitoring system and provide details in real time to assess the state of the damage (i.e., crack propagation) and any global effects on the structure due to possible damage growth.

A realistic target reliability must be used for determination of inspection intervals accounting the safety and the cost considerations. Although CAT3 damage is recommended for determining the inspection intervals, more realistic damage threat levels can be used considering the probability of occurrence so that more practical or economical inspection levels can be determined. To further extend the CFR model for determination of inspection intervals for a fleet, the fleet size and the probability of detectability may have to be considered in addition to the above-mentioned parameters.

7. REFERENCES

1. Kan, H.P., Cordero, R., and Whitehead, R.S., "Advanced Certification Methodology for Composite Structures," FAA report DOT/FAA/AR-96/111, April 1997.

2. Whitehead, R.S., Kan, H.P., Cordero, R., and Saether, E.S., "Certification Testing Methodology for Composite Structures," Report No. NADC-87042-60, Volumes I and II, October 1986.

3. Horton, R E. and Whitehead, R.S., "Damage Tolerance of Composites," Report No. AFWAL-TR-87-3030, Volumes I, II, and III, July 1988.

4. Rapoff, A.J., Dill, H.D., Sanger, K.B., and Kautz, E.F., "Certification of Damage Tolerant Composite Structure," *Proceedings of the Eighth DoD/NASA/FAA Conference on Fibrous Composites in Structural Design*, NASA CP-3087, Part 2, November 1989, pp. 499–514.

5. Curtis, P.T., Lawrie, D., and Young, J.B., "The Effects of Impact on Pre-Fatigued Fiber Composites," *Structural Impact and Crashworthiness*, J. Morton, ed., Elsevier, London, 1984, pp. 494–509.

6. Sanger, K.B., "Certification Testing Methodology for Composite Structures," Report No. NADC-86132-60, January 1986.

7. Kan, H.P. and Whitehead, R.S., "Damage Tolerance Certification Methodology for Composite Structures," *Proceedings of Eighth DoD/NASA/FAA Conference on Fibrous Composites in Structural Design*, NASA CP-3087, Part 2, November 1989, pp. 479–498.

8. Deo, R., Starnes, Jr., J.H., and Holzwarth, R., "Low-Cost Composite Materials and Structures for Aircraft Applications," *NATO Applied Vehicle Technology Panel (AVT) Specialists' Meeting*, RTO-MP-069(II), Leon, Norway, May 2001.

9. Shah, C.H., Kan, H.P., and Mahler, M., "Certification Methodology for Stiffener Termination," FAA report DOT/FAA/AR-95/10, April 1996.

10. Kan, H.P. and Dyer, T.A., "Structural Integrity Evaluation of the Lear Fan 2100 Aircraft," FAA report DOT/FAA/AR-95/13, May 1996.

11. McCarty, J.E., Johnson, R.W., and Wilson, D.R., "737 Graphite-Epoxy Horizontal Stabalizer Certification," *Proceedings of the 23rd AIAA/ASME/ASCE/AHS Structures, Structural Dynamics and Materials Conference*, May 1982, pp. 307–322.

12. Gogkol, O., "A310-300 CRFP Fin—Damage Tolerance Demonstration," *Proceedings of the 7th International Conference of SAMPE*, European Chapter, Munich, June 1986.

13. Brandecker, B. and Hilgert, R., "A320 Full Scale Structural Testing for Fatigue and Damage Tolerance Certification of Metallic and Composite Structure," *Proceedings of the 16th Congress of the International Council of the Aeronautical Sciences*, ICAS-88-5.8.1, Jerusalem, Israel, 1988.

14. Fawcett, A., Trostle, J., and Ward, S., "777 Empennage Certification Approach," *Proceedings of the 11th International Conference on Composite Materials*, Australia, July 1997.

15. Vosteen, L.F. and Hadcock, R.N., "Composite Chronicles: A Study of the Lessons Learned in the Development, Production, and Service of Composite Structures," NASA CR-4620, November 1994.

16. Wong, R. and Abbott, R., "Durability and Damage Tolerance of Graphite/Epoxy Honeycomb Structures," *Proceedings of the 34th International Symposium*, Anaheim, California, 1990.

17. Kan, H.P. and Kane, D.M., "Probabilistic Certification of Integrally Bonded Composite Structures—an Assessment," *Proceedings of the 43rd AIAA/ASME/ASCE/AHS/ASC Structures*, Structural Dynamics and Materials, Denver, Colorado, April 2002.

18. Sumich, M. and Kedward, K.T., "Development of a Fatigue-Life Methodology for Composite Structures Subjected to Out-of-Plane Load Components," NASA TM-102885, February 1991.

19. Halpin, J.C., Jerina, K.L., and Johnson, T.A., "Characterization of Composites for the Purpose of Reliability Evaluation," *Analysis of Test Methods for High Modulus Fibers and Composites*, ASTM STP 521, American Society for Testing Materials, 1973, pp. 5–64.

20. Sendeckyj, G.P., "Fitting Models to Composite Materials Fatigue Data," *Test methods and Design Allowables for Fibrous Composites*, ASTM STP 734, C. C. Chamis, ed., American Society for Testing and Materials, 1981, pp. 245–260.

21. Sendeckyj, G.P., "Life Prediction for Resin Matrix Composite Materials," *Fatigue of Composite Materials*, K. L. Reifsnider, ed., Elsevier, Amsterdam, 1990.

22. O'Brien, T.K. and Reifsnider, K.L., "Fatigue Damage Evaluation Through Stiffness Measurements in Boron-Epoxy Laminates," *Journal of Composite Materials*, No. 15, 1981, pp. 55–70.

23. Hahn, H.T. and Kim, R.Y., "Fatigue Behavior of Composite Laminates," *Journal of Composite Materials*, Vol. 10, No. 2, 1976, pp. 156–180.

24. Hwang, W. and Han, K.S., "Cumulative Damage Model and Multi-Stress Fatigue Life Prediction," *Journal of Composite Materials*, Vol. 20, No. 2, 1986, pp. 125–153.

25. Hwang, W. and Han, K.S., "Fatigue of Composites—Fatigue Modulus Concept and Life Prediction," *Journal of Composite Materials*, Vol. 20, No. 2, 1986, pp. 154–165.

26. Mahfuz, H., Zaman, K., Haque, A., Foy, C., Mohamed, H., and Jeelani, S., "Fatigue Life Prediction of Thick-Section S2-Glass/Vinyl-Ester Composites Under Flexural Loading," *Journal of Engineering Materials and Technology*, Vol. 122, No. 4, October, 2000, pp. 402–408.

27. Halpin, J.C., Jerina, K.L., and Johnson, T.A., "Characterization of Composites for the Purpose of Reliability Evaluation," AFML-TR-77-289, WPAFB, Ohio, 1972.

28. Jeans, L.L., Grimes, G.C., and Kan, H.P., "Fatigue Spectrum Sensitivity Study for Advanced Composite Materials," U.S. Air Force Flight Dynamic Laboratory, Technical Report AFWAL-TR-80-3130, Volumes I, II, and III, 1980.

29. Rosenfeld, M.S. and Huang, S.L., "Fatigue Characteristics of Graphite/Epoxy Laminates Under Compression Loading," *Journal of Aircraft*, Vol. 15, No. 5, 1978, pp. 264–268.

30. Agarwal, B.D. and James, W.D., "Prediction of Low-Cycle Fatigue Behavior of GFRP: An Experimental Approach," *Journal of Materials Science*, Vol. 10, No. 2, 1975, pp. 193–199.

31. Yang, J.N. and Du, S., "An Exploratory Study Into the Fatigue of Composites Under Spectrum Loading," *Journal of Composite Materials*, Vol. 17, No. 6, 1983, pp. 511–526.

32. Kassapoglou, C., "Fatigue Life Prediction of Composite Structures Under Constant Amplitude Loading," *Journal of Composite Materials*, Vol. 41, No. 22, 2007.

33. Dost, E.F., Avery, W.B., Ilcewicz, L.B., Grande, D.H., and Coxon, B.R., "Impact Damage Resistance of Composite Fuselage Structure, Part 1," *Proceedings of the Ninth DoD/NASA/FAA Conference on Fibrous Composites in Structural Design*, Vol. 2, Lake Tahoe, NV, November 1991, pp. 1037–1069.

34. Dost, E.F., Ilcewicz, L.B., Avery, W.B., and Coxon, B.R., "Effects of Stacking Sequence on Impact Damage Resistance and Residual Strength for Quasi-Isotropic Laminates," *Composite Materials: Fatigue & Fracture (Third Volume), ASTM STP 1110*, T. K. O'Brien, ed., American Society for Testing Materials, Philadelphia, Pennsylvania 1991, pp. 476–500.

35. Sharma, A.V., "Low-Velocity Impact Tests on Fibrous Composite Sandwich Structures," *Proceedings of the Symposium on Test Methods and Design Allowables for Fibrous Composites,* American Society for Testing and Materials, Philadelphia, Pennsylvania, 1981, pp. 54–70.

36. Tomblin, J., Lacy, T., Smith, B., Hooper, S., Vizzini, A., and Lee, S., "Review of Damage Tolerance for Composite Sandwich Airframe Structures," FAA report DOT/FAA/AR-99/49, August 1999.

37. Tomblin, J., Raju, K.S., Liew, J., and Smith, B., "Impact Damage Characterization and Damage Tolerance of Composite Sandwich Airframe Structures," FAA report DOT/FAA/AR-00/44, January 2001.

38. Tomblin, J., Raju, K.S., and Arosteguy, G., "Damage Resistance and Tolerance of Composite Sandwich Panels—Scaling Effects," FAA report DOT/FAA/AR-03/75, February 2004.

39. Raju, K.S., "The Static Indentation Behavior of Composite Sandwich Panels With Thin Quasi-Isotropic Skins," Ph.D. Dissertation, Department of Aerospace Engineering, Wichita State University, December, 2001.

40. Tomblin, J. and Seneviratne, W., "Determining the Fatigue Life of Composite Aircraft Structures Using Life and Load-Enhancement Factors," FAA report DOT/FAA/AR-10/6, June 2011.

41. ARAMIS, v. 5.3.0 User Manual, GOM mbH, Braunschweig, Germany, 2004.

42. Tomblin, J.S., Seneviratne, W.P., and Borgman, M.D., "Electronic Speckle Pattern Interferometry for Investigating Defect Propagation of Honeycomb Sandwich Specimens," *SAMPE Technical Conference,* Baltimore, Maryland, November 2001.

43. Halpin, J.C., Kopf, J.R., and Goldberg, W., "Time Dependent Static Strength and Reliability for Composites," *Journal of Composite Materials,* Vol. 4, 1970, pp. 462–474.

44. Seneviratne, W. and Tomblin, J., "Scatter Analysis of Composites and Adhesive Joints for Substantiation of Modern Aircraft Structures," *FAA Joint Advanced Materials and Structures (JAMS) 2009 Technical Review Meeting,* July 2009.

45. Shyprykevich, P., Tomblin, J., Ilcewicz, L., Vizzini, A., Lacy, T., and Hwang, Y., "Guidelines for Analysis, Testing, and Nondestructive Inspection of Impact Damaged Composite Sandwich Structures," FAA report DOT/FAA/AR-02/121, March 2003.

46. AC 20-107B, FAA, "Composite Aircraft Structure," September 2009.

47. Tomblin, J.S. and Seneviratne, W.P., "Research on Structural Test and Analysis Protocol: Progress & Plan," *Commercial Aircraft Composite Repair Committee (CACRC) Meeting and Workshop for Composite Damage Tolerance & Maintenance,* Amsterdam, Netherlands, May 2007.

48. Seneviratne, W.P. and Tomblin, J.S., "Determination of Retirement Life Based on Service History and Load-Life Combined Approach," *Aircraft Airworthiness & Sustainment Conference*, Austin, Texas, May 2010.

49. Whittaker, I.C. and Besuner, P.M., "A Reliability Analysis Approach to Fatigue Life Variability of Aircraft Structures," AFML-TR-69-65, April 1969.

50. Abrate, S., *Impact on Composite Structures*, Cambridge University Press, United Kingdom, 1998.

51. Tomblin, J.S., Seneviratne, W.P., and Pillai, G.R., "Effects of Disbonds, Lightning Strikes, and Low-Velocity Impact Damages on Adhesively Bonded Composite Joints," FAA report DOT/FAA/AR-09/4, December 2009.

52. Stover, P., and Wong, R., "Forward Wing Damage Tolerance Test (FT-556) Model 2000," Report No. 122E349S, Hawker Beechcraft Corporation, Wichita, Kansas, January 1986.

53. "Fatigue Evaluation of Wing and Associated Structure on Small Airplanes," AFS-120-73-2, May 1973.

54. Krog, L., Tucker, A., Kemp, A., and Boyd, R., "Topology Optimization of Aircraft Wing Box Rib," *Proceedings of the 10th AIAA/ISSMO Multidisciplinary Analysis and Optimization Conference*, AIAA-2004-4481, Albany, New York, August 2004.

APPENDIX A—SCATTER ANALYSIS FOR CALCULATING LIFE AND LOAD-ENHANCEMENT FACTORS

Figure A-1 shows the procedure for analyzing S-N data using individual Weibull, Joint Weibull, and Sendeckyj analyses for generating the fatigue-life shape parameter for a particular test configuration ($\hat{\alpha}_{IW}$, $\hat{\alpha}_{JW}$, and $\hat{\alpha}_{Sendeckyj}$, respectively). As shown in this figure, the static data, if applicable, are analyzed using individual Weibull for generating the static-strength shape parameter ($\hat{\alpha}_{SS}$) for the same test configuration.

The fatigue-life shape parameter ($\hat{\alpha}_{FL}$) for each design detail or test configuration can be obtained using one of the three methods ($\hat{\alpha}_{IW}$, $\hat{\alpha}_{JW}$, or $\hat{\alpha}_{Sendeckyj}$) shown in figure A-1. The details for calculating life factor, load factor, and load-enhancement factors (LEF) are included in section 2.8 of the main report. The procedure for generating the modal static-strength (α_R) and fatigue-life (α_L) shape parameters for calculating the life factor and LEFs for a particular structure is shown in figure A-2. This process requires analysis of static/residual strength data and fatigue (S-N) data for multiple test configurations that represent critical design details of the structure, as shown in figure A-1.

Tables A-1 and A-2 contain the A- and B-basis LEF requirements, respectively, using α_R =17.5 to 32.5 and α_L =1.25 to 2.50 in equation 2 (a).

The fatigue scatter analysis is not limited to the three methods highlighted in this section, and the combinations of different techniques can also be used for generating the modal fatigue-life shape parameter (α_L) for the structure, as shown in figure A-2. It should be noted that the shape parameter using only one fatigue scatter analysis method per S-N curve is required. However, fatigue scatter analysis using different techniques may be useful for determining the most conservative approach for generating LEFs.

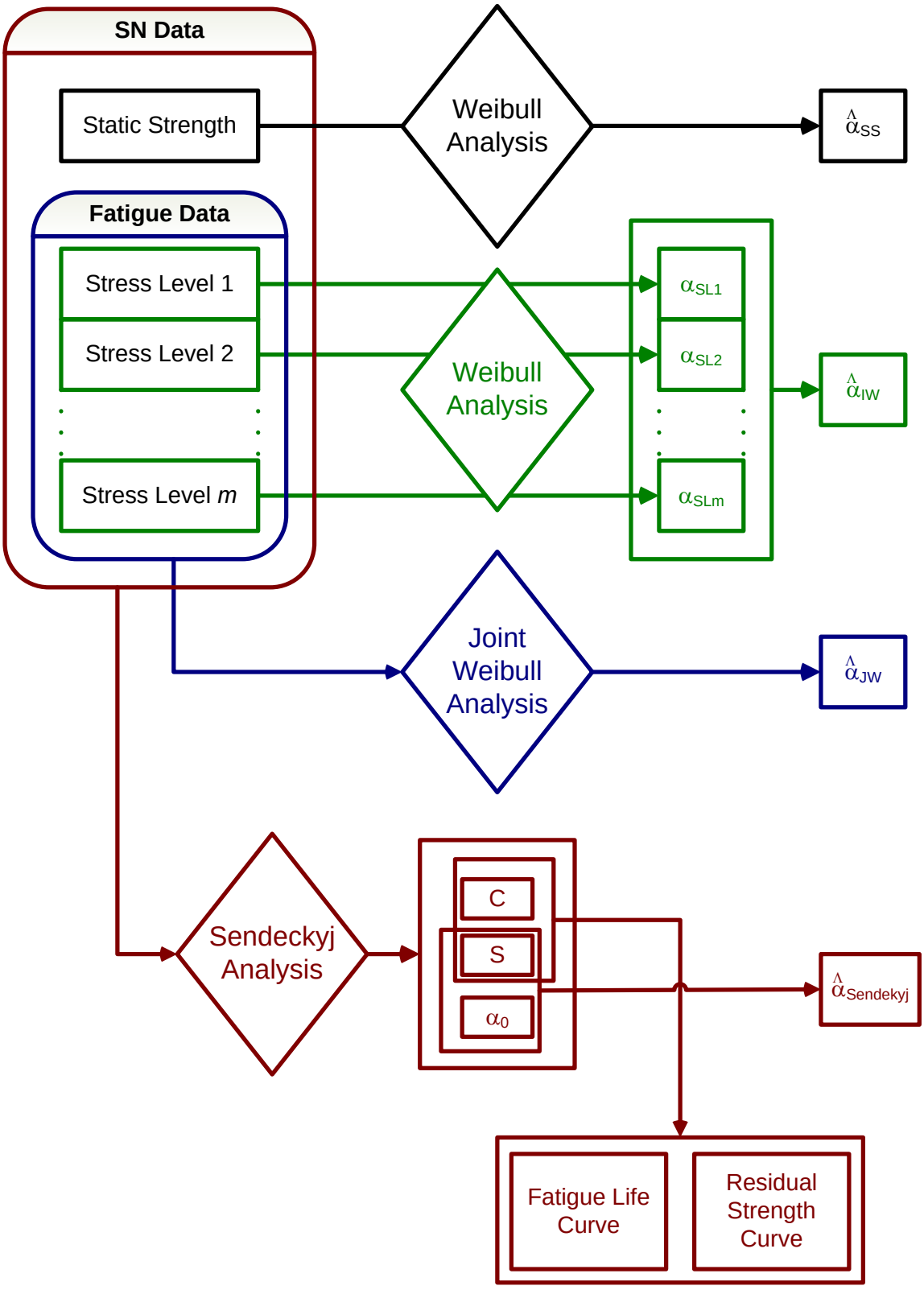

Figure A-1. Process for obtaining the fatigue-life shape parameters for an individual test configuration

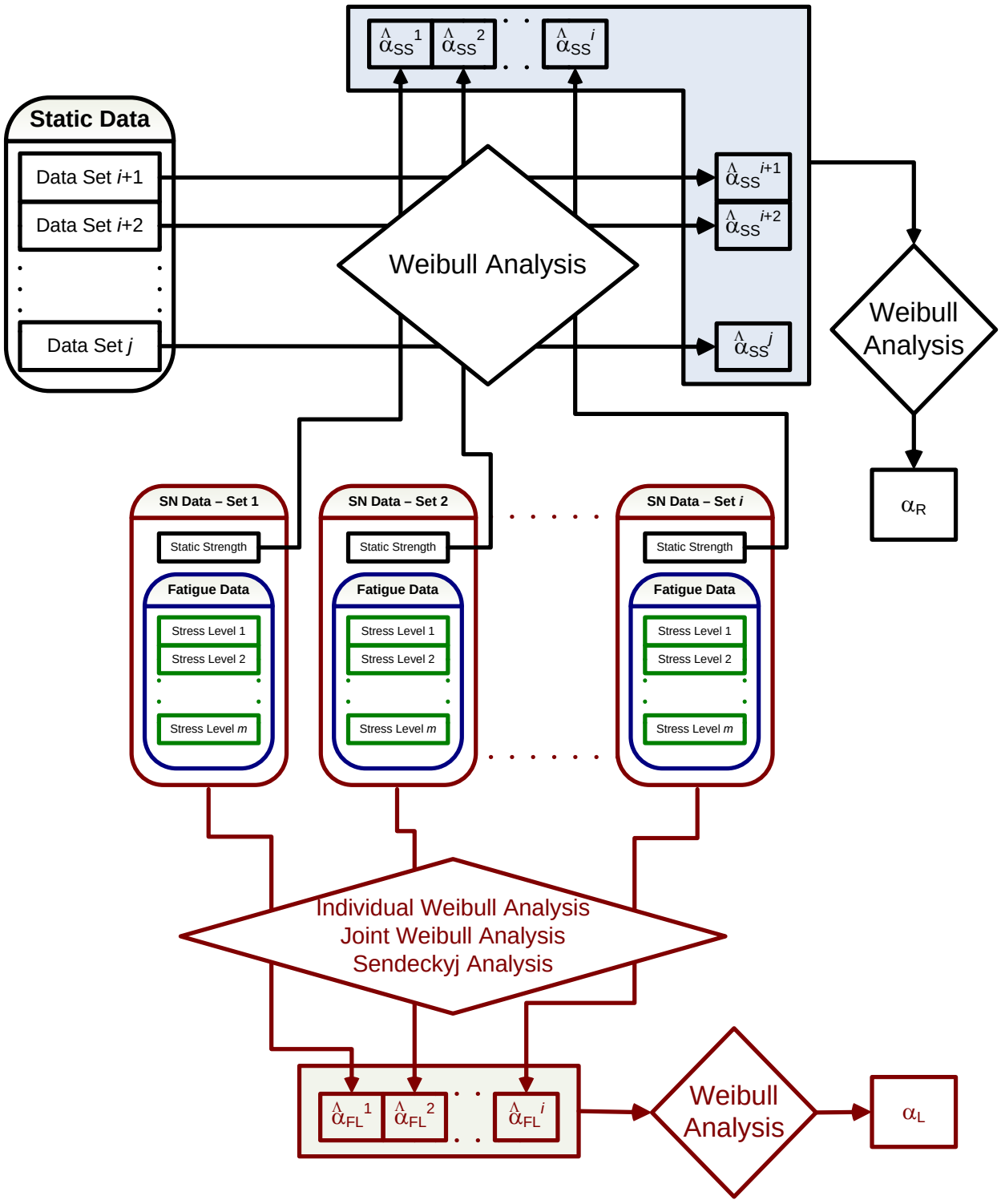

Figure A-2. Process for generating the MSSPs and MLSPs for calculating the life factor and LEFs for a particular structure

Table A-1. *A*-Basis LEFs

	n	1							2							3						
N	α_R \ α_L	1.00	1.25	1.50	1.75	2.00	2.25	2.50	1.00	1.25	1.50	1.75	2.00	2.25	2.50	1.00	1.25	1.50	1.75	2.00	2.25	2.50
1	17.5	1.385	1.378	1.373	1.369	1.366	1.363	1.361	1.366	1.360	1.355	1.351	1.348	1.345	1.343	1.357	1.350	1.345	1.341	1.338	1.336	1.334
	20.0	1.330	1.324	1.319	1.316	1.314	1.312	1.310	1.314	1.308	1.304	1.301	1.298	1.296	1.295	1.306	1.300	1.296	1.293	1.290	1.288	1.287
	22.5	1.288	1.283	1.279	1.277	1.274	1.273	1.271	1.275	1.270	1.266	1.263	1.261	1.259	1.258	1.268	1.263	1.259	1.257	1.254	1.253	1.251
	25.0	1.256	1.251	1.248	1.246	1.244	1.242	1.241	1.244	1.240	1.237	1.234	1.232	1.231	1.229	1.238	1.234	1.231	1.228	1.226	1.225	1.223
	27.5	1.230	1.226	1.223	1.221	1.219	1.218	1.217	1.220	1.216	1.213	1.211	1.209	1.208	1.207	1.214	1.210	1.208	1.205	1.204	1.202	1.201
	30.0	1.209	1.206	1.203	1.201	1.199	1.198	1.197	1.200	1.196	1.194	1.192	1.190	1.189	1.188	1.195	1.191	1.189	1.187	1.185	1.184	1.183
	32.5	1.192	1.188	1.186	1.184	1.183	1.182	1.181	1.183	1.180	1.178	1.176	1.174	1.173	1.172	1.179	1.175	1.173	1.171	1.170	1.169	1.168
	35.0	1.177	1.174	1.172	1.170	1.169	1.168	1.167	1.169	1.166	1.164	1.162	1.161	1.160	1.159	1.165	1.162	1.160	1.158	1.157	1.156	1.155
1.5	17.5	1.353	1.338	1.326	1.314	1.304	1.294	1.285	1.335	1.321	1.308	1.297	1.287	1.277	1.268	1.326	1.312	1.299	1.288	1.278	1.268	1.259
	20.0	1.303	1.291	1.280	1.270	1.261	1.253	1.245	1.288	1.276	1.265	1.256	1.247	1.239	1.231	1.280	1.268	1.257	1.248	1.239	1.231	1.223
	22.5	1.265	1.255	1.245	1.237	1.229	1.222	1.215	1.252	1.242	1.232	1.224	1.217	1.209	1.203	1.245	1.235	1.226	1.218	1.210	1.203	1.196
	25.0	1.236	1.226	1.218	1.211	1.204	1.198	1.192	1.224	1.215	1.207	1.200	1.193	1.187	1.181	1.218	1.209	1.201	1.194	1.187	1.181	1.175
	27.5	1.212	1.204	1.197	1.190	1.184	1.178	1.173	1.202	1.194	1.186	1.180	1.174	1.168	1.163	1.197	1.188	1.181	1.175	1.169	1.163	1.158
	30.0	1.193	1.185	1.179	1.173	1.167	1.162	1.157	1.184	1.176	1.170	1.164	1.158	1.153	1.148	1.179	1.171	1.165	1.159	1.154	1.149	1.144
	32.5	1.177	1.170	1.164	1.159	1.154	1.149	1.144	1.168	1.162	1.156	1.150	1.145	1.141	1.136	1.164	1.157	1.151	1.146	1.141	1.136	1.132
	35.0	1.163	1.157	1.151	1.147	1.142	1.138	1.133	1.155	1.149	1.144	1.139	1.134	1.130	1.126	1.151	1.145	1.140	1.135	1.130	1.126	1.122
2	17.5	1.331	1.311	1.294	1.277	1.262	1.247	1.233	1.313	1.294	1.276	1.260	1.245	1.231	1.217	1.304	1.285	1.267	1.251	1.236	1.222	1.208
	20.0	1.284	1.268	1.253	1.239	1.226	1.213	1.201	1.269	1.253	1.238	1.224	1.211	1.199	1.187	1.262	1.245	1.230	1.217	1.204	1.192	1.180
	22.5	1.249	1.235	1.222	1.210	1.198	1.187	1.177	1.236	1.222	1.209	1.197	1.186	1.175	1.165	1.229	1.215	1.202	1.191	1.179	1.169	1.158
	25.0	1.222	1.209	1.197	1.187	1.177	1.167	1.158	1.210	1.198	1.186	1.176	1.166	1.156	1.147	1.204	1.192	1.180	1.170	1.160	1.151	1.142
	27.5	1.200	1.188	1.178	1.168	1.159	1.151	1.143	1.189	1.178	1.168	1.159	1.150	1.141	1.133	1.184	1.173	1.163	1.153	1.145	1.136	1.128
	30.0	1.182	1.171	1.162	1.153	1.145	1.137	1.130	1.172	1.162	1.153	1.144	1.136	1.129	1.121	1.168	1.157	1.148	1.140	1.132	1.124	1.117
	32.5	1.166	1.157	1.149	1.141	1.133	1.126	1.119	1.158	1.149	1.140	1.133	1.125	1.118	1.111	1.154	1.144	1.136	1.128	1.121	1.114	1.107
	35.0	1.154	1.145	1.137	1.130	1.123	1.117	1.110	1.146	1.137	1.130	1.123	1.116	1.109	1.103	1.142	1.134	1.126	1.119	1.112	1.105	1.099
3	17.5	1.301	1.274	1.249	1.226	1.205	1.184	1.164	1.283	1.257	1.233	1.210	1.189	1.168	1.148	1.274	1.248	1.224	1.202	1.180	1.160	1.140
	20.0	1.259	1.236	1.215	1.196	1.177	1.159	1.142	1.244	1.222	1.201	1.182	1.163	1.146	1.129	1.236	1.214	1.194	1.174	1.156	1.139	1.122
	22.5	1.227	1.207	1.189	1.172	1.156	1.140	1.125	1.214	1.195	1.177	1.160	1.144	1.128	1.113	1.208	1.188	1.170	1.154	1.138	1.122	1.107
	25.0	1.202	1.185	1.169	1.154	1.139	1.125	1.112	1.191	1.174	1.158	1.143	1.129	1.115	1.102	1.185	1.168	1.152	1.137	1.123	1.109	1.096
	27.5	1.182	1.167	1.152	1.139	1.126	1.113	1.101	1.172	1.157	1.142	1.129	1.116	1.104	1.092	1.167	1.151	1.137	1.124	1.111	1.099	1.087
	30.0	1.166	1.152	1.139	1.126	1.115	1.103	1.092	1.157	1.143	1.130	1.118	1.106	1.095	1.084	1.152	1.138	1.125	1.113	1.102	1.090	1.080
	32.5	1.152	1.139	1.127	1.116	1.105	1.095	1.085	1.144	1.131	1.119	1.108	1.098	1.087	1.077	1.139	1.127	1.115	1.104	1.093	1.083	1.073
	35.0	1.140	1.129	1.118	1.107	1.098	1.088	1.079	1.133	1.121	1.110	1.100	1.090	1.081	1.072	1.129	1.117	1.106	1.096	1.086	1.077	1.068
4	17.5	1.279	1.248	1.219	1.192	1.166	1.141	1.117	1.262	1.231	1.203	1.176	1.150	1.126	1.102	1.254	1.223	1.194	1.168	1.142	1.118	1.094
	20.0	1.241	1.214	1.189	1.166	1.144	1.122	1.101	1.226	1.200	1.175	1.152	1.130	1.109	1.089	1.219	1.192	1.168	1.145	1.123	1.102	1.082
	22.5	1.211	1.188	1.166	1.146	1.127	1.108	1.090	1.199	1.176	1.154	1.134	1.115	1.096	1.078	1.192	1.169	1.148	1.128	1.109	1.090	1.073
	25.0	1.188	1.168	1.149	1.131	1.113	1.097	1.080	1.177	1.157	1.138	1.120	1.103	1.086	1.070	1.171	1.151	1.132	1.115	1.098	1.081	1.065
	27.5	1.170	1.151	1.134	1.118	1.102	1.087	1.073	1.160	1.142	1.125	1.109	1.093	1.078	1.064	1.155	1.137	1.120	1.104	1.088	1.073	1.059
	30.0	1.155	1.138	1.122	1.108	1.094	1.080	1.067	1.146	1.129	1.114	1.099	1.085	1.071	1.058	1.141	1.124	1.109	1.095	1.081	1.067	1.054
	32.5	1.142	1.127	1.112	1.099	1.086	1.074	1.061	1.134	1.119	1.105	1.091	1.078	1.066	1.054	1.129	1.114	1.100	1.087	1.074	1.062	1.050
	35.0	1.131	1.117	1.104	1.092	1.080	1.068	1.057	1.124	1.110	1.097	1.084	1.072	1.061	1.050	1.120	1.106	1.093	1.081	1.069	1.057	1.046
5	17.5	1.263	1.228	1.196	1.165	1.136	1.109	1.082	1.246	1.212	1.180	1.150	1.121	1.094	1.067	1.238	1.203	1.172	1.142	1.113	1.086	1.060
	20.0	1.227	1.197	1.169	1.143	1.118	1.094	1.071	1.213	1.183	1.156	1.130	1.105	1.082	1.059	1.205	1.176	1.149	1.123	1.099	1.075	1.052
	22.5	1.199	1.173	1.149	1.126	1.105	1.083	1.063	1.187	1.161	1.137	1.115	1.093	1.072	1.052	1.180	1.155	1.131	1.109	1.087	1.066	1.046
	25.0	1.178	1.155	1.133	1.113	1.094	1.075	1.057	1.167	1.144	1.123	1.103	1.083	1.065	1.047	1.161	1.138	1.117	1.097	1.078	1.060	1.042
	27.5	1.160	1.140	1.121	1.102	1.085	1.068	1.051	1.150	1.130	1.111	1.093	1.076	1.059	1.042	1.145	1.125	1.106	1.088	1.071	1.054	1.038
	30.0	1.146	1.127	1.110	1.093	1.077	1.062	1.047	1.137	1.119	1.101	1.085	1.069	1.054	1.039	1.132	1.114	1.097	1.080	1.065	1.049	1.035
	32.5	1.134	1.117	1.101	1.086	1.071	1.057	1.043	1.126	1.109	1.093	1.078	1.064	1.049	1.036	1.122	1.105	1.089	1.074	1.060	1.046	1.032
	35.0	1.124	1.108	1.094	1.080	1.066	1.053	1.040	1.116	1.101	1.086	1.072	1.059	1.046	1.033	1.113	1.097	1.082	1.069	1.055	1.042	1.030

Table A-2. *B*-Basis LEFs

	n	1							2							3						
N	α_R \ α_L	1.00	1.25	1.50	1.75	2.00	2.25	2.50	1.00	1.25	1.50	1.75	2.00	2.25	2.50	1.00	1.25	1.50	1.75	2.00	2.25	2.50
1	17.5	1.211	1.205	1.200	1.197	1.194	1.192	1.190	1.195	1.189	1.184	1.181	1.178	1.176	1.175	1.186	1.180	1.176	1.173	1.170	1.168	1.166
	20.0	1.182	1.177	1.173	1.170	1.168	1.166	1.165	1.168	1.163	1.160	1.157	1.154	1.153	1.151	1.161	1.156	1.152	1.150	1.147	1.146	1.144
	22.5	1.160	1.156	1.153	1.150	1.148	1.146	1.145	1.148	1.144	1.141	1.138	1.136	1.135	1.133	1.142	1.138	1.134	1.132	1.130	1.128	1.127
	25.0	1.143	1.139	1.136	1.134	1.132	1.131	1.130	1.133	1.129	1.126	1.124	1.122	1.120	1.119	1.127	1.123	1.120	1.118	1.116	1.115	1.114
	27.5	1.129	1.126	1.123	1.121	1.120	1.118	1.117	1.120	1.116	1.114	1.112	1.110	1.109	1.108	1.115	1.111	1.109	1.107	1.105	1.104	1.103
	30.0	1.118	1.115	1.112	1.111	1.109	1.108	1.107	1.109	1.106	1.104	1.102	1.100	1.099	1.098	1.105	1.102	1.099	1.097	1.096	1.095	1.094
	32.5	1.108	1.105	1.103	1.102	1.100	1.099	1.098	1.101	1.098	1.095	1.094	1.092	1.091	1.090	1.096	1.093	1.091	1.090	1.088	1.087	1.086
	35.0	1.100	1.098	1.096	1.094	1.093	1.092	1.091	1.093	1.090	1.088	1.087	1.086	1.085	1.084	1.089	1.086	1.084	1.083	1.082	1.081	1.080
1.5	17.5	1.183	1.170	1.159	1.149	1.140	1.132	1.123	1.167	1.155	1.144	1.134	1.125	1.117	1.108	1.159	1.147	1.136	1.126	1.117	1.109	1.101
	20.0	1.158	**1.148**	1.138	1.129	1.122	1.114	1.107	1.145	1.134	1.125	1.116	1.109	1.101	1.094	1.138	1.127	1.118	1.110	1.102	1.095	1.088
	22.5	1.140	1.130	1.122	1.114	1.107	1.101	1.095	1.128	1.118	1.110	1.103	1.096	1.090	1.083	1.122	1.112	1.104	1.097	1.090	1.084	1.077
	25.0	1.125	1.116	1.109	1.102	1.096	1.090	1.085	1.114	1.106	1.099	1.092	1.086	1.080	1.075	1.109	1.101	1.093	1.087	1.081	1.075	1.069
	27.5	1.113	1.105	1.099	1.093	1.087	1.082	1.077	1.104	1.096	1.089	1.083	1.078	1.073	1.068	1.099	1.091	1.084	1.079	1.073	1.068	1.063
	30.0	1.103	1.096	1.090	1.085	1.080	1.075	1.070	1.094	1.088	1.082	1.076	1.071	1.066	1.062	1.090	1.083	1.077	1.072	1.067	1.062	1.058
	32.5	1.095	1.088	1.083	1.078	1.073	1.069	1.065	1.087	1.081	1.075	1.070	1.065	1.061	1.057	1.083	1.077	1.071	1.066	1.061	1.057	1.053
	35.0	1.088	1.082	1.077	1.072	1.068	1.064	1.060	1.080	1.075	1.070	1.065	1.061	1.057	1.053	1.077	1.071	1.066	1.061	1.057	1.053	1.049
2	17.5	1.164	1.146	1.131	1.117	1.103	1.090	1.078	1.148	1.131	1.116	1.102	1.089	1.076	1.064	1.140	1.123	1.108	1.094	1.081	1.068	1.056
	20.0	1.142	1.127	1.114	1.101	1.090	1.079	1.068	1.129	1.114	1.101	1.089	1.077	1.066	1.056	1.122	1.107	1.094	1.082	1.071	1.060	1.049
	22.5	1.125	1.112	1.100	1.090	1.079	1.070	1.060	1.114	1.101	1.089	1.078	1.068	1.059	1.049	1.108	1.095	1.083	1.073	1.062	1.053	1.044
	25.0	1.112	1.100	1.090	1.080	1.071	1.062	1.054	1.102	1.090	1.080	1.070	1.061	1.053	1.044	1.096	1.085	1.075	1.065	1.056	1.047	1.039
	27.5	1.101	1.091	1.081	1.073	1.065	1.057	1.049	1.092	1.082	1.072	1.064	1.056	1.048	1.040	1.087	1.077	1.068	1.059	1.051	1.043	1.036
	30.0	1.093	1.083	1.074	1.067	1.059	1.052	1.045	1.084	1.075	1.066	1.058	1.051	1.044	1.037	1.080	1.070	1.062	1.054	1.047	1.039	1.033
	32.5	1.085	1.076	1.069	1.061	1.054	1.048	1.041	1.077	1.069	1.061	1.054	1.047	1.040	1.034	1.073	1.065	1.057	1.050	1.043	1.036	1.030
	35.0	1.079	1.071	1.063	1.057	1.050	1.044	1.038	1.072	1.064	1.056	1.050	1.043	1.037	1.031	1.068	1.060	1.053	1.046	1.040	1.034	1.028
3	17.5	1.137	1.114	1.092	1.072	1.053	1.035	1.017	1.122	1.099	1.078	1.058	1.039	1.021	1.004	1.114	1.091	1.070	1.051	1.032	1.014	
	20.0	1.119	1.099	1.080	1.063	1.046	1.031	1.015	1.106	1.086	1.068	1.051	1.034	1.019	1.003	1.099	1.079	1.061	1.044	1.028	1.012	
	22.5	1.105	1.087	1.071	1.056	1.041	1.027	1.014	1.094	1.076	1.060	1.045	1.030	1.017	1.003	1.088	1.070	1.054	1.039	1.025	1.011	
	25.0	1.094	1.078	1.064	1.050	1.037	1.024	1.012	1.084	1.068	1.054	1.040	1.027	1.015	1.003	1.079	1.063	1.049	1.035	1.022	1.010	
	27.5	1.085	1.071	1.058	1.045	1.034	1.022	1.011	1.076	1.062	1.049	1.037	1.025	1.014	1.002	1.071	1.057	1.044	1.032	1.020	1.009	
	30.0	1.078	1.065	1.053	1.042	1.031	1.020	1.010	1.069	1.057	1.045	1.034	1.023	1.012	1.002	1.065	1.052	1.040	1.029	1.019	1.008	
	32.5	1.072	1.060	1.049	1.038	1.028	1.019	1.009	1.064	1.052	1.041	1.031	1.021	1.011	1.002	1.060	1.048	1.037	1.027	1.017	1.008	
	35.0	1.066	1.055	1.045	1.036	1.026	1.017	1.009	1.059	1.048	1.038	1.029	1.019	1.011	1.002	1.056	1.045	1.035	1.025	1.016	1.007	
4	17.5	1.119	1.091	1.066	1.042	1.019			1.104	1.077	1.052	1.028	1.006			1.096	1.069	1.044	1.021			
	20.0	1.103	1.079	1.057	1.037	1.017			1.090	1.067	1.045	1.025	1.005			1.084	1.060	1.039	1.018			
	22.5	1.091	1.070	1.051	1.032	1.015			1.080	1.059	1.040	1.022	1.004			1.074	1.053	1.034	1.016			
	25.0	1.082	1.063	1.046	1.029	1.013			1.072	1.053	1.036	1.020	1.004			1.066	1.048	1.031	1.015			
	27.5	1.074	1.057	1.041	1.026	1.012			1.065	1.048	1.033	1.018	1.004			1.060	1.043	1.028	1.013			
	30.0	1.068	1.052	1.038	1.024	1.011			1.059	1.044	1.030	1.016	1.003			1.055	1.040	1.026	1.012			
	32.5	1.062	1.048	1.035	1.022	1.010			1.055	1.041	1.027	1.015	1.003			1.051	1.037	1.024	1.011			
	35.0	1.058	1.045	1.032	1.021	1.010			1.051	1.038	1.025	1.014	1.003			1.047	1.034	1.022	1.010			
5	17.5	1.104	1.074	1.046	1.019				1.090	1.060	1.032	1.005				1.082	1.052	1.025				
	20.0	1.091	1.064	1.040	1.017				1.078	1.052	1.028	1.005				1.072	1.046	1.021				
	22.5	1.080	1.057	1.035	1.015				1.069	1.046	1.025	1.004				1.063	1.040	1.019				
	25.0	1.072	1.051	1.032	1.013				1.062	1.041	1.022	1.004				1.057	1.036	1.017				
	27.5	1.065	1.046	1.029	1.012				1.056	1.038	1.020	1.003				1.052	1.033	1.016				
	30.0	1.060	1.042	1.026	1.011				1.051	1.034	1.018	1.003				1.047	1.030	1.014				
	32.5	1.055	1.039	1.024	1.010				1.047	1.032	1.017	1.003				1.043	1.028	1.013				
	35.0	1.051	1.036	1.023	1.009				1.044	1.029	1.016	1.003				1.040	1.026	1.012				

APPENDIX B—DAMAGE TOLERANCE ELEMENT TEST RESULTS

This appendix contains the results and statistical analysis results for damage tolerance element (DTE) tests. In addition, for several selected DTE test specimens, full-field strain and displacement data using the ARAMIS photogrammetry system are included. Such data are instrumental in evaluating the extent of damage after fatigue loading.

B.1. S-N DATA FOR AS4-PW DTE TESTS

Table B-1 includes the S-N data for AS4-PW 25/50/25 DTE tests. Figures B-1–B-3 show the S-N diagrams as well as the Sendeckyj fitting data.

Table B-1. The S-N data for AS4-PW 25/50/25 open-hole tension and CAI tests (FAA—load-enhancement factor)

CAI (R = 5) - BVID		CAI (R = 5) - VID		CAI (R = 5) - LID	
σ_A	n_f	σ_A	n_f	σ_A	n_f
37,188	1	29,149	1	25,147	1
34,745	1	31,335	1	25,601	1
35,658	1	29,443	1	24,627	1
36,526	1	29,282	1	25,370	1
36,364	1	29,950	1	25,228	1
35,669	1	28,866	1	26,695	1
28,820	12,243	22,374	37,690	19,083	42,897
28,820	14,342	22,374	24,001	19,083	38,476
28,820	9,651	22,374	55,768	19,083	18,155
28,820	8,152	22,374	28,958	19,083	13,719
28,820	15,155	22,374	11,897	19,083	32,463
28,820	26,005	22,374	16,335	19,083	17,564
27,019	92,926	20,882	127,451	16,539	201,380
27,019	31,634	20,882	94,625	16,539	214,807
27,019	104,891	20,882	128,689	16,539	374,375
27,019	152,023	20,882	59,749	16,539	278,234
27,019	47,635	20,882	143,030	16,539	165,086
27,019	31,642	20,882	180,742	16,539	193,821
25,217	678,421	19,391	626,039	15,267	2,233,805
25,217	596,825	19,391	397,153	15,267	1,352,887
25,217	323,026	19,391	270,784	15,267	1,618,147
25,217	252,255	19,391	638,545	15,267	1,236,307
25,217	575,983	19,391	222,775	15,267	928,401
25,217	252,433	19,391	595,875	15,267	1,228,113

CAI = Compression after impact; VID = Visual impact damage; R = Ratio; LID = Large impact damage; BVID = Barely visible impact damage

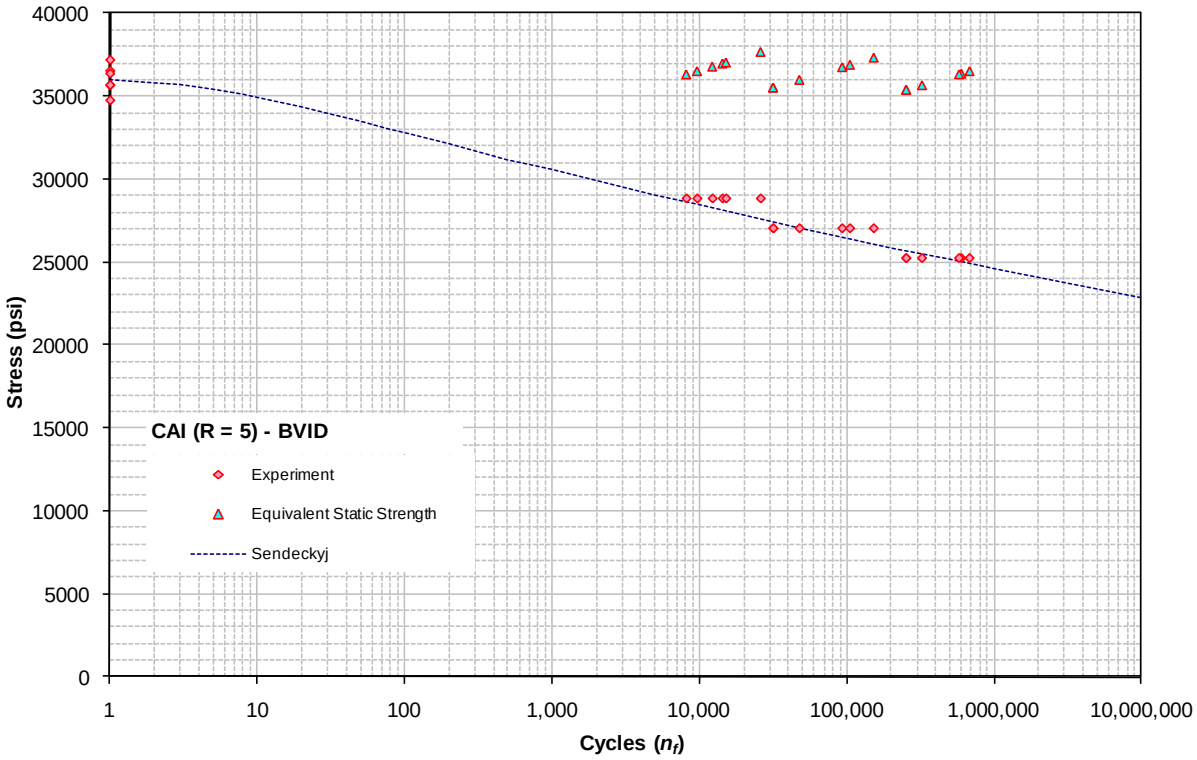

Figure B-1. AS4/E7K8 PW—25/50/25, CAI—BVID, *R* = 5

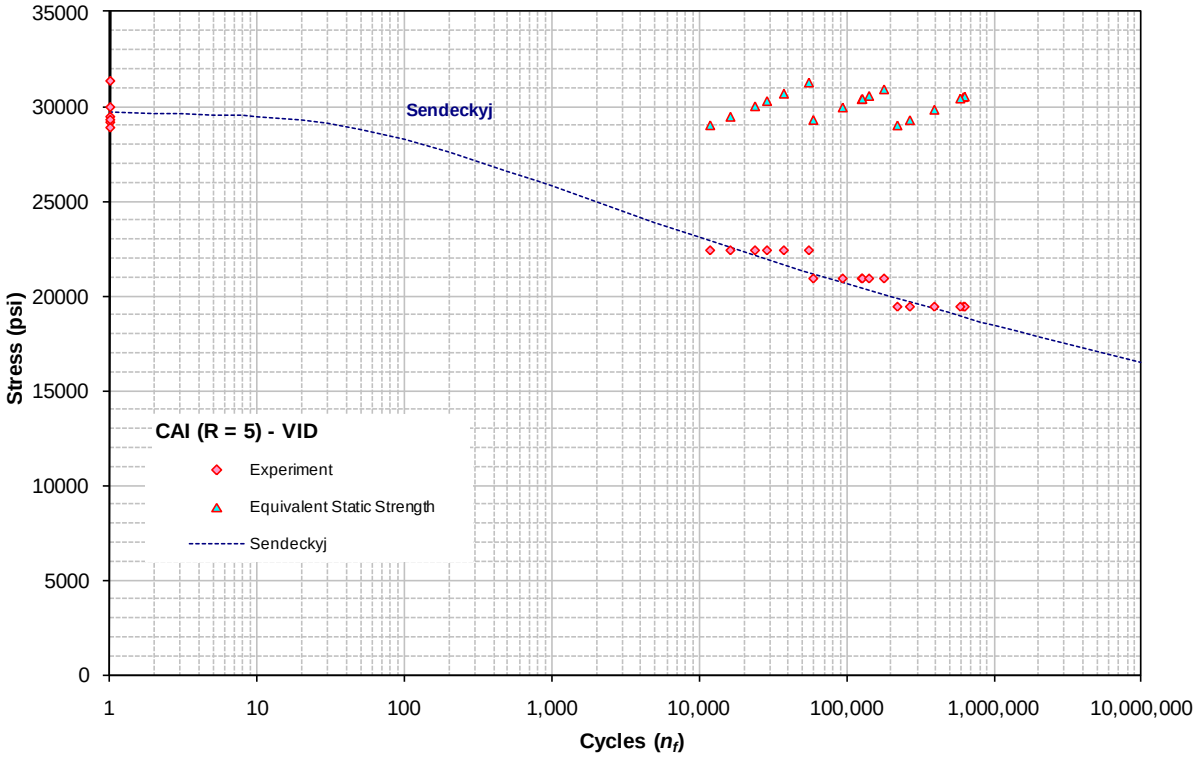

Figure B-2. AS4/E7K8 PW—25/50/25, CAI—VID, *R* = 5

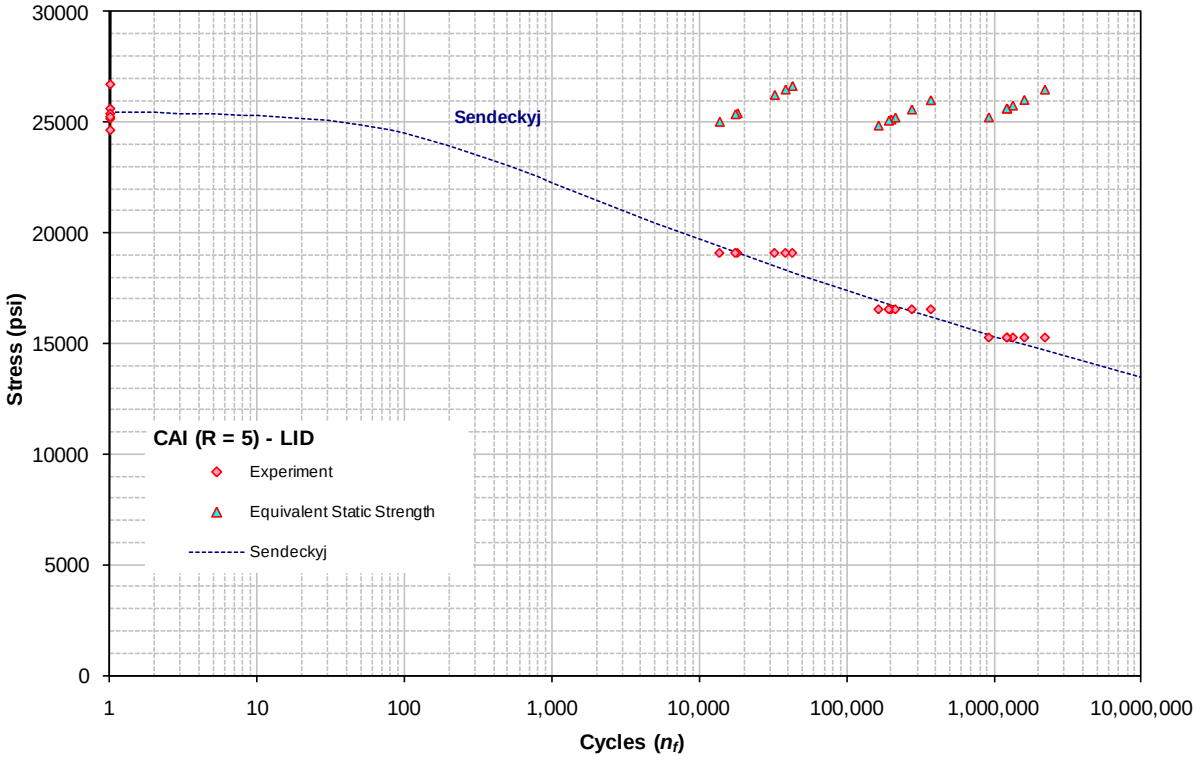

Figure B-3. AS4/E7K8 PW—25/50/25, CAI—LID, *R* = 5

B.2. FULL-FIELD STRAIN AND DISPLACEMENT DATA FOR DTE TESTS

Figures B-4–B-10 show the full-field strain and displacement data for several DTE test specimens.

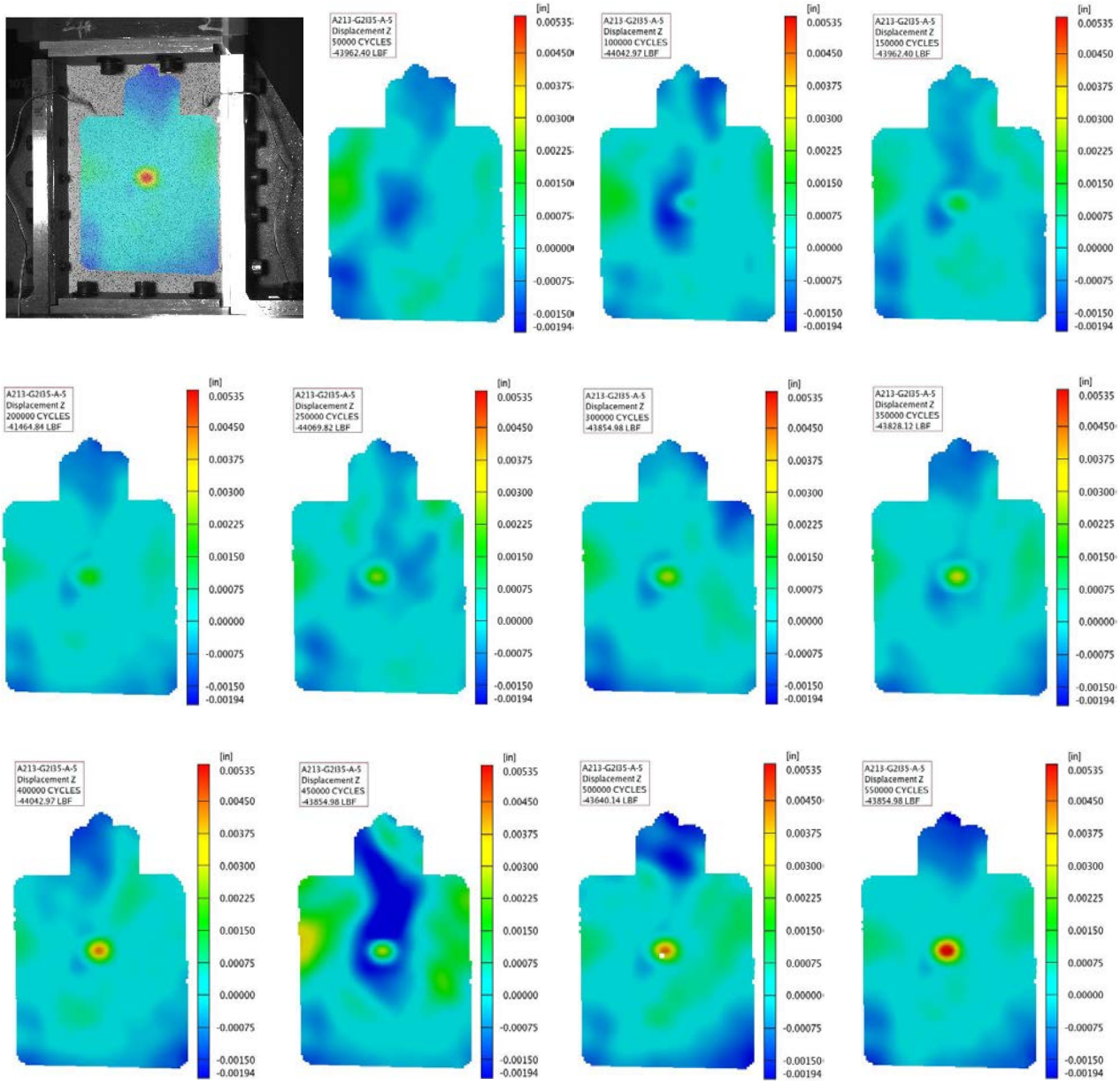

Figure B-4. Out-of-plane deformation for fatigue testing of DTE—BVID (750 in./lb/in.), 70% of static strength, *R* = 5

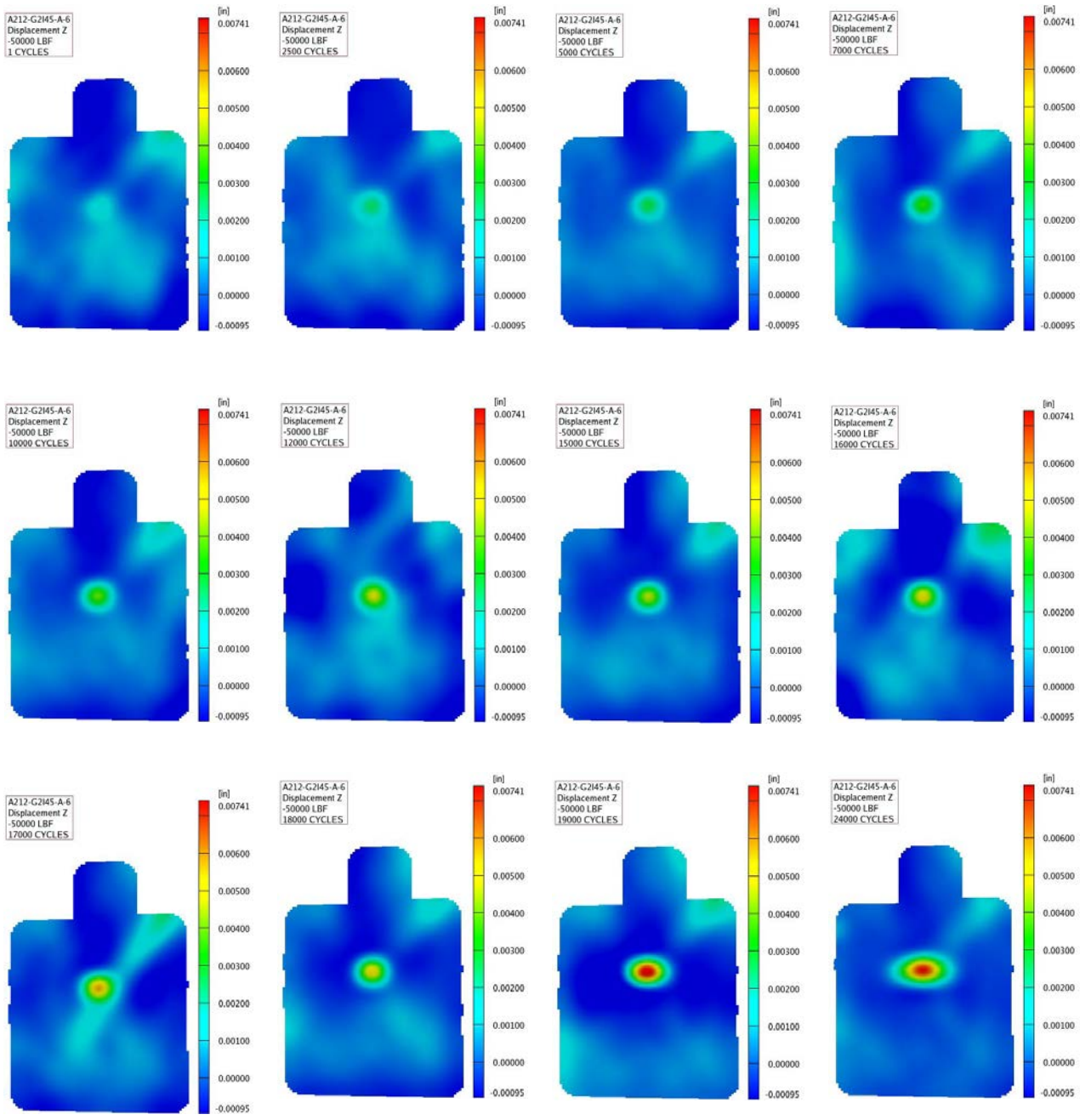

Figure B-5. Out-of-plane deformation for fatigue testing of DTE—BVID (750 in./lb/in.), 80% of static strength, *R* = 5

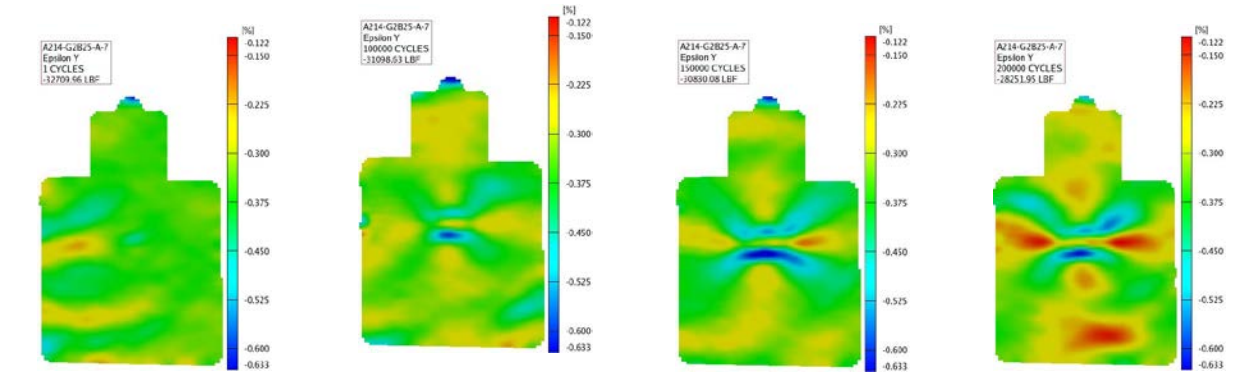

(a) Axial strain

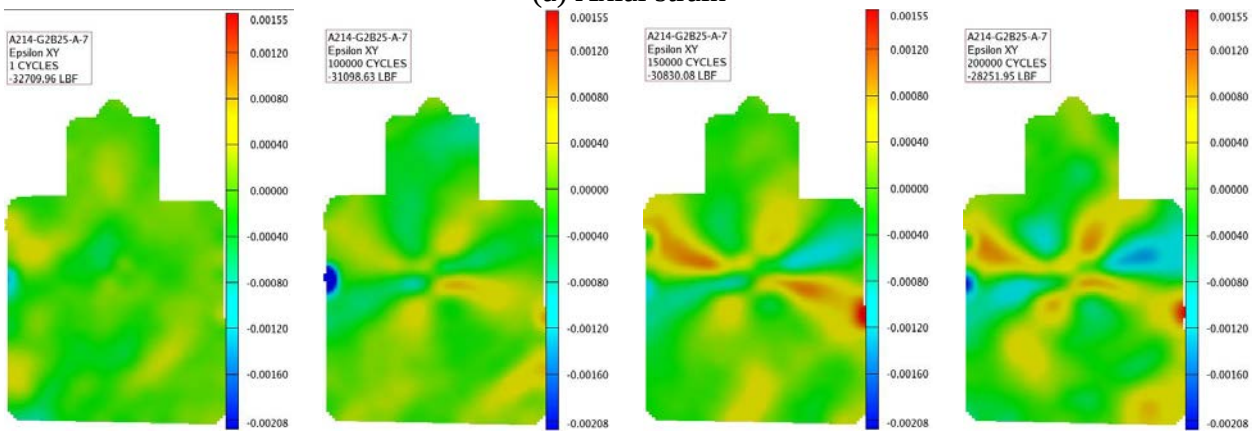

(b) Shear strain

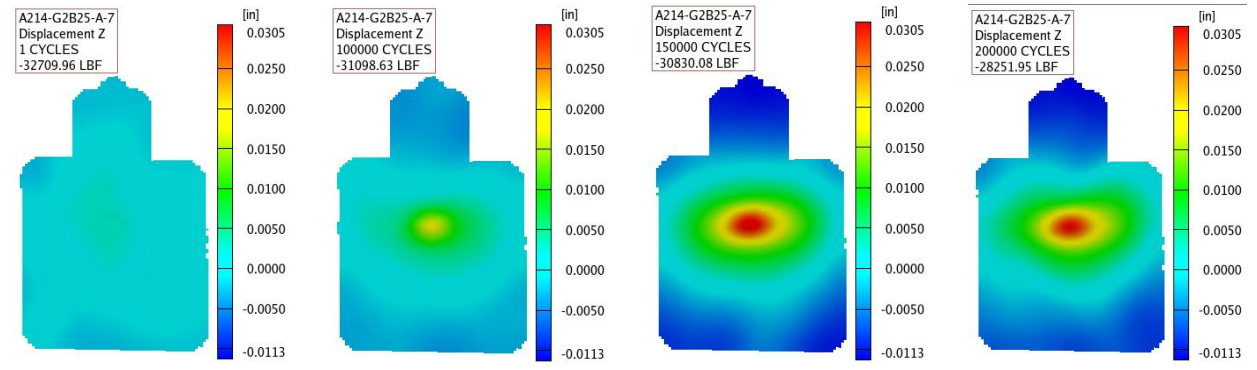

(c) Out-of-plane deformation

Figure B-6. Strain and displacement for fatigue testing of DTE—VID (1500 in./lb/in.), 65% of static strength, *R* = 5

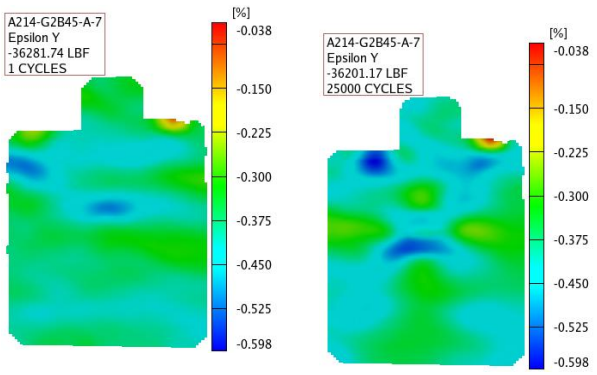

(a) Axial strain

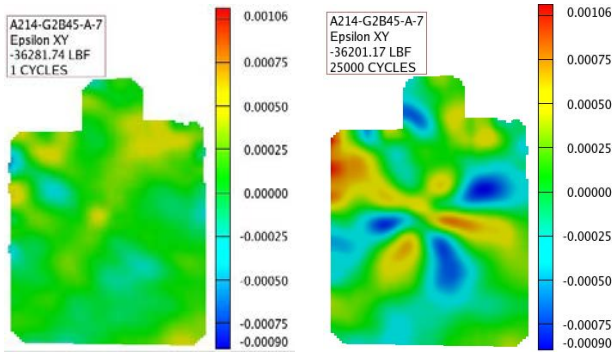

(b) Shear strain

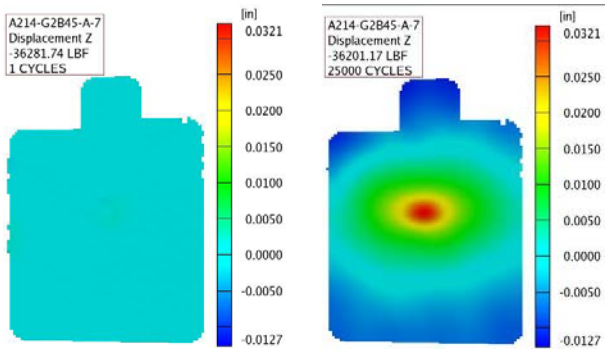

(c) Out-of-plane deformation

Figure B-7. Strain and displacement for fatigue testing of DTE—VID (1500 in./lb/in.), 70% of static strength, *R* = 5

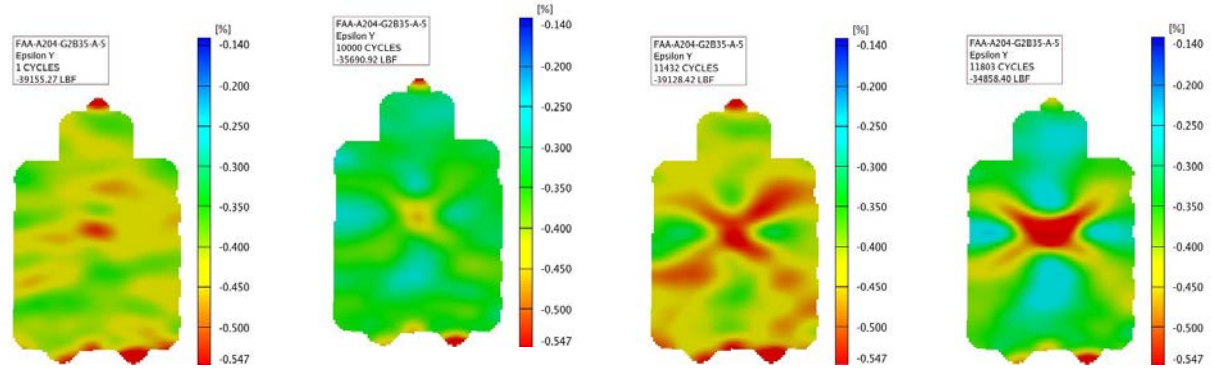

(a) Axial strain

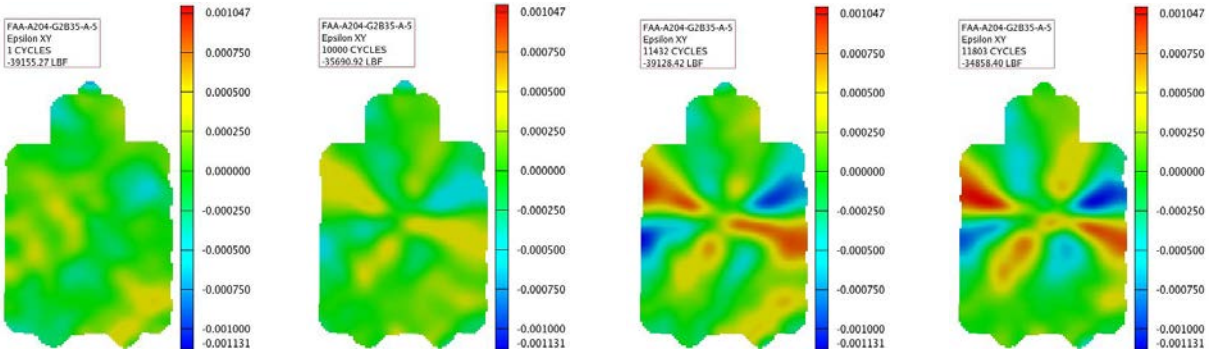

(b) Shear strain

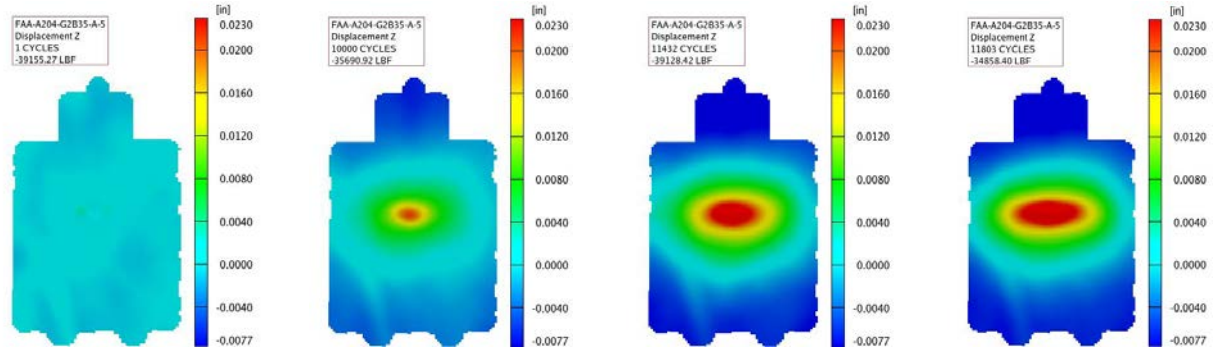

(c) Out-of-plane deformation

Figure B-8. Strain and displacement for fatigue testing of DTE—VID (1500 in./lb/in.), 75% of static strength, *R* = 5

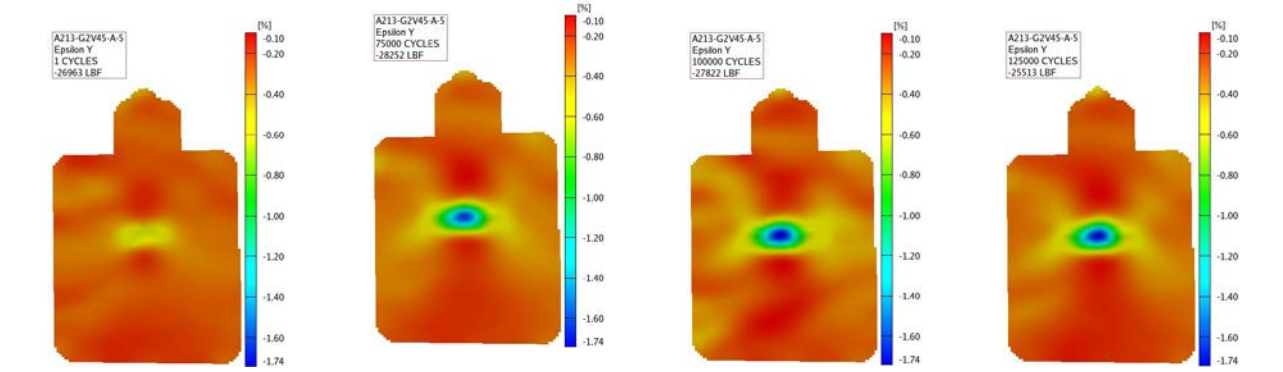

(a) Axial strain

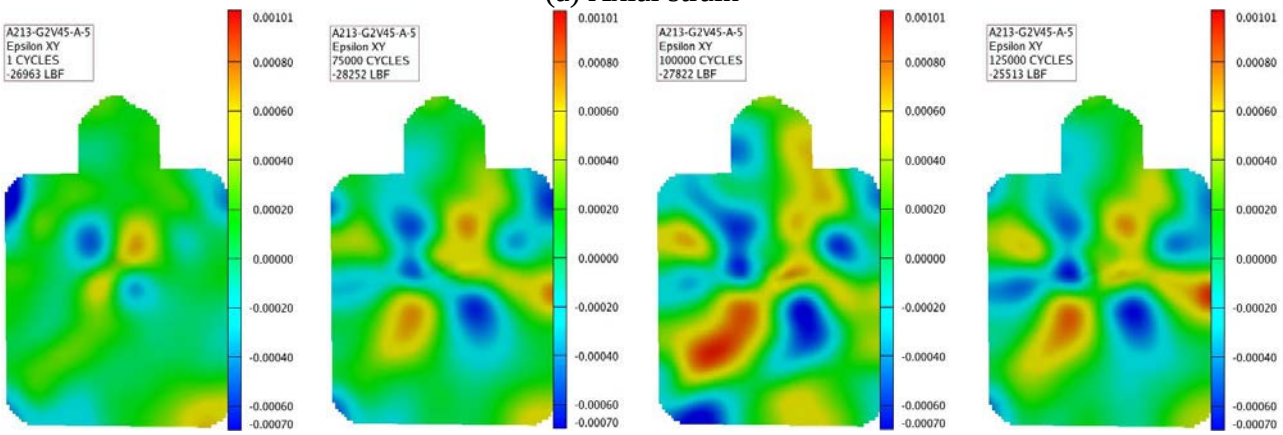

(b) Shear strain

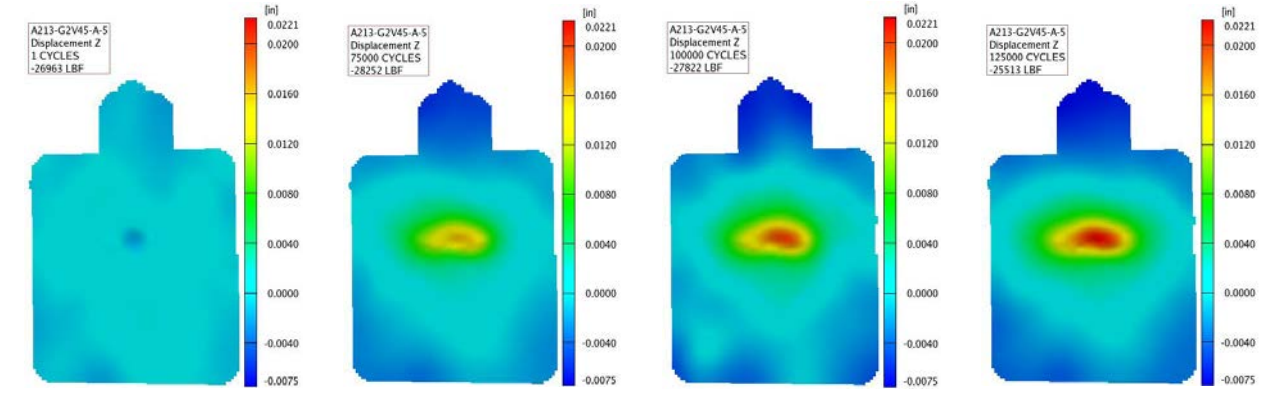

(c) Out-of-plane deformation

Figure B-9. Strain and displacement for fatigue testing of DTE—LID (3000 in./lb/in.), 65% of static strength, *R* = 5

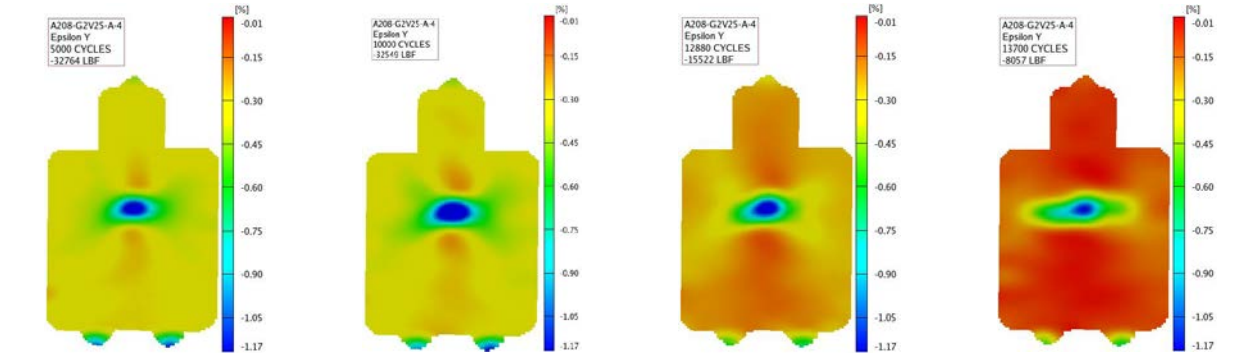

(a) Axial strain

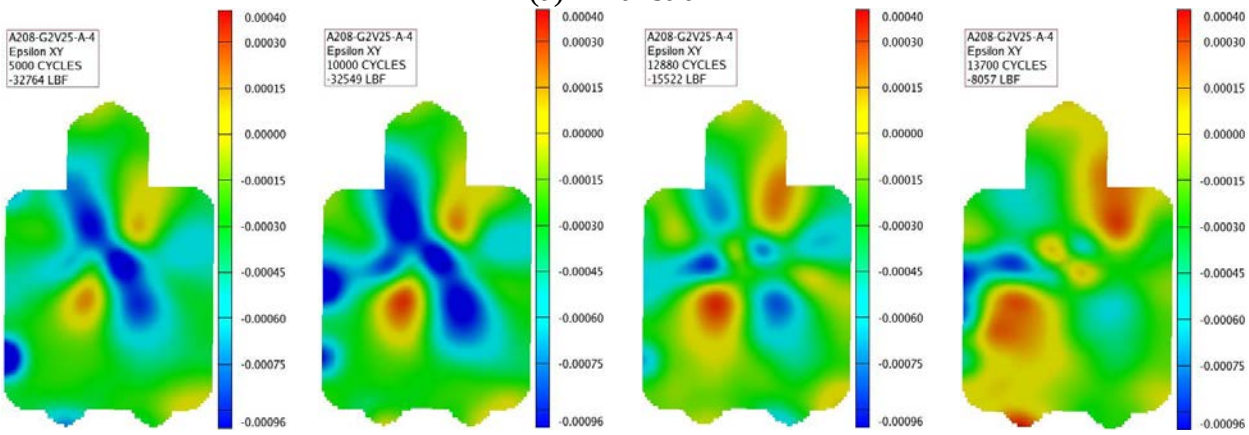

(b) Shear strain

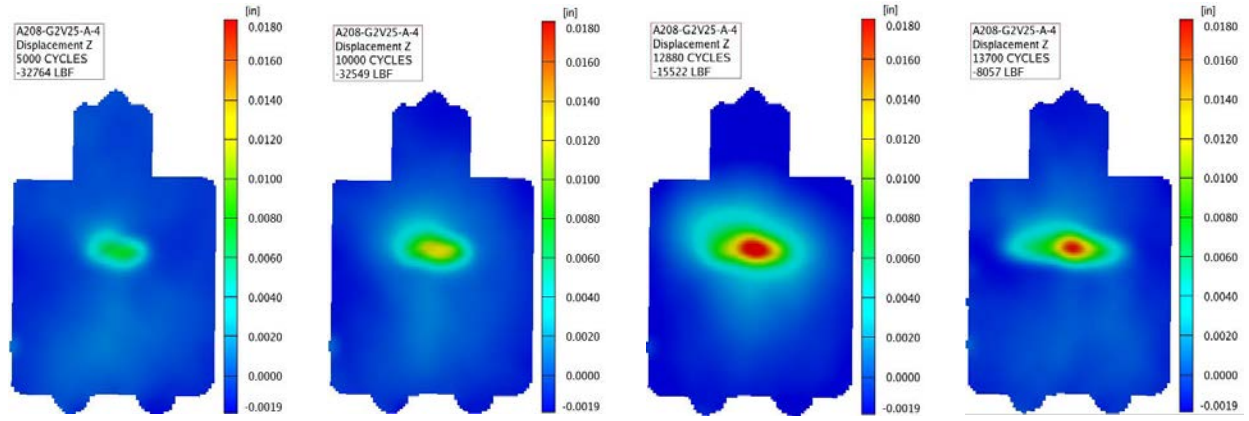

(C) Out-of-plane deformation

Figure B-10. Strain and displacement for fatigue testing of DTE—LID (3000 in./lb/in.), 75% of static strength, *R* = 5

APPENDIX C—SPECTRUM LOADS FOR FULL-SCALE DURABILITY AND DAMAGE TOLERANCE TESTING

One lifetime of the test article defined by the original aircraft manufacturer is equivalent to 20,000 flight hours, which corresponds to a spectrum of 160,033 cycles and includes 1-g and 3-g maneuvers, as well as positive and negative gust conditions.

The origin of the axis system for forward wing loads is at forward wing station 19.76 and lies on the central axis of the steel tube at the fixed end, as shown in figure C-1. This figure shows the positive load, moment, and torque directions ($+P_Z$, $+M_x$, and $+T_y$, respectively) for the right-hand wing using the right-hand rule. For the left wing, the positive torque axis is oriented outboard so that the positive load axis is upward using the left-hand rule.

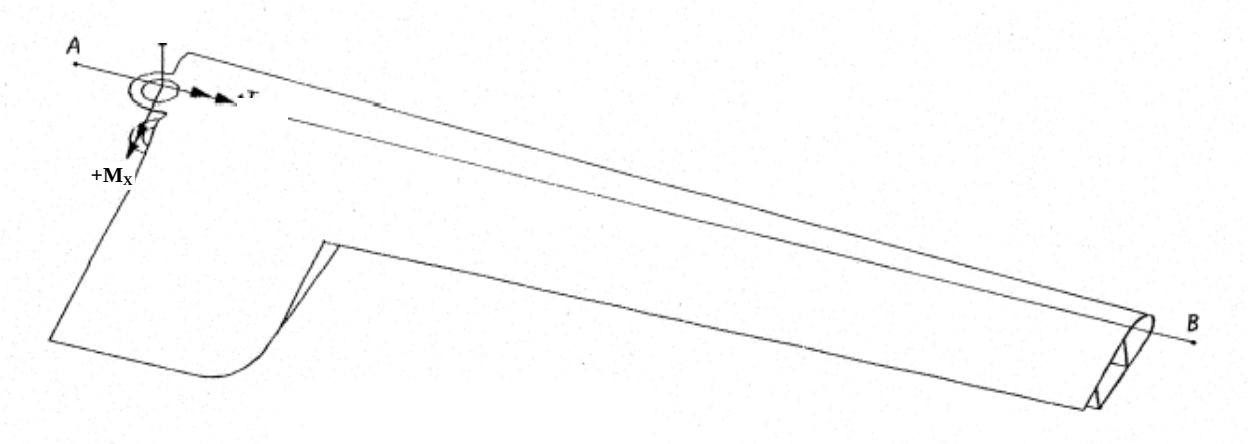

Figure C-1. Reference axis system for forward wing loads

Loads were applied to structures using load formers (figure C-2) and load patch (figure C-3) whiffletree settings for static and fatigue full-scale test articles, respectively. All static tests were performed only in the upbending configuration, and the majority of fatigue loads were in the up-bending configuration, whereby the test articles were mounted upside down for ease of inspection and safety. For fatigue tests, both top and bottom whiffletrees and four actuators were used so that both positive and negative SMT loads could be applied.

Figures C-4–C-9 show the spectrum loads with and without a load-enhancement factor of 1.072, after applying the conversion factor of 1.4.

Figure C-2. Forward wing static test whiffletree setup with bonded load formers

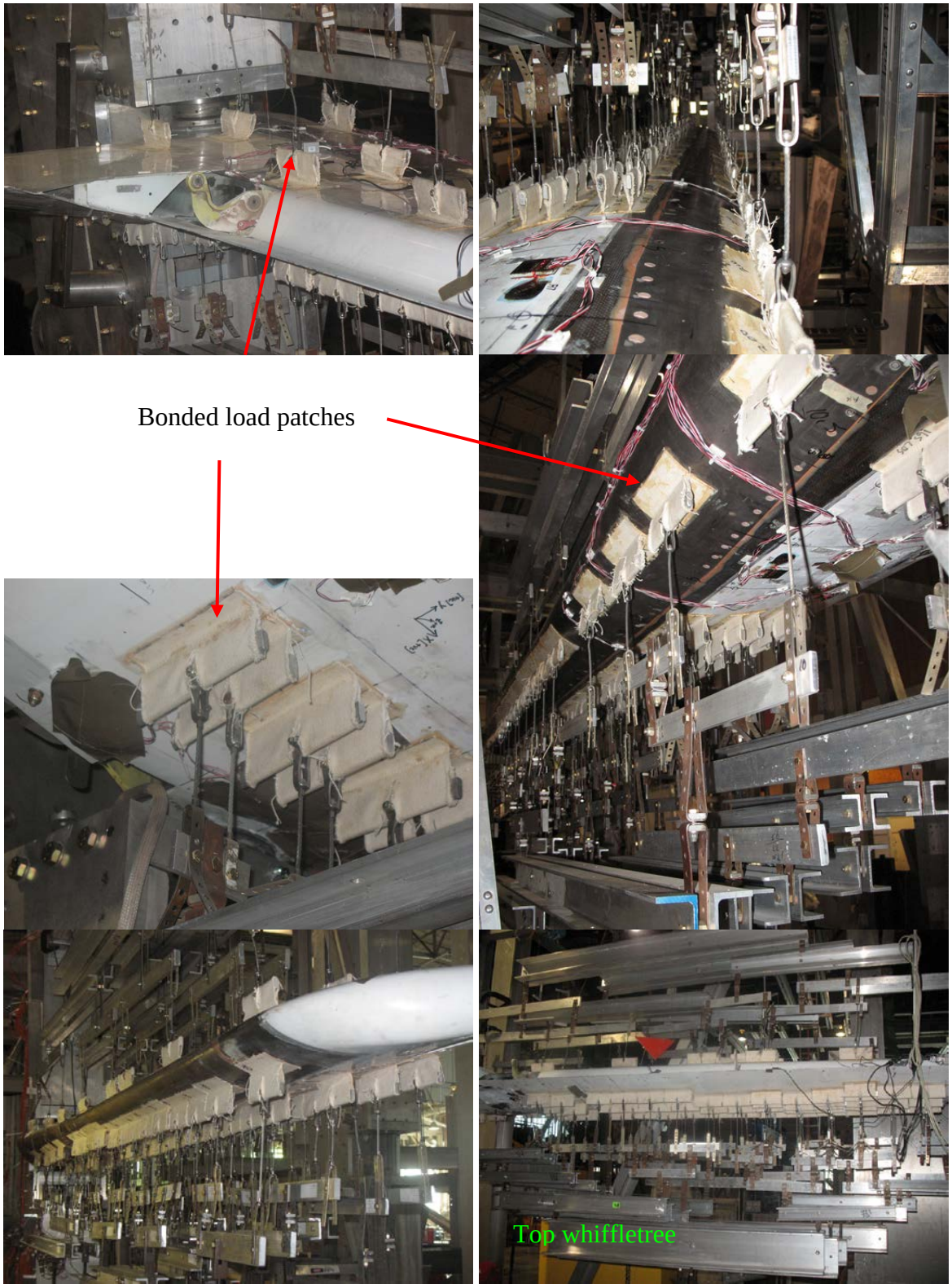

Figure C-3. Forward wing fatigue test whiffletree setup with bonded load patches

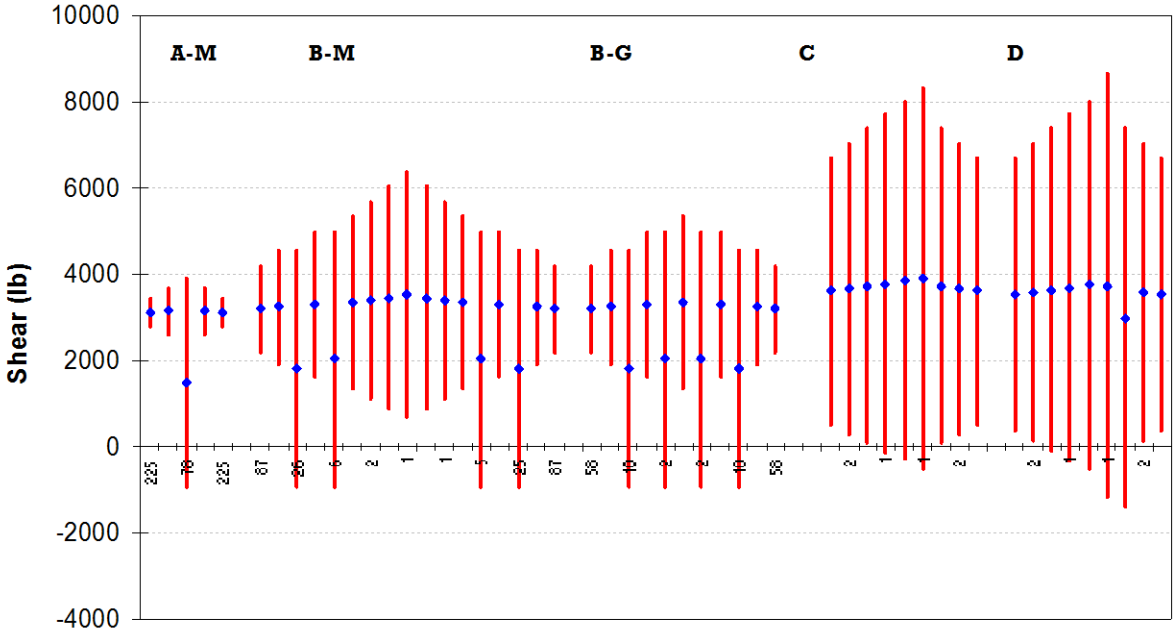

Figure C-4. Maneuver and gust shear spectrums, CF = 1.4 and LEF = 1.000

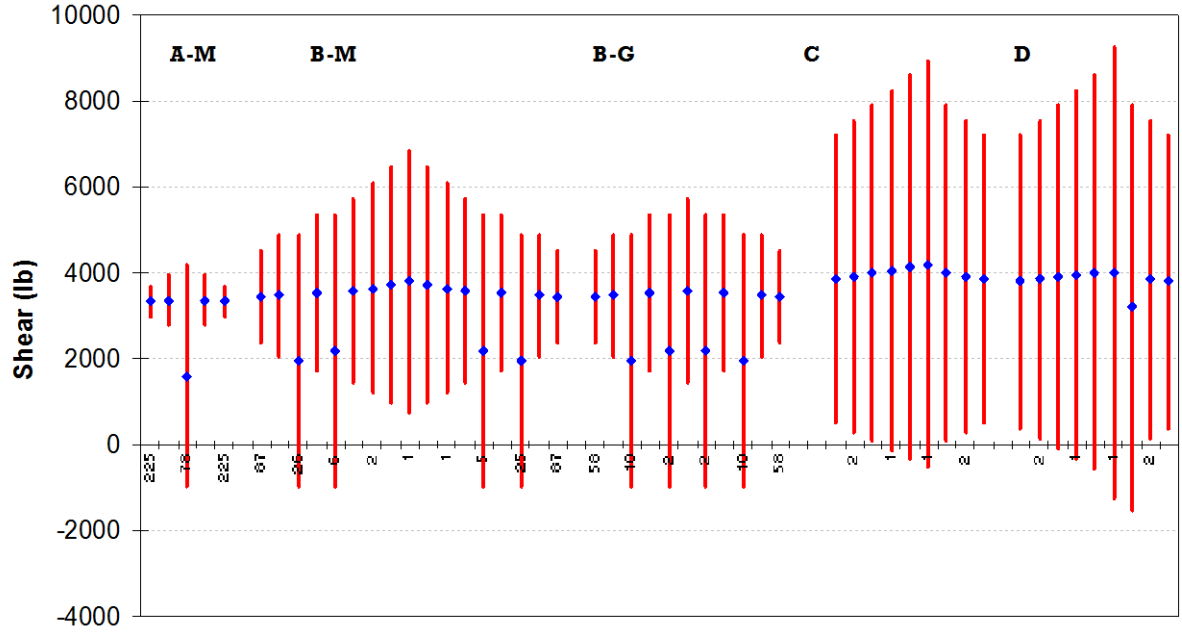

Figure C-5. Maneuver and gust shear spectrums, CF = 1.4 and LEF = 1.072

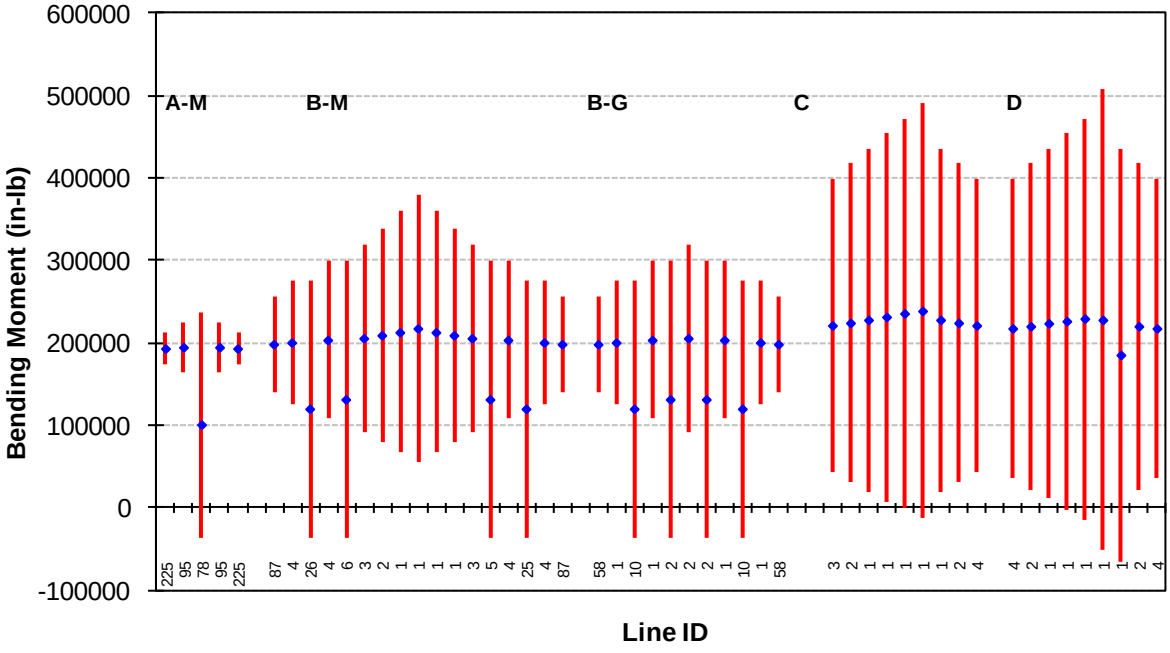

Figure C-6. Maneuver and gust bending moment spectrums, CF = 1.4 and LEF = 1.000

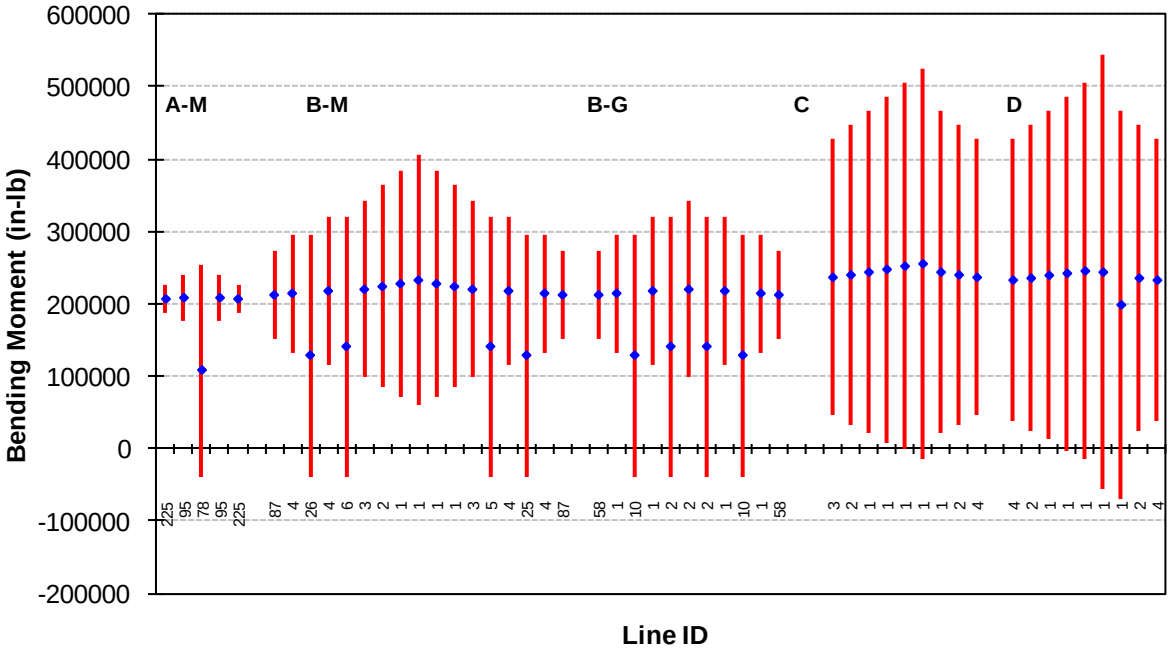

Figure C-7. Maneuver and gust bending moment spectrums, CF = 1.4 and LEF = 1.072

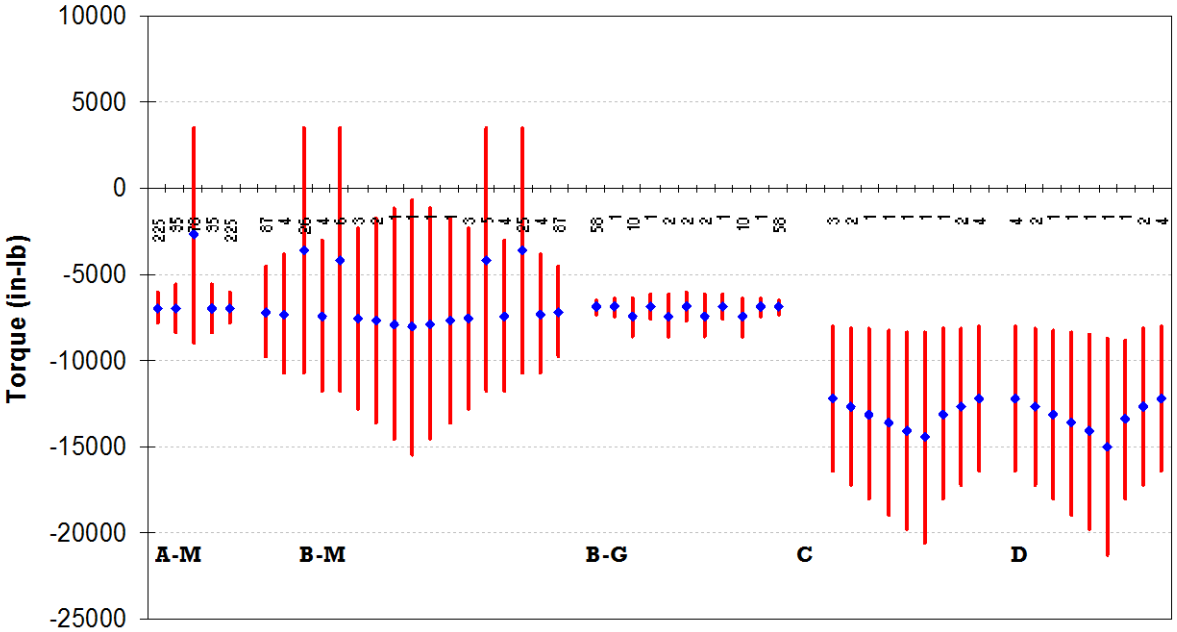

Figure C-8. Maneuver and gust torque spectrums, CF = 1.4 and LEF = 1.000

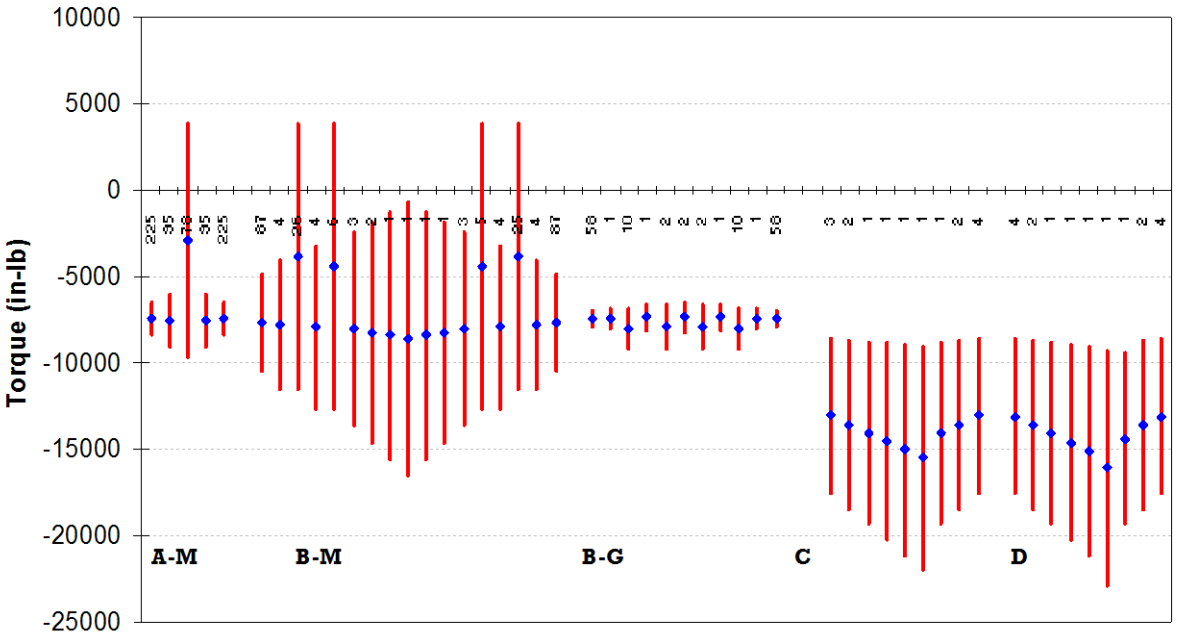

Figure C-9. Maneuver and gust torque spectrums, CF = 1.4 and LEF = 1.072

APPENDIX D—FULL-SCALE TEST RESULTS

The following are locations of displacement transducers for all full-scale forward wing station (FWS) tests (figure D-1):

- D1 and D2 = (FWS) 51.05
- D3 = FWS 76
- D4 = FWS 100
- D5 and D6 = FWS 130.90

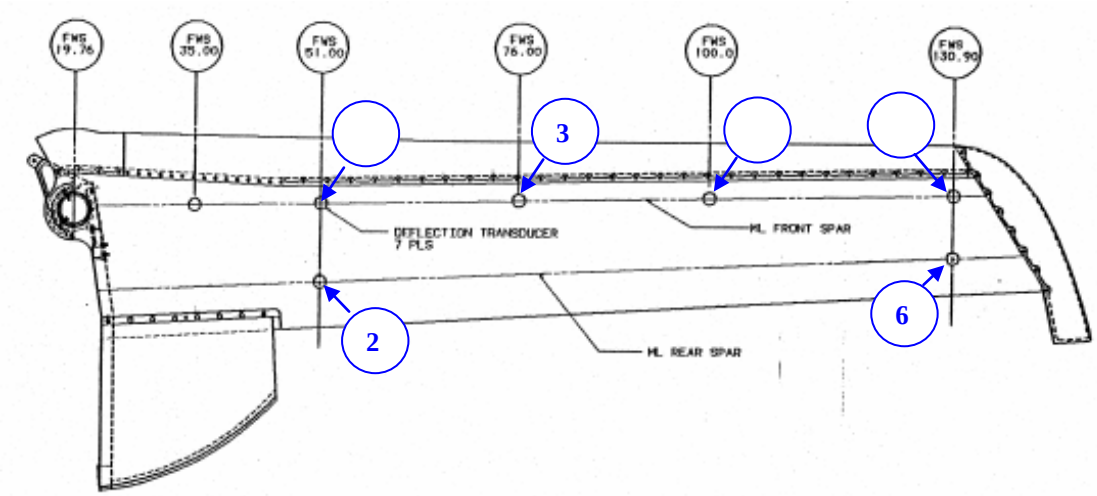

Figure D-1. Displacement transducer locations

D.1 THE ST001—STARSHIP FORWARD WING FULL-SCALE STATIC TEST

The first full-scale static test article, ST001, was tested with a total of eleven axial gages and seven rosettes were used for strain measurements (table D-1). The A and R prefixes indicate that the gages were either axial or rosette, respectively (note that three axial gages in 0°, 45°, and 90° directions are named as A, B, and C, respectively).

Table D-1. Strain gage locations of ST001

Strain Gage Number		Location
Axial	Rosette	
A1		Lower skin FWS 24.8″ on front spar
A2		Upper skin FWS 24.8″ on front spar
A3		Upper skin FWS 27.0″ on front spar
A4		Upper skin FWS 34.0″ on rear spar
A5		Upper skin FWS 42.5″ on rear spar
A6		Upper skin FWS 66.5″ on front spar
A7		Upper skin FWS 66.5″ on rear spar
A8		Upper skin FWS 90.5″ on front spar
A9		Upper skin FWS 90.5″ on rear spar
A10		Upper skin FWS 114.5″ on front spar
A11		Upper skin FWS 114.5″ on rear spar
	R1	Root rib at upper forward corner
	R2	Lower skin FWS 24.8″ and 2.5″ outboard of front spar
	R3	Upper skin FWS 24.8″ on rear spar
	R4	Lower skin FWS 38.0″ on front spar
	R5	Centered on rear web at FWS 50.44″
	R6	Upper skin FWS 24.8″ and 2.5″ outboard of front spar
	R7	Upper skin FWS 42.5″ on front spar

The ST001 test article was quasi-statically loaded up to 200% Beechcraft design limit load (BDLL) and unloaded. After unloading, a tap test and ultrasonic nondestructive inspections were performed around the rear and rear spar location that did not find any indications of delamination or debonds. This article was later retested on infliction of an impact damage at the aft spar.

In addition to strain gages, the ARAMIS photogrammetry image correlation system was used to obtain the full-field strain/displacement measurements during the quasi-static loading of ST001. Because the cameras' fields of depth were substantially low because of the whiffletree attachments, a rail system was designed to obtain full-field measurements along the length of the article at several different stations so that they could be combined later to form a single full-field image of the upper skin. ARAMIS measurements were first obtained for each section at multiple load steps until the limit load, as shown in figure D-2 (a). The cameras were then mounted away from the whiffletree, as shown in figure D-2 (b), to prevent possible damages to the sensors.

(a)

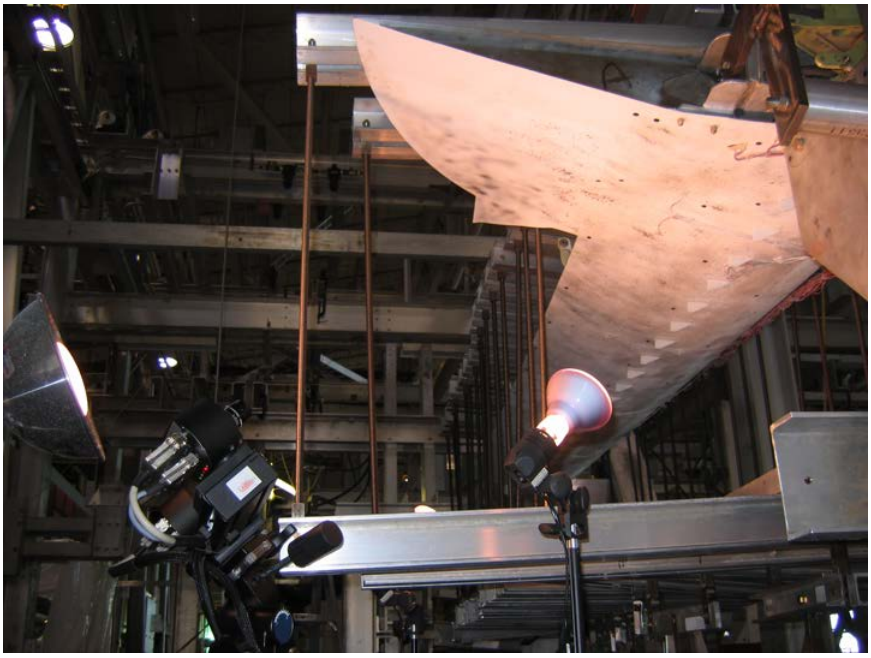

(b)

Figure D-2. The ARAMIS system setup (a) up to, and (b) after the limit load

Vertical displacement readings (D1-D2 and D5-D6 in figure D-3) indicated that there was minimal twisting at both the root and the tip of the test article. Overall displacements up to 200% BDLL were linear. Figure D-4 shows the axial strain data, and figure D-5 shows the strain data obtained from rosettes.

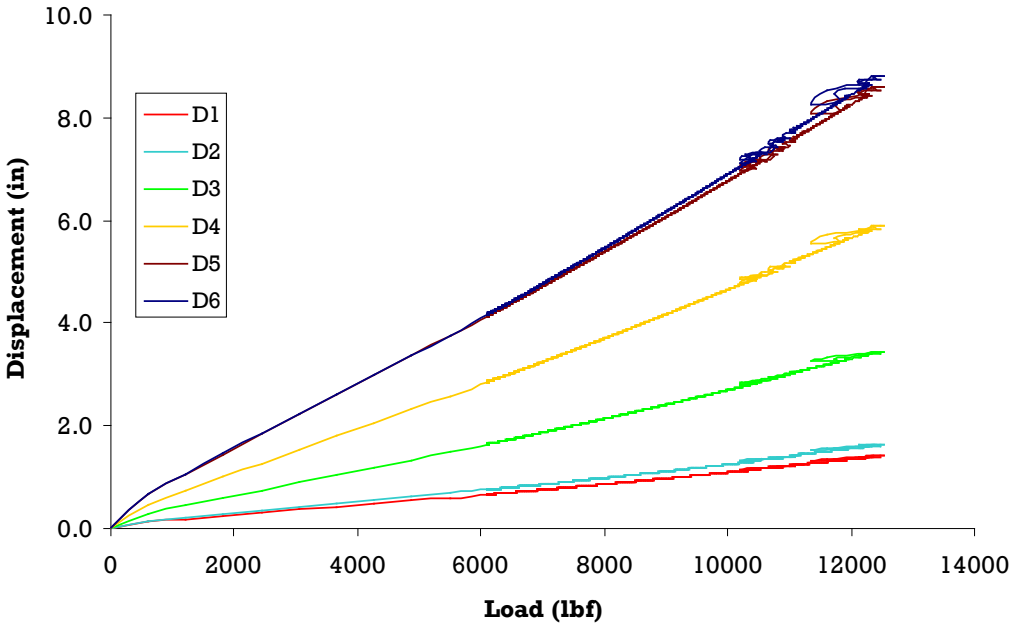

(a)

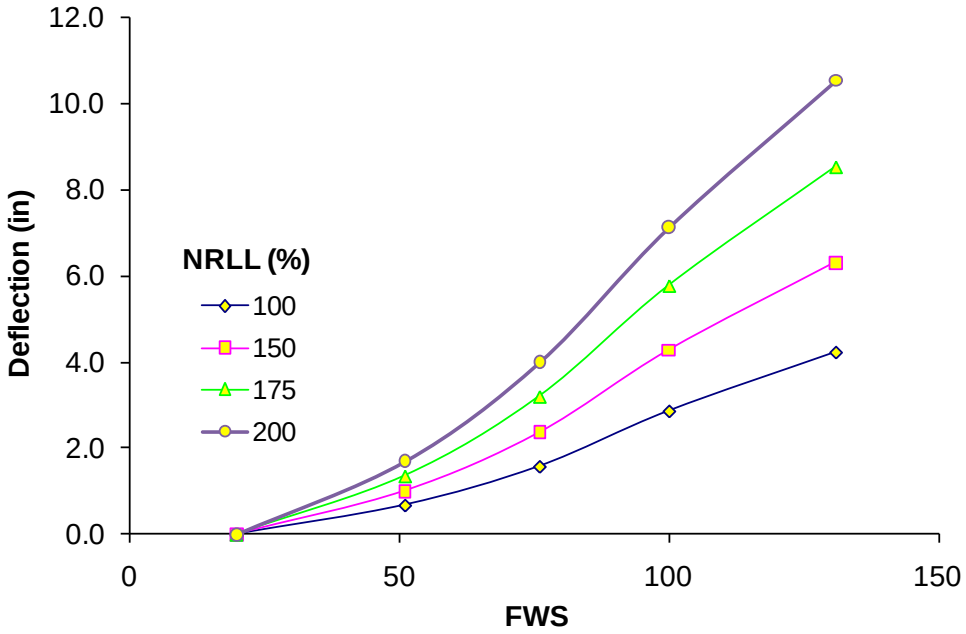

(b)

Figure D-3. Vertical displacements—ST001

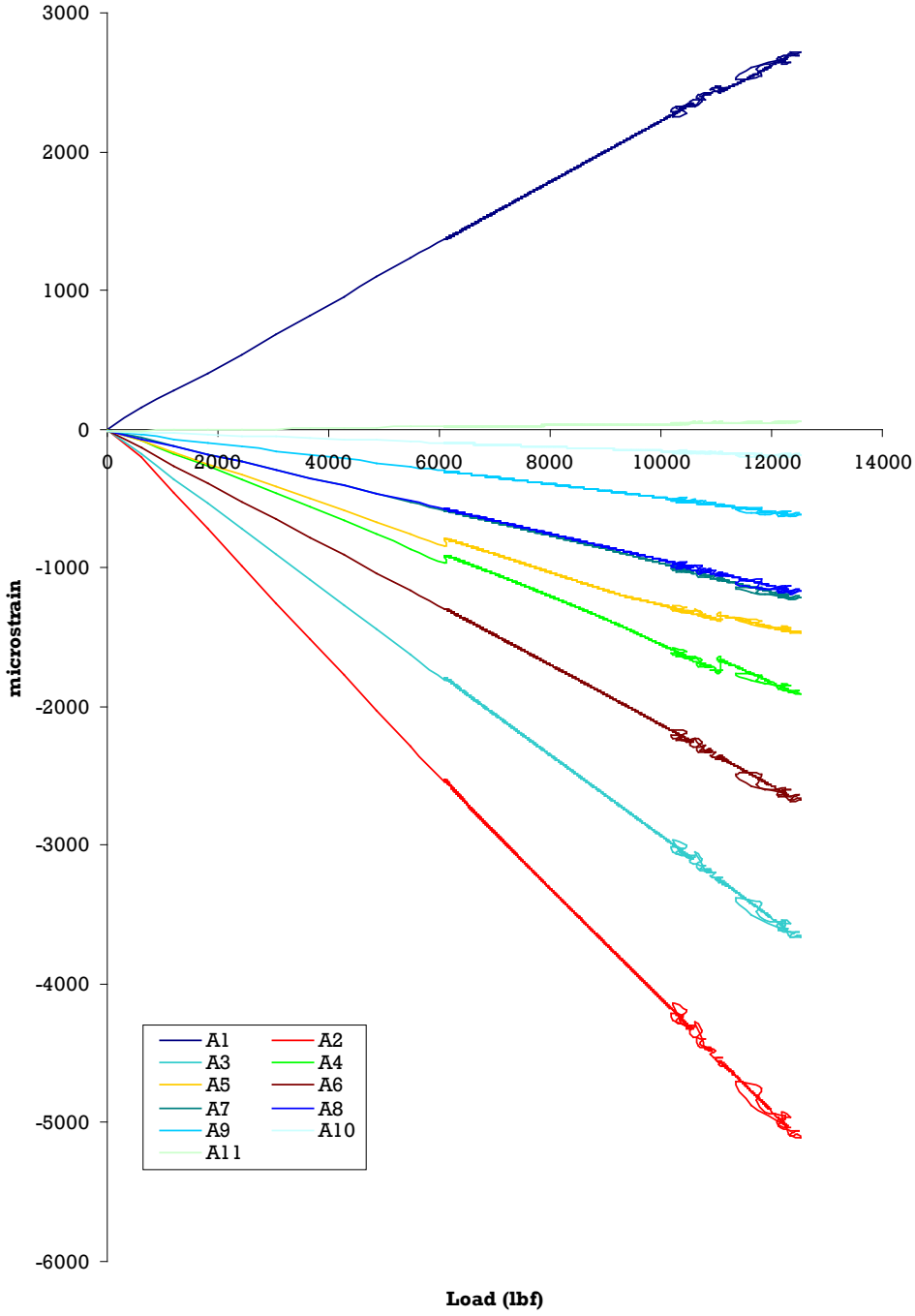

Figure D-4. Axial strain gage data for ST001

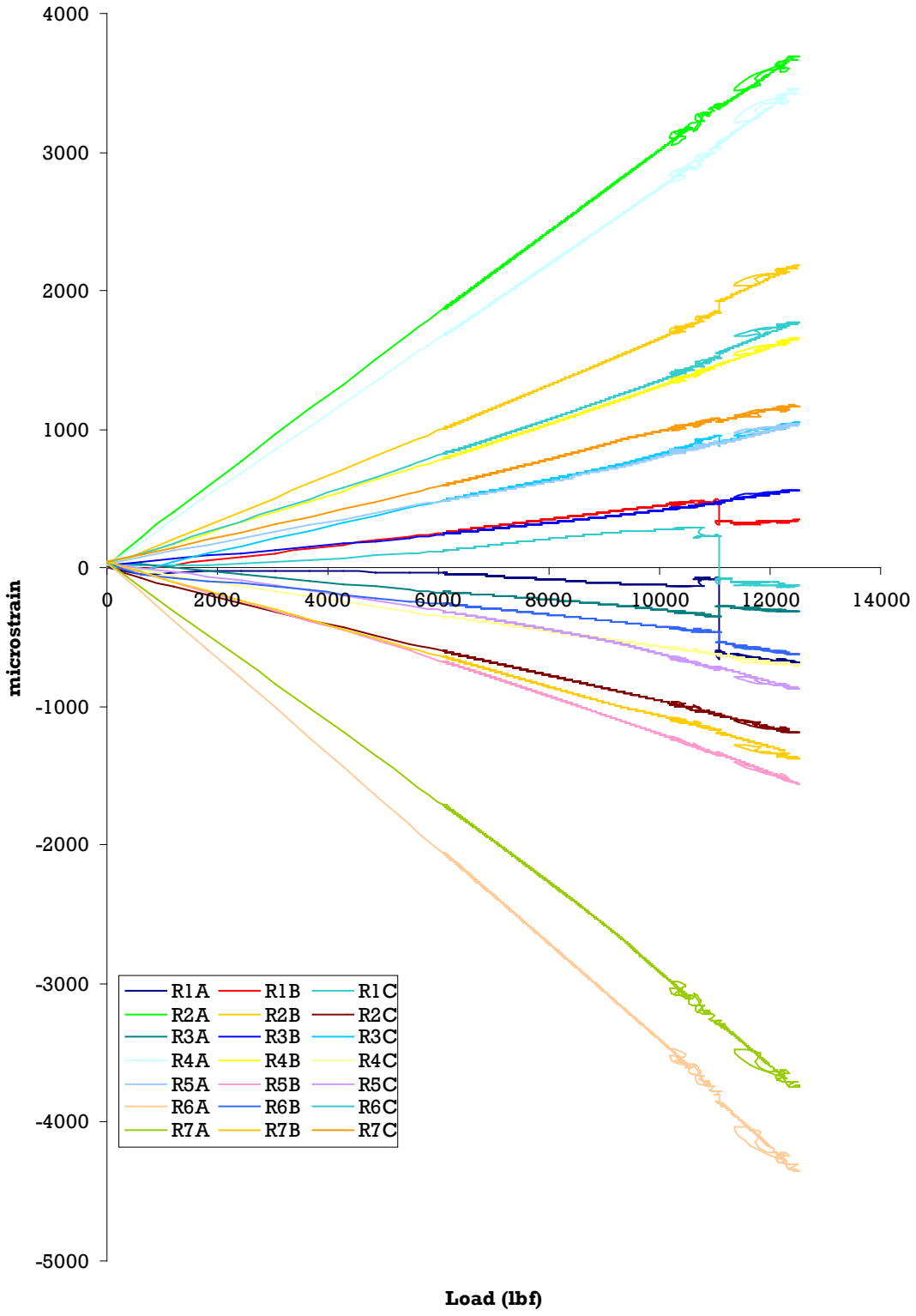

Figure D-5. Strain rosette data for ST001

Figure D-6 compares the ARAMIS full-field strain data along the front and aft spars with strain gage data. Strain gage data on both front and rear spars were linear until the maximum applied load.

	Raw Data from strain gage (microstrain)	ARAMIS Approximation (microstrain)	% Error
A2	962	840	12.7
A3	691	660	4.5
R7A	744	680	8.6
R8A	718	640	10.9
A6	616	610	1.0
A8	378	320	15.3
A4	398	370	7.0
A5	376	350	6.9
A7	370	340	8.1

Approximation of ARAMIS strain data: The average strain over a selected region near the strain gage location is reported. ARAMIS strain data is slightly lower than actual data in each case (can't give a reason for this).

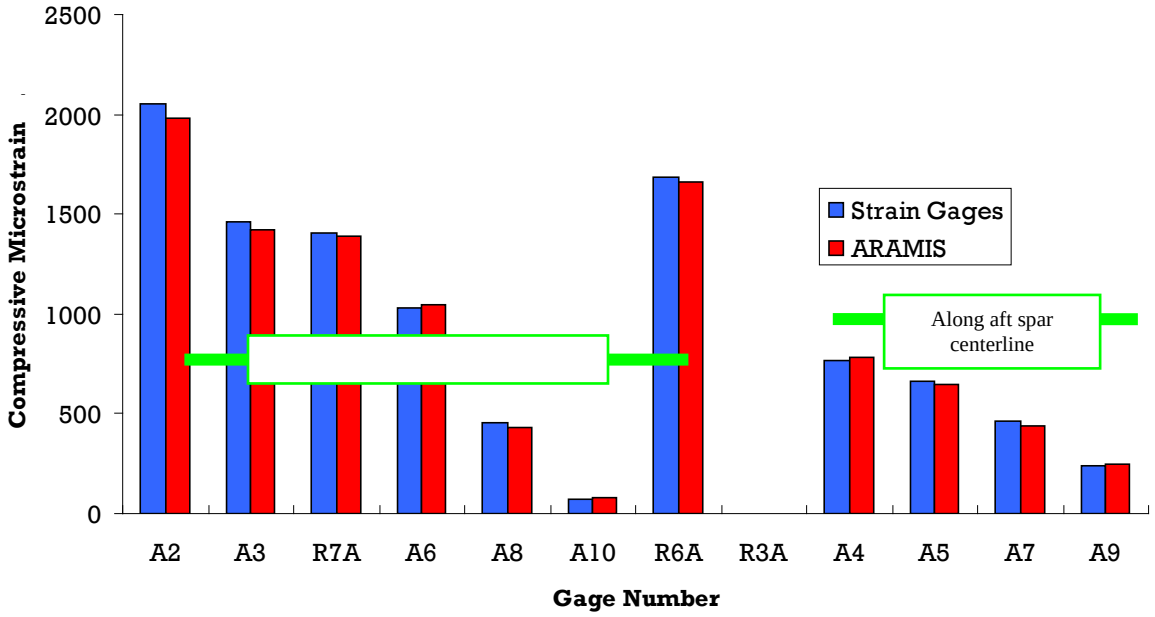

Figure D-6. Comparison of ARAMIS and strain gage data along front and aft spars of ST001

D.2 THE ST002—STARSHIP FORWARD WING FULL-SCALE STATIC TEST

The second full-scale static test article, ST002, was tested with a similar strain gage arrangement to ST001, except for the axial gages A9–A11 and the rosette R3 (these gages were replaced by the axial gages A12–A14 and the rosette R8, respectively). Gage A12 was placed at FWS 46.6, where the leading edge assembly fastener pitch increases; gage A14 was installed over the front spar at FWS 134.05; and gage A13 was installed at FWS 137.45 over the closure rib on the tip fairing (figure D-7).

Prior to installing the whiffletree, a point load was applied at FWS 100 in stepwise while recording the strain gage data, so that the full-field strain survey could be performed. This allowed the photogrammetry sensors to be placed at a distance further away from the upper skin to capture data from a larger field of view. The upper skin was divided into three overlapping segments for ARAMIS measurements so that the data could be "stitched" as a single image. The maximum applied point load was 1059.26 lbf, and the corresponding maximum strain was recorded as -962.7 microstrain from gage A2. Figure D-8 shows the full-field axial strain and a comparison of the ARAMIS and strain gage data along the front and aft spars.

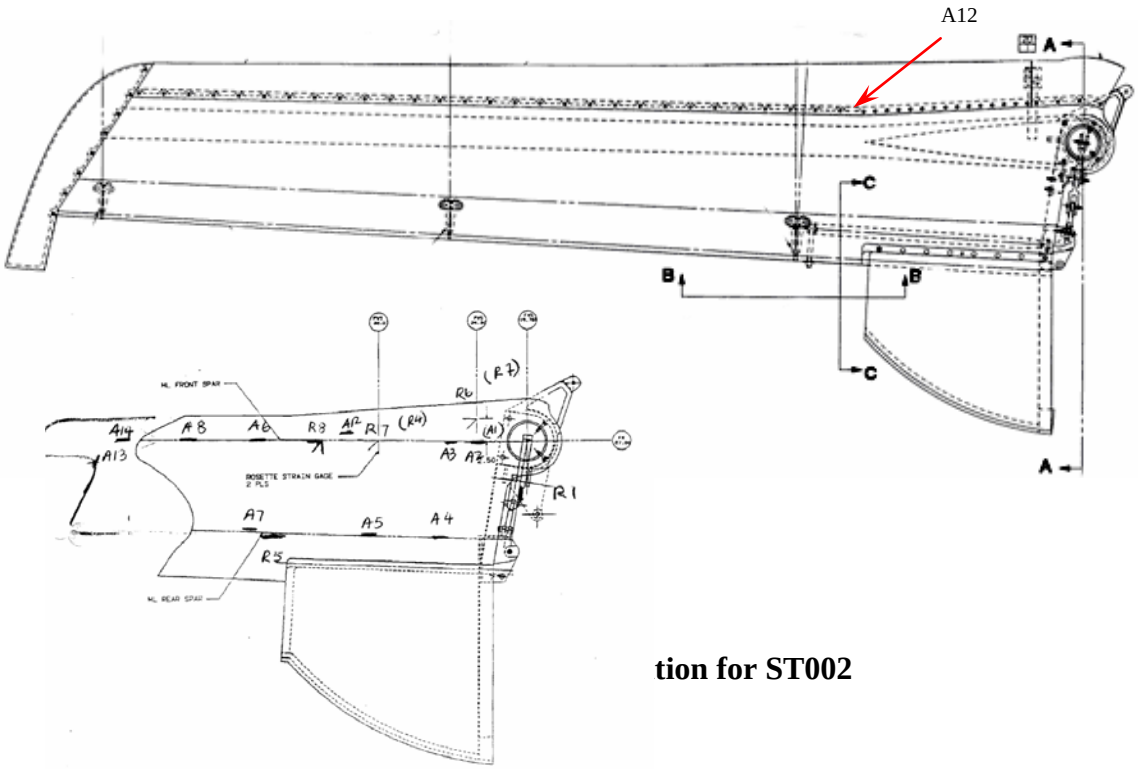

tion for ST002

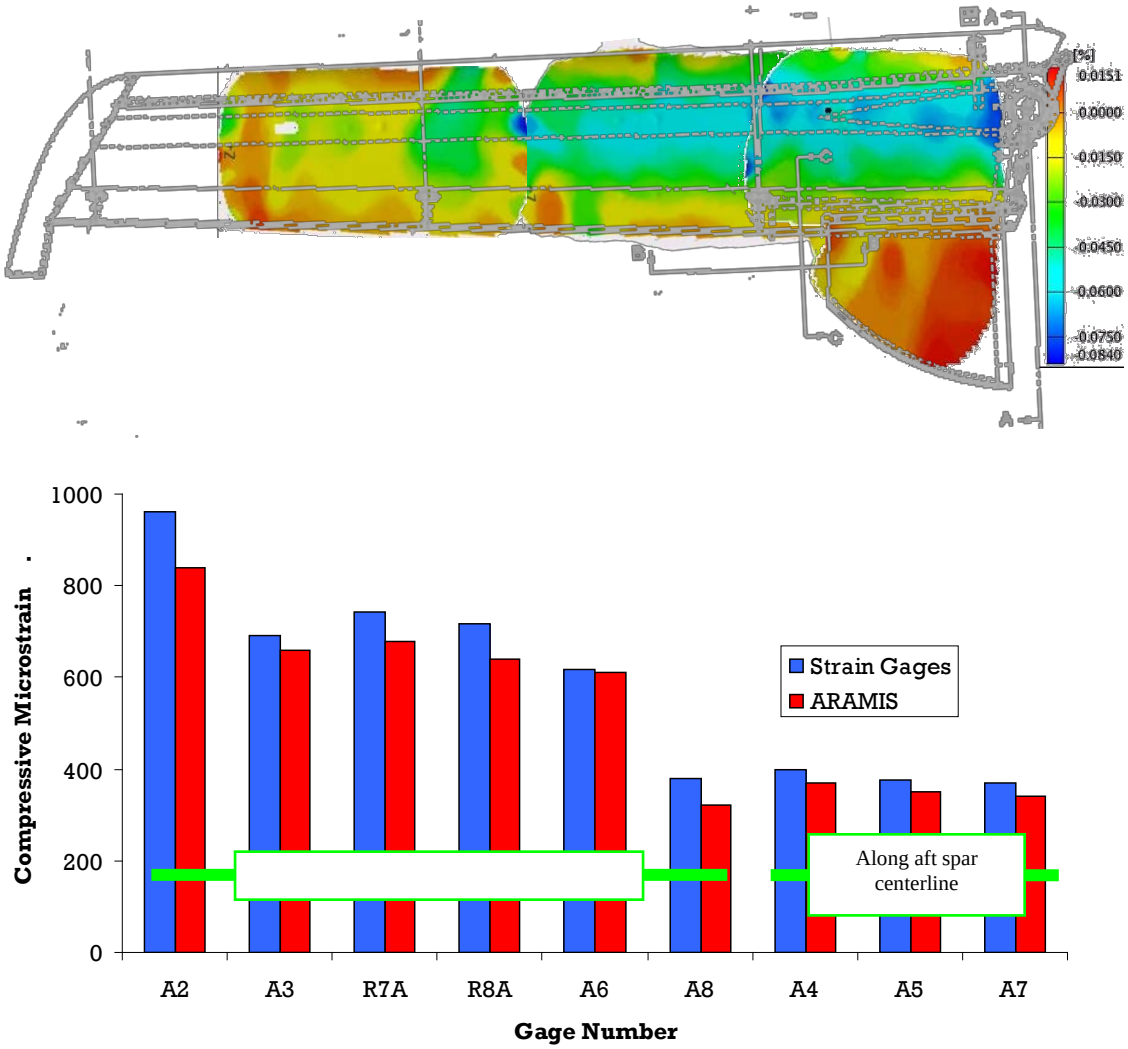

Figure D-8. Full-field strain survey and comparison with strain gage data for ST002

During quasi-static loading of ST002 with the whiffletree test setup, the load was initially applied in 5% increments until BDLL and then continuously until fracture. The vertical displacement gages indicated minimal twisting of the article during loading (figure D-9). The strain gages on the aft spar towards the root end (A4) indicated a sudden decrease in strain followed by an audible noise indicating an initial debond/delamination around 185% of BDLL (figure D-10). Rosette R1 located at the root rib (figure D-11) also indicated sudden changes in strain data around this load level.

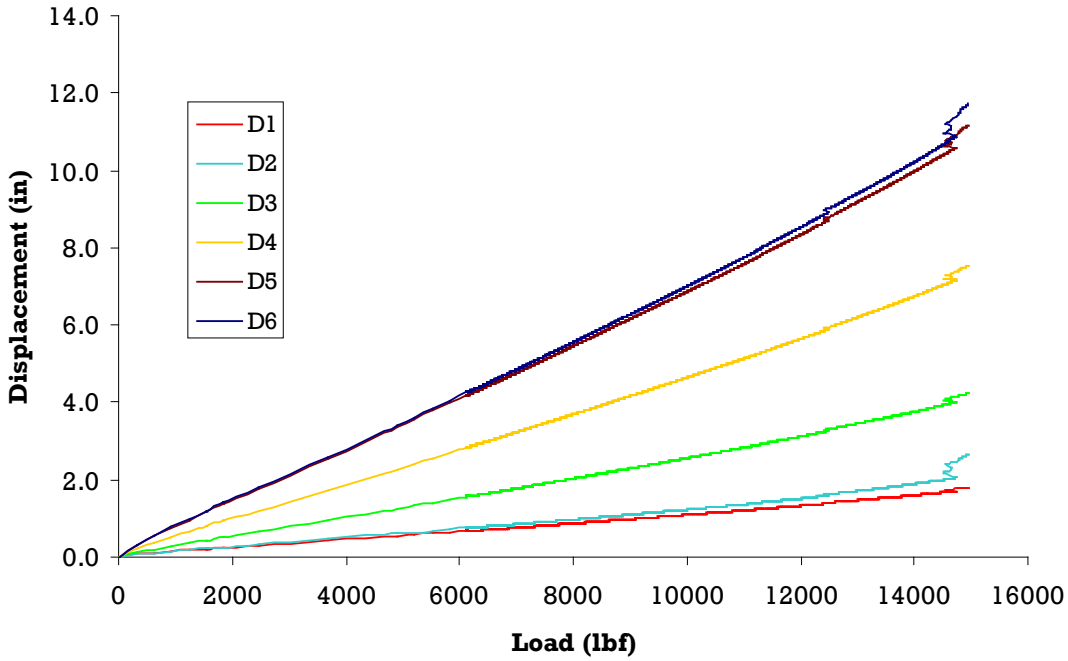

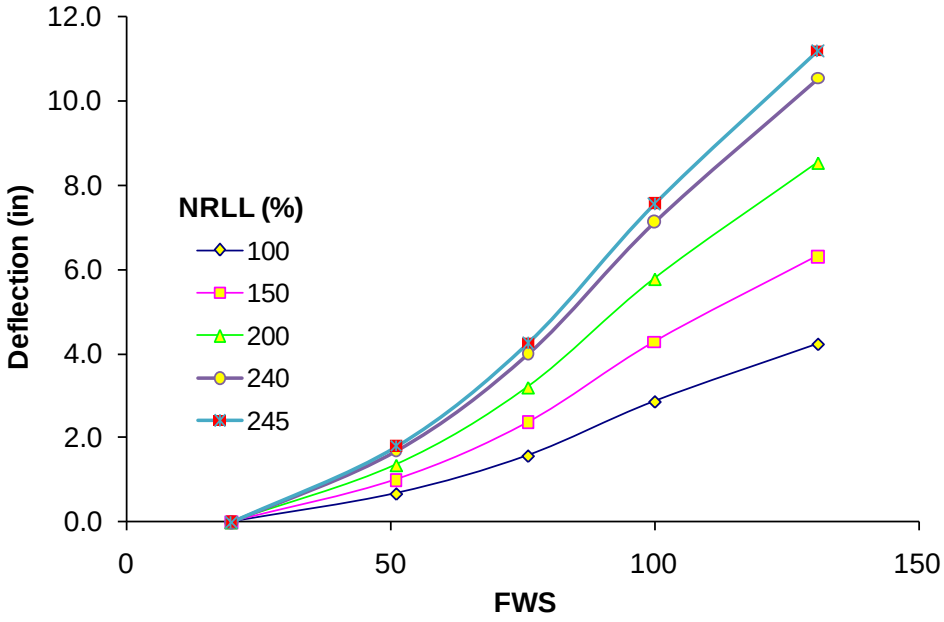

Figure D-9. Vertical displacements—ST002

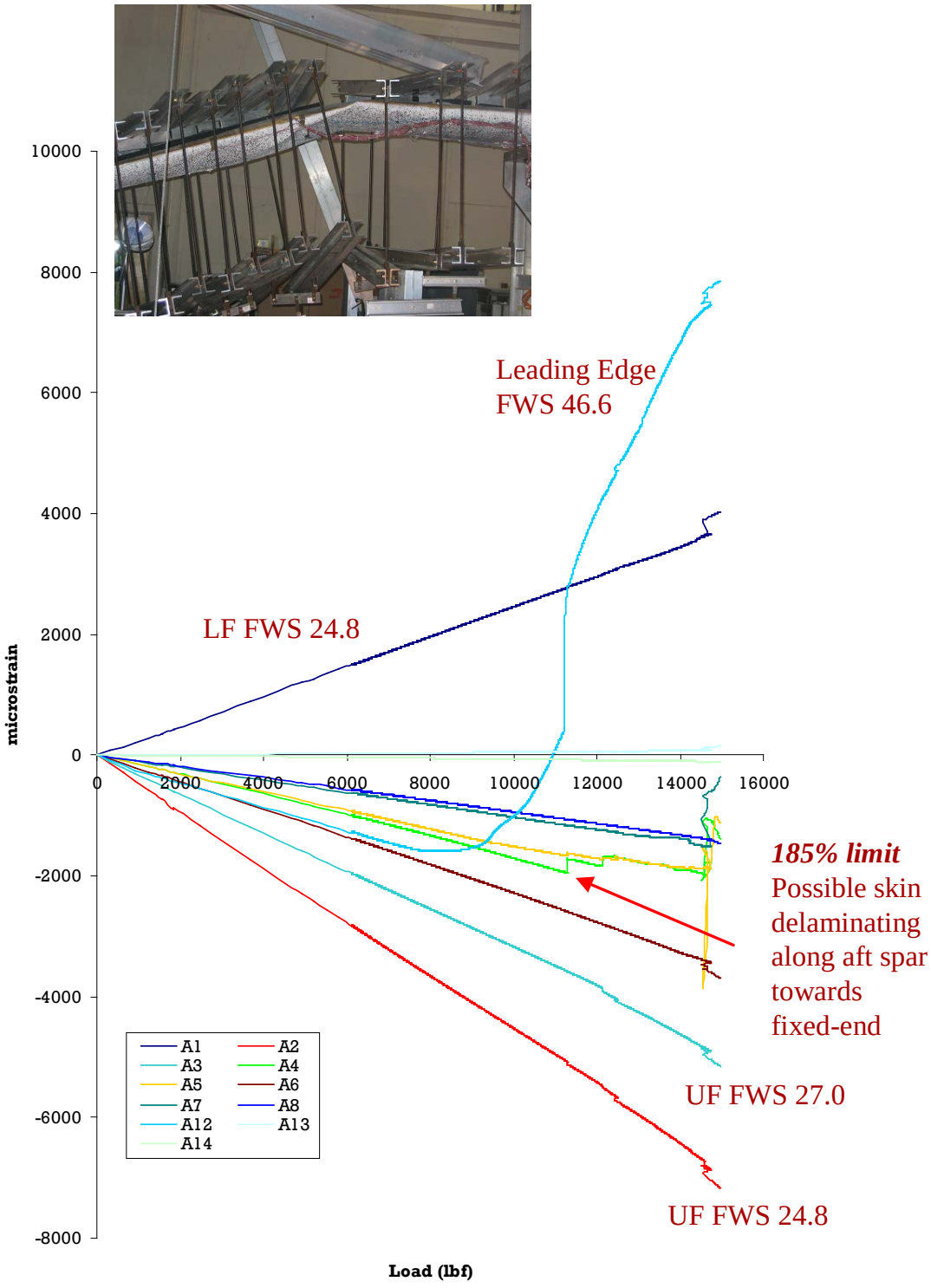

Figure D-10. Axial strain gage data for ST002

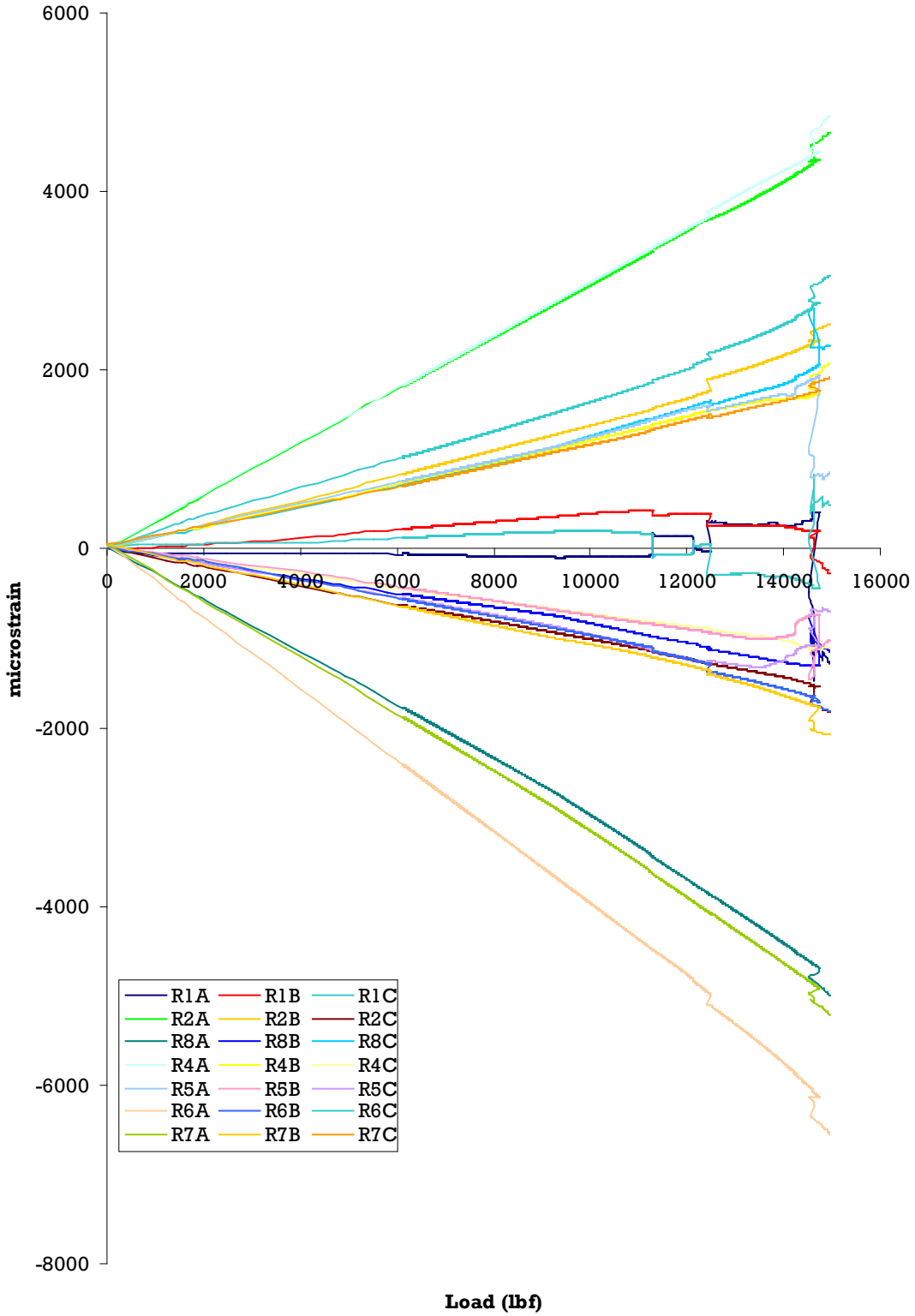

Figure D-11. Strain rosette data for ST002

D.3 THE ST003—FULL-SCALE STATIC TEST

The third full-scale static test article, ST003, was tested with modified strain gage locations to detect damage initiation and propagation around the fracture locations noted during the ST002 test. Strain gage locations are shown in figure D-12. Eight axial gages and eight rosettes were mounted. Axial gages A2 and A6 were replaced by rosettes R9 and R10. Rosette R7 was replaced with axial gage A15. Rosette R6 was removed and rosette R11 was added at FWS 59.5 on aft spar.

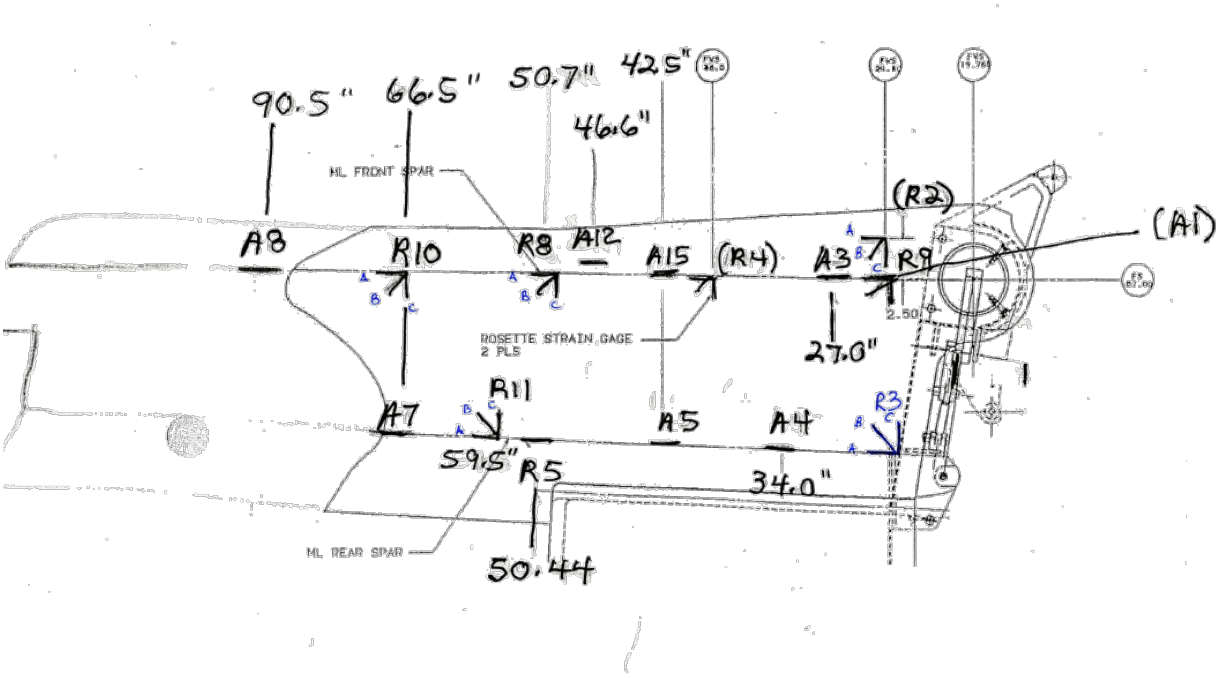

Figure D-12. Strain gage locations for ST003

As with ST002, a point load was applied at FWS 100 and the full-field strain survey was conducted. The maximum point load was 1000 lbf and the corresponding maximum strain was -677.8 microstrains recorded from rosette R9A. Figure D-13 shows the stitched full-field axial strain and a comparison of the ARAMIS and strain gage data.

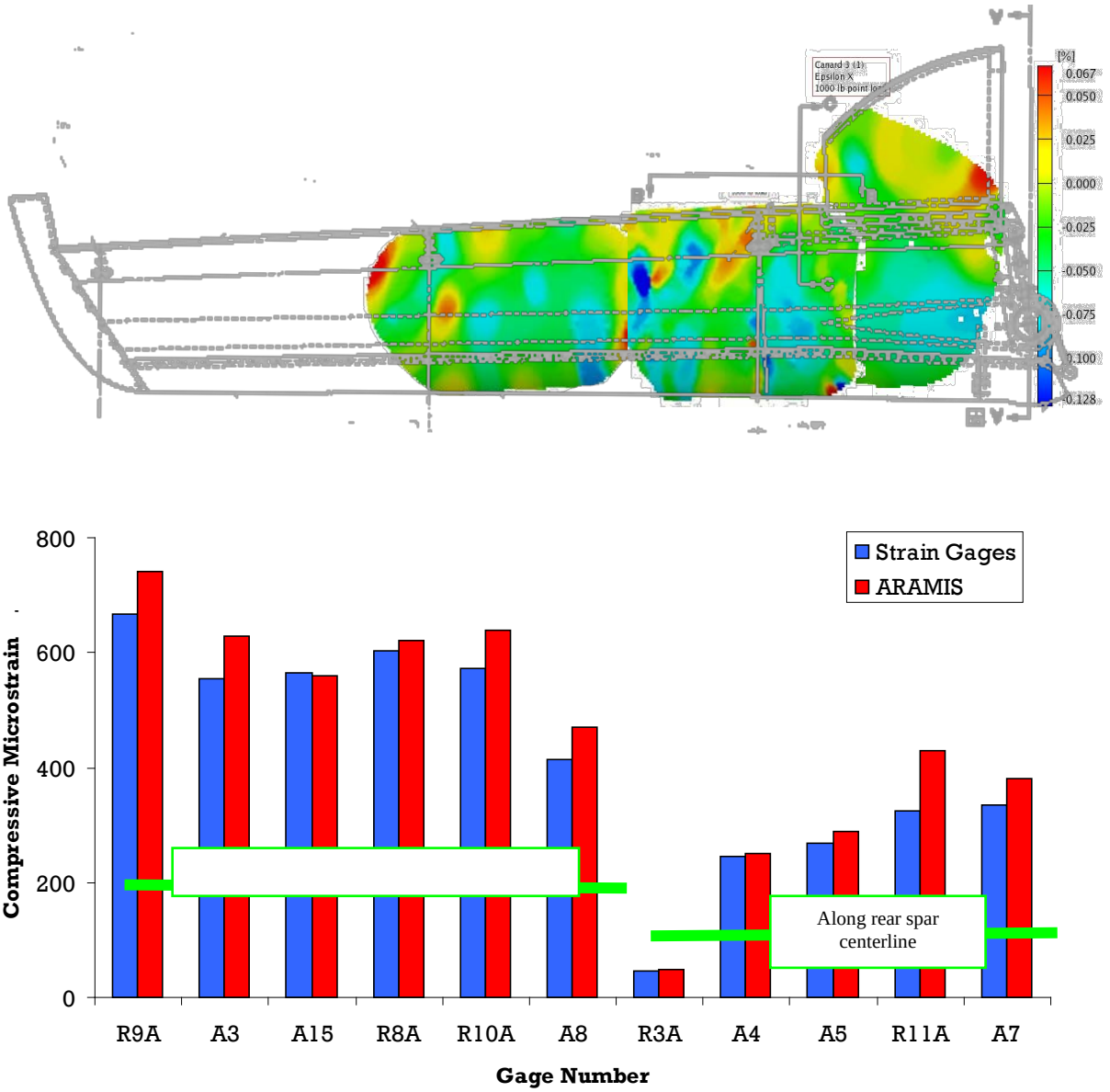

Figure D-13. Full-field strain survey and comparison with strain gage data for ST003

Figure D-14 shows the vertical displacement reading of ST003 during quasi-static loading with the whiffletree test setup. Figure D-15 shows the axial strain data during static loading. Axial gage A12 indicated leading-edge buckling around 4000 lbf. Axial gage A4 and rosette R3 (figure D-16) indicated delamination between top skin along aft spar that was initiated at the root end.

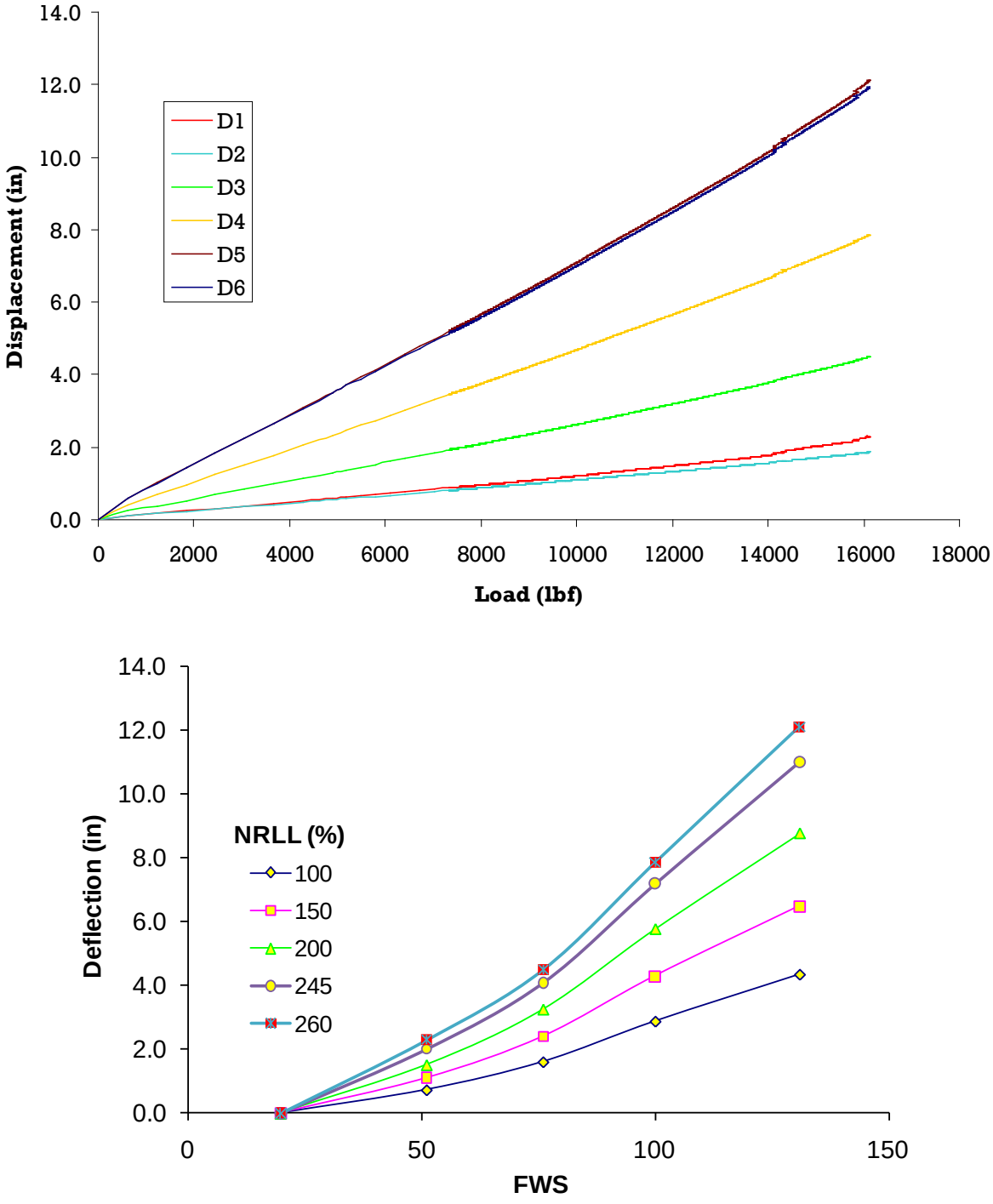

Figure D-14. Vertical displacements—ST003

The strain gage data along the front (F) and aft (A) spar on the upper (U) and lower (L) skins were compared for all three full-scale static test articles in figure D-17 at 100% and 200% BDLL. Overall strain distributions along both the front and aft spars for all three static articles were comparable.

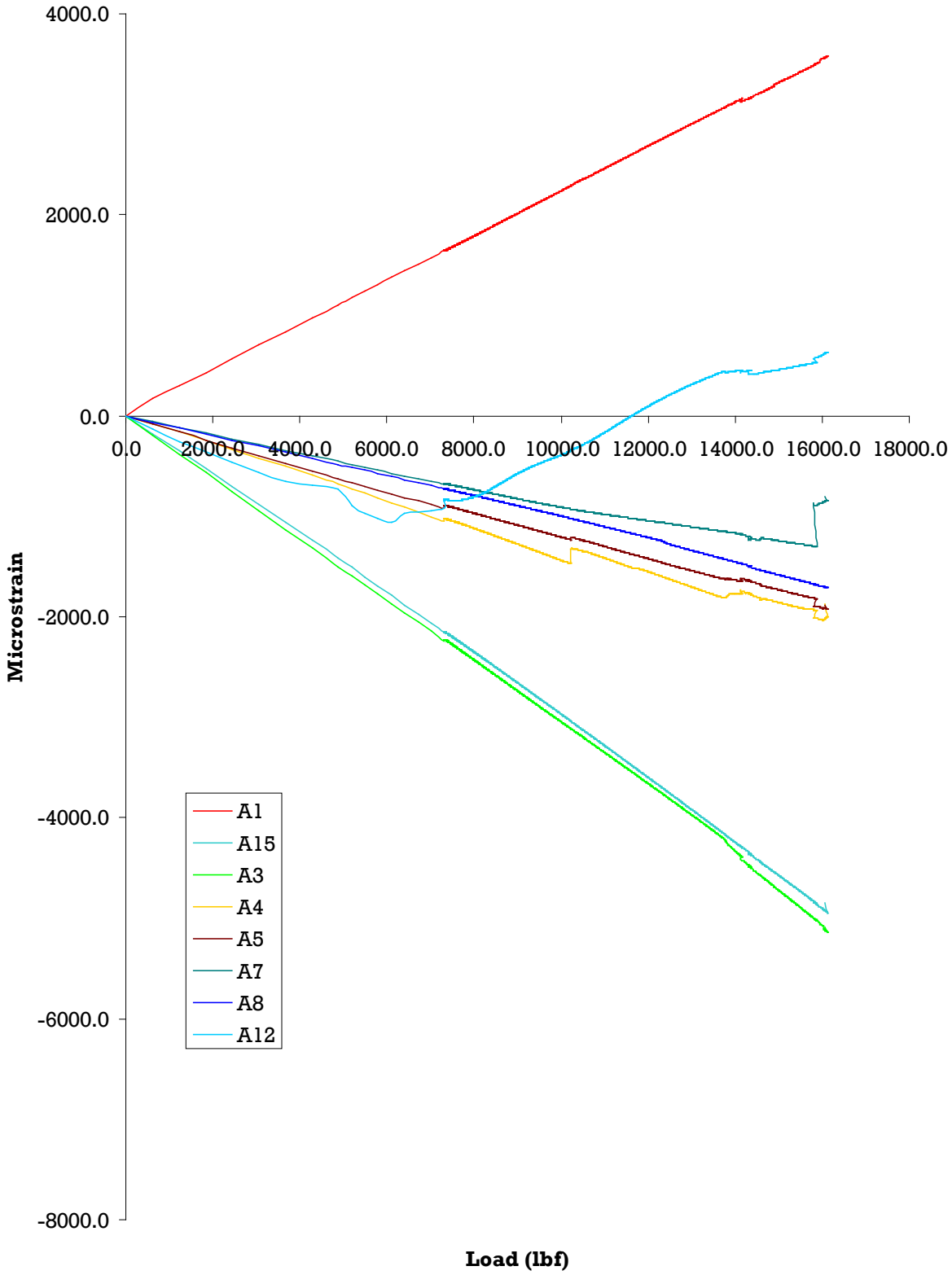

Figure D-15. Axial strain gage data for ST003

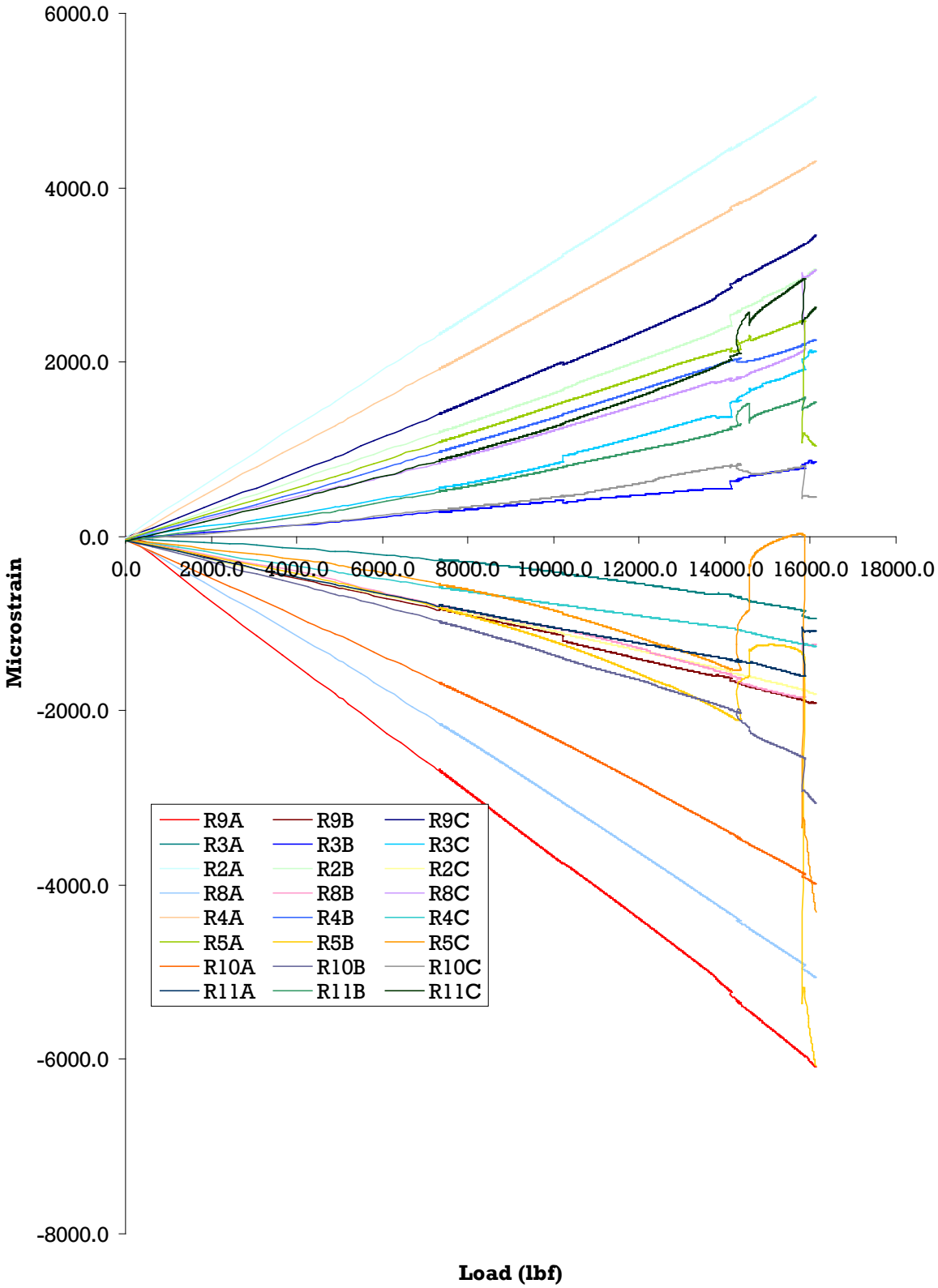

Figure D-16. Strain rosette data for ST003

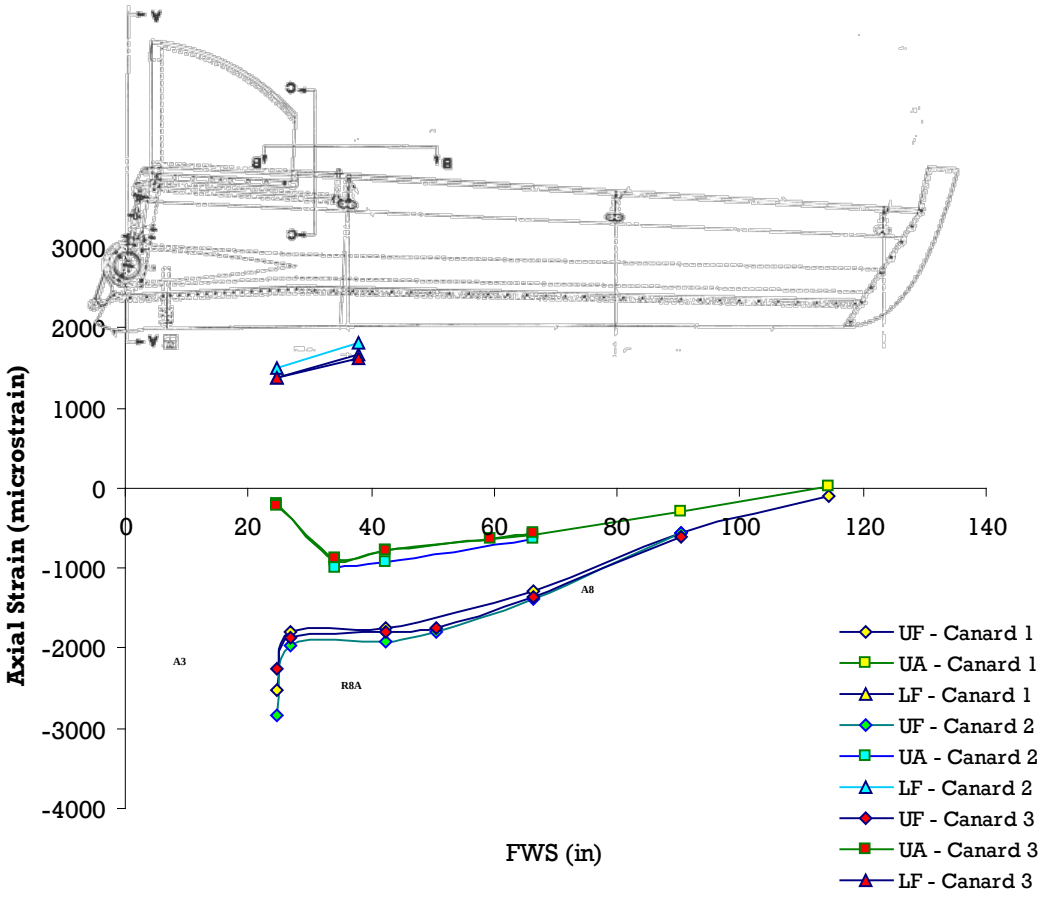

(a) 100% BDLL

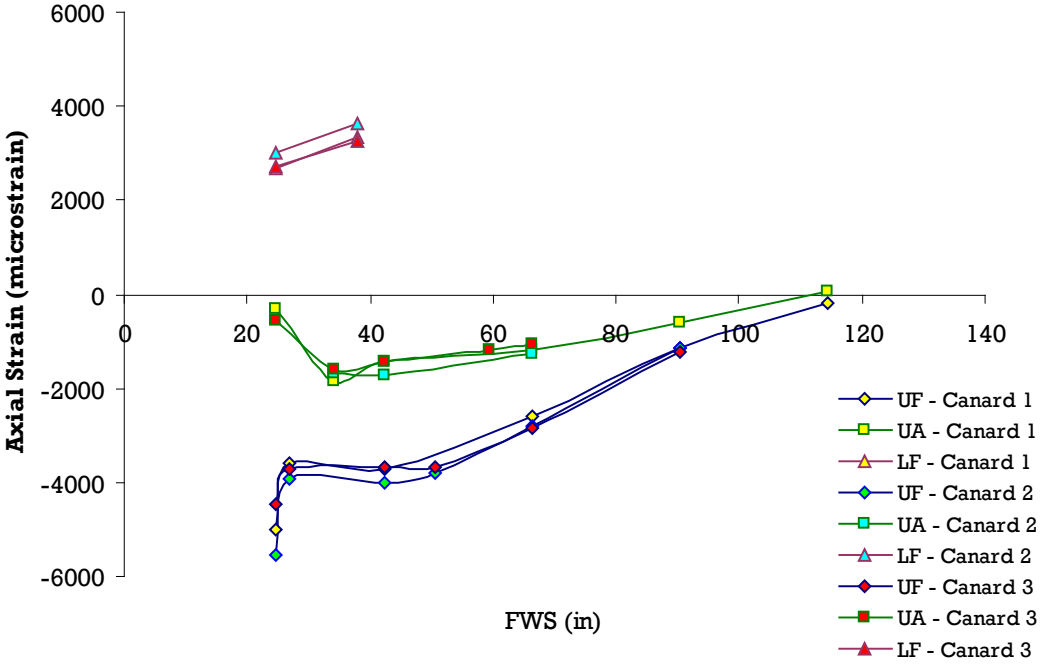

(b) 200% BDLL

Figure D-17. Strain comparison for all three test articles

D.4 THE ST001(R)—FULL-SCALE DAMAGE TOLERANCE TEST

The third full-scale static test, ST001(R), was tested with impact damage at FWS 45 on the top skin of the aft spar. Eleven axial gages, three biaxial gages, and nine rosettes were used for strain measurements for article ST001(R), as shown in table D-2 (see figure 66 in section 5.4.1.1 of the main document). The following gage locations were also used for the ST004 DaDT test article.

Table D-2. Strain gage locations of ST001(R)

Strain Gage Number			Location
Axial	Biaxial	Rosette	
A1			Lower skin FWS 24.8 on fwd spar
A2			Upper skin FWS 24.8 on fwd spar
A3			Upper skin FWS 27.0 on fwd spar
A4			Upper skin FWS 34.0 on aft spar
A5			Upper skin FWS 42.5 on aft spar
A6			Upper skin FWS 66.5 on fwd spar
A7			Upper skin FWS 66.5 on aft spar
A8			Upper skin FWS 90.5 on fwd spar
A9			Upper skin FWS 90.5 on aft spar
A10			Upper skin FWS 114.5 on fwd spar
A11			Upper skin FWS 114.5 on aft spar
		R1	Root Rib at upper forward corner
		R2	Lower skin FWS 24.8 and 2.5 forward of fwd spar
		R3	Upper skin FWS 24.8 on aft spar
		R4	Lower skin FWS 38.0 on fwd spar
		R5	Centered on Aft web at FWS 50.44
		R6	Upper skin FWS 24.8 and 2.5 forward of fwd spar
		R7	Upper skin FWS 42.5 on fwd spar
		R12	Upper skin at FWS 45 and 2.05 forward of aft spar
		R13	Upper skin at FWS 47 on aft spar
	B1		Upper skin at FWS 45 and 2.3 aft of aft spar
	B2		Rear spar web at 43.44
	B3		Rear spar web at 38.84

In addition to A5, which was mounted closer to the damage location, R12, R13, and B1 rosettes were mounted to monitor damage propagation. Furthermore, three gyro-enhanced orientation sensors (MicroStrain® model 3DM-GX1®) and one high-sensitivity accelerometer (Crossbow Technology CXL-LF series) were mounted, as shown in figure 66 in the main document, to support a validation of a health-monitoring technique (for discovering and recovering the unused service life) developed by Boeing Phantom Works™, St. Louis, Missouri.

Figure D-18 shows the vertical displacement results for the ST001(R) static test article. Displacement gages D1 and D2 indicated that there was a rotation of the test article in the $-T_Y$ direction (reference axis system may be found in figure C-1 of appendix C) at the root end, possibly due to damage propagation. The axial strain gages (figure D-19), biaxial gages (figure D-20), and rosettes (figure D-21) around the damage location indicated significant nonlinearity due to damage propagation.

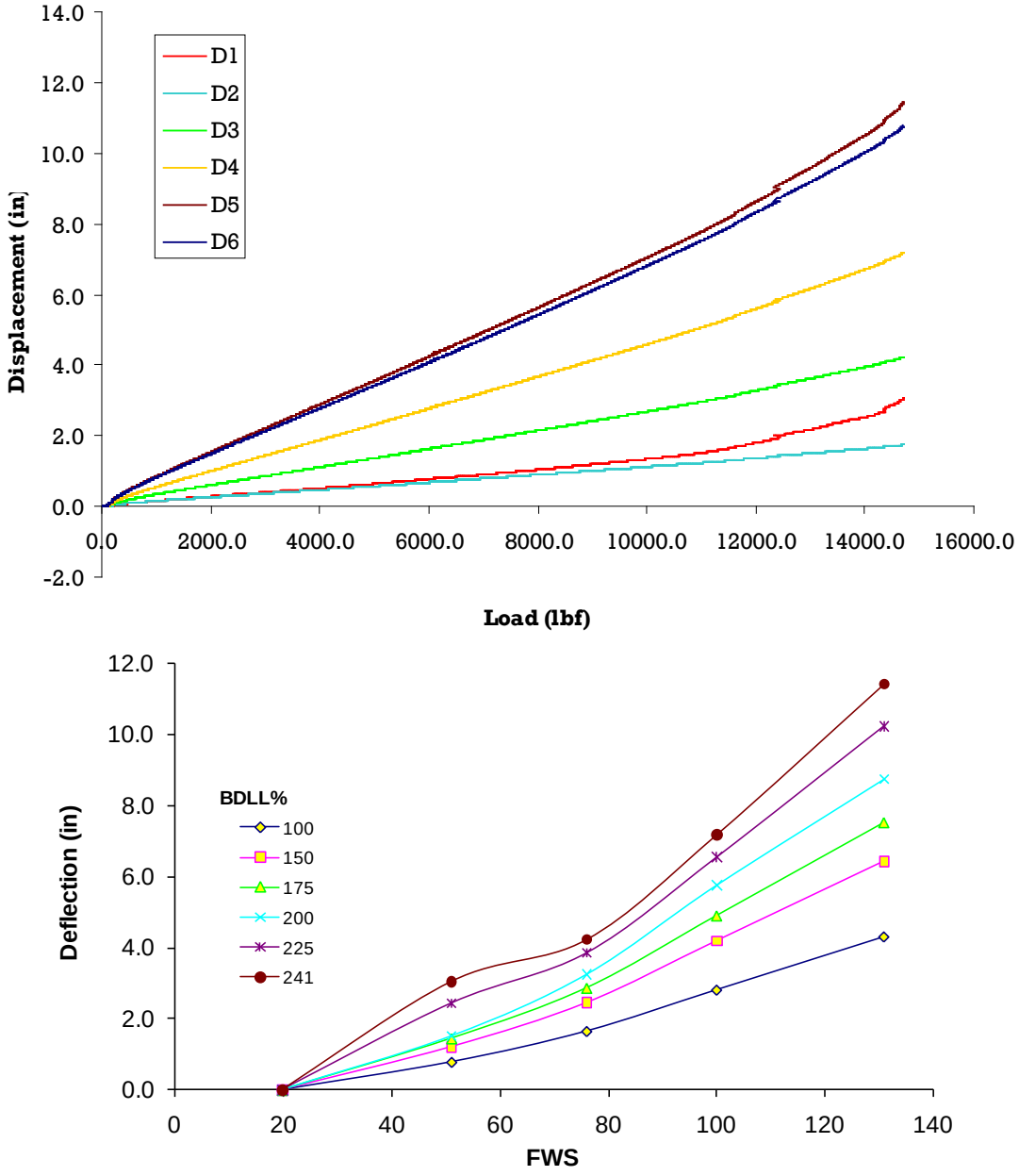

Figure D-18. Vertical displacements—ST001(R)

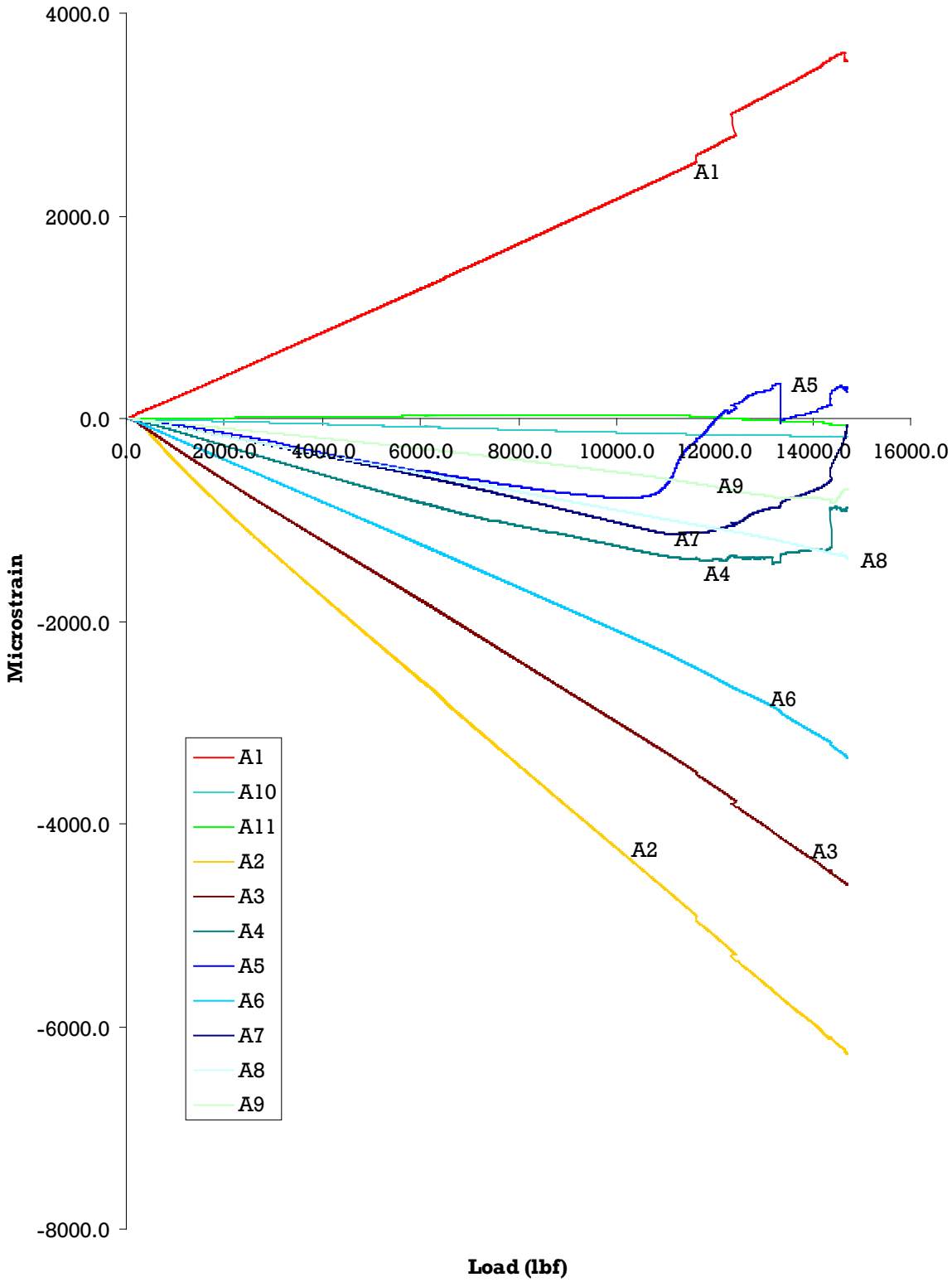

Figure D-19. Strains from axial gages—ST001(R)

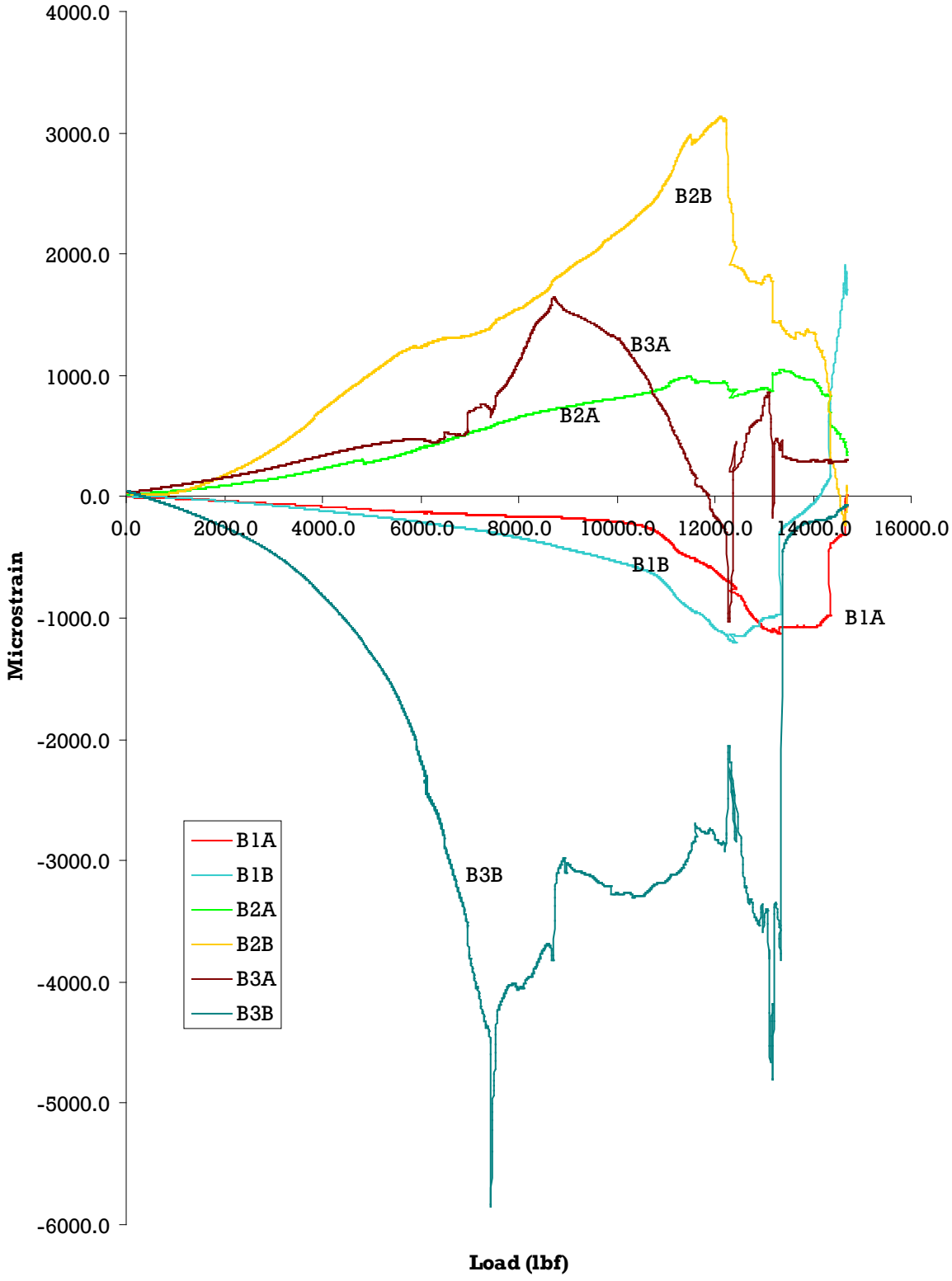

Figure D-20. Strains from biaxial gages—ST001(R)

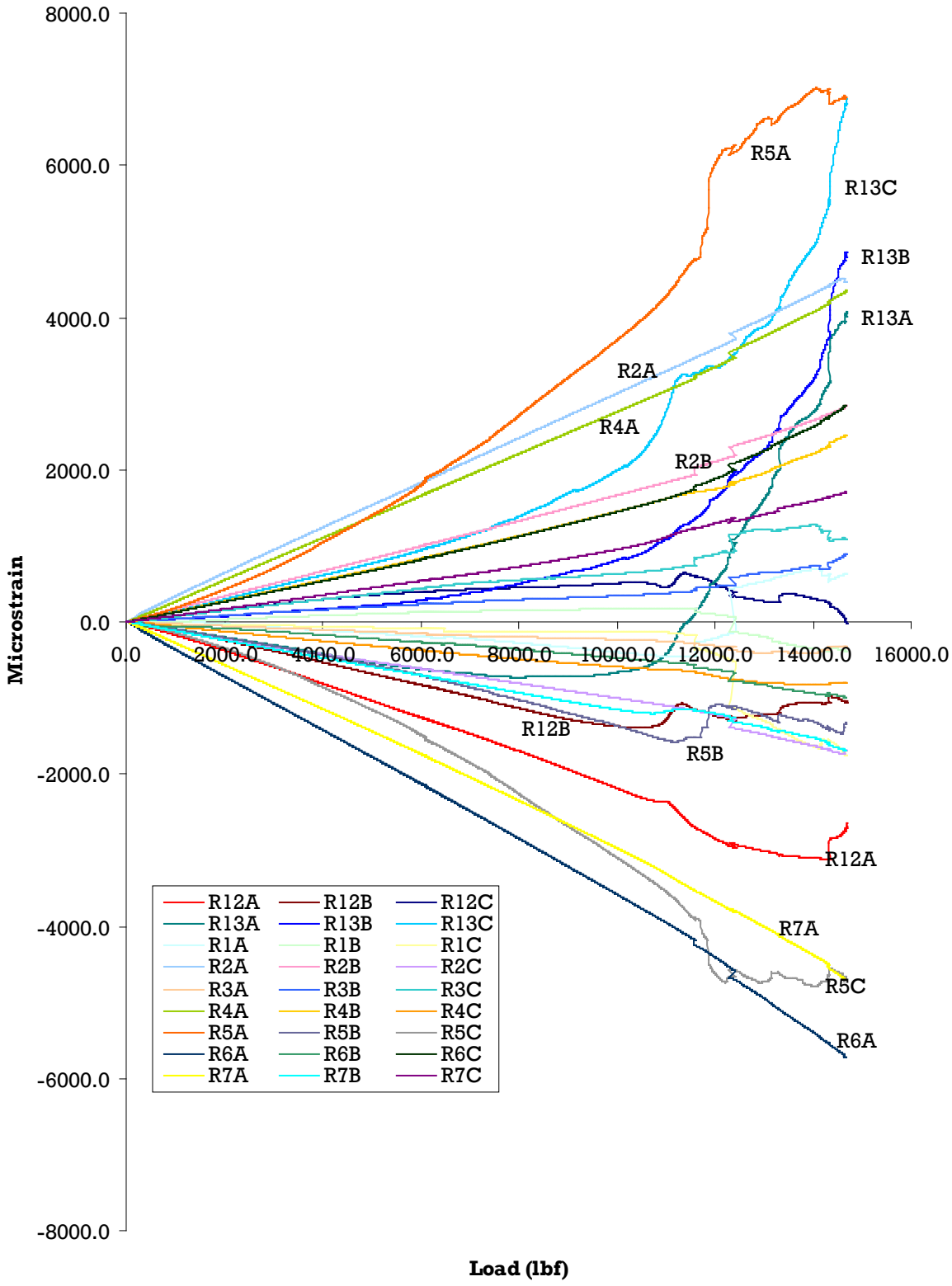

Figure D-21. Strains from rosettes—ST001(R)

D.5 RESIDUAL STRENGTH TEST DATA OF ST004 AFTER 2 DESIGN LIFETIME CYCLIC TEST.

Table D-3 shows the strain gage locations of the ST004 DaDT test article. They are shown in figures 73 and 74 of the main report.

Table D-3. Strain gage locations of ST004

Strain Gage Number			Location
Axial	Bi-Axial	Rosette	
A1			Lower skin FWS 24.8 on fwd spar
A2			Upper skin FWS 24.8 on fwd spar
A3			Upper skin FWS 27.0 on fwd spar
A16			Upper skin FWS 37.0 on aft spar
A17			Upper skin FWS 39.0 on aft spar
A18			Upper skin FWS 51.75 on aft spar
A19			Upper skin FWS 64.7 on fwd spar
A20			Upper skin FWS 64.7 on aft spar
		R2	Lower skin FWS 24.8 and 2.5″ forward of fwd spar
		R3	Upper skin FWS 24.8 on aft spar
		R4	Lower skin FWS 38.0 on fwd spar
		R5	Centered on aft web at FWS 50.44
		R6	Upper skin FWS 24.8 and 2.5″ forward of fwd spar
		R7	Upper skin FWS 42.5 on fwd spar
		R14	Upper skin FWS 44.0 and 4.5″ forward of aft spar
		R15	Upper skin FWS 49.7 and 5.0″ on aft spar
	B4		Upper skin FWS 44.0 and 4.45″ on aft spar

Figure D-22 shows the displacement results for post-DaDT residual strength of ST004. Displacement gages D1 and D2 indicated that there was a rotation of the test article in the $-T_Y$ direction (reference axis system may be found in figure C-1 of appendix C).

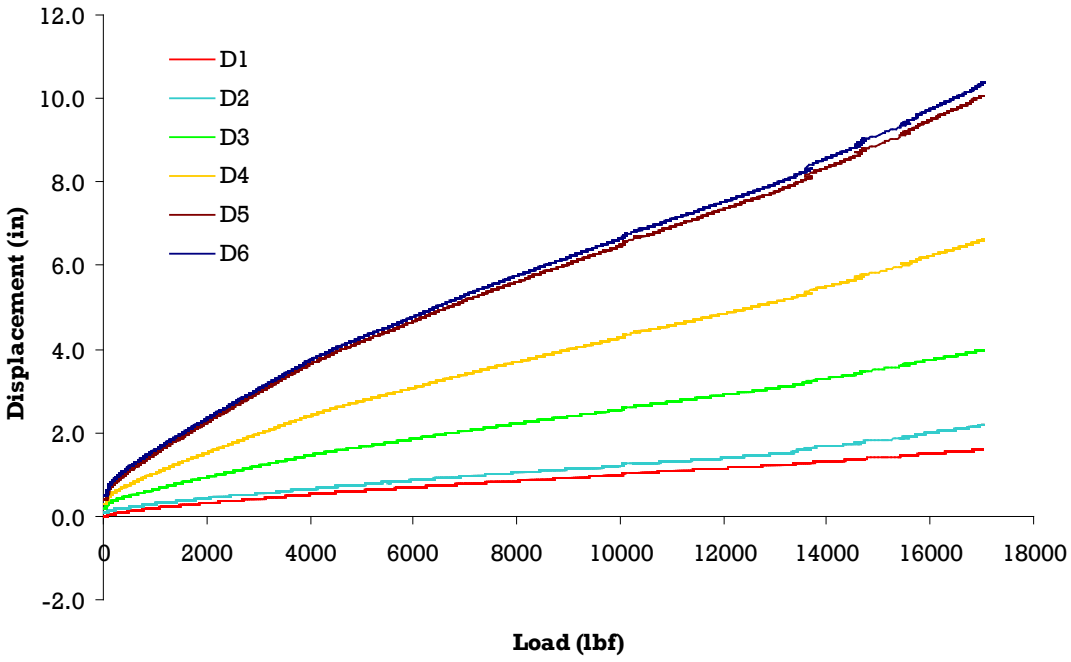

Figure D-22. Vertical displacements—ST004

Figure D-23 shows the strain gage reading around the impact damage on aft spar (top skin) of the ST004 test article during the post-DaDT residual strength test.

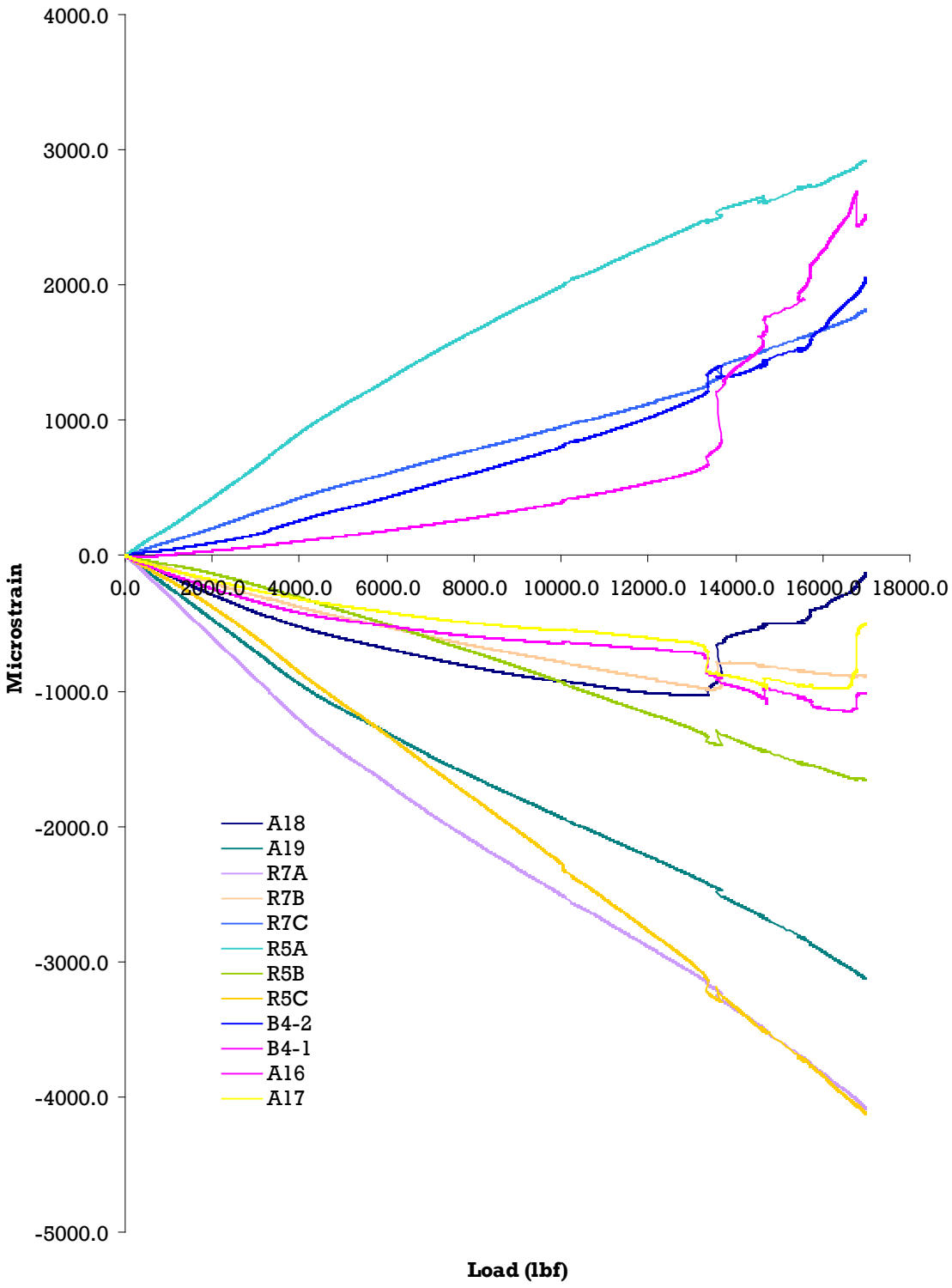

Figure D-23. Strains around category 2 damage—ST004

D.6 STATIC STRENGTH TEST DATA FOR ST005

The following gage locations were used for the ST005 DaDT test article (table D-4). They are shown in figure 70 of the main report.

Table D-4. Strain gage locations of ST005

Strain Gage Number			Location
Axial	Biaxial	Rosette	
A1			Lower skin FWS 24.8 on fwd spar
A2			Upper skin FWS 24.8 on fwd spar
A3			Upper skin FWS 27.0 on fwd spar
A7			Upper skin FWS 66.5 on aft spar
A8			Upper skin FWS 90.5 on fwd spar
A21			Upper skin FWS 38.25 on fwd spar
A22			Upper skin FWS 38.25 on aft spar
A23			Lower skin FWS 38.0 on fwd spar
		R1	Root sib at upper forward corner
		R2	Lower skin FWS 24.8 and 2.5″ forward of fwd spar
		R3	Upper skin FWS 24.8 on aft spar
		R7	Upper skin FWS 42.5 on fwd spar
		R16	Upper skin FWS 63.0 on fwd spar (2″ inboard of damage location FWS 65.0″)
		R17	Upper skin FWS 65.0 on fwd spar (2″ aft of damage location FWS 65.0″)
		R18	Upper skin FWS 67.0 on fwd spar (2″ outboard of damage location FWS 65.0″)
	B5		Upper skin FWS 50.7 centered between fwd and aft spar
	B6		Upper skin FWS 65.0 (2″ fwd of damage location FWS 65.0″)
	B7		Lower skin FWS 65.0 (2″ fwd of damage location FWS 65.0″)
	B8		Upper skin FWS 65.0 centered between fwd and aft spar

Figure D-24 shows the displacement results for the ST005 static test article. Displacement gages D1 and D2 indicated that there was a rotation of the test article in the $-T_Y$ direction (reference axis system may be found in figure C-1 of appendix C). Figures D-25–D-27 show the strain gage reading of the ST005 test article during the state strength test.

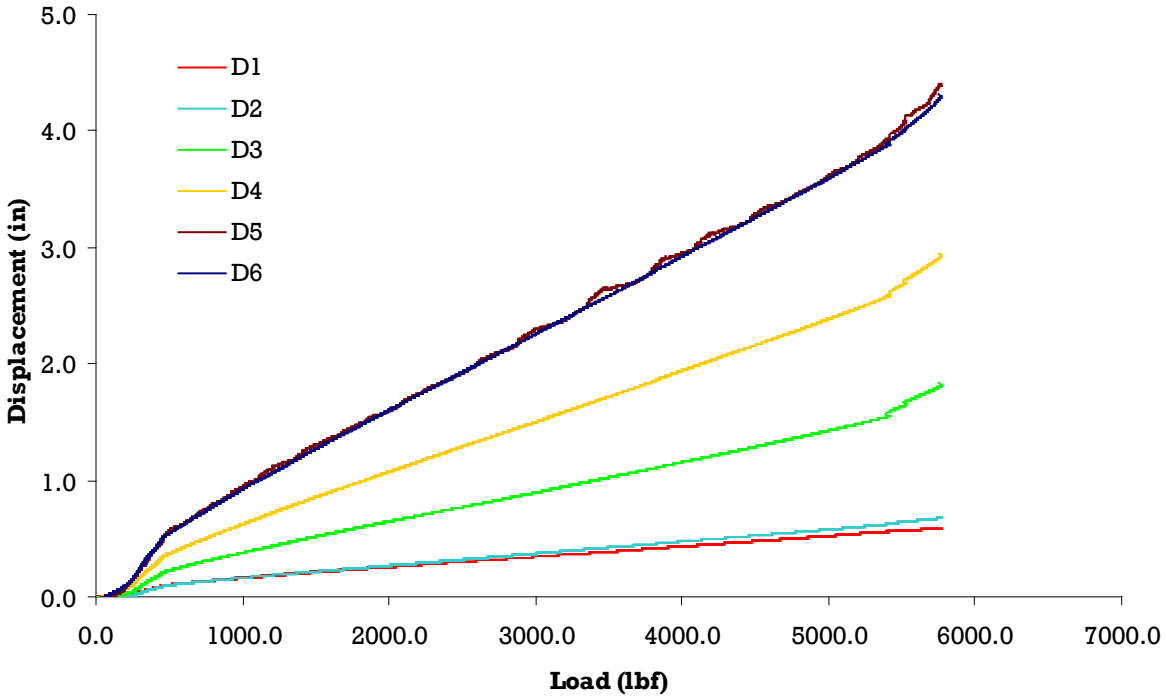

Figure D-24. Vertical displacements—ST005

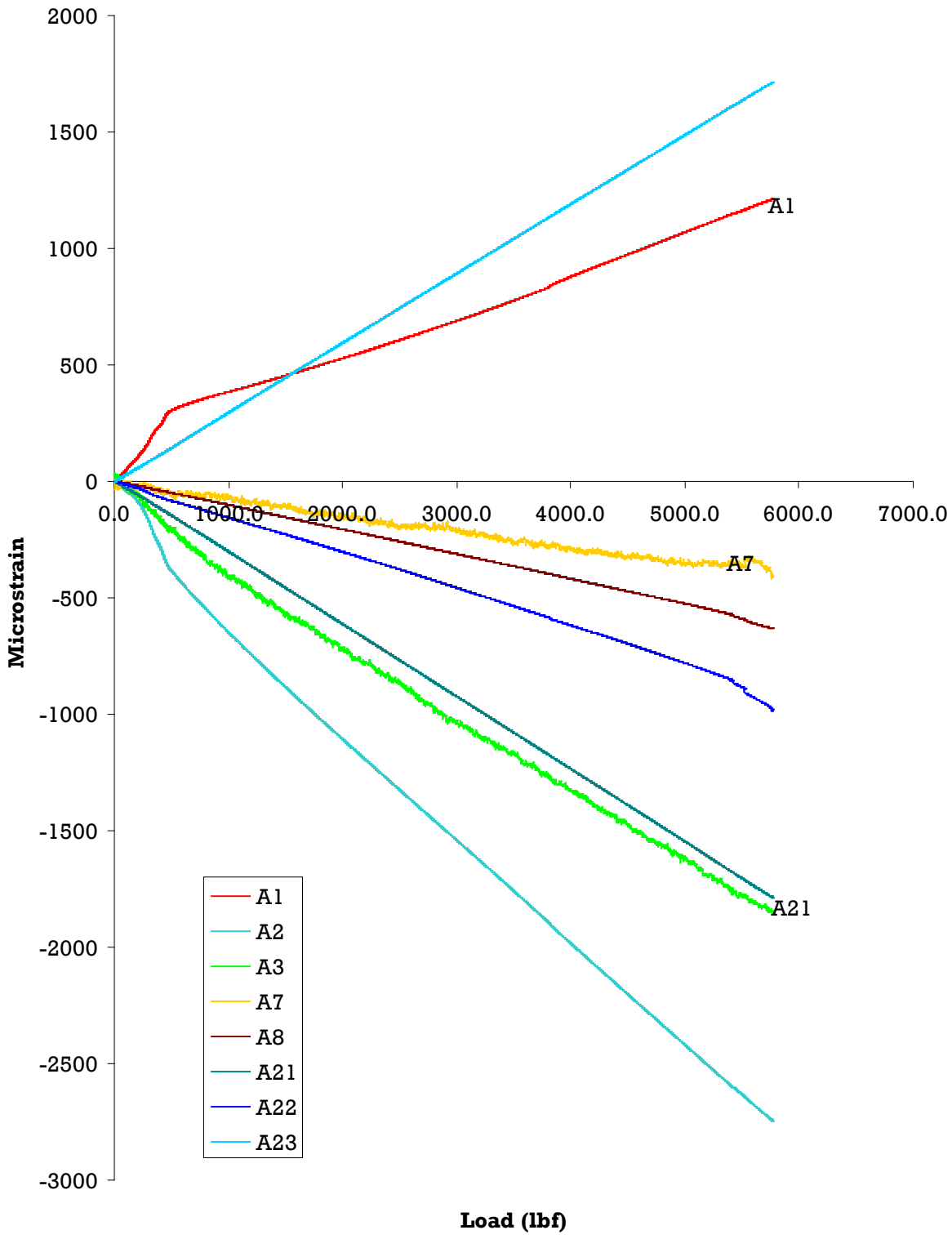

Figure D-25. Strains from axial gages—ST005

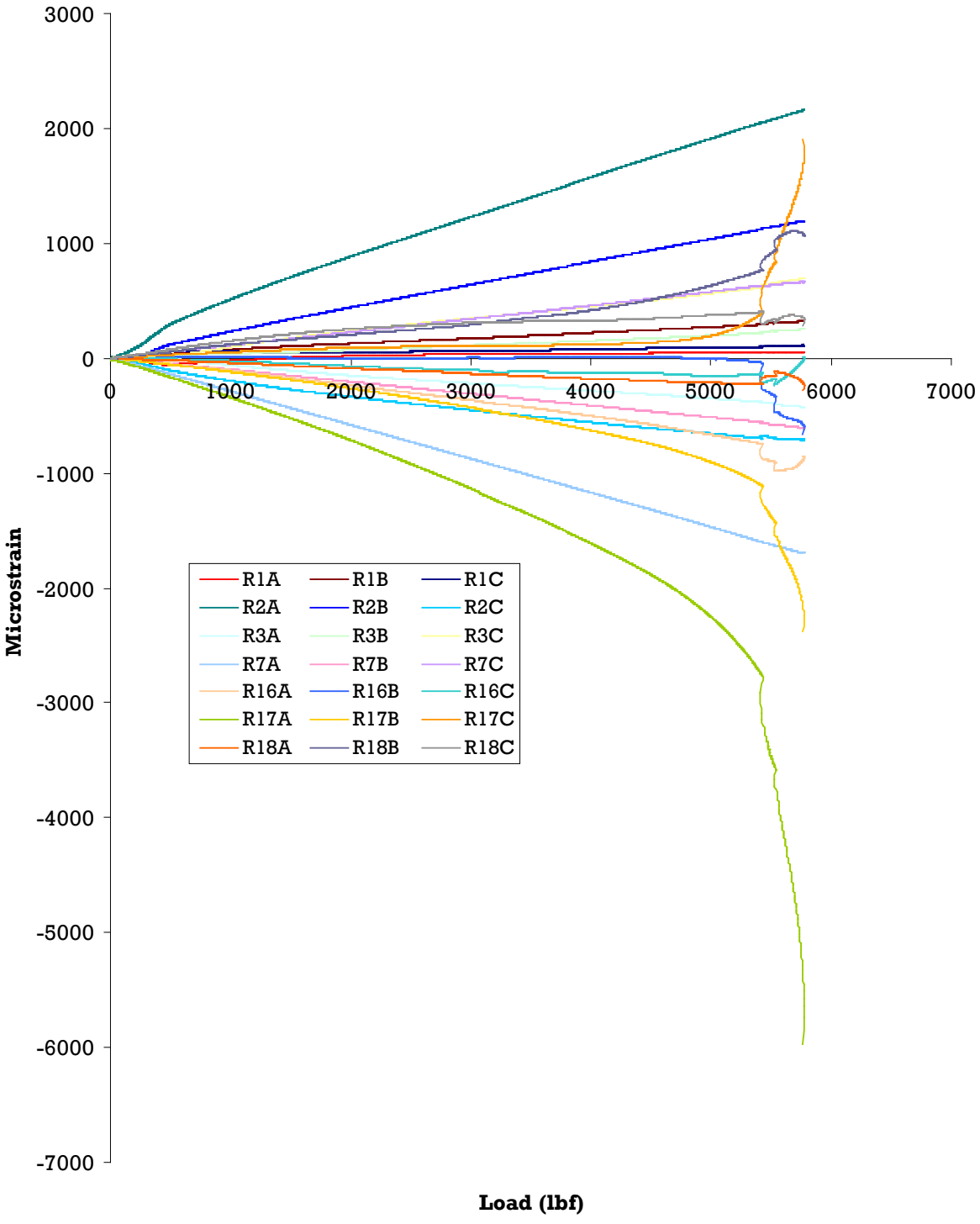

Figure D-26. Strains from rosettes—ST005

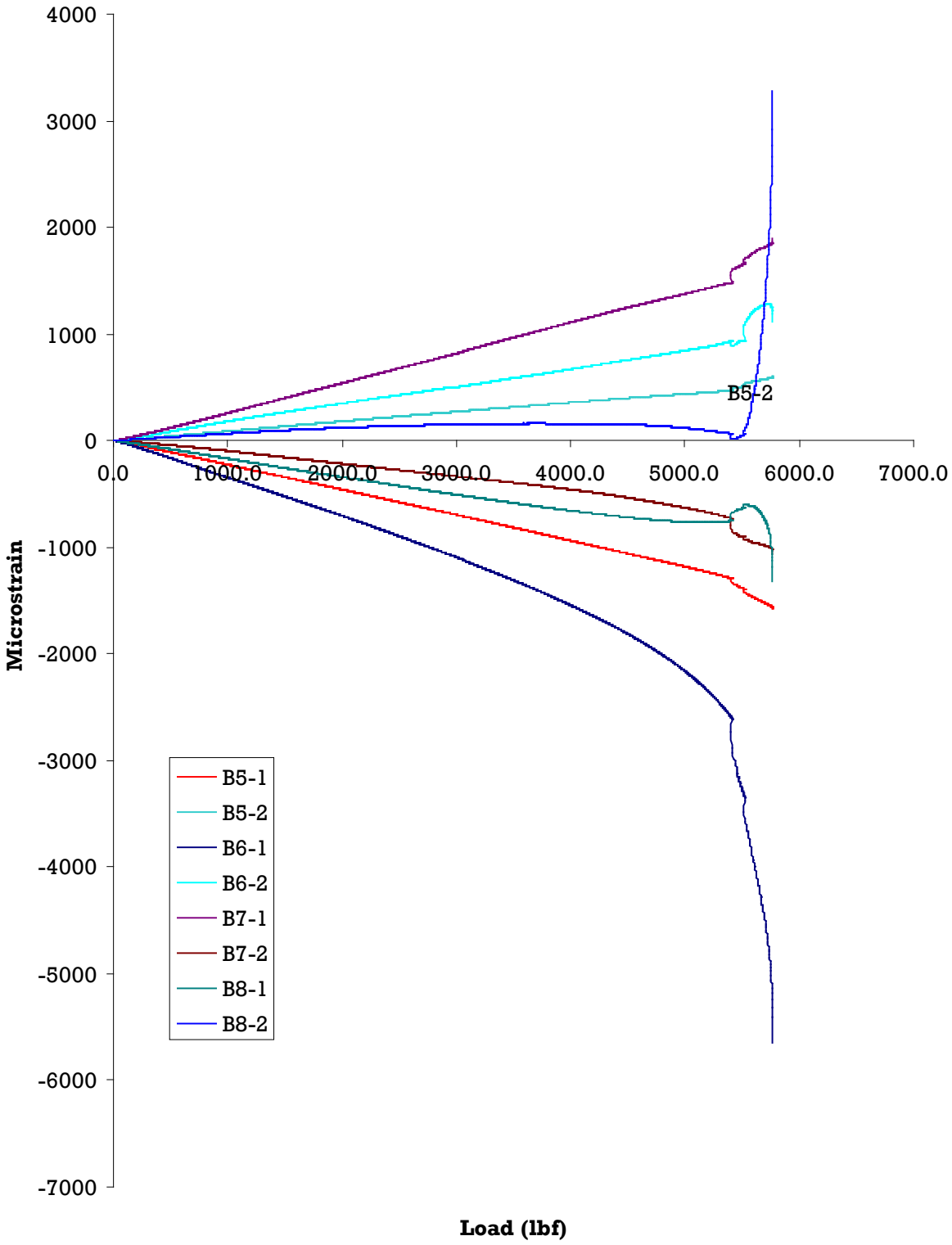

Figure D-27. Strains from biaxial gages—ST005

D.7 RESIDUAL STRENGTH TEST DATA OF ST006 AFTER 0.5 DLT CYCLIC TEST

Table D-5 shows the strain gage locations of the ST006 DaDT test article. They are also shown in figure 79 of the main report.

Table D-5. Strain gage locations of ST006.

Strain Gage Number			Location
Axial	Bi-Axial	Rosette	
A1			A1 Lower skin FWS 24.8″ on fwd spar
A2			A2 Upper skin FWS 24.8″ on fwd spar
A3			A3 Upper skin FWS 27.0″ on fwd spar
A7			A7 Upper skin FWS 66.5″ on aft spar
A8			A8 Upper skin FWS 90.5″ on fwd spar
A15			A15 Upper skin FWS 42.5″ on fwd spar
A21			A21 Upper skin FWS 38.25″ on fwd spar
A22			A22 Upper skin FWS 38.25″ on aft spar
A23			A23 Lower skin FWS 38.0″ on fwd spar
A24			A24 Upper skin FWS 53.25″ on fwd spar
A25			A25 Lower skin FWS 53.25″ on fwd spar
A26			A26 Upper skin FWS 76.25″ on fwd spar
A27			A27 Lower skin FWS 76.25″ on fwd spar
		R1	R1 Root rib at upper fwd corner
		R2	R2 Lower skin FWS 24.8″ and 2.5″ forward of fwd spar
		R3	R3 Upper skin FWS 24.8″ on aft spar
		R16	R16 Upper skin FWS 61.2″ on fwd spar
		R17	R17 Upper skin FWS 64.4″ on fwd spar
		R18	R18 Upper skin FWS 68.15″ on fwd spar
	B5		B5 Upper skin FWS 50.7″ centered between fwd and aft spar
	B6		B6 Upper skin FWS 64.4″ (1.67″ fwd of damage FWS 64.4″)
	B7		B7 Lower skin FWS 64.4″ (1.67″ fwd of damage FWS 64.4″)
	B8		B8 Upper skin FWS 64.4″ centered between fwd and aft spar

Figure D-28 shows the vertical displacement results for post-DaDT residual strength of the ST006 test article. Displacement gages D1 and D2 indicated that there was a rotation of the test article in the $-T_Y$ direction (reference axis system may be found in figure C-1 of appendix C). Figures D-29–D-31 show the strain gage readings of the ST006 test article during the post-DaDT residual strength test.

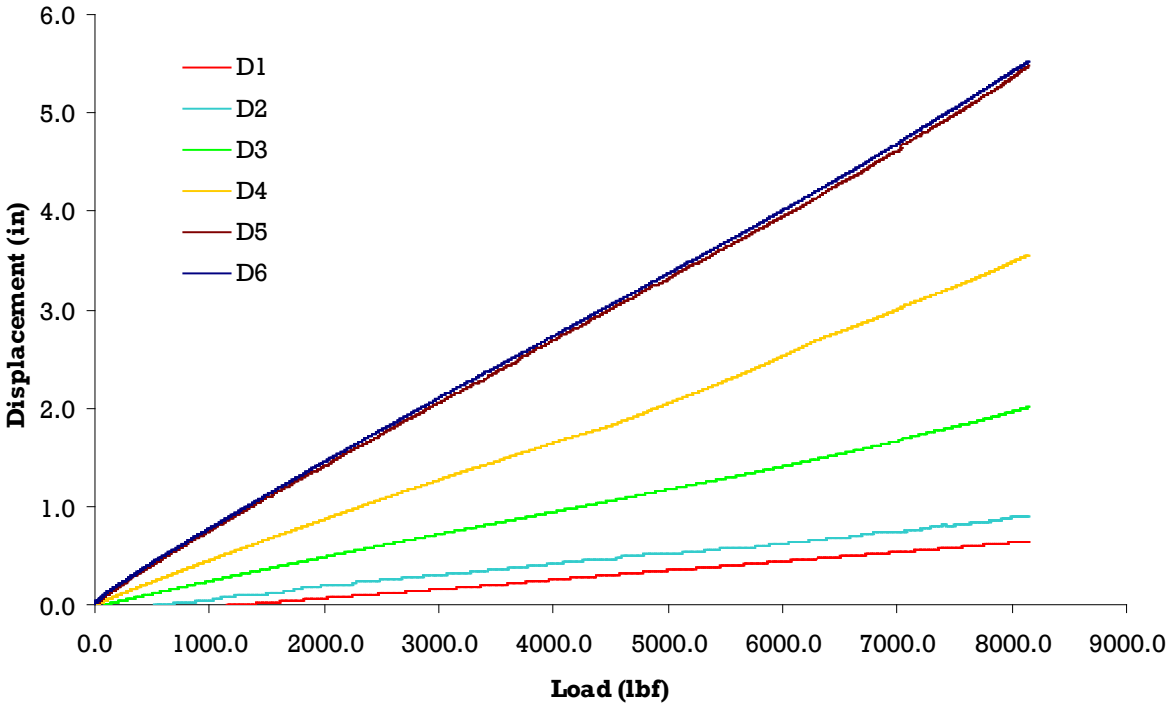

Figure D-28. Vertical displacements—ST006

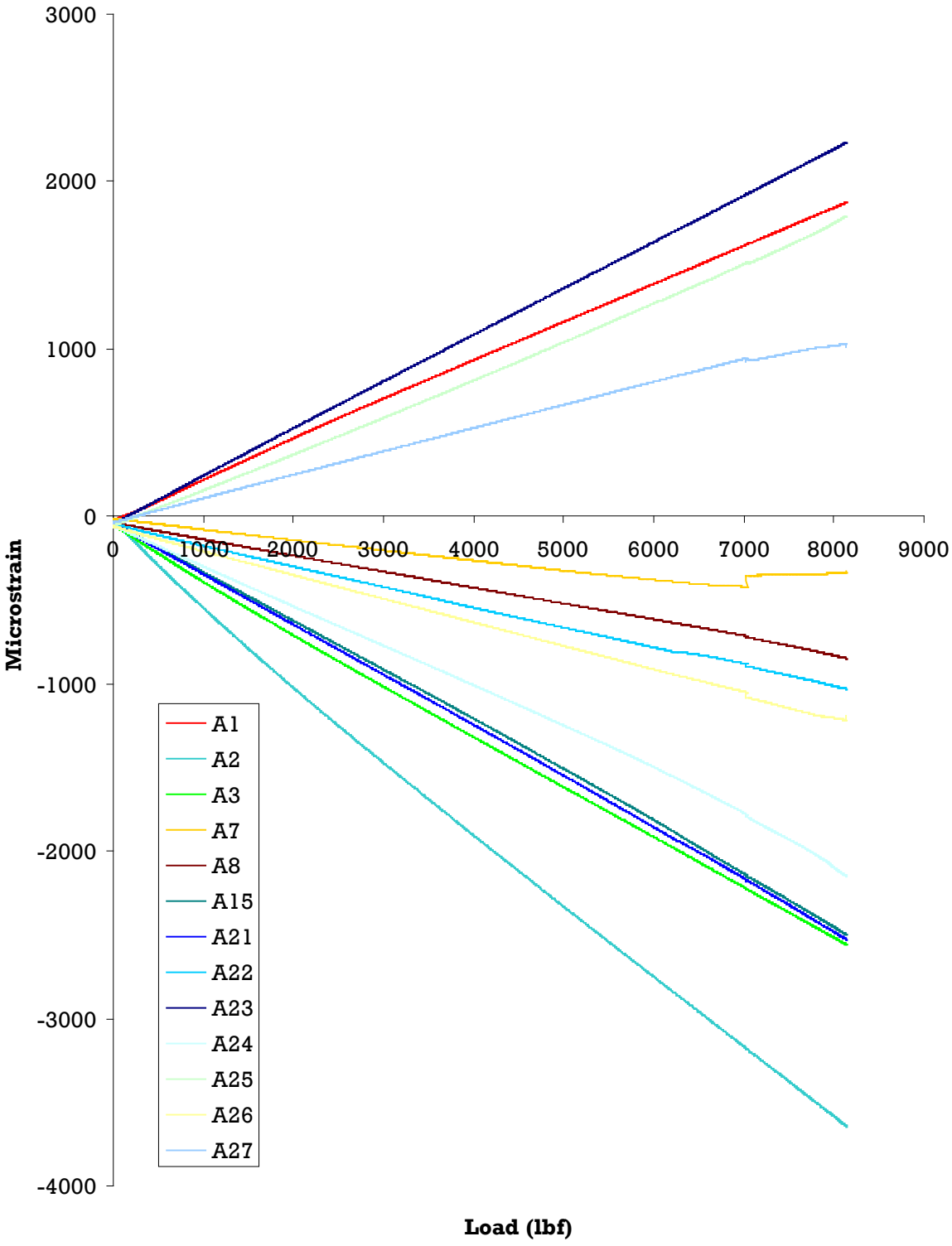

Figure D-29. Strains from axial gages—ST006

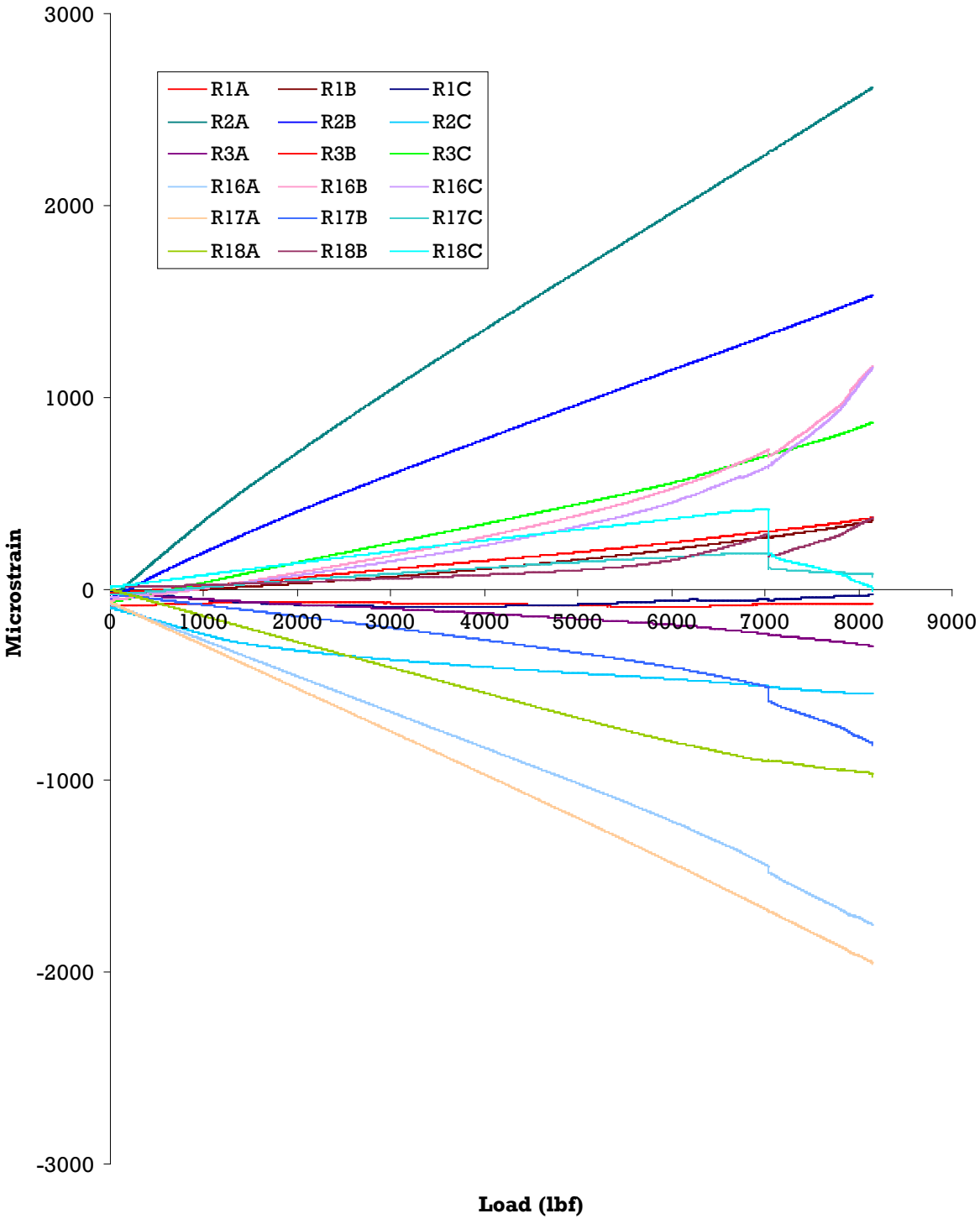

Figure D-30. Strains from rosettes—ST006

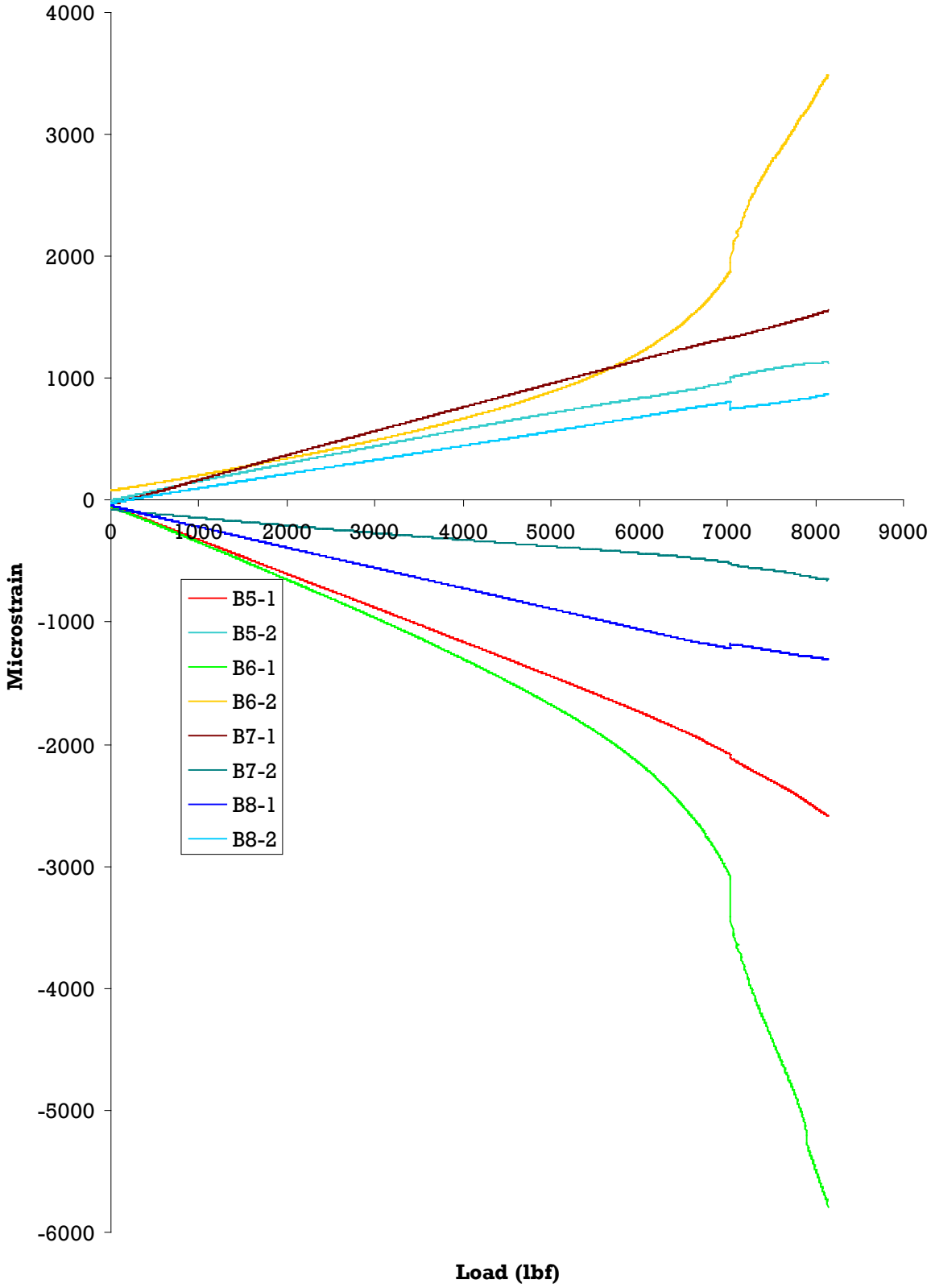

Figure D-31. Strains from biaxial gages—ST006

APPENDIX E—FOUR-POINT BEND ELEMENT TEST RESULTS

Static-tested forward wing ST003 was sectioned to machine several four-point bend (4PB) specimens to determine the severity of the damage and the configuration (i.e., impact with a knife edge or 1-in. hole to simulate Category 3 [CAT3] damage on the front spar that shifts the residual strength of the test article to the limit conditions). These 4PB specimens were extracted after sectioning the article at several stations, as shown in figure E-1.

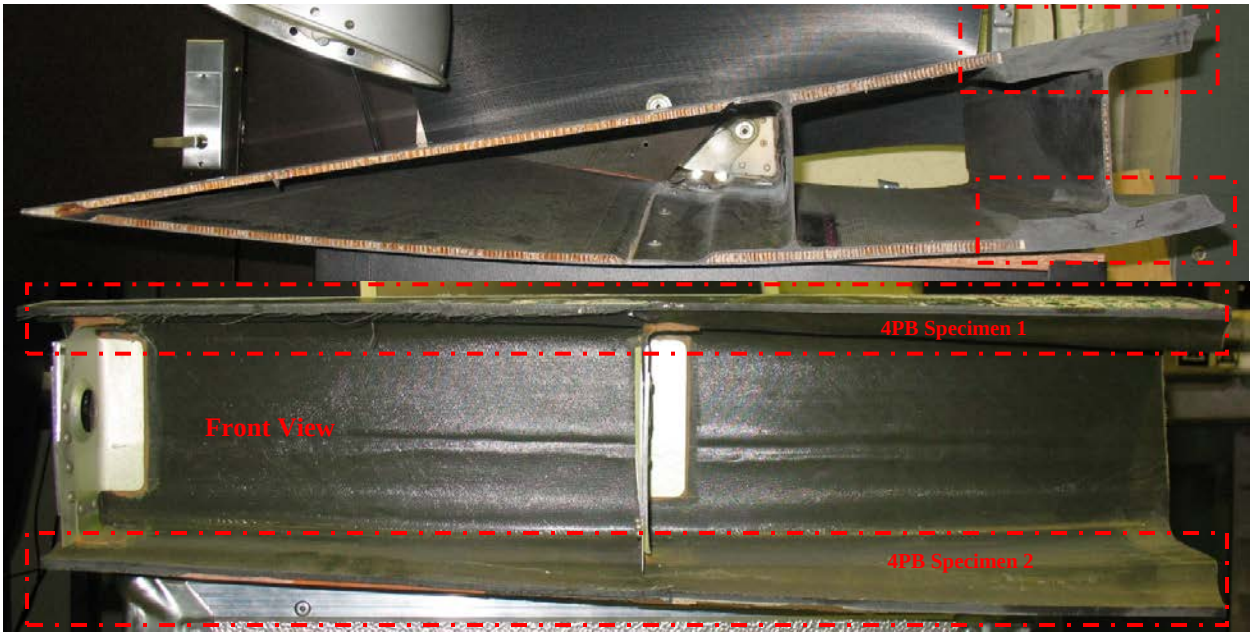

Figure E-1. 4PB test specimen extraction

Several 24-in.-long specimens were cut from both top and bottom spar caps (front spar) to be tested in 4PB test configuration. The web was cut and cleaned to form relatively flat specimens. Several damage configurations, along with the undamaged 4PB specimens, were tested (figure E-2). Test specimens were named using the forward wing station (FWS) corresponding to the center of the specimen followed by "T" or "B" to indicate whether the specimen was extracted from the top or bottom spar cap, respectively (i.e., specimen name 90.5B corresponds to a specimen extracted from the bottom spar cap and the center of the specimen corresponds to FWS 90.5). Two holes, a 1/2- and a 1-in., were drilled at the center of test specimens 66.5B and 114.5T, respectively, while test specimens 90.5T and 90.5B were impacted with a 180 ft-lb energy level using a 1-in.-wide knife edge (as shown in figure E-3). Specimen 90.5T was impacted while resting on two wood bases placed 5 in. apart and lightly clamped. Because the backside of this specimen indicated significant delaminations, specimen 90.5B was sandwiched between the wood bases and an aluminum picture frame with an 8-by-8-inch opening (figure E-3).

(a) Damaged 4PB elements (post-test)

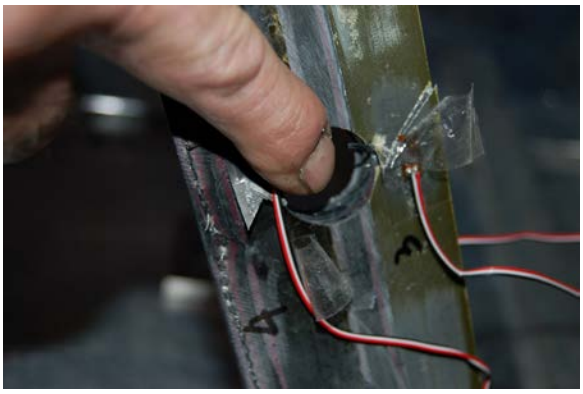

(b) 114.5T failure mode

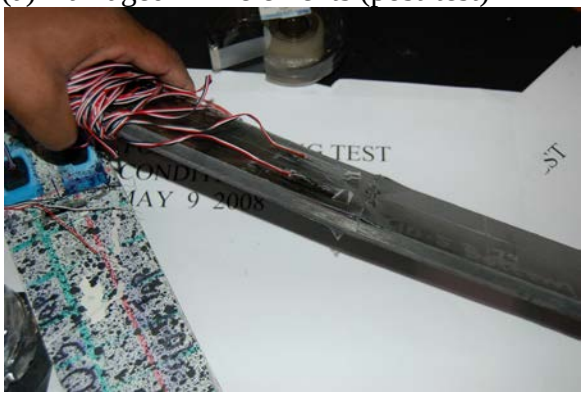

(c) 90.5B failure mode

(d) 90.5T failure mode

Figure E-2. 4PB test specimens (before and after test)

Figure E-3. Impact setup for 90.5B 4PB test specimen

Damaged specimens were then strain-gaged and tested in 4PB test configurations, as shown in figure E-4. Strain data from damaged specimens were compared with those of undamaged 4PB specimens in figure E-5. Next, the stress and strain data corresponding to the onset of damage growth of open hole and impacted specimens were normalized by the corresponding data from the undamaged specimens and compared in figure E-6. The 1/2- and 1-in. open-hole specimens indicated approximately 20% and 40% decrease, respectively, in load-carrying capability, whereas the strain values corresponding to the onset of damage growth were approximately 10% and 20% lower than those for undamaged specimens. Both impacted specimens indicated significant load-carrying capabilities because the damage spread mostly across the width of the specimen, especially on outer plies.

Figure E-4. 4PB element test setup

Because there were insufficient data to conduct a full failure analysis, the data obtained from the 4PB tests and the full-scale impact trials (shown in table 9 of the main report), along with the post-impact inspections, were used to determine an appropriate energy level and an impactor configuration to inflict CAT3 damage on ST005 and ST006 full-scale test articles.

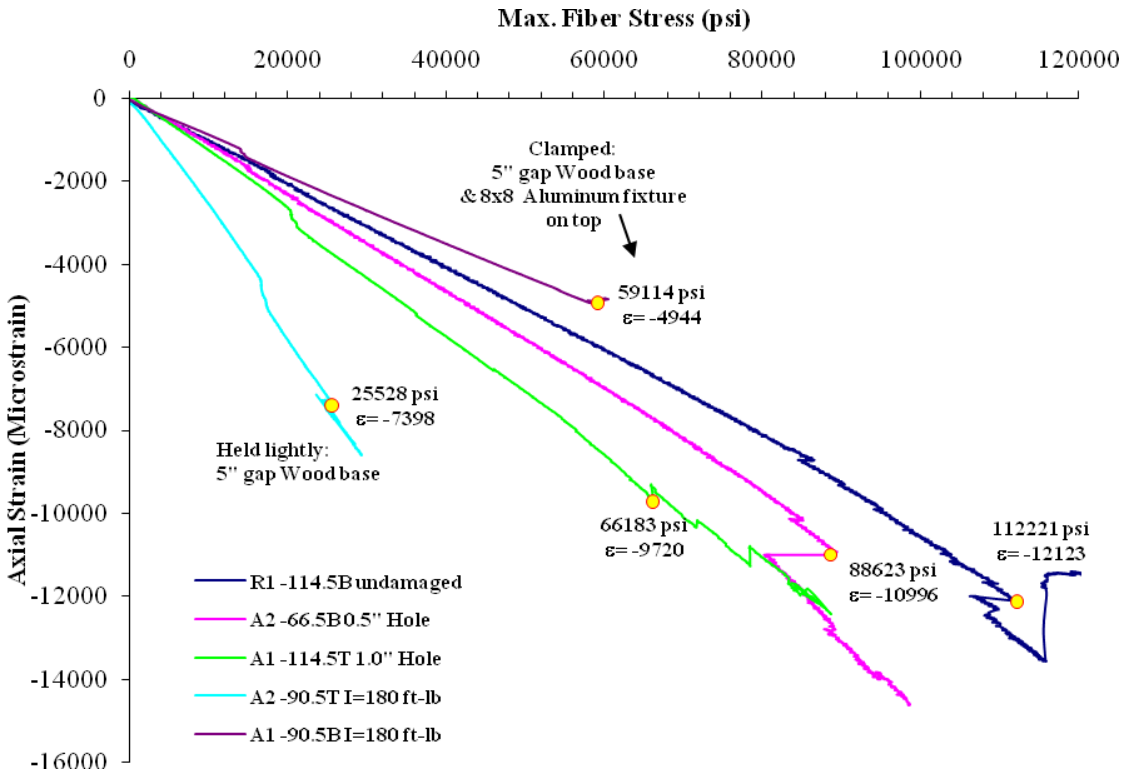

Figure E-5. Summary of 4PB test results

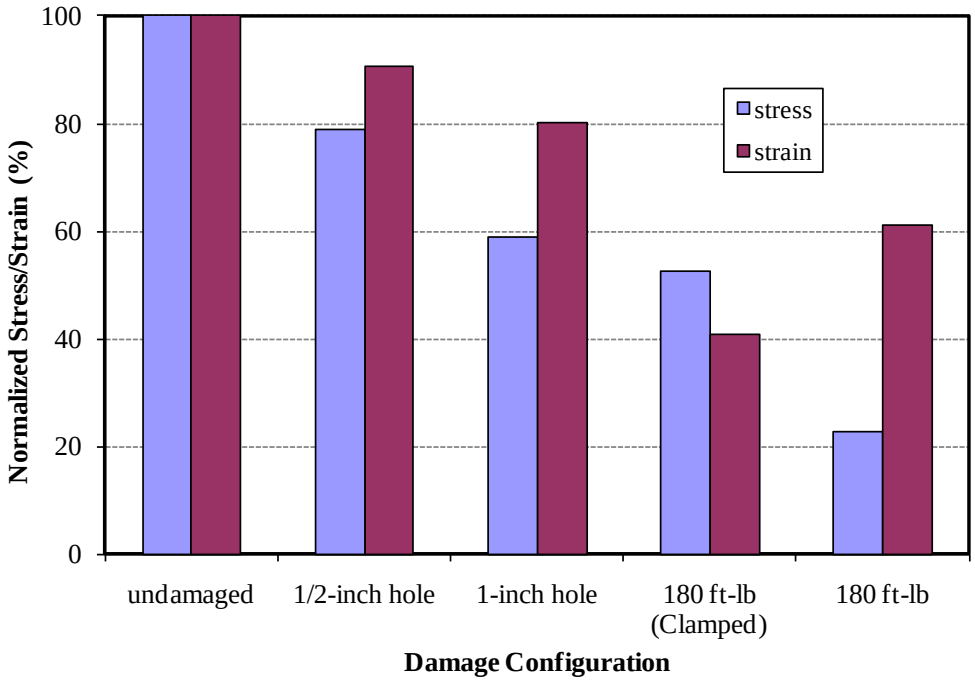

Figure E-6. Failure stress/strain comparison (normalized by the data from undamaged specimens)